A Power Efficient Spectrophotometry & PPG Integrated Circuit for Mobile Medical Instruments

DISS. ETH NO. 24241

A Power Efficient Spectrophotometry & PPG Integrated Circuit for Mobile Medical Instruments

A thesis submitted to attain the degree of
DOCTOR OF SCIENCES of ETH ZURICH
(Dr. sc. ETH Zurich)

presented by
PHILIPP CHRISTOPH SCHÖNLE
MSc ETH EEIT
born on 14th December 1986
citizen of Bern BE, Switzerland

accepted on the recommendation of

Prof. Dr. Qiuting Huang, examiner
Prof. Dr. Christian Enz, co-examiner

2017

Abstract

Numerous non-invasive spectrophotometry and photoplethysmography (PPG) based monitoring and imaging techniques have been developed in the past decades, including arterial oxygenation estimation with pulse oximetry, tissue perfusion assessment with near-infrared spectroscopy (NIRS), and thereon based brain activity imaging. Applications in medical- and neuroscience research as well as mobile diagnostics, long-term monitoring devices, and fitness trackers require a small form factor. The non-invasive and convenient optical interface to tissue is a major reason for the popularity of the aforementioned techniques, especially in the consumer market and in monitoring particularly vulnerable neonate patients. This however comes with considerable power consumption for tissue illumination which renders data acquisition current consumption relevant – if not dominant – in the system. This thesis presents a PPG analogue front-end designed for integration in a multi-biosensor system-on-chip. Compared to the state-of-the-art, a power saving of 68% has been achieved for equal signal quality and conditions. Further emphasis lies on low receiver noise, high maximum sampling rate, ambient light suppression, multi-channel capability, and area efficiency. In addition to the front-end circuit implementation, preliminary hardware prototypes for wearable and implantable medical instrumentation are presented, and the use of pulse wave velocity for blood pressure estimation is investigated as a potentially less-invasive alternative to catheter based pressure transducers in implantable telemetric systems for long-term experiments in laboratory animals. In such a device multiple vital signs, i.e., heart rate, blood pressure, respiratory rate, and arterial oxygenation could be covered by a single PPG probe.

Cumpigliament

Els davos decennis ein diversas metodas d'analisa e surveglionza da parameters vitals vegnidas sviluppadas sin basa da spectroscopia e foto-pletismografia (FPG). Denter auter per mesirar l'oxygenaziun dil saung e giudicar la circulaziun en differents organs sin basa da spectroscopia egl infra-tschietschen maneivel (engles: near-infrared spectroscopy, NIRS); ina tecnica che lubescha schizun da far maletgs dall'activitad cerebrala. Differentas applicaziuns ella scrutaziun medicinala ed en apparats mobils da diagnosa e surveglionza a liung temps pretendan ina miniaturisaziun dall'electronica. Dapi cuort vegn FPG era duvrau en uras da sport per mesirar il battacor. La popularitad da quellas metodas sebasa per ina gronda part sin l'emperneivladad dalla colligiaziun nuninvasiva optica cun il tissiu. Denton drova l'illuminaziun dil tissiu in bien ton energia, relevant sche buc dominant per il total. En quella dissertaziun vegn presentau la concepziun e realisaziun d'in microchip analog per FPG e NIRS e l'integraziun da quel en in sistem-en-in-chip. Cumparegliau cul stan actual dalla tecnica drova in sistem cun quel mo in tierz dall'energia. Plinavon porscha quel sin surfatscha minimala in spert retschevider da bassa ramur e buna suppressiun da glisch d'ambient che ha la capabilitad da supportar in grond diember da canals. Ulteriuramein vegnan emprems prototips d'apparats mobils ed implantabels sin basa da nos chips presentai, ed in'alternativa per la schazegiada dalla pressiun dil saung discussiunada per implantats da telemetria per experiments en animals da labor pigns. Utilisond mesiraziuns pletismograficas dalla spertadad dall'unda da pressiun sanguina per quella schazegiada, sa in tal implantat registrar plirs indicaturs vitals cun ina singula sonda optica: il battacor, la rata da respiraziun, l'oxygenaziun e la pressiun dil saung.

Zusammenfassung

Die Photoplethysmographie (PPG) und die Spektralphotometrie bilden die Grundlage für eine Vielzahl von Verfahren der Medizintechnik, welche bildgebend sind oder der Überwachung von Vitalzeichen dienen, wie z.B. die Messung der Blutsauerstoffsättigung mittels Pulsoximetrie, die Beurteilung der Gewebedurchblutung mithilfe von Nahinfrarotspektroskopie und darauf basierend die Beobachtung der Hirnaktivität. Einige Anwendungen in den Medizin- und Neurowissenschaften aber auch in der mobilen- und Langzeitdiagnostik erfordern eine kleine Bauform und dadurch hohe Energieeffizienz. Die optische und nichtinvasive Messgerät-Gewebe-Schnittstelle ist ein Hauptgrund für die Popularität dieser Messverfahren – ist jedoch auch leistungshungrig und kann den Stromverbrauch des Gesamtsystems dominieren. In dieser Arbeit wird eine PPG-Sensorschaltung und ihre Integration in ein System-on-Chip vorgestellt, welche im Vergleich zum bisherigen Stand der Technik 68% weniger elektrische Leistung aufnimmt um unter gleichen Bedingungen Signale gleicher Qualität aufzuzeichnen. Weitere Schwerpunkte der Konstruktion liegen auf tiefem Empfängerrauschen, hoher maximaler Abtastrate, Umgebungslichtunterdrückung, Mehrkanalunterstützung und Flächeneffizienz.
Des Weiteren werden in dieser Dissertation Prototypen von mobilen und implantierbaren Medizinalgeräten beschrieben und die Blutdruckmessung basierend auf der Pulswellengeschwindigkeit als eine mögliche, potenziell weniger invasive, Alternative zu katheterbasierten Druckwandler in Langzeittierversuchen untersucht. Ein solches Gerät könnte verschiedene Vitalzeichen mit einer einzelnen optischen Sonde aufzeichnen: Puls, Atemfrequenz, Blutdruck und arterielle Blutsauerstoffsättigung.

Acknowledgements

The present thesis marks the conclusion of five years of doctorate. Many people contributed during this time to the success of this endeavour – credit shall be shared with them.
I would like to thank Prof. Qiuting Huang for giving me the opportunity to pursue my Ph.D. at the Integrated Systems Laboratory (IIS), for the freedom I was granted, and for his confidence in me and my work. I am grateful to Prof. Christian Enz from EPFL in Neuchâtel for co-examining this dissertation.
A special *thank you* goes to Pascale Meier, Noé Brun, and Jonathan Bösser who did most of the 'real' work on the wearable and implantable platforms and conduced to an enjoyable atmosphere in the analogue lab – and beyond. I most sincerely thank Tom Kleier for his support in PCB design as well as for his steady hand and patience, which proved to be crucial for the assembly of miniaturised electronics. Similar qualities are attributed to Martin Lanz: thank you for sawing wafers, for bonding dozens of chips, for etching many small PCBs, and for the great help with the manufacturing of the implantable optical probes. I also much appreciated the well-sorted work shop of Hansjörg Gisler and his exhortation for more precision in rapid prototyping.
My work being part of a system-on-chip meant close cooperation with the fellow PhD students Schekeb Fateh, Florian Glaser, and Giovanni Rovere – I greatly appreciate all their efforts in our common project. Roger Ulrich shall also be mentioned here, whose initial *Cerebro* chip design was a starting point for our work. The mutual help as well as the exchange of experiences and ideas among colleagues in the analogue and digital IC design groups of IIS crucially contributed to the success of this work – common after-work activities have been a

welcome diversion: I would like to particularly thank Thomas Burger, Jürg Treichler, Christian Benkeser, Felix Schulthess, Petrit Bunjaku, René Blattmann, Christoph Roth, Stephan Altorfer, Christoph Keller, Luca Bettini, Harald Kröll, Benjamin Weber, Sandro Belfanti, Xu Han, Mauro Salomon, David Mack, Lianbo Wu, Michael Gautschi, Pirmin Vogel, Michael Mühlberhuber, David Bellasi, Anne Ziegler, Michael Schaffner, and especially Benjamin Sporrer – with whom I shared a coffee machine for four years and had many pleasurable coffee break discussions.

I am deeply indebted to the design centre and IT staff for their enduring maintenance of the computer infrastructure and help with the CAD tools, in particular to Christoph Wicki, Beat Muheim, and Frank Gürkaynak – special mentioning deserves Frank's whisky bar where quite some long working day ended with a sip of finest malt while chatting about photography. I also much appreciate the administrative support of Alexandra Bakanova, Christine Haller, and Monika Zwahlen – most particularly their commitment in the organisation of the IIS winter- and summer parties.

The exchange and cooperation with researchers in the fields of medicine, biomedical engineering, neuroscience, and material sciences was a prerequisite for this work. I want to particularly thank Dr. med. Qing Wang from the division of nephrology and hypertension at CHUV in Lausanne with whom we tested our circuits in acute animal experiments for his enduring commitment and enthusiasm for our cause. I also enjoyed the continual communication with Frédéric Michoud and Prof. Stéphanie P. Lacour from the laboratory for soft bioelectronic interfaces (LSBI) at EPFL in Geneva with whom we worked on a neural stimulation and recording implant and an head-stage for experiments in optogenetics. The exchange with Stefan Kleiser and Nassim Nasseri from the biomedical optics research laboratory (BORL) of USZ and ETH on near infrared spectroscopy (NIRS) was very helpful to establish design specifications for my chip. The cooperation with Sebastian Segitz, Stéphanie Saxer, and Prof. Dr. med. Konrad E. Bloch from the pneumology division at USZ gave us the possibility to test the capabilities, flaws, and workings of various commercial pulse oximeters and gave insight in real-world usage scenarios of a mobile health device in a hospital environment.

Many thanks go also to Advanced Circuit Pursuit AG for helping with the production of the various test chips, particularly to Jürgen Rogin and David Tschopp. I further thank the latter for his early suggestions on alternative usage scenarios for my chip. They contributed significantly to the motivation for a design which covers a broad range of applications. I am very grateful to Jürg Nigg of Arcotronic AG for repeatedly lending me his high-resolution spectrometer.
Finally, I want to thank friends and family for their support and diversion throughout the years: In particular, I thank Martin Caduff and Curdin Maissen for their long-time friendship and for all the profound debates on anything ranging from quantum physics to architecture. I am equally grateful for the friendship of Johannes Widmer, Manuel Widmer, and Andreas Romer, for the good times we had during our studies and have on regular reunions ever since. Many thanks to you, my brother Jonas: for travelling with me to the (northern) end of the earth and for the bottle of chilled beer which reliably awaits me at the train station, marking the beginning of a common week-end back home. Foremost, I thank my parents Marianne and Stephan for their enduring support and encouragement.
I much appreciate the proof-reading of the present thesis by Jonathan Bösser, Thomas Burger, and Schekeb Fateh – the author alone however takes full responsibility for any remaining errors and mistakes. This work has been funded by *Nano-Tera.ch*, an initiative financed by the Swiss Confederation and scientifically evaluated by the Swiss National Science Foundation. I am grateful for the effort which personae of the scientific community put into the realisation of such programs and for the political intend, as well as the taxpayers' willingness, to invest in education and research.

Zurich, February 2017

Philipp Schönle

Contents

Chapter 1

Introduction

1.1 Spectrophotometry in Medicine

Today, non-invasive and *in-vivo* spectrophotometry based monitoring and imaging are widely used in clinical diagnostics and research. Most prominently in pulse oximetry, which is routinely used in diagnostics as a fast, convenient, and low-price alternative to chemical blood-gas analysis for the measurement of arterial oxygenation. It is indeed so prevalent today that it's sometimes considered a *fifth vital sign* along with heart rate, blood pressure, respiratory rate, and body temperature. Continuous arterial oxygen saturation monitoring is standard in today's emergency care, intensive care units, and operating theatres.

Near-infrared spectroscopy (NIRS) [1, 2] is a related technology to measure tissue perfusion and oxygenation. The *optical window* in the spectral range of 700-1000 nm, where light is comparatively weakly absorbed by water, fat, bone, proteins, collagen, melanin, and haemoglobin, allows light to penetrate relatively deep and thus to transcutaneously assess regional perfusion of organ tissue. Widespread is the use for cerebral oxygenation assessment but the superficial location of organs like liver and kidney allow for non-invasive transcutaneous oxygenation measurements thereof as well – at least in neonates and infants where skin and fat layers are thin [3]. The use of regional

NIRS for organ specific oxygenation measurements as early indicator for different serious conditions is investigated in various clinical and preclinical studies, e.g., [4–6], and is found to be in combination a good base for the estimation of global venous oxygenation while the additional organ-specific oxygenation and blood flow information correlates well with organ function [7]. NIRS systems with up to 32 emitter and receiver channels have been developed for near-infrared imaging (NIRI) – spatially resolved cerebral oxygenation imaging. A tool which is frequently used in neuroscience as a non-invasive brain activity imaging method based on the measurement of local changes in the cerebral blood flow [8–10]. Advanced multi-wavelength NIRS systems can additionally to oxygenation and perfusion also assess changes in cytochrome-c-oxidase (CCO) and total haemoglobin [11]. The photoplethysmography (PPG) waveform, on which the arterial oxygenation estimation is based in pulse oximetry, is a useful measurand in its own right [12]: When continuously monitored in combination with other vital signs, waveform amplitude changes can, e.g., indicate sudden peripheral vasoconstriction (a measure for the depth of anaesthesia) while exceptionally high respiratory variability of the waveform can be a sign for hypovolemia (low blood volume) and thus for occult bleeding.

Simultaneous recording of the photoplethysmographic waveform at multiple sites (or the combined recording of a single PPG and a single-lead ECG) allows for the estimation of the propagation velocity of the arterial pressure wave which is known to be correlated to blood pressure and artery stiffness. Pulse wave velocity (PWV) measurement is clinically used for the assessment of arterial condition and significant research effort is observed in using it for a new generation of non-obtrusive long-term blood pressure monitoring devices [13–17].

Finally, PPG is nowadays widely used in consumer electronics for heart-rate measurement in 'smart'-watches and fitness-bands where it increasingly replaces the less convenient to wear ECG chest straps. The commercial potential of this mass market led to notably increasing interest in integrated circuit (IC) solutions for PPG signal acquisition [18–21]. High interest in wearable long-term oximetry is anticipated and considerable research resources are committed on

increasing reliability under harsh conditions with respect to motion, ambient light, and probe (dis)placement [19, 20, 22–25].

Optical *in-vivo* monitoring and imaging has found a variety of applications in medical diagnostics, surveillance, and research thanks to its advantages over previous state-of-the-art, i.e., non-invasiveness and continuous monitoring in blood-gas analysis, respectively the more convenient interface in heart-rate and brain activity monitoring.

1.2 Technological Evolution

The wide spread of photoplethysmographic and spectrophotometric monitoring techniques with applications ranging from pulse meters to brain activity imaging and implantable vital signs telemetry systems drives academic and industrial effort in advancing the state-of-the-art of the underlying electronics and data analysis. The technological development in microelectronics and related fields enabled the miniaturisation of monitoring and imaging devices from bench apparatuses to portable and indeed wearable devices.
Fiberoptics allowed for locally confined light application and sensing in early oximeters [26] and NIRS [27] instruments although lamps, filters, and detectors were bulky. E.g., fiberoptic catheters have been developed to monitor arterial oxygenation prior to the invention of the pulse oximeter and the first pulse oximeter itself was based on fiberoptics, an halogen lamp, and filters [26]. Advances in optoelectronics allowed to replace bulky optics and lamps with light emitting diodes (LEDs) and photodiodes. The confined spectral emission of the LEDs makes filters obsolete while silicon photodiodes cover quite exactly the near-infrared *optical window* of tissue. More recently, laser-diodes with an even narrower spectrum are used as well [8]. Fiberoptics are still widely used in NIRS imaging since it provides the medical researcher flexibility in the placement of emitters and detectors [28] which is not given in preconfigured miniaturised systems. Most of the latter are two-wavelength systems and thus lack spectral diversity for some applications, e.g., the measurement of CCO variability, which is covered by fiberoptical broadband near-infrared instrumentation like [11].

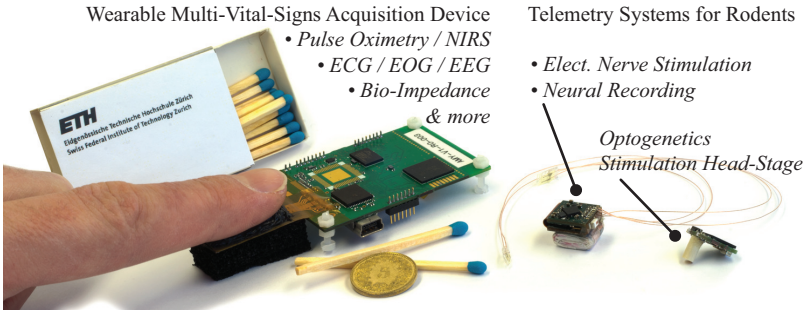

Figure 1.1: Recent demonstrators for wearable and implantable multi-functional telemetry devices.

Simultaneous advances in integrated circuit technology and design reduced size and costs of data acquisition electronics and provided increasing computation performance in ever-smaller hardware – crucial for online analysis of the acquired signals. Decreasing feature sizes in CMOS technology allows for the integration of more functionality on the same area, both in the analogue and in the digital domain. This lead to the rise of systems-on-chip (SoC) which massively decreased the amount of chips and passive components in today's electronic devices. This again allows for smaller device size, as does increasingly power efficient hardware by reducing required battery size which is often a dominant contributor to the device dimensions. Furthermore, RF CMOS [29, 30] enabled today's prevalent low-cost wireless short- and long-range digital data transmission.

Together, the technological advances of the past decades in microelectronics, optoelectronics, printed circuit board (PCB) manufacturing, batteries, and microelectromechanical systems (MEMS) enable us today to build health monitoring patches [31, 32] or matchbox sized multi-vital-signs acquisition telemetry devices for non-invasive long-term monitoring in humans and even smaller devices for implantation in rodents for prolonged animal experiments – e.g., our telemetry prototypes shown in Fig. 1.1 and described in more detail in Chap. 5 and Chap. 6.

Decrease in cost and size of medical instrumentation enables cost

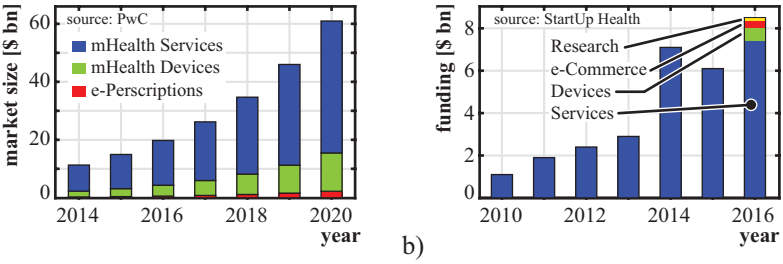

Figure 1.2: Global mobile health market estimate by PwC [33] (a) and recent development of global investment in *digital health* (b) [34]. *In (b) data for 2016 is extrap. to incl. Q4 – only publicly available data is incl.*

reductions in hospitals, e.g., by earlier moving of patients from the intensive care unit to the nursing ward without losing the ability to continuously monitor specific vital signs, allows for less obtrusive long-term monitoring, and enables new applications in sports medicine, medical research, and neuroscience.

1.3 The Dawn of Mobile Health

Today – ever better access to mobile broadband internet and the prevalence of 'smart'-phones and tablet computers coincides with ever-rising health costs and ageing populations in industrialised and emerging countries. A constellation that comes with great business potential for innovative approaches to counter the latter with the former. The buzzwords digital- or mobile health (mHealth) summarise a multi-faceted young industry which spans from consumer electronics to interconnected hospitals and from the *quantified self* trend to *big data* analytics. PricewaterhouseCoopers (PwC) sees the industry currently emerging from a niche market [33] and gives growth prognosis of 31% and 37% for, respectively, mHealth services and -devices until the year 2020 (Fig. 1.2a). By then, it expects the mHealth market to reach a volume of 61 billion[1] US-$. About a fourth of which is expected

[1] 1 billion = 10^9

to be spent on mobile health devices while the remaining market is dominated by (software) services. The latter however depend on mHealth devices such as wearable ECG and oximetry patches [31, 32] in hospitals, ECG 'smart'-phone companions (e.g., *AliveCor* [35]), sport watches or fitness trackers. Another example of mHealth is *DoctorKePaas* [36], an Indian service that comes with a small suitcase carrying various medical instrumentation that connects via the included tablet computer to the service's cloud server – enabling video-call remote doctor's consultations in secluded areas.
The development of global investment since 2010 (Fig. 1.2b) reflects the high hopes into this market. A sudden increase is observed for the year 2014 in which the term *'smart'-watch* and the brand *fitbit* found their way into the vocabulary of the public at large – following the presentation of novel devices in late 2013. In 2016, 61 million fitness- & sports trackers and 33 million 'smart'-watches are expected to be sold corresponding to a 10.1 billion US-$ in value [37]. Many of these gadgets include an optical heart-rate meter based on PPG. By 2020 sales are predicted to increase to totally 289 million devices worth 17.4 billion US-$ [37]. The link between the two markets is mainly due to various *wellness* services providing, e.g., *apps* intending to motivate the owners of such devices to engage more in sports by granting performance-linked benefits from health insurances or employers [38]. Independent of the acceptance and long-term success of single mHealth services, we may expect the following trends concerning medical instrumentation hardware:

- *Boom in quantity.* Disposable data acquisition patches or a wearable device for each patient in hospitals, a complete set of vital-signs monitoring instruments in each home, and continuous monitoring of some data on everybody's wrist. Every single of these scenarios causes additional growth in the market for medical instrumentation.

- *Miniaturisation.* A small device size is essential for many of the continuous monitoring concepts. It also enables the integration of mHealth functionality into prevalent devices such as watches and phones.

- *Pricing pressure.* Mobile health concepts require medical grade instrumentation to be affordable for consumers. Low unit prices are also required in hospital scenarios in which many patients will be continuously monitored with wearable or even disposable devices.

- *Fragmentation.* Although related, the envisioned applications are not equal. Thus a single device cannot cover all of them – but different embodiments of a single hardware platform may cover a wide variety of applications.

The silicon industry requires high volume in order to distribute its high research and development (R&D) and initial production costs, if the market however is big enough, it can produce at very low unit cost. Given the expected application diversity, a multi-biosensor SoC covering the requirements of a multitude of devices may be the key to success in this fragmented market.

1.4 Contributions

The main focus of the present dissertation is on the design and implementation of an application-specific integrated circuit (ASIC) for PPG and continuous wave (CW) NIRS based medical instrumentation, destined to be used with external photodiodes and LEDs as photodetecting and light-emitting devices. Herein, special emphasis is put on:

- *Power Efficiency.* Power consumption is typically dominated by the LEDs rather than the front-end circuitry. To achieve low power consumption not only in the datasheet but in a real application, a thorough system level analysis of the power-noise trade-off is provided. The discussion comprises the optoelectronic external components, physiological parameters as well as design choices for receiver and transmitter circuits. A figure-of-merit is introduced which covers all relevant (system level) parameters to allow for comparison to current state-of-the-art chips from academia and industry.

- *Performance Requirements.* Overall noise and linearity requirements for accurate arterial oxygenation estimation in pulse oximetry are derived as a function of physiological parameters. Countermeasures for interference of ambient light, motion, and physical conditions on the measurement are presented. Effectiveness of the implemented ambient light cancellation scheme is demonstrated with measurements.
- *Receiver Design.* Capacitive and resistive feedback transimpedance amplifier (TIA) receiver architectures are analysed and compared with respect to performance, circuit area, and power efficiency. It is shown that both topologies come with advantages for a certain range of input signal strengths and consequently both are implemented in order to cover a wide range of photogenerated currents and thus applications.
- *Noise Curbing.* Different techniques are discussed to curb ADC and amplifier excess noise in the receiver. A provided comparison of expected $k_\mathrm{B}\mathsf{T}/C$ noise and measurements with those techniques enabled and disabled demonstrate their effectiveness.

Besides ASIC design and implementation, this thesis comprises:

- *Physiological Background.* Reviews on the background of photoplethysmography, pulse oximetry, and pulse wave velocity are given with a special emphasis on physiological interdependencies and possible interferences. Where possible, this includes quantitative values or estimations.
- *Platform for Implantable Medical Instrumentation.* The PPG front-end circuit is incorporated in a multi-biosensor SoC. We present an envisioned platform for implantable medical instrumentation in long-term animal experiments based on this SoC and first prototypes thereof for different applications. The challenging conditions impose an excellent test case for the practicability of hard- and software designs.
- *Implantable Blood Pressure Measurement.* A novel blood pressure measurement method for rodent implants based on PPG pulse wave velocity measurements is introduced and preliminary results are presented.

1.5 Outline

The remainder of the present thesis is organised as follows:

Chapter 2 is a review on spectrophotometry in general and pulse oximetry in particular. Optical properties of tissue and their influence on therein travelling photons of different wavelengths are discussed and a quantitative estimation is given for the different absorption components associated with venous and arterial blood. In combination with an analysis of acceleration on the blood flow, this gives important insight in the cause of motion artefacts and observed wavelength-depended differences thereof.

Chapter 3 reviews haemodynamics and mechanics necessary for the understanding of the interdependence of various physiological parameters on the pulse wave velocity and reveals under which conditions blood pressure can be calculated from measured pulse wave velocity.

Chapter 4 presents a top-down approach towards an optimised PPG front-end integrated circuit. It starts with a system level discussion on performance- and functionality requirements as well as limitations by the optoelectronic components and the statement of a fundamental limit in the noise-power trade-off. A thorough analysis of transimpedance amplifier architecture and ambient light cancellation techniques follows before describing the actual implementation of both, receiver and LED driver. The chapter concludes with measurement results and a comparison to the state-of-the-art which reveals that the presented chip is unrivalled in terms of power efficiency.

Chapter 5 provides a short summary on ongoing work on a system-on-chip which the reported PPG front-end is part of. It includes a short description of its ExG recording front-end and its neural stimulation hardware designed for implantable telemetry systems.

Chapter 6 describes an envisioned platform based on the above system-on-chip for telemetric implants in rodents and other laboratory animals. First prototypes for specific applications are presented and preliminary experimental results for an implantable system recording heart rate, blood pressure, arterial oxygenation, and respiration rate with a single PPG probe are reported.

Chapter 7 concludes this dissertation with a summary of main research contributions. Possible future research and expected development in the field is outlined.

Chapter 2

Background: Pulse Oximetry

2.1 Spectrophotometry

Spectrophotometry is the quantitative measurement of transmissive or reflective properties of material. Precise laboratory instrumentation able to resolve the spectrum from 200 nm to 2 µm with up to 0.1 nm precision became available in the 1940s [39]. Spectrophotometers are widely used in chemistry to identify the components and their relative concentration in a solution by decomposing the measured transmittance spectrum into a superposition of known spectra of expected ingredients:
The transmittance ($\mathcal{T}$) of a substance is the ratio of the light intensity ($\mathcal{I}_\mathrm{T}$) transmitted through a substance to the incident light intensity ($\mathcal{I}_0$) on the substance for a given wavelength λ [40]

$$\mathcal{T}(\lambda) = \frac{\mathcal{I}_\mathrm{T}(\lambda)}{\mathcal{I}_0(\lambda)}. \tag{2.1}$$

The absorbance ($\mathcal{A}$) is given as

$$\mathcal{A}(\lambda) = -\log_{10}(\mathcal{T}). \tag{2.2}$$

The Beer-Lambert law [41] states a linear relation between the absorbance, the substance concentration (k) and the length (d) of the light path through this substance:

$$\mathcal{A}(\lambda) = \varepsilon(\lambda) \cdot k \cdot d, \tag{2.3}$$

where $\varepsilon(\lambda)$ is the extinction coefficient of the substance at a given wavelength λ. For a solution consisting of n different components, the absorbance is thus

$$\mathcal{A}(\lambda) = d \sum_{i=1}^{n} k_i \varepsilon_i(\lambda). \tag{2.4}$$

Equation (2.4) has $(n+1)$ unknowns, assuming the spectra of the extinction coefficients are known: the path length d and the different concentrations k_i. A linear equation system can be built with absorbance measurements at different wavelengths to solve for the concentrations. A minimum number of n measurements is required, the last equation is given by the sum of all concentrations being 1. Written in form of a matrix equation, we get

$$\begin{bmatrix} \varepsilon_1(\lambda_1) & \varepsilon_2(\lambda_1) & \cdots & \varepsilon_\mathrm{n}(\lambda_1) & 0 \\ \varepsilon_1(\lambda_2) & \varepsilon_2(\lambda_2) & \cdots & \varepsilon_\mathrm{n}(\lambda_2) & 0 \\ \vdots & \vdots & \ddots & \vdots & \vdots \\ \varepsilon_1(\lambda_\mathrm{n}) & \cdots & \cdots & \varepsilon_\mathrm{n}(\lambda_\mathrm{n}) & 0 \\ 1 & 1 & \cdots & 1 & -1 \end{bmatrix} \cdot \begin{bmatrix} k_1 \\ k_2 \\ \vdots \\ k_\mathrm{n} \\ 1 \end{bmatrix} d = \begin{bmatrix} \mathcal{A}(\lambda_1) \\ \mathcal{A}(\lambda_2) \\ \vdots \\ \mathcal{A}(\lambda_\mathrm{n}) \\ 0 \end{bmatrix} \tag{2.5}$$

which can be solved with basic linear algebra algorithms [42]. The set of wavelengths λ_i has to be chosen with care to maximise the contrast and to avoid that any two equations are linearly dependent.
The extinction coefficients for oxyhaemoglobin (HbO_2), deoxyhaemoglobin (Hb), carboxyhaemoglobin (HbCO) and methehaemoglobin (Hi) for both, human and rat haemoglobin, are depicted in Fig. 2.1.

2.2 In-Vitro Oximetry

In-vitro oximeters, devices capable of measuring the relative concentrations of HbO_2 and Hb, and CO-oximeters, apparatuses further

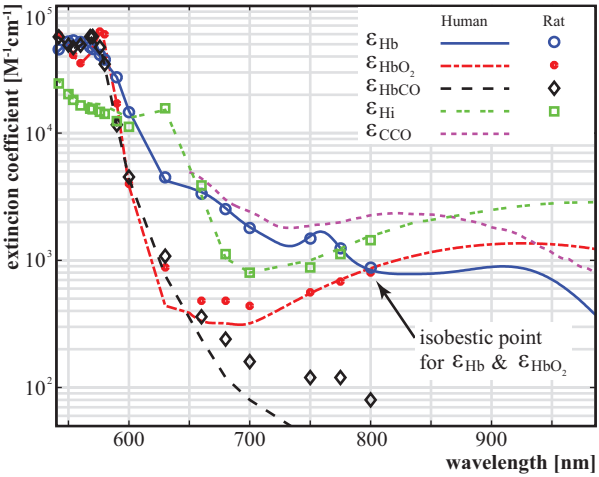

Figure 2.1: Extinction coefficients for HbO_2, Hb, HbCO, Hi and CCO in human adults [43, 44] and rats [45].
Values are expressed on a haemoglobin molecule basis (4 haemes) [46].

measuring HbCO and Hi, based on the above shown principle have been available since the 1960s [26] . These instruments relied on solving (2.5) for a minimum set of wavelengths. Usually two wavelengths in the visible to near infra-red spectrum for oximeters, respectively four wavelengths for CO-oximeters.
Blood is composed of ca. $56\,\%_{\text{Vol.}}$ plasma, which itself mainly consists of water, and $44\,\%_{\text{Vol.}}$ red blood cells, being rich in haemoglobin. The overall haemoglobin concentration of blood is ca. $35\,\text{g}/100\,\text{ml}$ [47]. Although a two-wavelength measurement does not account for the extra compounds in the solution, the contrasts (e.g., $k_{\text{Hb}}\varepsilon_{\text{Hb}}/k_i\varepsilon_i$), are usually high enough at the chosen wavelengths to neglect these additional substances for the calculation [40]. To account for the potential inaccuracy, the estimation of the functional arterial oxygen saturation ($S_{\text{a}}O_2$) obtained by this method is denoted as $S_{\text{p}}O_2$:

$$S_{\text{p}}O_2 = \frac{k_{\text{HbO}_2}}{k_{\text{HbO}_2} + k_{\text{Hb}}}, \tag{2.6}$$

$k_{\mathrm{HbO_2}}$ and k_{Hb} denoting the calculated relative concentrations of $\mathrm{HbO_2}$ and Hb, respectively.
Dysfunctional haemoglobin measurements are more error prone since the concentration remains usually below 1% for Hi and 2% for HbCO [48]. Furthermore, HbCO is rather transparent to infra-red light (Fig. 2.1). In such low concentrations dysfunctional haemoglobin is difficult to measure while it has little effect on the $S_{\mathrm{p}}\mathrm{O_2}$ obtained by a two-wavelength oximeter. In patients with carbon monoxide poisoning however, k_{HbCO} can be considerably higher [49], e.g. 20%, and lead to erroneous $S_{\mathrm{p}}\mathrm{O_2}$ readings by two-wavelength oximetry [48]. For the measurement with a four-wavelength CO-oximeter, treated blood samples are used: To minimise scattering, the red blood cell membranes are removed. Performance can be further improved when measuring at more distinct wavelengths [40], resulting in an overdetermined equation system (2.5). This *spectral diversity* can be used to detect measurement inaccuracy and to discriminate affected subsets of wavelengths.

2.3 In-Vivo Oximetry

The accuracy of the first attempts for in-vivo $S_{\mathrm{a}}\mathrm{O_2}$ measurement was fairly limited. Unlike for the in-vitro spectrophotometric setup, large shares of the incident light is no longer absorbed by arterial blood (the substance under test) but by tissue and venous blood. Attempts have been made to overcome this limitation by initial calibration of the measurement setup, e.g., against its bloodless condition – generated by tissue compression [50]. Successful separation of an absorption share given by arterial blood from other components was finally achieved with the pulse oximeter, first published in 1975 by *Minolta* engineers [26]. As illustrated in Fig. 2.3, the arterial pressure wave – originating from the heart beat – leads to a blood volume modulation in arteries and arterioles which results in a periodic pulsatile absorption component, associated to arterial blood only. At rest, this is the only time-variant contribution and causes an amplitude modulation of the transmitted light by 1-2% [40, 51] for the classical transmission type finger pulse oximeter (Fig. 2.4a).
At that time recent advances in optoelectronics allowed to replace

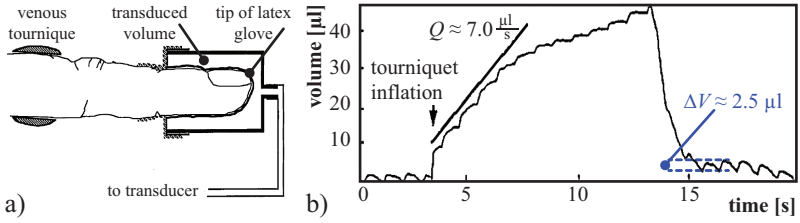

Figure 2.2: Quantitative volume plethysmographic trace reported in [52] for the analysis of fingertip blood flow. A venous tournique is inflated at the marked instant of time, hindering venous blood reflux. As a consequence, the finger volume increases allowing for a measurement of the blood flow. A pulsatile component related to the arterial pressure wave can be observed and quantified.

the optical fibres used in earliest apparatuses with in-situ LEDs and photodiodes while advances in microelectronics, i.e., the availability of microprocessors, were necessary for real-time computation of S_pO_2 and heart rate. Further technological progress lead to smaller, more accurate, and cheaper devices and to the wide spread of pulse oximetry in clinical diagnostics and patient monitoring.

2.3.1 A Quantitative Estimation of Absorbance Contributions

Although PPG is used as a means of perfusion monitoring [53], no literature is found on the quantitative composition of the absorption. In difference to the qualitative drawings found in textbooks [40,51,54] and various other publications [53, 55, 56], haemodynamic considerations suggest that only a small share of arterial blood volume is modulated. While knowledge on the quantitative composition is, as will be shown later, not necessary for the computation of S_pO_2, it might improve the understanding of the difficulties encountered in wearable pulse oximeters.
Rubinstein and Sessler [52] published a quantitative volumetric measurement in an analysis of fingertip blood flow, see Fig. 2.2: The fingertip volume is continuously measured, a tournique can be inflated

to hinder venous blood reflux. This allowed them to measure and quantify the blood flow as the increase in fingertip volume over time. The provided graph further reveals the volume change $\Delta\mathsf{V}$ due to the arterial pulse wave – a value of ca. 2.5 µl can be extracted from the curve. Taking into consideration that a capillary refill time (CRT) – i.e., the time t_{CRT} needed to refill the fingertip capillaries and regain 'normal' skin colour after having evacuated them by applying pressure (squeezing the fingertip) – of roughly 2 s is observed for healthy persons [57], the total arterial blood volume $\mathsf{V}_{\mathrm{art}}$ in the fingertip can be estimated with the given blood flow measurement of $Q \approx 7.0\,\mu\mathrm{l/s}$ as

$$\mathsf{V}_{\mathrm{art}} \approx Q \cdot t_{\mathrm{CRT}} = 14\,\mu\mathrm{l}. \tag{2.7}$$

Circulating arterial blood makes only 20% of the total blood volume, 75% are venous and the remaining 5% are capillary [58]. The relative absorbance contribution of the pulsatile arterial component to the total absorbance by blood is thus estimated to be

$$\frac{\mathcal{A}_{\mathrm{AC}}}{\mathcal{A}_{\mathrm{art}} + \mathcal{A}_{\mathrm{ven}} + \mathcal{A}_{\mathrm{cap}}} \approx \frac{\Delta\mathsf{V}}{5 \cdot \mathsf{V}_{\mathrm{art}}} = 3.6\%. \tag{2.8}$$

The observed pulsatile signal is thus caused by just 3.6% of the overall fingertip blood volume (Fig. 2.3). Whenever the assumption that the remaining share is constant does not hold, the measurement can be severely impacted.

Overall transmission, i.e., the ratio between LED current and photodiode current, is highly dependent on the probe geometry and skin pigmentation. We found it to be in the order of $10 - 50$ppm for transmission type finger probes (Fig. 2.4). Somewhat higher values (< 200ppm) have been obtained for reflexive finger probes. Note, that this values include losses given by probe geometry and due to limited LED external efficiency and photodiode quantum efficiency, which are in the order of $10 - 50\%$ and 90%, respectively [59].

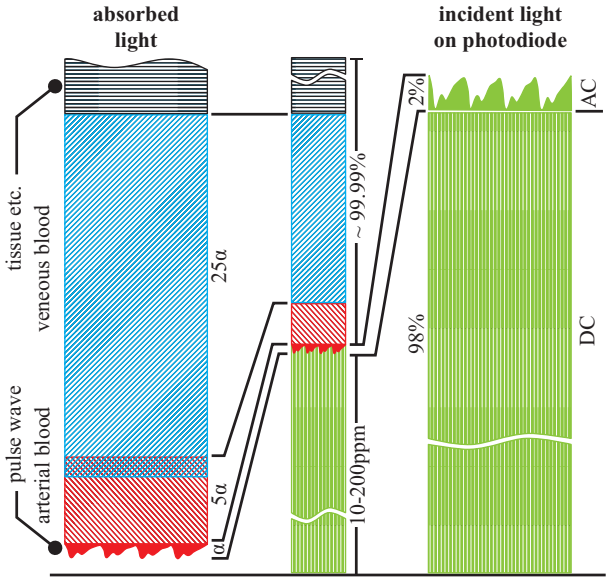

Figure 2.3: Quantitative estimation of the absorption components at the isobestic point and resulting photodiode signal for a transmission type finger pulse oximeter.

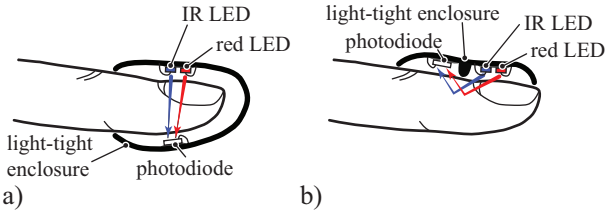

Figure 2.4: Transmission (a) and reflection type (b) sensor probes for two-wavelength pulse oximetry.

2.4 Optics in Pulse Oximetry

Pulse oximetry is a in-vivo two-wavelengths arterial blood oxygenation measurement method using the pulsatile component of PPG signals for the separation of absorbance by arterial blood from the remaining absorbance components, which are assumed to be constant over time. Fig. 2.4 shows two common variations of pulse oximetry sensor probes. Both use two LEDs as light sources at different wavelengths (usually 660 nm and $800 - 940$ nm) and a common photodiode. The LEDs are turned on alternately to acquire PPGs at different wavelengths. As the following analysis shows, the arterial blood oxygen saturation can be computed from these PPGs.

2.4.1 Beer-Lambert Law

The current generated by a photodiode for a given incident light intensity is [59]

$$I_{\mathrm{PD}} = P_{\mathrm{o}}\mathcal{R}_{\mathrm{PD}} = \mathcal{I}_{\mathrm{PD}}\Omega_{\mathrm{PD}}\mathcal{R}_{\mathrm{PD}} = \mathcal{I}_{\mathrm{PD}}\Omega_{\mathrm{PD}}\eta_{\mathrm{q}}\frac{\lambda_0}{1.24}, \tag{2.9}$$

with incident optical power P_{o}, photodiode responsivity $\mathcal{R}_{\mathrm{PD}}$, incident light intensity $\mathcal{I}_{\mathrm{PD}}$, illuminated photodiode area – expressed as solid angle with respect to the emitting light source – Ω_{PD} and quantum efficiency η_{q}. Similarly, the emitted light intensity of an LED is given as

$$\mathcal{I}_{\mathrm{LED}} = \frac{\mathcal{R}_{\mathrm{LED}}}{\Omega_{\mathrm{LED}}}I_{\mathrm{LED}} = \frac{1}{\Omega_{\mathrm{LED}}}\eta_{\mathrm{ex}}\frac{1.24}{\lambda_0}I_{\mathrm{LED}}. \tag{2.10}$$

with LED current I_{LED}, emission solid angle Ω_{LED}, LED responsivity $\mathcal{R}_{\mathrm{LED}}$ and external efficiency η_{ex}. Note that responsivity is defined differently for an LED and a photodiode [59], having unit [W/A] in the first case and [A/W] in the latter.
For a pulse oximetry setup, we can thus express the sensed current as

$$I_{\mathrm{PD}} = \frac{\Omega_{\mathrm{PD}}}{\Omega_{\mathrm{LED}}}\mathcal{R}_{\mathrm{PD}}\mathcal{R}_{\mathrm{LED}}\mathcal{T}I_{\mathrm{LED}} = \frac{\Omega_{\mathrm{PD}}}{\Omega_{\mathrm{LED}}}\eta_{\mathrm{q}}\eta_{\mathrm{ex}}\mathcal{T}I_{\mathrm{LED}}, \tag{2.11}$$

for a given transmittance $\mathcal{T}$ (2.1) and geometric setup ($\Omega_{\mathrm{PD}}/\Omega_{\mathrm{LED}}$).

Normalising the local maximum of the signal (AC+DC) to the constant share (DC) (which is the local minimum) of the photodiode current makes the measurement independent of probe geometry:

$$\frac{I_{\mathrm{PD,AC}} + I_{\mathrm{PD,DC}}}{I_{\mathrm{PD,DC}}} = \frac{\mathcal{T}_{\mathrm{DC}}}{\mathcal{T}_{\mathrm{AC}}\mathcal{T}_{\mathrm{DC}}} = \frac{10^{-\varepsilon_{\mathrm{a}} d_{\mathrm{a,DC}} - \varepsilon_{\mathrm{v}} d_{\mathrm{v}} - \varepsilon_{\mathrm{t}} d_{\mathrm{t}}}}{10^{-\varepsilon_{\mathrm{a}} d_{\mathrm{AC}} - \varepsilon_{\mathrm{a}} d_{\mathrm{a,DC}} - \varepsilon_{\mathrm{v}} d_{\mathrm{v}} - \varepsilon_{\mathrm{t}} d_{\mathrm{t}}}} = 10^{\varepsilon_{\mathrm{a}} d_{\mathrm{AC}}},$$

with ε_{a} denoting the extinction coefficient of the arterial whole blood. The kind reader notes that a photo-generated current maximum coincides with a transmission minimum (constant part) and vice versa. Assuming constant path-lengths d_{AC} for measurements at different wavelengths, the ratio $\Re$ of the logarithms of normalised signals acquired at two different wavelengths thus depends only on the arterial blood extinction coefficients at the two wavelengths [40]

$$\Re = \frac{\log_{10}\left(\frac{I_{\mathrm{PD,AC}}(\lambda_1) + I_{\mathrm{PD,DC}}(\lambda_1)}{I_{\mathrm{PD,DC}}(\lambda_1)}\right)}{\log_{10}\left(\frac{I_{\mathrm{PD,AC}}(\lambda_2) + I_{\mathrm{PD,DC}}(\lambda_2)}{I_{\mathrm{PD,DC}}(\lambda_2)}\right)} = \frac{\varepsilon_{\mathrm{a}}(\lambda_1)}{\varepsilon_{\mathrm{a}}(\lambda_2)}, \tag{2.12}$$

while

$$\frac{\varepsilon_{\mathrm{a}}(\lambda_1)}{\varepsilon_{\mathrm{a}}(\lambda_2)} \approx \frac{k_{\mathrm{HbO_2}}\varepsilon_{\mathrm{HbO_2}}(\lambda_1) + k_{\mathrm{Hb}}\varepsilon_{\mathrm{Hb}}(\lambda_1)}{k_{\mathrm{HbO_2}}\varepsilon_{\mathrm{HbO_2}}(\lambda_2) + k_{\mathrm{Hb}}\varepsilon_{\mathrm{Hb}}(\lambda_2)}. \tag{2.13}$$

Due to the low modulation of the signal, the approximation

$$\log_{10}(1+x) \approx x \qquad x \approx 0 \tag{2.14}$$

leads to the simplified formula

$$\Re \approx \frac{\frac{I_{\mathrm{PD,AC}}}{I_{\mathrm{PD,DC}}}(\lambda_1)}{\frac{I_{\mathrm{PD,AC}}}{I_{\mathrm{PD,DC}}}(\lambda_2)}, \tag{2.15}$$

known as the ratio-of-ratios [40].
With (2.6) and (2.13), the arterial oxygen saturation $S_{\mathrm{p}}O_2$ can be calculated from $\Re$:

$$S_{\mathrm{p}}O_2 = \frac{\varepsilon_{\mathrm{Hb}}(\lambda_1) - \Re\varepsilon_{\mathrm{Hb}}(\lambda_2)}{\varepsilon_{\mathrm{Hb}}(\lambda_1) - \varepsilon_{\mathrm{HbO_2}}(\lambda_1) + \Re\left[\varepsilon_{\mathrm{HbO_2}}(\lambda_2) - \varepsilon_{\mathrm{Hb}}(\lambda_2)\right]}. \tag{2.16}$$

The usual choice of wavelenghts is red ($\lambda_1 = 660\,\mathrm{nm}$) and near-infrared ($\lambda_2 = 800 - 940\,\mathrm{nm}$). As can be observed in Fig. 2.1, extinction coefficients for HbO_2 and Hb have maximum relative separation

at the former wavelength while they are equal at 800 nm (isobestic point) and have only low (but inverse) separation at 940 nm. The chosen wavelengths thus promise high contrast $\Delta\Re/\Delta S_\mathrm{p}O_2$. Equally important, LEDs are available and both wavelenghts are covered by the responsitivity spectrum of standard silicon photodiodes.
Considering this high contrast, i.e.,

$$\frac{\varepsilon_\mathrm{Hb}(\lambda_1) - \varepsilon_{\mathrm{HbO}_2}(\lambda_1)}{\varepsilon_\mathrm{Hb}(\lambda_2) - \varepsilon_{\mathrm{HbO}_2}(\lambda_2)} \gg 1, \tag{2.17}$$

the arterial oxygen saturation (2.16) is an approximately linear function of $\Re$:

$$S_\mathrm{p}O_2 \approx 1 + \frac{\varepsilon_{\mathrm{HbO}_2}(\lambda_2)}{\varepsilon_\mathrm{Hb}(\lambda_1) - \varepsilon_{\mathrm{HbO}_2}(\lambda_1)} \left[\frac{\varepsilon_{\mathrm{HbO}_2}(\lambda_1)}{\varepsilon_{\mathrm{HbO}_2}(\lambda_2)} - \Re\right]. \tag{2.18}$$

In practice however, the measured $\Re$ value differs from the theoretically calculated one: mainly due to scattering (Fig. 2.12a).

Perfusion Index

The ratio of infrared AC to DC signal shares is denoted as perfusion index (PI) and has strong influence on receiver dynamic range requirements as will be seen in Sec. 2.6.2 – respectively on $S_\mathrm{p}O_2$ estimation accuracy [60] if a limited dynamic range is given. Although maybe counter-intuitive, it shall be noted that the perfusion index is in theory independent of the constant absorption share:

$$\begin{aligned} PI &= \frac{I_\mathrm{PD,AC}}{I_\mathrm{PD,DC}} = \frac{I_\mathrm{PD,max} - I_\mathrm{PD,min}}{I_\mathrm{PD,min}} \\ &= \frac{\frac{\Omega_\mathrm{PD}}{\Omega_\mathrm{LED}}\eta_\mathrm{q}\eta_\mathrm{ex}I_\mathrm{LED}\mathcal{T}_\mathrm{DC}(1-\mathcal{T}_\mathrm{AC})}{\frac{\Omega_\mathrm{PD}}{\Omega_\mathrm{LED}}\eta_\mathrm{q}\eta_\mathrm{ex}I_\mathrm{LED}\mathcal{T}_\mathrm{DC}\mathcal{T}_\mathrm{AC}} = \frac{1-\mathcal{T}_\mathrm{AC}}{\mathcal{T}_\mathrm{AC}}. \end{aligned} \tag{2.19}$$

When assuming that all modulation derives from arterial haemoglobin (oxy. and deoxy. – HbX), it depends thus only on

$$\mathcal{T}_\mathrm{AC} = 10^{-\varepsilon_\mathrm{HbX} k_\mathrm{MCHC} d_\mathrm{AC}}, \tag{2.20}$$

with exctinction coefficient $\varepsilon_\mathrm{HbX} \approx 1\ \frac{\mathrm{l}}{\mathrm{mmol\cdot cm}}$ (Fig. 2.1), mean corpuscular haemoglobin concentration $k_\mathrm{MCHC} \approx 20\ \frac{\mathrm{mmol}}{\mathrm{l}}$ [61][1] and

[1] conversion from g/dl to mmol/l according to [62]

path-length modulation d_{AC}. The latter can be estimated for the above quantitative estimation of the absorbance contributions in a fingertip pulse oximetry as:

$$d_{\mathrm{AC}} = d_{\mathrm{TR}} \, \frac{\Delta \mathsf{V}}{\mathsf{V}_{\mathrm{finger}}} \approx 8\,\mathrm{mm} \, \frac{2.5\,\mu\mathrm{l}}{3\,\mathrm{ml}} \approx 7\,\mu\mathrm{m}, \tag{2.21}$$

with d_{TR} denoting the mean photon path between transmitter (LED) and receiver.
The perfusion index for above assumptions is according to (2.19) and (2.20) thus ca. 3.2%. In reality, direct light paths between LED and photodiode and ambient light reduce the perfusion index further.
We conclude that the perfusion index depends directly on the tissue perfusion, LED-photodiode separation and haematocrit. DC transmission however has no direct influence – indirectly however, lower DC transmission increases the effect of direct light-paths and ambient light.

2.4.2 Tissue Scattering

The Beer-Lambert law (Sec. 2.1) describes the absorbance of light by dissolved substances in a solution. While this holds for in-vitro spectrophotometry of treated (blood) samples, it does not for the analysis of whole-blood samples and eminently not for in-vivo oximetry.
In whole-blood, haemoglobin is not dissolved in the plasma, but is a component of the erythrocytes (red blood cells). A part of the incident light is scattered by the erythrocyte membrane: Due to their disc shape, scattering properties depend on the cell orientation, which itself is flow-velocity dependent [63] – adding to the pulsatile transmittance modulation and thus altering $\Re$ with respect to the Beer-Lambert prediction.
In pulse oximetry, this is aggravated by tissue scattering. Although the apparent light loss due to tissue scattering is constant (and thus unaccounted for in $\Re$), it does interfere with the measurement by affecting the path on which the photons travel through tissue.
The probability that a photon has a free path (is neither absorbed nor scattered) of length d in a given medium is [64]

$$p_{\mathrm{t}} = \exp\left(-[\Sigma_{\mathrm{a}} + \Sigma_{\mathrm{s}}] \cdot d\right), \tag{2.22}$$

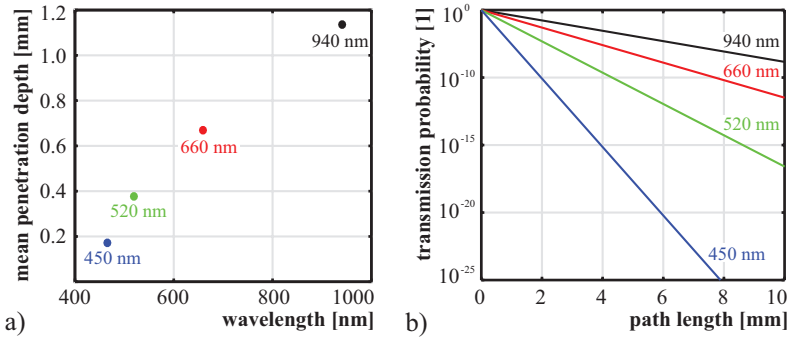

Figure 2.5: Mean skin penetration depth before absorption or scattering (a) and probability for a photon of passing a certain path-length in skin without being scattered or absorbed (b). Based on the parameters given in Tbl. 2.1.

with Σ_s and Σ_a denoting tissue scattering and absorption coefficients. The mean distance between two interactions is found to be

$$d_{t,mean} = \frac{1}{\Sigma_a + \Sigma_s}. \tag{2.23}$$

Fig. 2.5 shows the mean free path-length and free transmission probabilities for photons of different wavelengths.

Transmittance Probe

To analyse the effect of scattering on pulse oximetry measurements, we consider its impact on the photons travelling paths through the tissue. In case of a transmission probe, the emitter (LED) is placed opposite to the detector (photodiode). In absence of scattering, all photons would travel on a straight path of length d (independent of wavelength) – and would get absorbed on this journey with the probability

$$p_a = \exp(-\Sigma_a d). \tag{2.24}$$

As imminently evident from Fig. 2.5, the probability of a photon travelling unhindered through tissue is marginal when scattering is

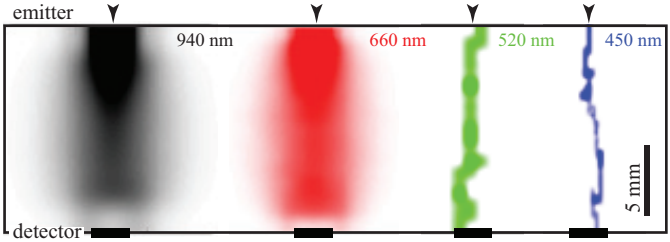

Figure 2.6: Transmittance probe: Relative visitation probability maps for photons of different wavelengths travelling in tissue.
Darker colour stands for higher probability. Emitter-detector separation: 15 mm. Random paths of > 2500 photons reaching the detector. Parameters: Tbl. 2.1.

considered. Note that overall transmission was measured to be in the order of $10 - 50$ppm, which is orders of magnitude higher than the probability of a photon travelling straight from emitter to detector. We therefore conclude, that most of the photons reaching the detector have been subject to multiple scattering along their travel – the higher the scattering coefficient, the larger gets the expected value of the photon path length. Absorption on the other side has the effect of confining the path: The cost of a longer path is a high probability of absorption – thus, the photons actually reaching the detector have most probably travelled along a short path. This effect can be observed in the Monte-Carlo simulation results presented in Fig. 2.6: The infrared (940 nm) light is least confined while green (520 nm) and blue (450 nm) light did travel on a narrow path. However, the tissue volume with highest visitation probability is still formed by the direct path between emitter and detector, independent of wavelength. In pulse oximetry, this means that most of the light at both wavelengths has travelled through the same portion of the tissue. This explains why, nonetheless, the empirical $\Re_e$ is close to the predicted $\Re$ by the Beer-Lambert law and does not depend much on the emitter-detector separation.

Reflectance Probe

Although the term *reflectance pulse oximetry* suggests that it is based on light being *reflected* on a certain surface, it is rather based on

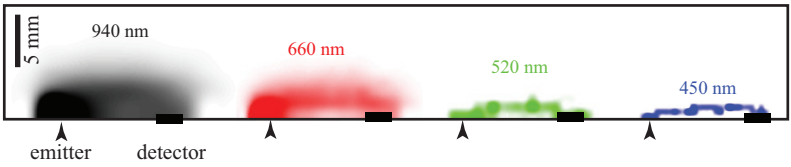

Figure 2.7: Reflectance probe: Relative visitation probability maps for photons of different wavelengths travelling in tissue.
Darker colour stands for higher probability. Emitter-detector separation: 15 mm. Random paths of > 2500 photons reaching the detector. Parameters: Tbl. 2.1.

light being *scattered* in tissue. The penetration depth into tissue depends on the wavelength as illustrated by the Monte-Carlo light-path simulation in Fig. 2.7. In difference to the above studied situation for a transmittance probe, the confining effect of absorption does not only narrow the volume of high visitation probability, but does further lead to different volumes of highest visitation probability. Short wavelengths travel on a shallow path, while longer wavelengths penetrate deeper into the tissue, leading to PPG recordings at different vascular depths [65–67]. For a pulse oximetry measurement, this means that the travelling paths of red and infrared light are different. It has been demonstrated in [64] by simultaneous recording with photodiodes placed at three different distances from the same LEDs, that both, relative pulse amplitude (AC/DC) and $\Re_r$, increase with increasing emitter-detector distance. Furthermore, the mean light penetration is also depending on the tissue oxygenation [68]. This effect is illustrated in Fig. 2.8 for red and infrared light-paths at two different arterial oxygenation (S_aO_2) levels.
The assumption of constant path-lenghts d_{AC} is thus no longer valid in reflectance pulse oximetry and the ratio-of-ratios (2.12) modifies to

$$\Re_r = \frac{\varepsilon_a(\lambda_1)}{\varepsilon_a(\lambda_2)} \cdot \frac{d_{AC}(\lambda_1, S_aO_2)}{d_{AC}(\lambda_2, S_aO_2)}. \tag{2.25}$$

For reflectance oximetry, the *empirical calibration*, i.e., the correlation of obtained $\Re_r$ to S_pO_2 values is probe geometry dependent.
While the wavelength dependence of the photons travelling in tissue is an undesired effect for S_pO_2 measurement and might affect accuracy, it is beneficial for the separation of signals corresponding to different

vascular depths – which can help to overcome motion artefacts, as showed in Sec. 2.5.

Monte-Carlo Simulation

The Monte-Carlo simulation used for the generation of the presented probability maps in this section is implemented according to [68, 70, 71]. It is based on a cubic lattice with edge-length corresponding to the mean free path length ($1/\Sigma_s$). At each node, the photon is scattered, i.e., it proceeds its travel randomly to one out of the six adjacent nodes. If a photon reaches one of the defined detector nodes, the travelled path is weighted with the transmission probability for the given path length and added to the 3D result matrix, which thus reflects the visitation probability of each node in the lattice for photons which did reach the detector. Photons travelling to the boundaries of the simulation space are absorbed.

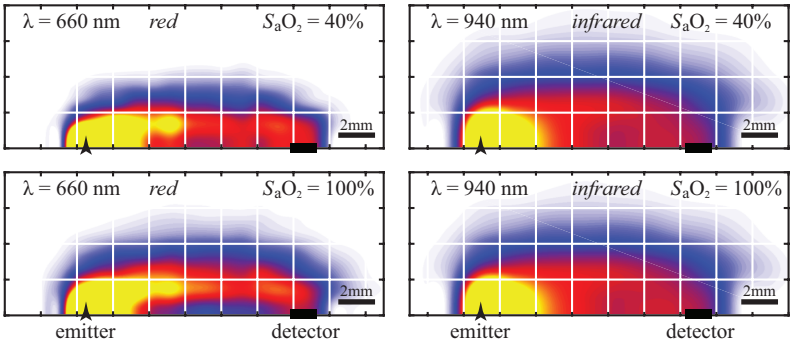

Figure 2.8: Reflectance probe: Relative visitation probability maps for red and infrared light and different arterial blood oxygen saturations. Emitter-detector separation: 15 mm. Random paths of > 2500 photons reaching the detector. Parameters given in Tbl. 2.1.

Table 2.1: Scattering and Absorption Coefficients of Tissue

colour	λ [nm]	$\Sigma_a^{100\%}$ [mm^{-1}]	$\Sigma_a^{40\%}$ [mm^{-1}]	Σ_s [mm^{-1}]
blue	450	3.23	2.91	2.61
green	520	1.21	1.21	1.79
red	660	0.043	0.136	1.45
infrared	940	0.084	0.067	0.80

The parameters have been calculated on basis of data from [43, 64, 69] according to [69]. All values are given for an haematocrit $H = 0.45$, erythrocyte volume $\mathsf{V}_i = 90\,\mu m^3$, blood-less tissue absorbption coefficient $\Sigma_a^{tiss} = 0.02\,mm^{-1}$, arterial and venous blood volume fractions $\mathsf{V}_a = \mathsf{V}_v = 5\%$ and difference of arterial to venous oxygen saturation $\Delta S_a = 10\%$. Absorption coefficients are given for $S_aO_2 = 100\%$ and $S_aO_2 = 40\%$.

2.5 Motion Artefacts

As discussed in Sec. 2.4.1, pulse oximetry is based on the assumption that the arterial pulse pressure wave is the only time-variant contribution to light absorption. While this is valid at rest, substantial artefacts are observed in PPG signals when in motion. We can differ five potential sources contributing to motion artefacts:

- *Probe-skin displacement.* An issue resulting from abrupt motion – especially with relative large and heavy probes, e.g., finger-clip or a somewhat loose sport watch. It can be overcome with simple mechanical measures, such as lightweight and adhesive probes and good fixation or avoidance of cables.

- *Deformation due to acceleration.* Although a well fixated probe might not displace against the skin underneath it, inertia will cause local deformation of skin and tissue. The emitted light will thus pass through different tissue, resulting in a variation of absorbance.

- *Tendons.* At certain sites tendons run just below the skin, e.g., on the wrist. Movements of tendons cause deformation of the surrounding tissue.

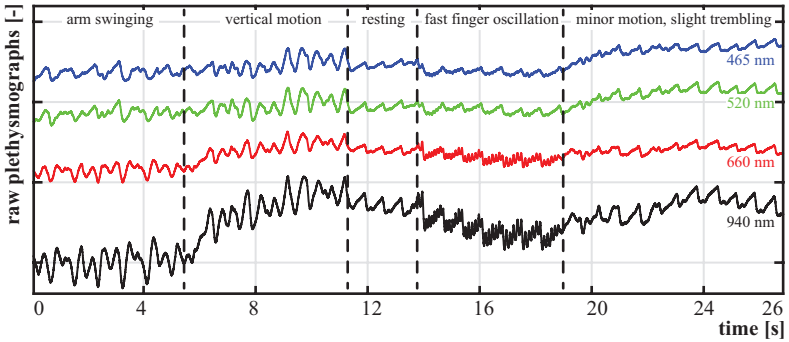

Figure 2.9: Simultaneously recorded PPG signals with LEDs of different wavelengths with a reflective finger probe under various motion patterns. As an effect of lower penetration depth for short wavelengths motion artefacts are less pronounced for those recordings when compared to PPG with (infra)red light.

- *Hydrostatic blood pressure.* According to Bernoulli's law [72], the arterial pressure depends on the vertical position of the limb. Vertical movements change the local blood pressure which causes arteries and arterioles to dilate or contract. A change in arterial blood volume is observed.

- *Acceleration of blood.* The main source for motion artefacts in PPG. A more detailed discussion follows below.

2.5.1 Effect of Acceleration on the Blood Flow

The effect of acceleration on the blood flow has been studied mainly in concern for the perfusion in a body exposed to acceleration, e.g., [73] gives a model for the blood flow in a single cycle of body acceleration, while [74, 75] study the math of periodic acceleration. Nonetheless, their findings give some insight into the cause of motion artefacts.
The effect of body acceleration on the blood can be considered equivalent to a pressure gradient superimposed to the pressure gradients given by normal heart action [73]. The latter are given for arteries by a static and a periodic (due to the pulse wave) pressure gradient.

While the ratio between the two components is constant, the gradients vary widely for different vessels [75]: Large arteries have low resistance and pressure gradients [72] – the low flow rates of small arteries and arterioles lead according to Bernoulli's law to high pressure gradients. The pressure gradient in arterioles corresponds to ca. 270 times the aorta pressure gradient [75]. With the gradually widening, the pressure gradient drops on the way via capillaries (similar size as arterioles, but multiple in parallel per arteriole [72]) to venules, small and finally larger veins. The venous reflux has only a static pressure gradient, no periodic component. It has been concluded, that the additional pressure gradient due to body acceleration has a higher effect on larger arteries than on small arteries and arterioles [74, 75]. This argument – the lower the natural pressure gradient, the higher the impact of acceleration on the blood flow – can be extended to the venous vascular system. Most veins have valves to prevent back-flow [58] which restricts the flow disturbance to local interferences – in arteries however, no mechanism prevents a disturbance to spread.
In skin, no vessels are found in the outermost layer, the epidermis. The subsequent layer, the dermis, is enwrought by capillaries, arterioles and venules which join into small arteries and veins in the lower subcutaneous layer. The blood flow in the small vessels on the outermost layers is thus less influenced by motion than the flow in larger vessels in lower levels.
Reflectance PPG at shorter wavelengths (green, blue) with its low penetration depth is found to be less affected by motion than for longer wavelengths (red, infrared) [23], as illustrated in the simultaneously recorded PPG signals depicted in Fig. 2.9. Large variations in PPG signal amplitude and motion interference have been found for different probe placement sites which reflect the different structure and perfusion of skin and subjacent tissue [76].

2.6 Performance Requirements

In this section, key performance requirements for the electronic circuitry of a pulse oximeter are established. A simplified circuit block diagram is shown in Fig. 2.10: A TIA converts the photodiode current into a voltage which is sampled at a rate of f_s and digitised by

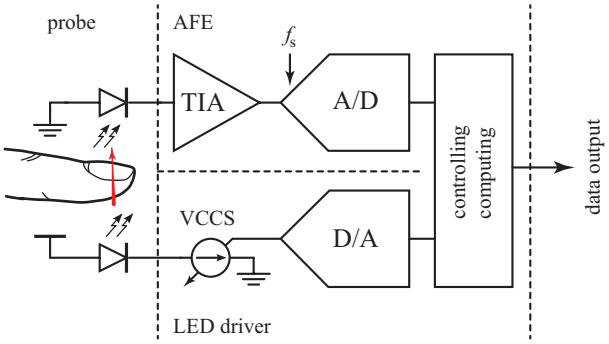

Figure 2.10: Basic PPG circuit: The photodiode current is converted into a voltage by a transimpedance amplifier and digitised. To adapt on the transmittance, both, transimpedance and LED current, can usually be adjusted.

an analogue-to-digital converter (ADC). The LED current can be adjusted to cope with different probes and transmittances.
We model the sampled and digitised PPG signal $x[k]$ as

$$x[k] = DC + \Delta + AC[k] + n[k] \qquad k = t \cdot f_s \quad k \in \mathbb{Z}, \tag{2.26}$$

with Δ representing the deviation of the DC signal from its theoretical value, i.e., the integral non-linearity (INL) [77], mainly caused by analogue front-end (AFE) non-linearity and $n[k]$ summarising all noise contributions (LED driver, LED, photodiode, AFE and ADC). The ratio-of-ratios (2.15) for noisy and distorted PPG signals is thus

$$\Re' \approx \frac{\left(\frac{AC+n_{\mathrm{AC}}}{DC+\Delta+n_{\mathrm{DC}}}\right)(\lambda_1)}{\left(\frac{AC+n_{\mathrm{AC}}}{DC+\Delta+n_{\mathrm{DC}}}\right)(\lambda_2)}. \tag{2.27}$$

The noise contributions n_{AC} and n_{DC} are derivatives of $n[k]$ depending on the applied digital signal conditioning prior to the computation of $\Re$.

2.6.1 Linearity

In absence of noise, (2.27) simplifies to

$$\Re' \approx \frac{\left(\frac{AC}{DC+\Delta}\right)(\lambda_1)}{\left(\frac{AC}{DC+\Delta}\right)(\lambda_2)} = \Re \frac{1+\frac{\Delta_{\lambda_2}}{DC_{\lambda_2}}}{1+\frac{\Delta_{\lambda_1}}{DC_{\lambda_1}}}, \tag{2.28}$$

with $\Re$ denoting the ideal result for the ratio-of-ratios in absence of distortion, as given in (2.15). The impact on non-linearity depends on its characteristic and thus finally its source. Fig. 2.11a depicts a 3rd order non-linearity as typically encountered in an amplifier [78] and thus in an AFE. Considering the photodiode current being strictly positive, an offset will be induced (see. Sec. 4.5.3) to make use of the full swing. The resulting distorted transimpedance is indicated in Fig. 2.11b. The distortion can be modelled as the transfer function

$$y = \underbrace{\alpha_1 x}_{DC} + \underbrace{\alpha_3 x^3}_{\Delta}, \tag{2.29}$$

with α_1 denoting the linear and α_3 the 3rd order non-linearity term. To cope with different transmittances, the LED current will be regulated to keep the input current in a certain predefined range. Ideally, DC input currents for both signals would be equal. In this case, non-linearity has virtually no effect on $\Re'$ (2.28). In reality however, perfect DC equality will not be reached. Assuming a maximum DC mismatch of $\pm 20\%$, the worst case scenario, with respect to 3^{rd} order non-linearity, is

$$I_{\text{pd},\lambda_1} = \frac{1+\sqrt{1/3}}{2} I_{\text{FS}} \tag{2.30}$$

$$I_{\text{pd},\lambda_2} = 1.2 \cdot I_{\text{pd},\lambda_1} \tag{2.31}$$

with I_{FS} denoting the input range (full-swing) of the TIA, which eventually results in an $\Re'$ of

$$\Re' = \Re \frac{1+0.244\frac{\alpha_3}{\alpha_1+\alpha_3}}{1+0.098\frac{\alpha_3}{\alpha_1+\alpha_3}}. \tag{2.32}$$

In the flattest point of the $\Re$-$S_{\text{p}}O_2$ correlation (Fig. 2.12), a 0.5% $S_{\text{p}}O_2$ variation corresponds to 1.75% in $\Re$ deviation. The minimum

ratio α_1/α_3 is thus found to be 7.24. For the 3rd order non-linearity assumption (2.29), the minimum spurious free dynamic range (SFDR) guaranteeing a maximum error of half a percent S_pO_2 reading is thus found to be

$$SFDR = 20\log_{10}\left(\frac{4\alpha_1 + 3\alpha_3}{\alpha_3}\right) = 30.1\,\text{dB}. \tag{2.33}$$

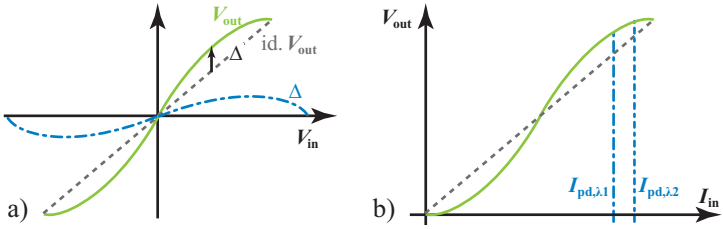

Figure 2.11: Qualitative drawing of typical differential front-end non-linearity (a) and resulting TIA non-linearity (b).

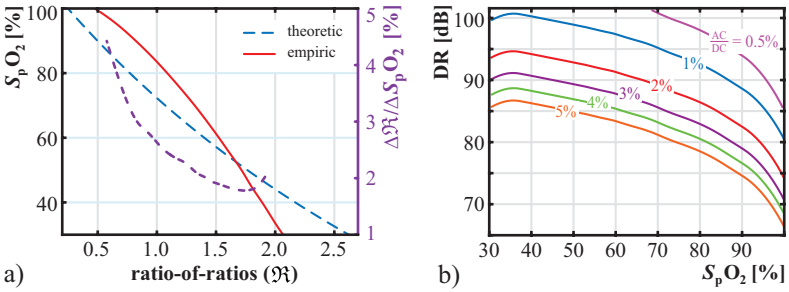

Figure 2.12: Correlation between the ratio-of-ratios $\Re$ and blood oxygen saturation S_pO_2 (a) as theoretically predicted by the Beer-Lambert law and empirically found for a finger-probe pulse oximeter. The purple dashed line (right y-axis) shows the slope of $\Re$, i.e., $\Delta\Re$ for a ΔS_pO_2 of 1%. Dynamic range requirement (b) for 0.2% RMS noise on the S_pO_2 reading for different PI assuming $DC/FS = 75\%$.

2.6.2 Noise

Considering noise as the only source of non-ideality, (2.27) simplifies to

$$\Re' \approx \Re \frac{\left[1 + \frac{n_{\mathrm{AC},\lambda_1}}{AC_{\lambda_1}}\right]\left[1 + \frac{n_{\mathrm{DC},\lambda_2}}{DC_{\lambda_2}}\right]}{\left[1 + \frac{n_{\mathrm{AC},\lambda_2}}{AC_{\lambda_2}}\right]\left[1 + \frac{n_{\mathrm{DC},\lambda_1}}{DC_{\lambda_1}}\right]} \approx \Re \frac{1 + \frac{n_{\mathrm{AC},\lambda_1}}{AC_{\lambda_1}}}{1 + \frac{n_{\mathrm{AC},\lambda_2}}{AC_{\lambda_2}}}. \tag{2.34}$$

The noise shares n_{AC} and n_{DC} are derivatives of the same noise source $n[k]$. Generally, the bandwidth of the DC conditioning is lower than for AC conditioning, resulting in lower root mean square (RMS) noise. Given the typically low perfusion index $(AC/DC) \approx 2\%$, we conclude that n_{AC} clearly dominates and n_{DC} can be neglected.
Assuming additive white Gaussian noise (AWGN) with RMS value well below the AC signal and equal noise and signal levels for the measurements at both wavelengths, the standard deviation of $\Re'$ can be approximated as

$$\sigma(\Re') \approx \Re \frac{\sqrt{2} \cdot \sigma(n_{\mathrm{AC}})}{AC}. \tag{2.35}$$

When targeting a RMS noise $e_{\mathrm{rr}} = 0.2\%$ on the calculated $S_{\mathrm{p}}O_2$ value at 30% oxygen saturation, $\sigma(\Re')$ must be as low as 0.4%. Assuming a DC to full-scale (FS) ratio of 75%, the required dynamic range (DR) is found to be

$$DR = 20 \log_{10}\left(\frac{\sqrt{2}\,\Re}{e_{\mathrm{rr}} \frac{\Delta\Re}{\Delta S_{\mathrm{p}}O_2}} \cdot \frac{FS}{AC}\right) = 93.8\,\mathrm{dB}. \tag{2.36}$$

The DR requirement for a certain target noise on the $S_{\mathrm{p}}O_2$ reading highly depends on the perfusion index (AC/DC) and the oxygen saturation as illustrated in Fig. 2.12b. The latter is due to a simultaneous increase in $\Re$ and decrease in its slope $\frac{\Delta\Re}{\Delta S_{\mathrm{p}}O_2}$.

Bandwidth

The PPG signal bandwidth depends on the measurement location. A pulse wave measured on the aorta has components up to ca. 85 Hz. The series of bifurcations on its way to the arterioles and capillaries act as low-pass filter. The bandwidth reduces to ca. 15 Hz for reflectance skin photoplethysmography [79].

Chapter 3

Background: Pulse Wave Velocity

The preceding chapter gave an insight into pulse oximetry, one of the most prominent applications for PPG. For a better understanding of potential interferences and physiological factors affecting the performance requirements on the circuit, the absorption components contributing to the acquired raw signals were studied, a short summary on tissue optics was given, and an overview on common artefact sources was provided. Finally, specific performance requirements were derived for a typical finger probe scenario and more generally in dependence of physiological parameters.

Similarly, this chapter shall provide insight into arterial haemodynamics and the influence of blood pressure, heart rate, and respiration rate on waveform and propagation velocity of the arterial pressure wave. The goal is to provide the necessary background for a discussion on the chances and potential difficulties of pulse wave velocity (PWV) based blood pressure estimation. Preliminary experimental results for an implantable system in small rodents for such blood pressure measurement are later presented in Sec. 6.4.

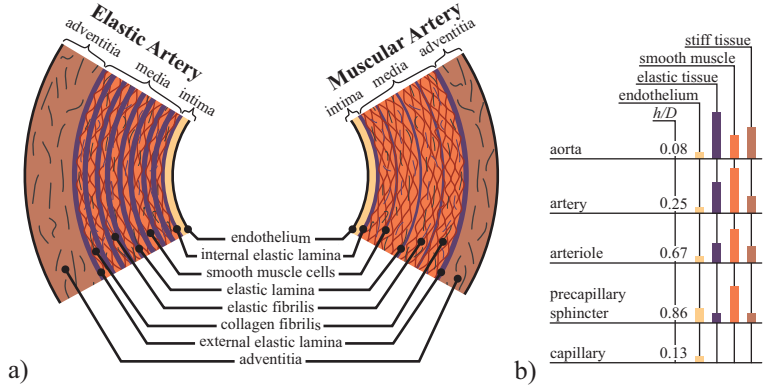

Figure 3.1: Structure of the arterial walls of elastic and muscular arteries (a), according to [58, 80]. Wall thickness h to vessel diameter D ratio and relative shares of the different compounds to the walls of different arteries (b), adapted from [81] in [58].

3.1 Arterial Haemodynamics

3.1.1 Hystology

In general, the vessels of the arterial system are subdivided into two types: *elastic* and *muscular arteries* [80]. The first category comprises the trunk of the arterial tree (Fig. 3.3), i.e., aorta, carotid, iliac, and pulmanory arteries – while the peripheral arteries, e.g., femoral and radial arteries, form the second category. The arterial walls of both vessel types have the same structure (Fig. 3.1a) of three distinct layers: intima, media, and adventitia. The innermost layer, the intima, is thin ($0.5-1\,\mu m$) compared to media and adventitia [58], and has only little effect on the solid mechanical properties of young and healthy vessels. With age however, it thickens and stiffens (arteriosclerosis) such that its contribution may become significant [80].

The media dominates the elastic mechanical properties of the artery. It is a compound of concentrically distributed elastic laminae and smooth muscle cells [58] reinforced with collagen and elastin fibers [80]. Both, number and thickness of those elastic laminae are considerably

higher in elastic arteries, while muscular arteries contain more smooth muscle cells. Inner- and external elastic laminae separate the media from intima and adventitia. For muscular arteries, they are prominent structures – whereas in elastic arteries, they are indistinguishable from the numerous other elastic laminae. The outer layer, the adventitia, is mainly formed by a fibrous collagen tissue. It is stiff under physiological conditions and serves as a tube jacket preventing overstretch and rupture.
While the structure is equal for all arteries (but different from capillaries and venules), the relative shares of the components vary widely (Fig. 3.1b). Furthermore, the relative wall thickness h to the vessel diameter D increases towards the periphery, so does the stiffness [82].

3.1.2 Elasticity and Compliance

Elasticity

Young's modulus of elasticity E is a *material property* characterising the lengthening of a sample subjected to a force F as illustrated in Fig. 3.2a. It is defined as the ratio of stress σ to strain ϵ [72]:

$$E = \frac{\sigma}{\epsilon} = \frac{F \cdot l_0}{\mathsf{A}_0 \cdot \Delta l}, \tag{3.1}$$

where F denotes the force applied to a cylindrical material sample of initial length l_0 and cross-sectional area A_0, resulting in a length increase by Δl. The Young's modulus of elasticity is a measure of the stiffness, i.e., stiff materials have higher E than elastic materials.
A *perfectly elastic* material is characterised by a straightforward stress-strain relation, independent on the rate at which stress is applied (Fig. 3.2b). Many materials, including living tissue, however appear stiffer when rapidly extended than when slowly stretched – resulting in strain creep when suddenly increasing stress, respectively stress relaxation after a sudden strain increase [72]. Stress-strain hysteresis is thus observed for a stretch-relax cycle of a *viscoelastic material* (Fig. 3.2c). The stress difference between distention and retraction is the result of (thermal) energy dissipation by the material. A phase lag between applied stress and resulting strain is observed for periodic dilation [83]. The elastic modulus of a blood vessel is found to be

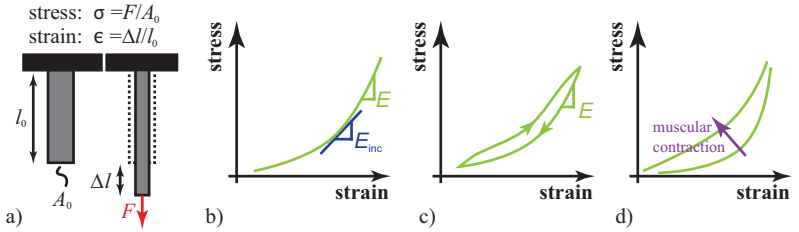

Figure 3.2: The Young's modulus of elasticity $E = \sigma/\epsilon$ for a non-linear perfectly elastic material (b) and for a non-linear viscoelastic material (c). Contraction of smooth muscles increases the artery wall stiffness (d). Definitions of stress σ and strain ϵ are given in (a).

frequency dependent: In difference to the standard mechanical models for viscoelastic materials, e.g., Maxwell and Voigt, the dynamic modulus and phase of arterial walls increase only for frequencies below 2 Hz and remain fairly constant thereafter [83].

The elasticity of an arterial wall is mainly determined by the elastin and collagen fibers as well as smooth muscle cells: Elastin has a roughly 1000 times lower E than collagen [72]. At low strain, the adventitia bears no load and the collagen fibers are wavy – the observed elasticity is determined by elastin and smooth muscle only. At higher strains however, the widening straightens the collagen fibers which start bearing load and thus lead to an increase in wall stiffness. The Young's modulus of the artery wall composite is thus non-linear, approaching E_{elastin} at low strains and E_{collagen} at high strains. In the physiologically interesting range, E is highly non-linear – the term *incremental Young's modulus* E_{inc} is often used in literature to underline that E is a function of strain, i.e., increases with strain. For muscular arteries, hysteresis is low in relaxed condition – however, pronounced viscoelasticity is observed if the smooth muscle cells are contracted [84]. Muscle contraction increases arterial stiffness for both phases (distention and retraction) as demonstrated in [84] and qualitatively illustrated in Fig. 3.2d. In large elastic arteries however, the smooth muscle cells contribute much less to the mechanical properties [83]. Under normal conditions, they are close to the maximal state of

relaxation [85], and thus, the large arteries can be considered to be close to perfectly elastic [80]. In case of an acute pressure increase however, the vascular smooth muscle cells contract [86], leading to arterial stiffening. This active phase might endure only a few seconds, but it has been observed that the contraction can be maintained over days if the overload is maintained – then it slowly relaxes while the media thickens, reducing wall stress.

Compliance

Compliance C is a *structural parameter*, not a material parameter. It is defined by Young's modulus of elasticity and the geometry of the vessel. Compliance is a measure for the relation of transmural pressure change to changes in volume, cross-section area or diameter [72]. For clarity, we differentiate volume compliance $\mathsf{C_V}$, area compliance $\mathsf{C_A}$, and diameter compliance $\mathsf{C_D}$ by their subscript – for the sake of legibility however, we may omit this reference in the text.

$$\mathsf{C_V} = \frac{\Delta \mathsf{V}}{\Delta \mathsf{P}} \qquad \mathsf{C_A} = \frac{\Delta \mathsf{A}}{\Delta \mathsf{P}} \qquad \mathsf{C_D} = \frac{\Delta D}{\Delta \mathsf{P}} \tag{3.2}$$

For a cylindrical vessel of wall thickness h and inner radius r_i, an exact relation between area compliance and Young's modulus of elasticity E can be found [72]:

$$\mathsf{C_A} = \frac{3\pi \cdot r_\mathrm{i}^2 \left(\frac{r_\mathrm{i}}{h} + 1\right)^2}{E \cdot \left(2\frac{r_\mathrm{i}}{h} + 1\right)} \approx \frac{\alpha\pi \cdot r_\mathrm{i}^3}{E_\mathrm{inc} \cdot h} \qquad \alpha = 1.5...2. \tag{3.3}$$

The inverse of compliance is denoted as *elastance* $\mathsf{E} = \frac{1}{\mathsf{C}}$, not to be confused with Young's modulus of elasticity E, although often the same symbol is used in literature. However, they are proportional, i.e., $\mathsf{E} \propto E$.
For the comparison of the elastic properties of different vessels, compliance is normalised to the expanse at a reference pressure P_0. The normalised compliance is referred to as *distensibility* K:

$$\mathsf{K_V} = \frac{\mathsf{C_V}}{\mathsf{V}_0} \qquad \mathsf{K_A} = \frac{\mathsf{C_A}}{\mathsf{A}_0} \qquad \mathsf{K_D} = \frac{\mathsf{C_D}}{D_0}. \tag{3.4}$$

Note that volume and area distensibility are equal when neglecting elongation of the vessel. The inverse of distensibility is sometimes denoted as *bulk modulus* or *(volume) elasticity*.
It follows from Young's modulus non-linearity and (3.3), that also compliance and distensibility are not constant but are a function of transmural pressure [72, 84]. The data provided in [87, 88] for the physiological range show a dilation-saturation, i.e., a lower distensibility for higher blood pressure. This is in accordance to the earlier observation of the collagen fibres rich adventitia bearing load at higher pressures.

3.1.3 Arterial Distribution System

In a simplistic model of the cardiovascular system, four distinct functions are associated with different anatomical regions: The left ventricle serves as a pump, injecting blood which has been re-oxygenated in the pulmonary circulation into the arterial system. The trunk of the arterial tree, i.e., the large elastic arteries, serves as cushioning reservoir (Windkessel), maintaining pressure during diastole. The long muscular arteries distribute the blood and actively modify the flow to some degree by contraction of smooth muscle. Finally, the arterioles control local perfusion of tissue and organs by changing their calibre over a large range, altering the peripheral resistance R_p [72, 83, 89].
The sustained pressure during diastole allows for a continuous flow in the capillaries although blood injection is pulsatile.

Arterial Pressure Wave & Blood Flow

The contraction of the left ventricle injects a volume of blood into the aorta, leading to a sudden rise in local transmural pressure and so the spreading of a pressure wave. In a young and healthy subject, the waveform of the pressure wave changes considerably on its way through the arterial tree, as illustrated in Fig. 3.3: Increasing wall stiffness leads to a gain in pulse amplitude towards the periphery. Branching and impedance discontinuities lead to reflections, superimposing backwards travelling reflected waves to the forwards traveling wave and altering the measured waveform [58,90]. The amplitude gain

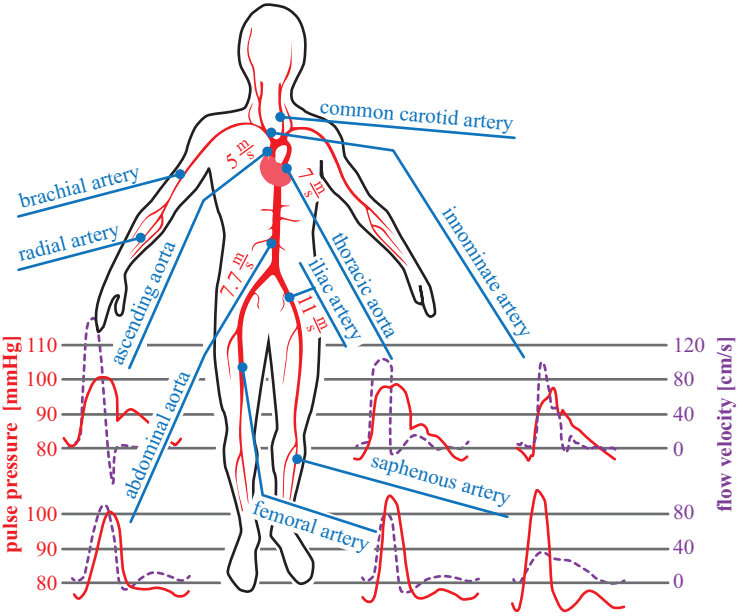

Figure 3.3: Simplified arterial tree comprising the large elastic and long conducting muscular arteries. Pressure- and flow wave-forms as well as PWV are given for different sites in the tree. Adapted from [72, 83, 90].

reduces with age from ca. 2.0 (24 years) to 1.05 (80 years) [83], most probably due to elastic artery degeneration, i.e., reduced distensibility of the elastic arteries.

The transition from small arteries to arterioles and finally from arterioles to capillaries comes with a steep increase in vascular resistance [72] – the resulting impedance mismatch leads to a nearly total reflection of the pressure wave, the pressure drop due to the widening of subsequent venous vessels and increasing compliance further absorb the remainders of the arterial pressure wave, such that virtually none is observed in venous vessels.

Due to the pulsatile pumping of the heart, the blood flow is non-constant as well. As illustrated in Fig. 3.3, blood flow occurs in

the ascending aorta only during a short period of time. While the flow-wave widens on the way to peripheral arteries, the peak flow velocity decreases simultaneously. Capillary flow is rather constant and slow.
Peak blood flow velocity in the aorta is ca. 1 $\frac{\mathrm{m}}{\mathrm{s}}$ while its mean value is about 15 $\frac{\mathrm{cm}}{\mathrm{s}}$ – the wave velocity, i.e., the velocity with which pressure and flow waves travel is considerably higher and ranges between 4 $\frac{\mathrm{m}}{\mathrm{s}}$ and 10 $\frac{\mathrm{m}}{\mathrm{s}}$ [72].

3.2 Pulse Wave Velocity

The Moens-Kortweg equation describes an approximate relation between the propagation speed c of a pressure wave in a fluid filled elastic tube [72]:

$$c = \sqrt{\frac{Eh}{\rho D}}, \tag{3.5}$$

with the elastic modulus E, wall thickness h, tube diameter D, and mass density ρ of the fluid. The Bramwell-Hill equation is derived from (3.5) and relates c to the compliance C of the tube [91]:

$$c = \sqrt{\frac{\mathsf{V}}{\rho \mathsf{C}_\mathsf{V}}} = \sqrt{\frac{1}{\rho \mathsf{K}_\mathsf{V}}}. \tag{3.6}$$

A more rigorous analysis considering non-idealities in blood flow can be found in [92].

3.2.1 Blood Pressure

As discussed in Sec. 3.1.2, the elasticity modulus of arteries is a function of applied stress and therefore of transmural pressure. The observed pressure-distensibility relation of arteries can be approximated in the physiological range as [88]

$$\mathsf{K}_\mathsf{V} \approx \frac{\alpha}{1 + \left(\frac{\mathsf{P} - \beta}{\gamma}\right)^2}, \tag{3.7}$$

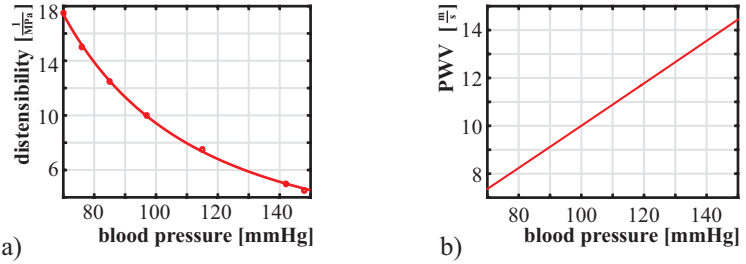

Figure 3.4: Human carotid artery area distensibility [88] (a) and corresponding PWV (b).

with empirical constants α, β, and γ of unit [Pa] and P denoting the transmural pressure, i.e., blood pressure.
The propagation speed of the arterial pressure wave, i.e., the PWV, is thus:

$$c \approx \sqrt{\frac{\gamma^2 + (\mathsf{P} - \beta)^2}{\alpha\gamma^2\rho}}. \tag{3.8}$$

The distensibility measurements of the human carotid artery for varying blood pressure reported in [88] are reproduced in Fig. 3.4a together with a fitting curve according to (3.7). On the latter, the PWV has been calculated according to (3.8). One can observe that in the physiological range, the relation between PWV and blood pressure is linear. For practical applications, (3.8) can thus be approximated to:

$$c \approx \zeta + \xi\mathsf{P}. \tag{3.9}$$

Where ζ and ξ denote constants of unit $[\frac{\mathrm{m}}{\mathrm{s}}]$ and $[\frac{\mathrm{m}}{\mathrm{s}\cdot\mathrm{Pa}}]$, respectively.

3.2.2 Heart Rate

First observations that arterial distensibility depends on heart rate were reported for the common carotid and the femoral arteries of Wistar rats during *in-vivo* experiments by Mangoni et al. [93]. Equation (3.6) implies that PWV is thus a function of heart rate as well. A study in 22 human patients with cardiac pacemakers (allowing for precise control of the heart beat) followed and confirmed the influence

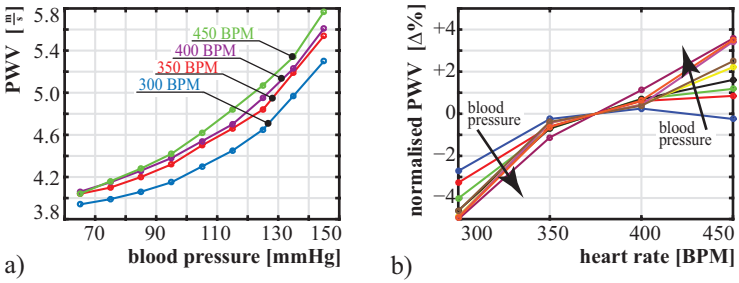

Figure 3.5: PWV as a function of blood pressure and heart rate in rats (a), reproduced from [96]. Blood pressure dependent relative deviation of PWV (b) normalised to its 375 BPM value, based on the data given in [96].

of heart rate on measured PWV [94]. After initial scepticism [95] – triggered by the implications of the new findings in questioning older conclusions based on PWV – today, the heart rate influence on PWV is widely accepted and has been confirmed in recent experiments. Most notably the comprising work of Tan et al. [96] in 7 Sprague-Dawley rats paced between 300 and 450 BPM under controlled blood pressure levels in the range $60 - 150$ mmHg. Their measurement results are reproduced in Fig. 3.5a. Both, absolute and relative PWV-variance due to heart rate increase with blood pressure. A deviation of up to ca. $\pm 5\%$ is observed (Fig. 3.5b).
The physical reason for the phenomenon is disputed: published hypotheses include the frequency-dependency of Young's modulus of elasticity (Sec. 3.1.2) and reduced recoil time for the arterial walls [94, 96].

3.2.3 Smooth Muscle Tone

If PWV is measured at the periphery, e.g., with means of wrist-to-finger PPG [14, 15] or ECG-to-finger-PPG [13, 17], muscle tone of muscular arteries influence the overall compliance and thus the measured PWV. Calibration algorithms to overcome the impact of

vasomotion have been reported [14], however it seems that more reliable measurements are achieved when avoiding muscular arteries and performing the measurement on the elastic trunk of the arterial tree [16].

3.2.4 Clinical and Physiological Relevance

As discussed above, PWV depends on compliance (or distensibility), which again is a function of blood pressure and heart rate. PWV allows thus for estimation of arterial compliance [72] if calibrated against blood pressure and heart rate. Different measurement approaches have been reported, ranging from catheterised pressure measurements to non-invasive methods based on velocity-encoded magnetic resonance imaging (MRI) [97], Doppler ultrasound [98], multiple pressure sensors placed on the body surface [99] or the above mentioned PPG-based methods. Recently, a chest-PWV device combining electrocardiography (ECG), phonocardiography (PCG), impedance cardiography (ICG) and PPG was proposed as an easier to use alternative for routine PWV measurement [100]. Due to the relatively recent discovery, older publications and measurement setups do not cope with the heart rate influence on PWV.
An increase in PWV with age has been observed [83, 101] and quantified as ca. $8 - 16$ $\frac{\text{mm}}{\text{s}}$ per year [97, 102] for healthy subjects. It is associated with an increase in aortic stiffness which is attributed to progressive thinning and fracturing of the elastic laminae, likely due to persistent mechanical stress [72]. Lower aortic compliance leads to higher pulse-pressure in the aorta as discussed in Sec. 3.1.3 and [83] and does thus further increase attrition.
Analogously, PWV can be used to estimate blood pressure when the distensibility is known, e.g., after an initial calibration to the readings of a conventional blood pressure monitoring device. This is of particular interest for non-invasive non-obstructive long-term blood pressure measurement [13–17]. However, achieving precise results in PWV based wearable blood pressure monitoring has shown to be difficult. Mainly due to the chosen – easily accessible – peripheral sensor sites and the negligence of the heart rate induced PWV modulation.
We conclude this chapter with a brief digression on blood pressure, its regulation, and its cyclic modulation by respiration.

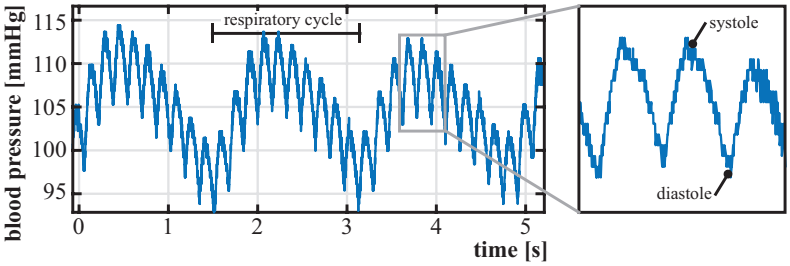

Figure 3.6: Arterial blood pressure of an anaesthetised Wistar rat recorded on the right carotid artery by means of a catheter. The respiratory influence on the blood pressure is clearly visible.

3.3 Blood Pressure

Blood pressure of healthy humans lies between $70 - 80$ mmHg for diastolic pressure and $110 - 150$ mmHg for systolic pressure. An increase with age due to higher arterial stiffness (see Sec. 3.1.3) is observed. Maintaining blood pressure under varying ambient conditions and physical activity is vital to ensure sufficient perfusion of all organs [103].

3.3.1 Blood Pressure Regulation

The peripheral resistance of the arterial distribution system is subject to perpetual variation due to local perfusion regulation by arteriole calibre adjustments – initiated either by local automatic regulation (adaptation on metabolic requirements triggered by chemoreceptors / intrinsic response of smooth muscle on transmural pressure changes) or remotely controlled by the *cardiovascular centre* [89]. E.g., blood flow in skeletal muscle may be $10 - 15$ times higher in action than at rest [89] and skin perfusion is highly dependent on ambient temperature [103]. Decrease and increase of the peripheral resistance leads to blood pressure drop and rise, respectively.

The central cardiovascular system is monitored by multiple baroreceptors – sensible to strain and located on the aortic arch and the carotid sinus – and chemoreceptors – sensible to variations in O_2,

CO_2, and pH, mainly located on the carotid- and aortic bodies. The receptors are connected by the carotid sinus nerve (CSN) and aortic depressor nerve (ADN) to the cardiovascular centre of the brain. Their neural discharge frequency is higher when high blood pressure is sensed than for low pressure. The outputs of the cardiovascular centre control contraction rate and force of heart muscles and smooth muscle contraction in arterioles and veins [58]. The regulation is achieved by two opposing regions in the cardiovascular centre and neural subsystems: the sympathetic system (pressor region) and the parasympathetic system (depressor region). While sharing sensory inputs, concurring sympathetic (cardiac nerve) and parasympathetic (vagus) nerves connect the cardiovascular centre to the heart muscles. Stimulation of the former leads to an increase in heart rate and heart muscle contraction force, and thus to an increase in blood pressure, while stimulation of the latter lowers heart rate and blood pressure.

3.3.2 Respiratory Blood Pressure Modulation

A cyclic modulation of blood pressure coinciding with respiratory movements is observed, see Fig. 3.6. It has been found that the modulation amplitude depends on the respiratory rate [104, 105]. As most probable reasons for the phenomenon are listed [104]:

- *Mechanical effects.* Breathing mechanically affects intrathoracic pressure, which again modulates venous return to the right heart chamber and thus periodically increases and decreases stroke volume. Finally, lower stroke volume results in lower systolic blood pressure.

- *Chemoreceptors.* Local autoregulation directly changes peripheral vascular resistance by arteriole calibre regulation according to S_aO_2, which again affects blood pressure.

- *Cardiopulmonary and arterial baroreflex.* Mechanical stretch applied to sensors of the baroreflex 'control loop' effects a blood pressure (and heart rate) drop. A cyclic stretch modulation due to breathing can effect a periodic modulation of blood pressure and heart rate.

Chapter 4

TMA-O: A PPG & NIRS AFE

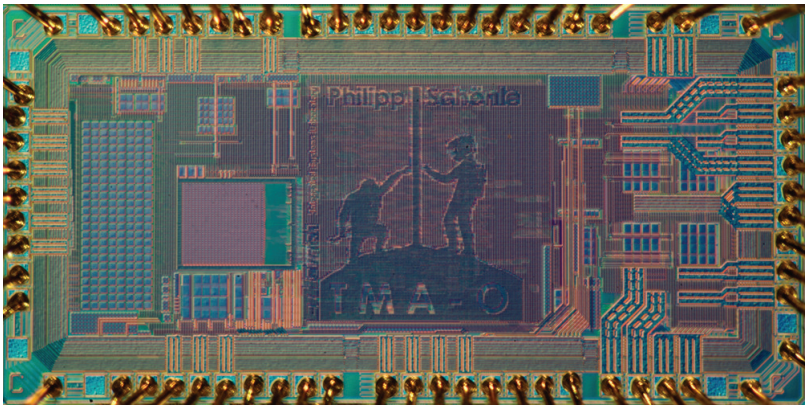

Figure 4.1: Chip micrograph of the *TMA-O* multi-channel PPG ASIC.

This chapter discusses the design of the *transimpedance medical amplifier for oximetry (TMA-O)* PPG ASIC, implemented in a 130 nm CMOS technology. The block diagram in Fig. 4.2 gives an overview on the circuit. It comprises a fully differential TIA with four multiplexed photodiode input channels as receiver. A differential current subtraction (DCS) circuit for partial removal of the large DC component in

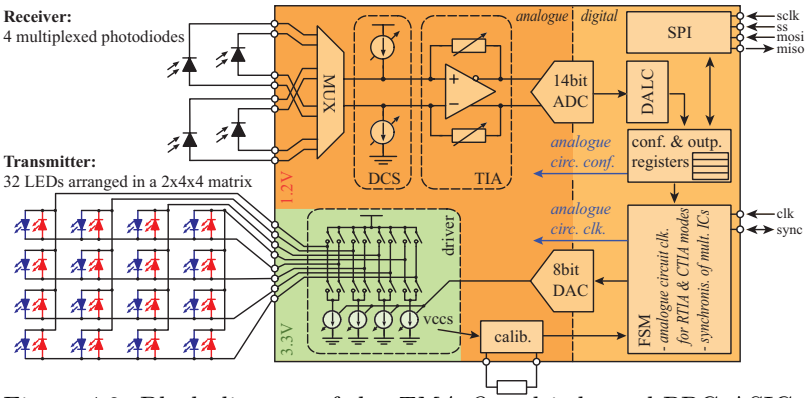

Figure 4.2: Block diagram of the *TMA-O* multi-channel PPG ASIC.

PPG signals precedes the TIA. A 14 bit SAR ADC [106] digitises the signal conditioned by the AFE. The transmitter can drive up to thirty-two LEDs arranged in a 2×4×4 matrix. Driving strength can be adjusted in 255 steps and, if required, the output current can be calibrated by means of an external resistor. The analogue circuitry of both, the receiver front-end and the transmitter are simultaneously controlled by a common finite state machine (FSM). For applications demanding more channels than provided by a single chip, or those taking advantage of simultaneous but spatially separated recordings, multiple ICs can be synchronised in a master/slaves setup.
The remainder of this chapter is organised as follows. It begins with the discussion of the requirements on a PPG ASIC for use in pulse oximetry, NIRS, and PWV applications. In Sec. 4.2 the definitions of commonly used *performance metrics* are given and a figure-of-merit (FoM) is introduced as a measure of PPG circuit energy efficiency. Subsequently, Sec. 4.3 on *system architecture* discusses a general PPG circuit and its components – emphasis is put on the optoelectronic components, i.e., photodiode and LED, and the implications of their physics on the design of a PPG circuit. Considerations on *receiver architecture* and its *implementation* follow in Sec. 4.4 and 4.5. The design of the *LED driver* is explained in Sec. 4.6, followed by a short insight in the *digital circuit* in Sec. 4.7. Finally, measurement results and a comparison to the state-of-the-art are presented in Sec. 4.8.

4.1 Requirements on the PPG ASIC

Pulse Oximetry

Noise and linearity requirements for an accurate pulse oximetry reading are derived in Sec. 2.6: While linearity requirements are low and easily met, an overall dynamic range higher than 90 dB is required – given by the low amplitude of the pulsatile component in the PPG associated with arterial blood (Fig. 2.3). As illustrated in Fig. 2.12b the dynamic range requirements are not constant but depend on both, arterial blood oxygenation and perfusion index AC/DC. In practice various conditions and situational parameters influence the accuracy of pulse oximeters and vast literature reports on observed (in)accuracy under specific circumstances – an overview is, e.g., given by Chan et al. in [107]. From a technical point-of-view, observed inaccuracies stem from four different effects on PPG each of which can result from various primary causes: low perfusion index, high DC absorbance, and additional AC components with distinguishable or indistinguishable absorption spectrum. Table 4.1 summarises primary conditions, resulting effects on the acquired signals and consequent PPG ASIC characteristics required for effective countermeasures.
Reportedly increased inaccuracy with commercial pulse oximeters [60, 108, 109] for conditions causing a low perfusion index is no surprise when considering the increasing requirements in dynamic range on the PPG circuit (Fig. 2.12b). Hummler et al. [60] for instance observed increased inaccuracy for measurements with a perfusion index lower than 1%. Ambient light can further increase overall DR requirements since the DR available to the PPG signal gets reduced. Correlated double sampling based ambient light cancellation (ALC) does not counter this effect but does remove DC and in-band AC interference. High efficacy of ALC against the latter can be important when considering changing ambient illumination due to motion.
Dark skin pigmentation [108] and nail polish [110] don't directly affect the perfusion index, as discussed in Sec. 2.4.1. However, it reduces the optical transmission which results in a lower photo-generated current at the receiver. Best counteraction is to compensate by increasing the LED current accordingly. As will be discussed in Sec. 4.3.2, this can cause an undesired spectral shift of the LED emission which

must be prevented by low duty-cycle operation. Otherwise, if LED current cannot be further increased, lower transmission requires lower receiver noise, makes the measurement more vulnerable to ambient light, and accentuates the problem of direct light paths between LED and photodiode.

Pulse oximetry is based on two-wavelength spectrophotometry. This is sufficient to distinguish two components contributing to the measured absorbance but leads to false readings if other substances contribute to the absorption. In normal conditions, absorption by whole blood is clearly dominated by oxyhaemoglobin and deoxyhaemoglobin, and pulse oximeters compensate for additional absorbance by empiric calibration. When the arterial blood contains components which have not been accounted for they will interfere with the S_pO_2 reading. Reported are false readings due to dysfunctional haemoglobin [111], intravenously administered dyes [113, 114], and variant haemoglobins [112]. The latter are rare genetic mutations of haemoglobin present in some people besides normal haemoglobin. Some variants have a different absorption spectrum than their normal counterpart. False readings due to such unaccounted absorption components can be avoided with spectral diversity, i.e., an increased count of wavelengths. It can be used to either detect the spectral anomaly and prevent the presentation of wrong results or to measure the concentration of those substances as well (if their absorption spectrum is known), which is especially useful in case of dysfunctional haemoglobin [111].

Motion artefacts and venous pulsation [116] result in AC absorption components which are spectrally indistinguishable from arterial blood (with lower oxygenation). As discussed in Sec. 2.5.1 the effect of motion on the PPG signal is lower for small vessels in the outermost tissue layers than for larger and deeper laying vessels – this effect can be taken advantage of by reflective PPG with short wavelength (green, blue) light which has a low penetration depth. Adding a third, green, LED thus eases separation of motion artefact and pulsatile signal by serving as a less affected reference signal. Similarly, in parallel recorded PPG signals with different LED-photodiode paths, the impact by motion differs from channel to channel. The redundancy in such a setup with *spatial diversity* eases separation [115] and can reduce the effect of badly placed probes by an automatic search for good LED-photodiode combinations.

Table 4.1: Challenges in Pulse Oximetry Accuracy

causes		*effects*	*countermeasures*
• low perfusion	[60]	• low perfusion index (PI)	⇒ high dynamic range
• sepsis	[60]	↪ incr. impact of ambient light	⇒ ambient light cancellation
• anaemia	[107, 108]		
• vasoconstriction	[109]		
• small finger	2.4.1		
• blood loss			
• skin colour	[108]	• incr. DC absorbance	⇒ high LED current
• nail polish	[110]	↪ in theory no influence on PI	↪ low duty-cycle to
		• incr. impact of direct paths	avoid spectral shift
		• incr. impact of ambient light	⇒ ambient light cancellation
		↪ reduced PI	• high dynamic range
• dysfunct. haemoglobin	[111]	• additional AC abs. source	⇒ spectral diversity (LED array)
• variant haemoglobin	[112]	with different spectrum	↪ spectral anomaly detection
• intraven. pigm. dyes	[113, 114]		↪ correction for known substances
• motion artefacts	[115]	• additional AC abs. source	• spatial diversity (LED array)
• venous pulsation	[116]	with indist. spectrum	• add. sensors

Table 4.2: Further Applications of PPG and NIRS

application		*difficulties*	*requirements*
• total haemoglobin	[117]	• separation of absorbance	⇒ spectral diversity (LED array)
• dysfunct. haemoglobin	[111]	shares by diff. molecules	↪ 4-12 LEDs
• CCO	[11, 118]	• distant emitter-receiver separation	
• tissue perfusion	[1–3]	↪ low transmission	⇒ high receiver gain
• muscle perfusion	[119]	↪ incr. impact of ambient light	⇒ ambient light cancellation
		↪ incr. impact of direct paths	⇒ enhanced dynamic range
↪ CW NIRS	[120]	⇒ absolute concentration values	⇒ spatial diversity
• PWV / PTT	3 / 6.4	• propagation velocity ca. 10 m/s	⇒ high sampling rate

Further applications of PPG and NIRS

The *TMA-O* chip is intended to cover a wide range of applications including NIRS for tissue- and muscle perfusion [1–3, 7, 119] or CCO [11, 118] measurement. Here, emitter and receiver are located more distant from each other than in pulse oximetry, which results in 15 to 65 times lower receive signal strength, as shown in App. A.1. This requires effective ambient light cancellation, a high dynamic range, and higher receiver gain settings. Then again, implantable PPG comes with much higher transmittance $\mathcal{T}$ and thus asks for low receiver gain. *TMA-O's* receiver TIA is thus supposed to span a wide transimpedance range. Most NIRS applications require spectral and spatial diversity for the separation of the different chromophores and the calculation of absolute concentrations [120] – including multiple input channels.
Other PPG-based measurements such as pulse wave velocity on a limited stretch of artery (Sec. 6.4) require a much higher sampling rate than a normal pulse oximeter.
Applications and additional requirements are summarised in Tbl. 4.2.

4.2 Performance Metrics

The characterisation of a PPG circuit usually focusses on the noise performance since the moderate linearity requirements (Sec. 2.6.1) are easily met. Noise metrics are most often given for a defined signal bandwidth rather than the Nyquist bandwidth. The different terms and metrics used throughout this thesis are defined below.

Signal-to-Noise Ratio

The signal-to-noise ratio (SNR) is defined as the ratio of signal power to noise power. For different applications and circuits, different waveforms are used for characterisation. Thus SNR values are only meaningful when the signal waveform for which it was measured is known. To avoid confusion, the following symbols and corresponding definitions are used in this thesis:

SNR_{PPG}. The ratio of PPG AC-signal power to noise power. It can be a useful measure of the signal quality under a certain condition, but is not suited as a performance metric for the circuit since it depends on the actual PPG waveform, the perfusion index AC/DC and the DC/FS ratio.

SNR_{FS}. The ratio of signal to noise power for a full-swing sinusoidal input signal. This measure reflects well a typical receiver test setup.

SNR_{DC}. The ratio of (single-ended) DC signal power to noise power.

Dynamic Range

The dynamic range (DR) is the ratio of the highest to the lowest distinguishable signal level. In case of a receiver front-end, this is the ratio of the highest resolvable DC input signal level to the overall RMS noise, including quantisation noise. Analogously, the dynamic range of an output is the ratio of the highest possible DC output level to either the minimum quantisation step or (if dominating) the RMS noise. Implicitly simultaneous dynamic range is assumed, i.e., the DR covered with a specific constant circuit configuration.
For a receiver, dynamic range is equal to SNR_{DC} of its maximum resolvable input signal. To full-swing SNR it is related by

$$DR = SNR_{\mathrm{FS}} + 9.03\,\mathrm{dB}, \tag{4.1}$$

with the additional 9.03 dB accounting for the waveform (3 dB) and single-ended (6 dB) definition. Depending on the peculiarities of the circuit under test, the dynamic range derived from SNR_{DC} and SNR_{FS} measurements might be somewhat different, but comparable.
The loop dynamic range, see Sec. 4.2.1 and Sec. 4.3.3, is defined as the power ratio of a full-scale DC input signal to the noise power measured with a DC input signal applied of half the full-scale.

Spurious-Free Dynamic Range

The SFDR is a measure of linearity. It is defined as the ratio of the carrier and the strongest distortion component of a sinusoidal test signal.

PRF, Sampling Frequency and Sample Rate

The pulse repetition frequency (PRF) is the number of LED pulses per second and channel, expressed in Hz. Usually identical to the sampling frequency and raw sample rate. However, averaging of multiple samples taken during a single LED flashing is a commonly used method to reduce receiver noise – in such cases pulse repetition frequency (PRF) and sampling frequency differ. Moreover, here *sampling frequency* might be an inappropriate term when sampling is performed at irregular time intervals.

4.2.1 Figure-of-Merit

Dynamic range and power consumption are the two critical performance metrics for a pulse oximetry circuit intended to be used in wearable or implantable electronics. As the optimal choices of PRF and LED current – as well as the signal bandwidth – depend on the target application, the numbers reported in publications and datasheets cannot be compared directly to each other. This section explores the interdependencies of the different metrics and finally provides a FoM for fair comparison of various circuits.
The TIA bandwidth $f_{\mathrm{BW,TIA}}$ has to be chosen considerably higher than the arterial pulse-wave signal bandwidth $f_{\mathrm{BW,SIG}}$ and the PRF f_{PR} in PPG circuits to allow for short LED pulses. Sampling thus unavoidably leads to noise aliasing: The RMS noise of the sampled signal $\sigma(n_{\mathrm{raw}})$ is – for a given TIA configuration – independent of the PRF, the noise floor in the signal-band however is proportional to $f_{\mathrm{BW,TIA}}/f_{\mathrm{PR}}$ when assuming white noise. RMS noise in the signal-band is thus:

$$\sigma(n_{\mathrm{sig}}) = \sqrt{\frac{2f_{\mathrm{BW,SIG}}}{f_{\mathrm{PR}}}}\,\sigma(n_{\mathrm{raw}})\,. \tag{4.2}$$

The overall power consumption is typically dominated by the LEDs and thus scales well with their duty cycle. For constant pulse width, the LED power consumption is proportional to the PRF:

$$P_{\mathrm{LED}} \propto f_{\mathrm{PR}}. \tag{4.3}$$

Equations (4.2) and (4.3) illustrate the DR-power trade-off, discussed in more detail in Sec. 4.3.4. For a given circuit, signal band noise

power can be halved by doubling PRF and thus LED power consumption. Reducing the latter by decreasing pulse current amplitude leads to an inversely proportional increase in photodiode shot noise, again lowering the dynamic range (see Sec. 4.3.1). Moreover, lower LED current means less ambient light interference resilience. We define the FoM for PPG circuits as:

$$FoM = DR_{\mathrm{f_{BW}}} + 10\log_{10}\left(\frac{f_{\mathrm{BW}}}{1\mathrm{Hz}} \cdot \frac{1\,\mathrm{mW}}{P_{\mathrm{tot}}} \cdot \frac{10\mathrm{ppm}}{\Theta}\right) \quad [\mathrm{dB}], \quad (4.4)$$

with f_{BW} denoting the bandwidth for which the loop dynamic range $DR_{f_{\mathrm{BW}}}$ has been measured, P_{tot} the total power consumption of the circuit including the two LEDs used in pulse oximetry, and $\Theta = \frac{I_{\mathrm{ph}}}{I_{\mathrm{LED}}}$ the transmission factor.

The loop dynamic range, discussed in more detail in Sec. 4.3.3, reflects overall PPG circuit performance. It includes noise added by all sub-circuits, i.e., LED driver, LED, photodiode and receiver. For convenient measurement, we define the DR as ratio of the maximum input signal power to the noise power measured with incident light corresponding to 50% full-scale receiver input current. This convention has to be defined as photodiode shot-noise tends to ultimately limit dynamic range and thus the FoM, as discussed in Sec. 4.3.4 in more detail.

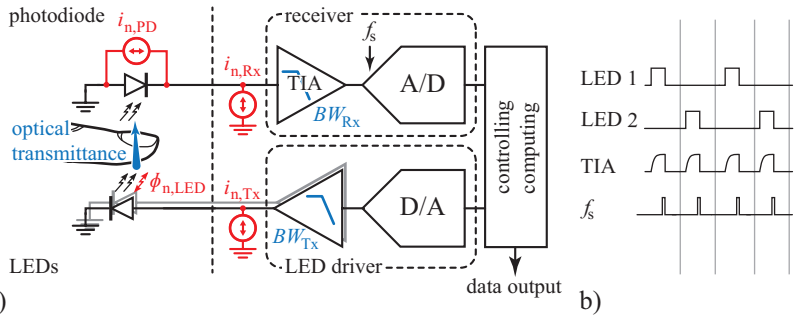

Figure 4.3: Basic PPG circuit with (summarised) noise contributors (a). Timing diagram for two-channel PPG signal acquisition (b).

4.3 System Architecture

A general system-level PPG circuit is depicted in Fig. 4.3. Receiver and driver circuitry are integrated in the *TMA-O* chip, while the optoelectronic devices, i.e., photodiode (PD) and LEDs, remain off-chip. The overall optical transmission $\Psi = \frac{\phi_{\mathrm{PD}}}{\phi_{\mathrm{LED}}} = \frac{\Omega_{\mathrm{PD}}}{\Omega_{\mathrm{LED}}}\mathcal{T}$ depends on the probe geometry, placement and skin pigmentation. Transmittance $\mathcal{T}$ is highly dependent on the latter. As discussed in Sec. 2.3.1, electrical transmission $\frac{I_{\mathrm{ph}}}{I_{\mathrm{LED}}} = \Psi\eta_{\mathrm{q}}\eta_{\mathrm{ex}}$ can be as low as 10ppm in pulse oximetry. The physics of photodiode and LED, and device-specific characteristics, determine design choices and will ultimatively limit the overall performance. The pursuit towards an optimum PPG circuit thus starts with the analysis of those external optoelectronic devices.

4.3.1 Photodiode

The photodiode equivalent circuit and the IV-characteristic are given in Fig. 4.4. The photo-generated current I_{ph} is represented with a current source in parallel to the ideal diode. The model accounts further for the dominant parasitics, i.e., series- and shunt resistances R_{s} & R_{sh}, and junction capacitance C_{j}. The series resistance is usually negligible compared to the receiver transimpedance and will be omitted for further analysis. Numeric values given below for PIN photodiode characteristics are based on datasheets [121–124] of typical devices with active areas similar to what is used in pulse oximetry probes.

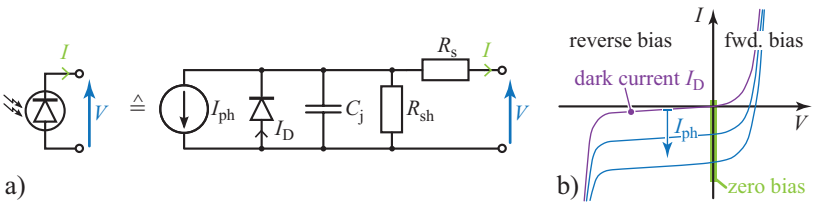

Figure 4.4: Photodiode equivalent circuit (a) and characteristic IV curves (b) [125].

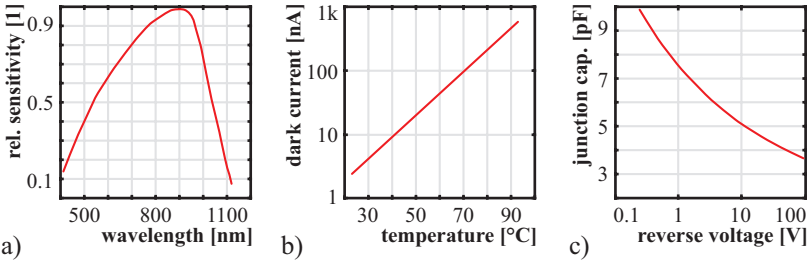

Figure 4.5: Typical silicon PIN photodiode characteristics on the example of the *Everlight* PD15 [123].

Shunt Resistance and Junction Capacitance

Shunt resistance values – measured as the IV relation at 10 mV bias voltage – range from 150 MΩ to 500 MΩ. Junction capacitance is highly dependent on the operating point as illustrated in Fig. 4.5c. At zero bias it is found to be in the order of $4 - 50$ pF.

Dark Current

The diode current in absence of incident light is denoted as *dark current* [125]

$$I_{\mathrm{D}} = I_{\mathrm{SAT}} \left[\exp\left(\frac{-qV_{\mathrm{R}}}{k_{\mathrm{B}}\mathsf{T}} \right) - 1 \right] \tag{4.5}$$

with V_{R} denoting the reverse bias voltage. The *dark current* is usually given in datasheets for a reverse bias of $5 - 10$ V at room temperature, where values in the range $3 - 30$ nA are reported. As follows from (4.5), this value corresponds roughly to the reverse saturation current I_{SAT}. The latter is highly temperature dependent and increases for silicon pn diodes by approximately a factor of four for every 10°C increase in temperature [126]. The dark current is thus equally temperature dependent, as shown in Fig. 4.5b. For photodiodes in PPG probes body temperature should be assumed, where $I_{\mathrm{SAT}} = 10 - 120$ nA is estimated.

Noise

Two noise sources contribute to the photodiode noise: thermal noise and shot noise [125], both are of white Gaussian nature. Thermal noise is associated with the shunt resistance and given by

$$\overline{i^2_{\mathrm{n,th}}} = \frac{4k_{\mathrm{B}}\mathsf{T}f_{\mathrm{BW}}}{R_{\mathrm{sh}}}. \tag{4.6}$$

Shot noise is the effect of fluctuations in both, the photo-generated current I_{ph} and the dark current I_{D}:

$$\overline{i^2_{\mathrm{n,s}}} = 2q(I_{\mathrm{ph}} + |I_{\mathrm{D}}|)f_{\mathrm{BW}}. \tag{4.7}$$

Generally, shot noise dominates over thermal noise: the current spectral density plots (Fig. 4.6a,b) for (4.6) and (4.7) in the above given shunt resistance and dark current ranges show that the dark current share of the shot noise dominates over thermal noise.
The overall dominant noise source however is shot noise associated with the photo-generated current. It defines the intrinsic maximum signal-to-noise ratio of a photodiode – i.e., the ratio of DC I_{ph} to the RMS noise:

$$SNR_{\mathrm{DC,PD}} = 10 \cdot \log_{10}\left(\frac{I_{\mathrm{ph}}}{2qf_{\mathrm{BW}}}\right). \tag{4.8}$$

A SNR_{DC} increase by 3 dB requires double photo-generated current, i.e., double incident photon flux, Fig. 4.6c.
While the impact of dark current is rather small for $I_{\mathrm{ph}} > 1\,\mu\mathrm{A}$, it can be considerable for photo-currents in the tens of nano-amperes as illustrated in Fig. 4.6d.

Optimum Operating Point

In optical communication receivers, photodiodes are usually operated in strong reverse bias to reduce the junction capacitance – allowing for higher system bandwidths. For PPG signal acquisition however, high bandwidth is not desired. Zero-bias operation minimises dark current according to (4.5) and thus shot noise, but requires good control over input offset: 10 mV correspond to 30% and 47% I_{SAT} in reverse- and forward bias, respectively.

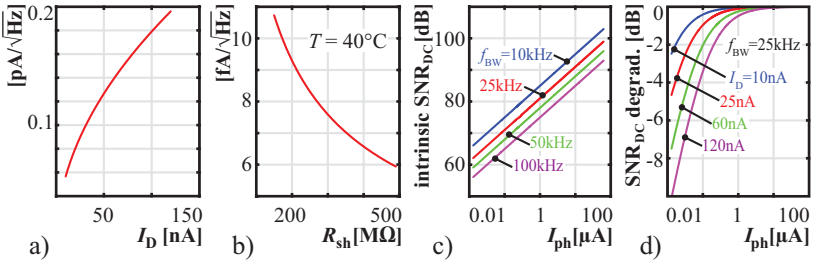

Figure 4.6: Current spectral density for shot noise (a) and thermal noise (b) for expected dark current and shunt resistance ranges. Intrinsic SNR_{DC} (limited by I_{ph}-shot-noise only) (c) and SNR_{DC} degradation due to I_{D}-shot noise (d).

4.3.2 Light Emitting Diode

As observed in the former section, the photodiode shot noise links the maximum achievable signal-to-noise ratio with the photo-generated current and thus to the incident photon flux. Which again is defined by the LED radiation, optical transmission, and photodiode sensitivity. Assuming a minimum overall transmission of 10ppm and aiming for $I_{\mathrm{ph}} = 1\,\mu\mathrm{A}$ demands a LED peak current of 100 mA.

Forward Voltage

The current-voltage characteristics of a forward biased diode, and thus LED, is given as

$$I_{\mathrm{LED}} = \mathsf{A}_{\mathrm{j}} J_{\mathrm{s}} \left[\exp\left(\frac{q V_{\mathrm{F}}}{k_{\mathrm{B}} \mathsf{T}} \right) - 1 \right], \tag{4.9}$$

with A_{j} denoting the junction cross-section area. The saturation current density J_{s} is known to be proportional to $\exp\left(-E_{\mathrm{g}}/(k_{\mathrm{B}}\mathsf{T})\right)$. However, it further depends on material properties and design process variables, i.e., donor and acceptor impurity densities [126]. Emission wavelength λ is inversely proportional to the bandgap energy E_{g}:

$$\lambda = \frac{\mathsf{hc}}{E_{\mathrm{g}}}. \tag{4.10}$$

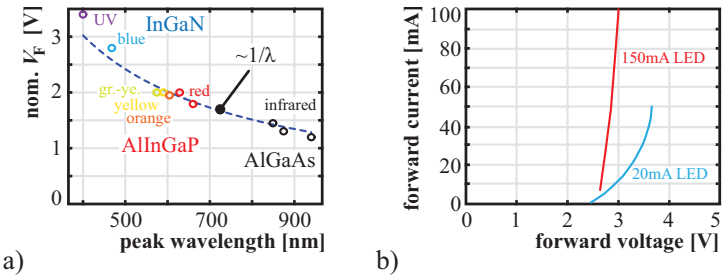

Figure 4.7: Nominal typical forward voltage for LEDs of different peak emission wavelengths designed for similar bias conditions [127–136] (a) and IV characteristics for two blue (460nm) LEDs [128, 137] designed for different DC forward currents (b).

For a constant $\frac{I_{\mathrm{LED}}}{\mathsf{A}_{\mathrm{j}} J_{\mathrm{s}}} >> 1$ we thus find that

$$V_{\mathrm{F}} \propto \frac{1}{\lambda}. \tag{4.11}$$

For LEDs of similar die size and forward current, forward voltage is thus inversely proportional to the emission wavelength. In Fig. 4.7a the nominal forward voltages for a series of commercial LEDs [127–136] of colours ranging from ultra-violet to infrared but with similar electrical and mechanical specifications is shown to correlate well to (4.11).

LEDs of red and infrared colour, used for pulse oximetry, have usually nominal forward voltages in the range $1.5-2.2\,\mathrm{V}$ while green and blue LEDs, used in pulse meters and optogenetics, have forward voltages close to $3\,\mathrm{V}$. From a thermal point of view, LED peak currents can be many times the specified DC current if duty-cycle and pulse-width are short. However, forward voltage increases with current density. Fig. 4.7b illustrates this with the IV-characteristics of two LEDs of equal wavelength but different dimensions. The first [128], a $200\times200\,\mu\mathrm{m}^2$ indication LED designed for $20\,\mathrm{mA}$ DC forward current shows $3.6\,\mathrm{V}$ forward voltage at $50\,\mathrm{mA}$ while the second [137], a much larger $1\times1\,\mathrm{mm}^2$ lighting LED has only $2.8\,\mathrm{V}$ for the same current.

Spectral Stability

The spectral emission of LEDs is reported to depend on both, ambient temperature and forward current [138, 139]. A measurement series on a commercial component for pulse oximeters featuring two LEDs (660 nm / 940 nm) in a single package [140] is summarised on page 62. The spectra have been acquired with an *Ocean Optics HR4000* high-resolution spectrometer under room temperature (25°C) for different forward currents and duty-cycles. In continuous-current operation (uppermost row) a shift towards longer wavelengths is observed for increasing forward current in the red LED. Peak emission difference is 22 nm for 80 mA versus 1.4 mA. For the infrared LED, the rise of a secondary local emission maximum is observed. The sub-figures in the lower rows depict the emitted spectra in pulsed operation. The applied forward currents are equal as for the measurements in continuous mode. Constant PRF of 630 Hz is used, while the duty-cycle is controlled by the pulse-width. The spectral spread is observed to reduce with duty-cycle, and finally the spectral emissions are indistinguishable from each-other over the whole current range for 1.8% duty-cycle LED operation. The observed spectral shift is thus independent of current density and most probably the result of increasing junction temperature due to self heating.
In fact, a similar effect on the spectrum is observed in Fig. 4.8 for LEDs operated at a constantly low 1.8% duty-cycle but under varying ambient temperatures. Assuming that PPG probes are placed on the skin or even implanted in the body, only little ambient temperature variance is expected given fairly accurate body temperature regulation. The lower figures show the temperature sweep for a conservative range of interest from 20°C to 50°C, for which a peak-wavelength variance of only 5 nm has been measured for the tested red LED.

Spectral shifts lead to altering of the effective absorption coefficients corresponding to the LEDs' emission spectrum, and thus to errors in the S_pO_2 reading [141]. Fig. 4.9 shows altered theoretical $\Re$ graphs and corresponding S_pO_2 value mismatch as a result of the above-mentioned wavelength shifts associated with thermal loss in a 47% duty-cycle operation mode (Fig. 4.9a,b) and over the ambient temperature range from 20°C to 50°C (Fig. 4.9c,d). Since LED forward

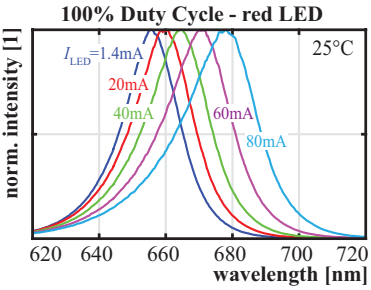
100% Duty Cycle - red LED
norm. intensity [1]
25°C
I_{LED}=1.4mA
20mA
40mA
60mA
80mA
620 640 660 680 700 720
wavelength [nm]

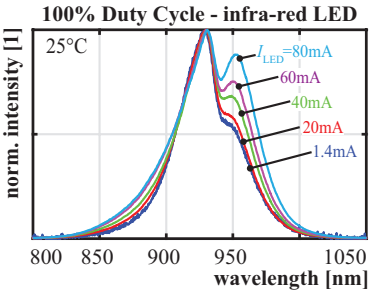
100% Duty Cycle - infra-red LED
norm. intensity [1]
25°C
I_{LED}=80mA
60mA
40mA
20mA
1.4mA
800 850 900 950 1050
wavelength [nm]

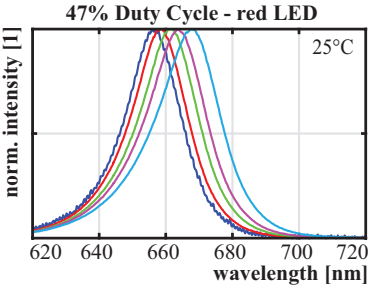
47% Duty Cycle - red LED
norm. intensity [1]
25°C
620 640 660 680 700 720
wavelength [nm]

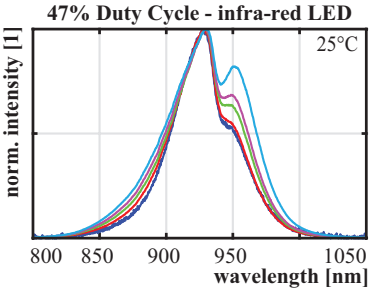
47% Duty Cycle - infra-red LED
norm. intensity [1]
25°C
800 850 900 950 1050
wavelength [nm]

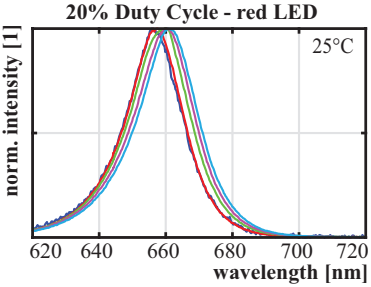
20% Duty Cycle - red LED
norm. intensity [1]
25°C
620 640 660 680 700 720
wavelength [nm]

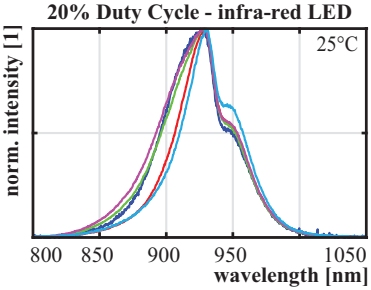
20% Duty Cycle - infra-red LED
norm. intensity [1]
25°C
800 850 900 950 1050
wavelength [nm]

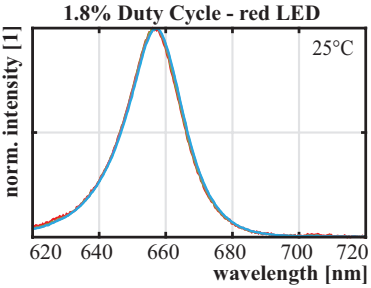
1.8% Duty Cycle - red LED
norm. intensity [1]
25°C
620 640 660 680 700 720
wavelength [nm]

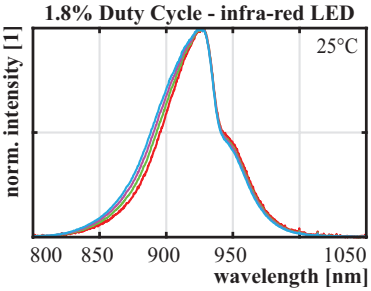
1.8% Duty Cycle - infra-red LED
norm. intensity [1]
25°C
800 850 900 950 1050
wavelength [nm]

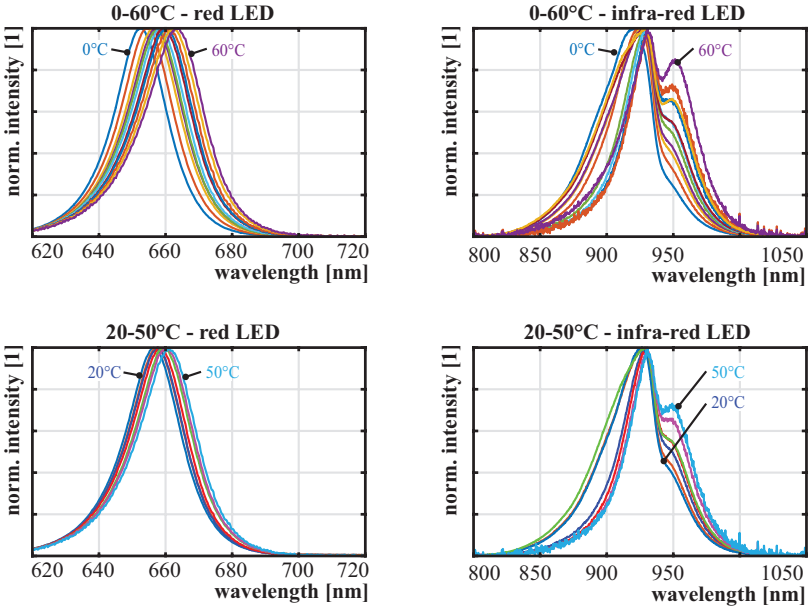

Figure 4.8: Spectra for [140] LEDs under varying ambient temperature and 1.8% duty-cycle.

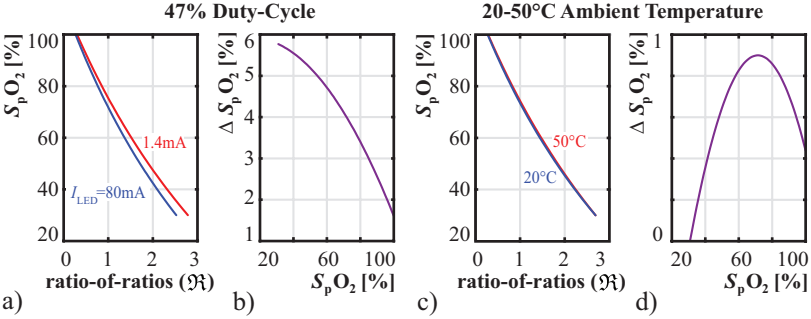

Figure 4.9: Effect of the wavelength shift on the ratio-of-ratios and resulting S_pO_2 discrepancy for (a,b) highest/lowest LED current in 47% duty-cycle operation and (c,d) for the ambient temperature range, respectively.

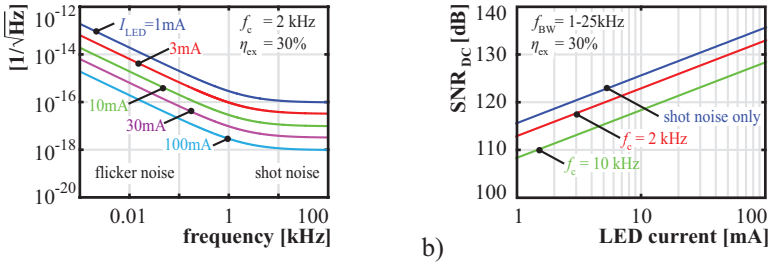

Figure 4.10: Spectral density normalised to emitted optical power (a) and signal-to-noise ratio of the emitted photon flux (b) for an LED.

current is usually regulated in a real-world application to deal with physiological differences, current level dependent wavelength shift can reduce the accuracy of computed S_pO_2 considerably. Ambient temperature on the other hand has only minor impact.

Noise

As for every pn-diode, the injected carriers show shot noise in LEDs. Photon generation is a second random process, independent of the shot noise source [126]: The probability that an injected electron recombines under generation of a photon is the internal quantum efficiency η_{iqe}. Not all generated photons are emitted, photon loss and absorption are further independent random processes described by the extraction efficiency η_{e}. The photon flux of a LED thus is expected to show shot noise with a signal-to-noise ratio [142]

$$SNR_{\mathrm{DC},\phi} = \frac{\phi_{\mathrm{DC}}}{\sqrt{\overline{\phi_{\mathrm{n}}^2}}} = \frac{1}{\sqrt{\eta_{\mathrm{iqe}}\eta_{\mathrm{e}}}} \frac{I_{\mathrm{DC}}}{\sqrt{\overline{i_{\mathrm{n},}^2}}} = \sqrt{\frac{I_{\mathrm{DC}}}{2\eta_{\mathrm{ex}} q f_{\mathrm{BW}}}}, \tag{4.12}$$

where $\eta_{\mathrm{ex}} = \eta_{\mathrm{iqe}}\eta_{\mathrm{e}}$ denotes the external efficiency of the LED.
LEDs also show low-frequency flicker noise. The corner frequency, below which flicker noise prevails shot noise, depends on the semiconductor material and the specific device. It is reported to be in the range of 300 Hz to 10 kHz for AlInGaP red and InGaN green LEDs [143]. Measurements presented in [144] show a constant corner

frequency over a wide range of LED forward current, suggesting a linear scaling of optical flicker noise power with electric current. The slope was found to be close to $1/f$. The above-mentioned work found that electrical and optical flicker noise do not correlate well – especially in case of the AlInGaP red LED.
Figure 4.10 displays expected power spectral density, normalised to DC power, and signal-to-noise ratio of an LED for the forward current range of interest in a typical pulse oximetry or NIRS application.

4.3.3 Tx - Rx Loop

In a generalised PPG circuit (Fig. 4.3) there are noise contributions from four distinguishable sub-circuits and components: transmitter (Tx), LED, photodiode, and receiver (Rx). The receiver ultimately limits the bandwidth for all noise sources – same bandwidth is in the following assumed for all contributions. A further – but less predictable – source of fluctuations is ambient light. It will be discussed later as a separate issue in Sec. 4.4.4.

Loop Dynamic Range

In terms of noise, overall PPG circuit performance is characterised by the loop dynamic range

$$DR_{\text{loop}} = \frac{I_{\text{in,FS}}^2}{\overline{i_{\text{n,tot,IR}}^2}}, \tag{4.13}$$

$$\frac{1}{DR_{\text{loop}}} = \left[\frac{1}{4SNR_{\text{DC,PD}}} + \frac{1}{\eta_{\text{q}}} \frac{1}{SNR_{\text{DC},\phi_{\text{LED}}}} + \frac{1}{DR_{\text{Rx}}} + \frac{1}{SNR_{\text{DC,Tx}}} \right]^{-1}$$

with $I_{\text{in,FS}}$ denoting the full-scale input current and $\overline{i_{\text{n,tot,IR}}^2}$ the total input-referred noise power (measured for a 50% full-scale input) for a certain circuit configuration and optical transmission. The factor four is given by the chosen dynamic range definition with noise measured for a DC input signal with amplitude corresponding to half the full-scale.
The input-referred noise is given according to Fig. 4.3 as

$$\overline{i_{\text{n,tot,IR}}^2} = \overline{i_{\text{n,PD}}^2} + \Psi^2 \eta_{\text{q}}^2 q^2 \overline{\phi_{\text{n,LED}}^2} + \overline{i_{\text{n,Rx}}^2} + \Psi^2 \eta_{\text{q}}^2 \eta_{\text{ex}}^2 \overline{i_{\text{n,Tx}}^2}. \tag{4.14}$$

As given by (4.7) and (4.12), shot noise of the optoelectronic components contribute to the input-referred noise with

$$\begin{aligned}\overline{i^2_{\mathrm{n,OE,IR}}} &= 2qI_{\mathrm{ph}}f_{\mathrm{BW}} + \Psi^2\eta_{\mathrm{q}}^2\eta_{\mathrm{ex}}I_{\mathrm{LED}}f_{\mathrm{BW}} \\ &= 2qI_{\mathrm{ph}}f_{\mathrm{BW}}(1+\Psi\eta_{\mathrm{q}}) \\ &\approx 2qI_{\mathrm{ph}}f_{\mathrm{BW}} = \overline{i^2_{\mathrm{n,PD}}}.\end{aligned} \tag{4.15}$$

For realistic transmissions ranging from 30ppm to 600ppm, it's apparent that photodiode noise clearly dominates over LED noise by a minimum of 30 dB. Thus, the intrinsic photodiode $SNR_{\mathrm{DC,PD}}$ shown in Fig. 4.6c reflects the upper limit of loop dynamic range any PPG circuit can achieve for a given input current and receiver bandwidth.

4.3.4 Power - DR Trade-off

In the following, the ultimate limitations on a PPG circuit in terms of loop dynamic range and power consumption are explored: An ideal PPG circuit with infinite receiver dynamic range DR_{Rx}, infinite transmitter signal-to-noise ratio $SNR_{\mathrm{DC,Tx}}$ and no power consumption is assumed. Loop dynamic range is thus equivalent to the intrinsic photodiode signal-to-noise ratio $4SNR_{\mathrm{DC,PD}}$ (4.8) while power consumption is solely due to the LED. The dynamic range to power ratio (DRPR) for a given signal bandwidth $f_{\mathrm{BW,SIG}}$ is thus

$$DRPR = \frac{4SNR^{f_{\mathrm{BW,SIG}}}_{\mathrm{DC,PD}}}{P_{\mathrm{LED}}} = \frac{4\frac{I_{\mathrm{ph}}}{2qf_{\mathrm{BW,Rx}}}}{I_{\mathrm{LED}}V_{\mathrm{LED}}\delta} \cdot \frac{f_{\mathrm{PR}}}{2f_{\mathrm{BW,SIG}}}. \tag{4.16}$$

The LED power P_{LED} is the product of the forward current I_{LED}, the supply voltage of the LED driver V_{LED}, and the duty-cyle δ.
The latter is itself the product of the pulse repetition frequency (PRF) and the LED on-time (pulse-width) $\delta = f_{\mathrm{PR}}T_{\mathrm{P}}$. Due to aliasing, the photodiode noise is spread over the Nyquist bandwidth which is half the PRF. When reorganising (4.16) it can be observed to be independent of the PRF:

$$DRPR = \frac{I_{\mathrm{ph}}}{qf_{\mathrm{BW,SIG}}I_{\mathrm{LED}}V_{\mathrm{LED}}} \cdot \frac{1}{T_{\mathrm{P}}f_{\mathrm{BW,Rx}}}. \tag{4.17}$$

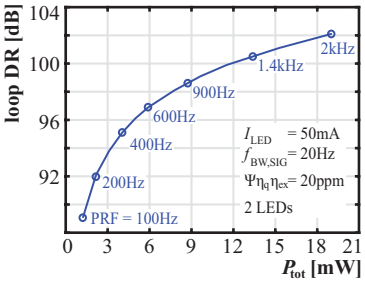

Figure 4.11: Measured loop dynamic range and power of the presented ASIC for different PRF configurations.

The photo-generated current is – in a given setup – directly proportional to the LED forward current, i.e., $I_{\mathrm{ph}} = \Psi\eta_{\mathrm{q}}\eta_{\mathrm{ex}}I_{\mathrm{LED}} = \Theta I_{\mathrm{LED}}$.

$$DRPR = \frac{\Theta}{q f_{\mathrm{BW,SIG}} V_{\mathrm{LED}}} \cdot \frac{1}{T_{\mathrm{P}} f_{\mathrm{BW,Rx}}}. \tag{4.18}$$

Assuming that the LED driver supply voltage V_{LED} is not adapted to the LED forward current, ideal DRPR is independent of the current with which the LED is driven.

The above analysis shows that power efficiency is in principal independent of PRF and LED current. Therefore, the two parameters can be traded against each other as best suited for the application and a real circuit's capabilities. It's worth to explicitly add that this insight should discourage to reduce power consumption by LED current reduction, as e.g., proposed in [145]. Not only is nothing gained in terms of efficiency by doing so, but rather is signal quality compromised: As a result of a lower LED light emission the relative share of ambient light incident to the photodiode increases.
In case of pulse oximetry, it was observed in Sec. 2.6.2 that requirements on loop dynamic range vary widely with both, perfusion index and oxygenation. Since the signal bandwidth of peripheral PPG signals is as low as 15 Hz, the PRF can be adapted in a wide range to satisfy dynamic range requirements at lowest possible power consumption, as demonstrated in Fig. 4.11.

4.4 Receiver Architecture

A photodiode receiver is fundamentally a transimpedance amplifier (current-to-voltage converter) followed by an ADC. There are two distinct ways to convert a DC current into a voltage: either the current is made to flow through a resistance or a capacitance is charged by it for a limited time. Both principles are commonly used to realise a transimpedance amplifier (TIA).
In case of the capacitive feedback TIA (CTIA) topology, the transimpedance R_{TI} is defined by the integration time. This allows to cover a wide transimpedance range with fine resolution without the need of configurable analogue circuitry. However, it is impractical for realising low transimpedance values $R_{\mathrm{TI}} < 1\,\mathrm{M\Omega}$ which would either require large capacitors (and thus silicon area) or a low integration time which is equivalent to a high receiver bandwidth and thus high (photodiode) noise. The contrary applies to the resistive feedback TIA (RTIA) topology, which is well suited for low R_{TI} but large feedback resistors would occupy considerable area.
The implemented receiver incorporates both topologies (Fig. 4.12) in a single circuit. Different clocking by the FSM decides on the operation mode. The two topologies are discussed in detail in the subsequent sections.

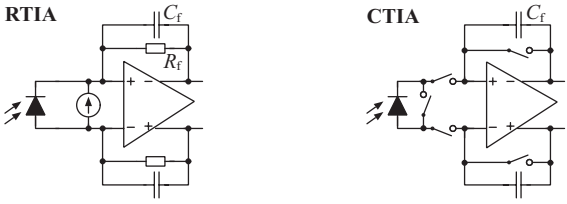

Figure 4.12: Two principal TIA topologies: resistive feedback (a) and capacitive feedback (b). The receiver circuit of *TMA-O* can realise both topologies to cover a wide range of transimpedance.

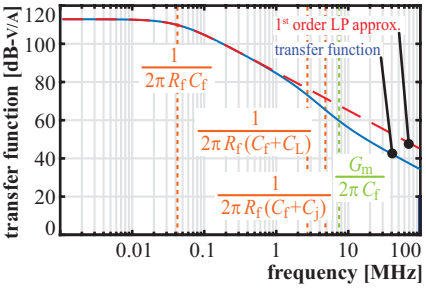

Figure 4.13: Transfer function of a RTIA.

4.4.1 Resistive Feedback TIA

Transfer Function

Assuming the RTIA circuit shown in Fig. A.1 with an ideal operational transconductance amplifier (OTA) as amplifier and the photodiode modelled as the parallel connection of an ideal current source and the photodiode's junction capacitance C_j, the transfer function is found to be

$$\frac{V_\mathrm{o}(s)}{I_\mathrm{ph}(s)} \approx \frac{R_\mathrm{f}\left(1 - s\frac{C_\mathrm{f}}{G_\mathrm{m}}\right)}{(1 + sR_\mathrm{f}C_\mathrm{f})\left(1 - s\frac{C_\mathrm{f}}{G_\mathrm{m}}\right) + \frac{1}{G_\mathrm{m}R_\mathrm{f}}[1 + s(C_\mathrm{f} + C_\mathrm{j})][1 + s(C_\mathrm{f} + C_\mathrm{L})]},$$

for $R_\mathrm{o} \gg R_\mathrm{f}$ and $G_\mathrm{m} \gg 1/R_\mathrm{f}$.
For noise analysis, the first-order approximation is sufficient:

$$\frac{V_\mathrm{o}(s)}{I_\mathrm{ph}(s)} \approx \frac{R_\mathrm{f}}{1 + sR_\mathrm{f}C_\mathrm{f}}. \tag{4.19}$$

An example of the transfer function magnitude characteristic with realistic values is given in Fig. 4.13 for $R_\mathrm{f} = 450\,\mathrm{k\Omega}$ and $C_\mathrm{f} = 8.4\,\mathrm{pF}$.

Figure-of-Merit

Recall the relation between dynamic range and LED power consumption given in (4.18). The low-pass characteristic of the RTIA links

receiver bandwidth and LED on-time by requirements on the settling – expressed with the *settling number* ξ:

$$f_{\mathrm{BW,Rx}} \geq \frac{\pi}{2}\frac{\xi}{2\pi T_{\mathrm{P}}} \qquad \xi = \frac{T_{\mathrm{P}}}{\tau} = \frac{T_{\mathrm{P}}}{R_{\mathrm{f}}C_{\mathrm{f}}}, \tag{4.20}$$

with τ the time constant of the first-order low-pass filter of bandwidth $f_{\mathrm{BW,Rx}}$. For a minimum bandwidth, (4.18) results in:

$$DRPR = \frac{4\Theta}{q f_{\mathrm{BW,SIG}} V_{\mathrm{LED}} \xi}. \tag{4.21}$$

The independence of the ideal DR-to-power ratio (4.21) from PRF, LED forward current, and receiver bandwidth for a given setup makes it a good figure-of-merit to compare the performance of various PPG circuit architectures and designs. The figure-of-merit (FoM) defined in Sec. 4.2.1 is further normalised to the current transmission factor Θ, bandwidth $f_{\mathrm{BW,SIG}}$, and units:

$$FoM = \frac{DRPR \cdot f_{\mathrm{BW,SIG}}}{2\Theta} \cdot \frac{1\,\mathrm{mW} \cdot 10\,\mathrm{ppm}}{1\,\mathrm{Hz}}. \tag{4.22}$$

The factor 1/2 results from the pulse oximetry orientation of the FoM definition, taking the power of two LEDs into account instead of just one as in the DRPR definition. Plugging (4.21) in above equation results in

$$FoM_{\mathrm{ideal}} = \frac{2}{q V_{\mathrm{LED}} \xi} \cdot \frac{1\,\mathrm{mW} \cdot 10\,\mathrm{ppm}}{1\,\mathrm{Hz}} \tag{4.23}$$

which is the maximum FoM a circuit can achieve for a given choice of ξ and V_{LED}.

Incomplete Settling

As apparent from (4.23) a low settling number ξ is favorable. For low ξ, the signal will not fully settle prior to sampling. This comes with a gain loss $e^{-\xi}$, which however has no impact on the ideal FoM (4.23): for infinite receiver dynamic range, the signal can be resolved equally well. In a real implementation however the gain loss corresponds to a proportional increase of the receiver noise and thus dynamic range will considerably drop for $\xi < 2$.

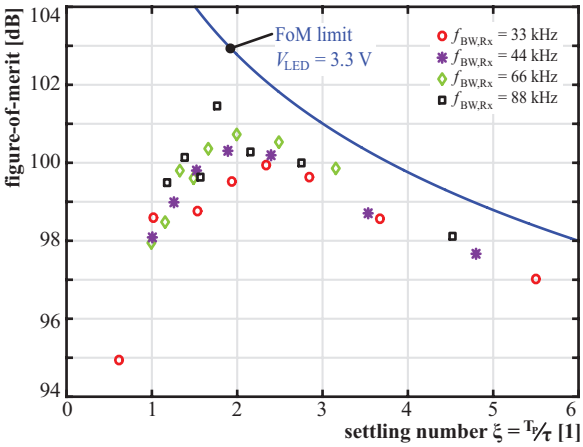

Figure 4.14: Incomplete settling allows for higher energy efficiency. The solid blue trace shows the theoretical FoM limit. Measurements of the presented *TMA-O* ASIC are given for different configurations.

Figure 4.14 depicts this limit for a 3.3 V LED driver supply. We observe that the considerable gain loss for $\xi < 3$ is outweighed by the power savings due to lower LED duty-cycle. Measured FoM for various circuit configurations is maximal around $\xi = 2$, values drop for lower settling numbers due to power overhead, limited receiver dynamic range, and clock jitter.

Input Offset

As derived in App. A.2.1, a constant RTIA input current i_{ph} leads to an OTA input voltage

$$v_{\mathrm{i}} \approx -\frac{i_{\mathrm{ph}}}{G_{\mathrm{m}}}. \tag{4.24}$$

For a G_{m} in the hundreds of µS and currents in the lower µA, this results in a slight reverse bias of ten to lower hundreds of mV. As discussed in Sec. 4.3.1, photodiode shot noise is minimum at zero bias and is increased under reverse bias due to dark current. However, as illustrated in Fig. 4.6d, the effect of dark current is in the sub-1dB

range for photo-generated currents above 1 µA – for lower currents, the input offset is too low to cause considerable dark current.
The junction capacitance however is a non-linear function of the reverse voltage, as illustrated in Fig. 4.5c and given in [125] as

$$C_\mathrm{j} = \sqrt{\frac{\varepsilon_\mathrm{si}\varepsilon_0 \mathsf{A}}{2(V_\mathrm{R} + V_\mathrm{bi})}} + C_\mathrm{p}, \tag{4.25}$$

with $V_\mathrm{bi} \approx 0.7$ V the built-in potential and an additional, voltage-independent parasitic capacitance C_p.
A part of the photo-generated current is initially absorbed to charge the junction capacitance. This 'lost charge' is equivalent to a shortening of the pulse duration T_p by a junction capacitance charging time

$$T_\mathrm{ch,j}(v_\mathrm{i}) = \frac{Q_\mathrm{j}(v_\mathrm{i})}{i_\mathrm{ph}} = \frac{-v_\mathrm{i} C_\mathrm{j}(v_\mathrm{i})}{i_\mathrm{ph}} = \frac{C_\mathrm{j}(v_\mathrm{i})}{G_\mathrm{m}}. \tag{4.26}$$

When denoting the step response of the lossy integrator as

$$\alpha(T) = 1 - e^{-\frac{T}{\tau}}, \tag{4.27}$$

the signal-to-distortion ratio (SDR) is given by:

$$SDR = \frac{\alpha(T_\mathrm{p} - T_\mathrm{chj}(0))}{\alpha(T_\mathrm{p} - T_\mathrm{chj}(v_\mathrm{i})) - \alpha(T_\mathrm{p} - T_\mathrm{chj}(0))}. \tag{4.28}$$

Figure 4.15 illustrates the effect for realistic conditions:
A graph of the junction capacitance equation (4.25) mapped on the data provided for the *Everlight* PD15 diode [123] is provided in (a). The non-linear capacitance-to-voltage relation causes non-linear distortion, illustrated for various settling numbers ξ in (b) and for constant ξ but different transimpedance settings in (c). The estimated input offset v_i for full-scale input current is marked in both plots. It can be observed that for the standard settings shown in (b), no significant linearity degradation is observed. For lower transimpedance settings however, which come with low LED on-times for the same ξ, the impact on linearity increases as illustrated in (c).
For long settling times, the effect of the initially lost charge on the final output voltage of the lossy integrator vanishes.

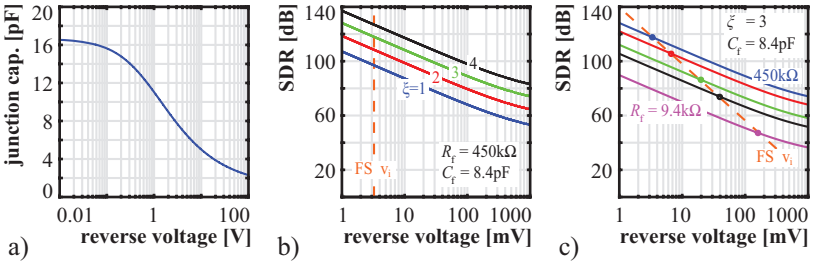

Figure 4.15: The photodiode junction capacitance (a) is a non-linear function of the applied reverse voltage. Signal dependent input offset v_i thus causes non-linear distortion (b-c). $G_\mathrm{m} = 400\,\mu\mathrm{S}$ is assumed.

4.4.2 Capacitive Feedback TIA

Transfer Function

As derived in detail in App. A.4, the gain characteristics of the CTIA transfer function is approximatly

$$\left|\frac{V_\mathrm{o}(f)}{I_\mathrm{ph}(f)}\right| \approx \left|\frac{T_\mathrm{int}}{C_\mathrm{f}} \cdot \mathrm{sinc}(f \cdot T_\mathrm{int}) \cdot \frac{1}{1 + jf\frac{C_\mathrm{f}+C_\mathrm{j}}{GBP \cdot C_\mathrm{f}}}\right|. \tag{4.29}$$

An example with realistic values is given in Fig. 4.16 for $T_\mathrm{int} = 10\,\mu\mathrm{s}$. The sinc-function dominates bandwidth limitation while the amplifier's gain-bandwidth product (GBP) leads to further damping at high frequencies. For noise considerations, a first-order low-pass characteristic with corner frequency

$$f_\mathrm{c} \approx \frac{0.443}{T_\mathrm{int}} \tag{4.30}$$

is a convenient and conservative approximation for $\mathrm{sinc}(f \cdot T_\mathrm{int})$.

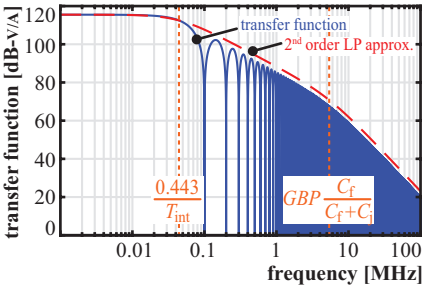

Figure 4.16: Transfer function (solid blue graph) of a CTIA with integration period T_{int} and corresponding 2^{nd} order low-pass approximation (dashed red line) used in noise-bandwidth considerations.

Figure-of-Merit

Similar as for the RTIA, the low-pass characteristic of the sampled integrator links the LED on-time to the receiver bandwidth. The latter is according to (4.30)

$$f_{\mathrm{BW}}[Rx] \approx \frac{\pi}{2}\frac{0.443}{T_{\mathrm{int}}} \approx \frac{0.696}{T_{\mathrm{p}}} \qquad T_{\mathrm{int}} = T_{\mathrm{p}}. \tag{4.31}$$

In difference to the RTIA, there is a fixed ratio of bandwidth to LED on-time – equivalent to a settling number $\xi = 2.78$. The maximum achievable FoM (4.23) is for a CTIA based PPG thus limited to

$$FoM_{\mathrm{ideal}} = \frac{0.714}{qV_{\mathrm{LED}}} \cdot \frac{1\,\mathrm{mW} \cdot 10\,\mathrm{ppm}}{1\,\mathrm{Hz}}. \tag{4.32}$$

For $V_{\mathrm{LED}} = 3.3\,\mathrm{V}$ the maximum FoM thus is 101.3 dB.

Input Offset

Similar as for the RTIA, a constant input current leads to an OTA input offset voltage as derived in App. A.3.1 of

$$v_{\mathrm{i}} = -i_{\mathrm{ph}}\frac{C_{\mathrm{f}} + C_{\mathrm{L}}}{G_{\mathrm{m}}C_{\mathrm{f}}}. \tag{4.33}$$

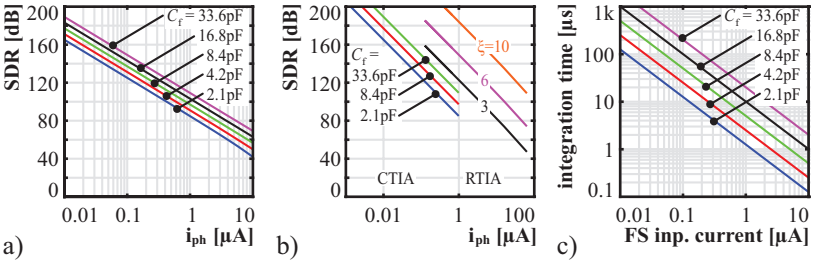

Figure 4.17: Input offset induced non-linear distortion for CTIAs of various C_f (a) and in comparison with RTIA (b). Integration time in dependence of input current and C_f (c). $G_\mathrm{m} = 400\,\mu\mathrm{S}$ is assumed.

Again, the photodiode junction capacitance C_j is charged to the input voltage v_i by absorbing some of the photo-generated charge:

$$Q_\mathrm{j}(v_\mathrm{i}) = v_\mathrm{i} C_\mathrm{j}(v_\mathrm{i}) = -\frac{i_\mathrm{ph} C_\mathrm{j}(v_\mathrm{i})}{G_\mathrm{m}} \frac{C_\mathrm{f} + C_\mathrm{L}}{C_\mathrm{f}}. \tag{4.34}$$

The charge integrated over T_p on the feedback capacitor is thus:

$$Q_\mathrm{int} = -i_\mathrm{ph} T_\mathrm{p} - Q_\mathrm{j}(v_\mathrm{i}) = -i_\mathrm{ph} \left(T_\mathrm{p} - \frac{C_\mathrm{j}(v_\mathrm{i})}{G_\mathrm{m}} \frac{C_\mathrm{f} + C_\mathrm{L}}{C_\mathrm{f}} \right). \tag{4.35}$$

The non-linear dependence of the junction capacitance on diode reverse bias voltage thus leads to distortion. The signal-to-distortion ratio is given as

$$SDR = \frac{i_\mathrm{ph} T_\mathrm{p} - Q_\mathrm{j}(0)}{Q_\mathrm{j}(0) - Q_\mathrm{j}(v_\mathrm{i})} = \frac{G_\mathrm{m} T_\mathrm{p} \frac{C_\mathrm{f}}{C_\mathrm{f}+C_\mathrm{L}} - C_\mathrm{j}(0)}{C_\mathrm{j}(0) - C_\mathrm{j}(v_\mathrm{i})}. \tag{4.36}$$

In Fig. 4.17a SDR is plotted versus photo-generated current for various C_f. The higher the latter, the lower the distortion – however, reasonable linearity for input currents above ca. 1 µA demands for excessively large feedback capacitors or OTA G_m. Large C_f is further required to keep integration time reasonably high to avoid any impact of clock-jitter on the DR and to maintain high FoM: shorter integration time increases overhead power consumption – due to the inverse proportionality of integration time T_int and receiver bandwidth,

shorter T_{int} requires higher PRF to maintain constant loop dynamic range.
The CTIA topology is well suited for photo-generated input currents below ca. 1 µA, while the RTIA topology is suited only for currents above ca. 100 nA. To cover a large input current range, the *TMA-O* ASIC supports both topologies. As observed in Fig. 4.17b, reasonably high linearity is maintained for the RTIA up to ca. 10 µA for $\xi = 3$.

4.4.3 Amplifier Topology

In the above analysis of the input voltage offset for both TIA topologies, it was assumed that a single-stage OTA is used as amplifier. This reflects the receiver circuit implementation of *TMA-O*. The pros and cons of this choice in comparison to the alternative use of a two-stage Miller amplifier is briefly discussed in the following.
The use of a two-stage amplifier instead of the single-stage OTA is advantageous in RTIA configurations with low R_{f} values to maintain reasonable loop gain and thus closed-loop linearity by keeping the differential amplifier input voltage low. The latter is given for an RTIA circuit by

$$v_{\mathrm{in}} = \frac{v_{\mathrm{out}}}{A} = -\frac{i_{\mathrm{ph}} R_{\mathrm{f}}}{A}, \tag{4.37}$$

with A denoting the loop gain. For mathematical derivations of the input voltage offset encountered in RTIA implementations with amplifiers of both topologies, the kind reader may refer to App. A.2.
The CTIA topology on the other hand does not profit from a two-stage amplifier. As derived in App. A.3.2, the input offset voltage is

$$v_{\mathrm{i}} = -i_{\mathrm{ph}} \frac{C_{\mathrm{M}}}{G_{\mathrm{m1}} C_{\mathrm{f}}}, \tag{4.38}$$

which is of equal order of magnitude as when a single-stage OTA is employed.
Using a single-stage amplifier however eases reconfigurability of the feedback passive components with respect to stability – necessary to support a wide transimpedance range. Both, dominant- and second pole of a Miller amplifier depend on the applied load. It is thus usually required to adapt the compensation on the load in order to maintain

phase margin. In contrast, a single-stage OTA needs no adaptation on the load as long as a minimum capacitive load is ensured.

The pole splitting in the Miller amplifier comes with a lower GBP which is of no concern when considering the low bandwidth requirements of a TIA for PPG. It is indeed beneficial since it comes with lower amplifier noise bandwidth. The amplifier excess noise curbing technique described in Sec. 4.5.4 presents an alternative which ensures minimum noise bandwidth independent of a higher OTA GBP.

TMA-O has originally been designed for a maximum input current of 4 µA – corresponding to a minimum feedback resistance of 150 kΩ. For such input currents, a single-stage OTA design is sufficient: input offset voltage remains below 10 mV and high linearity could be verified in measurements showing a SFDR above 80 dB for all transimpedance settings with $R_f > 150\,k\Omega$. Considering a highly configurable feedback, the intrinsically stable single-stage design was thus favoured to the two-stage amplifier with its delicate compensation.

Later, the feedback resistor range has been extended to ease the use of the chip in implants with probes directly attached to small arteries (see Sec. 6.4). Here light absorption is much lower than in typical non-invasive pulse oximetry or NIRS applications and thus photogenerated currents above 4 µA may be obtained even for sub-mA LED pulse currents. As illustrated in Fig. 4.18, considerable linearity degradation is observed for this extended R_f range below 100 kΩ. Here, a two-stage amplifier design would be favourable. Nonetheless, measured linearity is still sufficient for accurate pulse oximetry measurements – a minimum SFDR of ca. 30 dB was derived in Sec. 2.6.1.

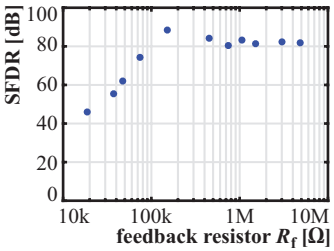

Figure 4.18: Measured RTIA linearity shows significant degradation for feedback resistance values below 100 kΩ.

4.4.4 Ambient Light Cancellation

Ambient light is a major concern in pulse oximetry since the signal band includes a DC component. Although effort is made to ensure optical shielding by the mechanical design of the sensor probe, the residual ambient light incident to the photodiode can be large enough to distort $S_\mathrm{p}O_2$ readings.

Correlated Double Sampling

A common approach to cope with ambient light is correlated double sampling (CDS) [40]: First the signal is sampled while one of the LEDs is turned on, later a second sample is taken while all LEDs are turned off. This *dark sample* is then subtracted from the *signal sample*, cancelling DC ambient light.
When assuming the two sampling points to be separated by T_ALC, as illustrated in Fig. 4.19a, we can model CDS based ALC as a time-discrete system Fig. 4.19b:

$$y[n] = x[n-1] - x[n], \tag{4.39}$$

with z-transform

$$Y(z) = X(z) \cdot [z^{-1} - 1]. \tag{4.40}$$

The equivalent continuous-time filter characteristics are thus

$$H_\mathrm{ALC}(f) = \frac{Y(f)}{X(f)} = e^{-j2\pi f T_\mathrm{ALC}} - 1. \tag{4.41}$$

The frequency characteristics are illustrated in Fig. 4.20a for various sampling time differences T_ALC.
While sunlight interference can be assumed to be close to DC, indoor ambient light comprises often frequency modulated parts. Spectra of the resulting intensity modulation, measured by means of a photodiode illuminated with different common types of lamps, are given in [146] and summarised in Fig. 4.20b combined with findings of own measurements. Most lamps are modulated with double the mains frequency. High-frequency fluorescence lamps (FLs) and some LED 'bulbs' show further frequency modulation at $25 - 50\,\mathrm{kHz}$. Since the PPG receiver bandwidth is one or two orders of magnitude higher than the sampling frequency (PRF), aliasing might fold these components into the signal band.

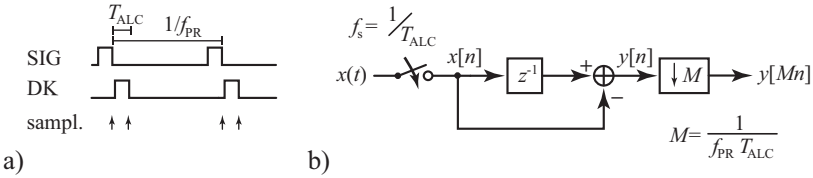

Figure 4.19: Timing diagram of ambient light cancellation by CDS(a) and diagram of the discrete-time processing of ambient light (b).

Interference Scrambling

Recently, the use of a cross-coupled sigma delta modulator was proposed in [25] to generate chaotically timed sampling sequences and thus avoiding sampling in step with any interferer. The concept comprises two steps:

1. Instead of periodic sampling, the time period between two samples is determined by a random process with uniform distribution and configurable average PRF. For low LED duty-cycles – preferable considering power consumption – the range of possible inter-samples times is wide. Granularity is favored to be low – 1 µs is assumed for the simulations presented in Fig. 4.21 and 4.22.

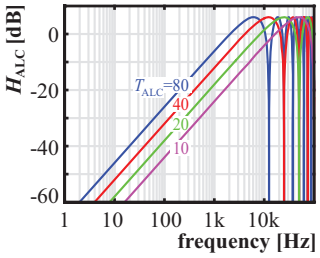

Light Source	Modulation Frequencies
Sunlight	DC
Tungsten	100 Hz - no harmonics
low-freq. FL	100 Hz + harmonics
high-freq. FL	100 Hz + harmonics & ~30 kHz + harmonics
LED 'bulb'	DC or ~45 kHz + harmonics

b)

Figure 4.20: CDS ambient light cancellation frequency characteristics (a) and modulation frequencies [146] of most common sources of ambient light (b).

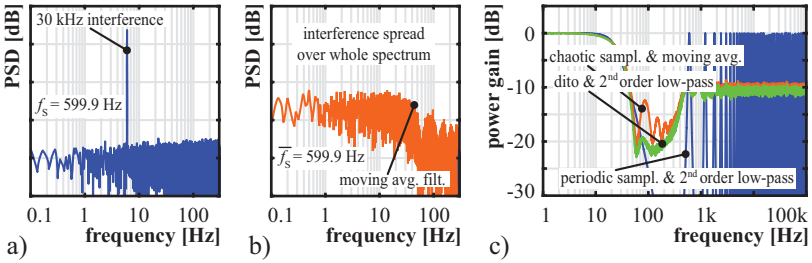

Figure 4.21: Chaotic sampling whitens (b) the interferer (a) and spreads its power over the whole spectrum. Interference power is then reduced by a moving-average low-pass filter (c).

2. Periodic averaging: the average of all samples $x(t)$ taken in $nT_s - T_w < t \leq nT_s$ is computed. It represents the estimation $\tilde{x}[n] \approx x(nT_s)$ of a periodically sampled $x(t)$. The averaging window T_w can be chosen differently from T_s: T_w defines the low-pass characteristic of the moving average, while T_s defines the sampling rate of $\tilde{x}$.

The effect is illustrated with numeric simulation results in Fig. 4.21: (a) shows the spectrum of a 30 kHz interferer which is periodically subsampled at a rate of 599.9 Hz. Aliasing leads to an in-band interference at ca. 5 Hz. Chaotic sampling results in whitening for out-of-band interferers as illustrated in (b) with the output spectrum for the very same 30 kHz interferer subsampled non-uniformly with equal mean sampling rate. The whitened interferer is indistinguishable from an increased noise floor. In (c) the power attenuation is plotted versus frequency for chaotig sampling followed by moving average resampling (red) in comparison to conventional periodic sampling followed by digital low-pass filtering (blue). The green graph represents a version of the former which is followed by a steep digital low-pass filter. Note that the depicted power gain corresponds to the magnitude transfer function for in-band signal components – for out-of-band components however, it is a measure for the white noise power added by scrambling a sinusoidal interferer of a certain frequency. White Gaussian noise

power is not affected by scrambling.

The power attenuation for high-frequency interferers is determined by the window length of the moving average filter and thus proportional to the PRF. The power gain is given by:

$$PG = 10 \cdot \log_{10}\left(\frac{1}{N_{\mathrm{AVG}}}\right) \approx 10 \cdot \log_{10}\left(\frac{2.5 f_{\mathrm{BW,SIG}}}{f_{\mathrm{PR}}}\right), \qquad (4.42)$$

with N_{AVG} the mean number of averaged samples.
The chaotic subsampling scheme [25] effectively improves resilience against out-of-band interferers. However, it does not against in-band interferers – most prominently sunlight. Figure 4.22 depicts the power gain spectra for two approaches to include DC interference removal:

a) A DC estimation of the dark signal is obtained by taking dark samples in-between the signal samples and averaging them over a considerable longer window. Thus this DC signal does not correlate with the signal and subtraction from the signal does neither increase input-referred noise considerably nor does it affect high-frequency interference scrambling and attenuation. However, there is no in-band interference suppression, except for DC.

b) The combination of CDS and chaotic sampling allows for high attenuation of in-band interferences while high-frequency interferers are scrambled. Constant time difference T_{ALC} between signal and dark sampling points results in best low-frequency suppression. However, when also randomising T_{ALC}, better power attenuation for out-of-band frequencies can be achieved.

Considering that the illuminance by sunlight can be orders of magnitude higher than what is encountered in an artificially illuminated indoor environment, the second approach (b) is favourable: Motion causes variations in the illumination of the photodiode by ambient light, i.e., amplitude modulation of the interference signal. Thus there can be non-DC in-band ambient light interference caused by sunlight.

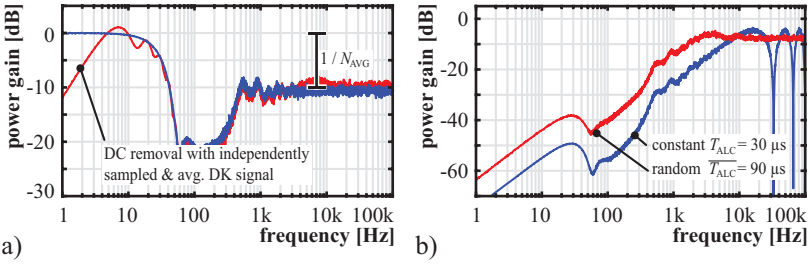

Figure 4.22: In-band interference cancellation by independent DC-DK estimation (a) and CDS (b).

Interference Avoidance

Interference scrambling effectively suppresses tones – but since the signal power of the interferer gets spread all over the Nyquist band, the loop dynamic range is reduced. In order to minimise the effect of non-uniformly distributed sampling instances on the signal itself, the local (in time) mean is re-sampled uniformly – this however requires a certain minimum mean oversampling factor to be effective, and thus limits the method to mean PRFs significantly higher than twice the signal bandwidth.

The targeted interferes are in the tens of kHz which means a high folding number

$$\kappa = \left\lfloor \frac{f_{\mathrm{IF}}}{f_{\mathrm{s}}} \right\rceil , \tag{4.43}$$

with f_{IF} the interference frequency and f_{s} the sampling frequency. Aliasing results in an image of the interferer within the Nyquist band with frequency

$$f_{\mathrm{IM}} = |f_{\mathrm{IF}} - \kappa f_{\mathrm{s}}|. \tag{4.44}$$

A high folding number, e.g., fifty for $f_{\mathrm{s}} = 600$ Hz and $f_{\mathrm{IF}} = 30\,\mathrm{kHz}$, means that the image frequency can be shifted significantly with a change in sampling frequency (PRF) of only a few Hertz. Thus in combination with a (sharp) digital low-pass filter, high-frequency interference can be avoided by analysing a (separate) dark samples

channel and adjusting the PRF when necessary such that the image frequency lies above the cut-off frequency.

This interference avoidance scheme requires low PRF configuration granularity and a microcontroller unit (MCU) for controlling and dark samples analysis.

4.5 Receiver Implementation

An overview schematic of the receiver implemented for *TMA-O* is depicted in Fig. 4.23 and its micrograph is given in Fig. 4.25. Nominal values of the circuit elements shown in the schematic are given in Tbl. 4.3.
The analogue circuits of both, receiver and transmitter, are controlled by a common FSM which can use the receiver hardware either in RTIA or CTIA configuration. For both of these main operation modes there are a multitude of variations to choose from. A true mixed-signal design approach enables this high degree of flexibility. All analogue circuitry is directly clocked by the central digital circuit to which the front-end circuitry is connected by 89 clock- or configuration lines – the successive approximation register (SAR) ADC [106, 147] comes with an extra of 353 lines.

A fully differential topology is chosen for its improved robustness against common-mode interference, but comes with the cost of an increased pin count. All receiver circuitry is powered by a 1.2 V supply.

4.5.1 Circuit Description

The receiver circuit (Fig. 4.23) is based on a single OTA to implement both, the transimpedance stage and a switched capacitor summation for analogue ambient light cancellation. The states succession diagrams in Fig. 4.24 illustrate the use of the circuit in both RTIA and CTIA modes with analogue ambient light cancellation active. The FSM also supports digital cancellation for both TIA topologies, where the subtraction is performed digitally after the digitisation of separate

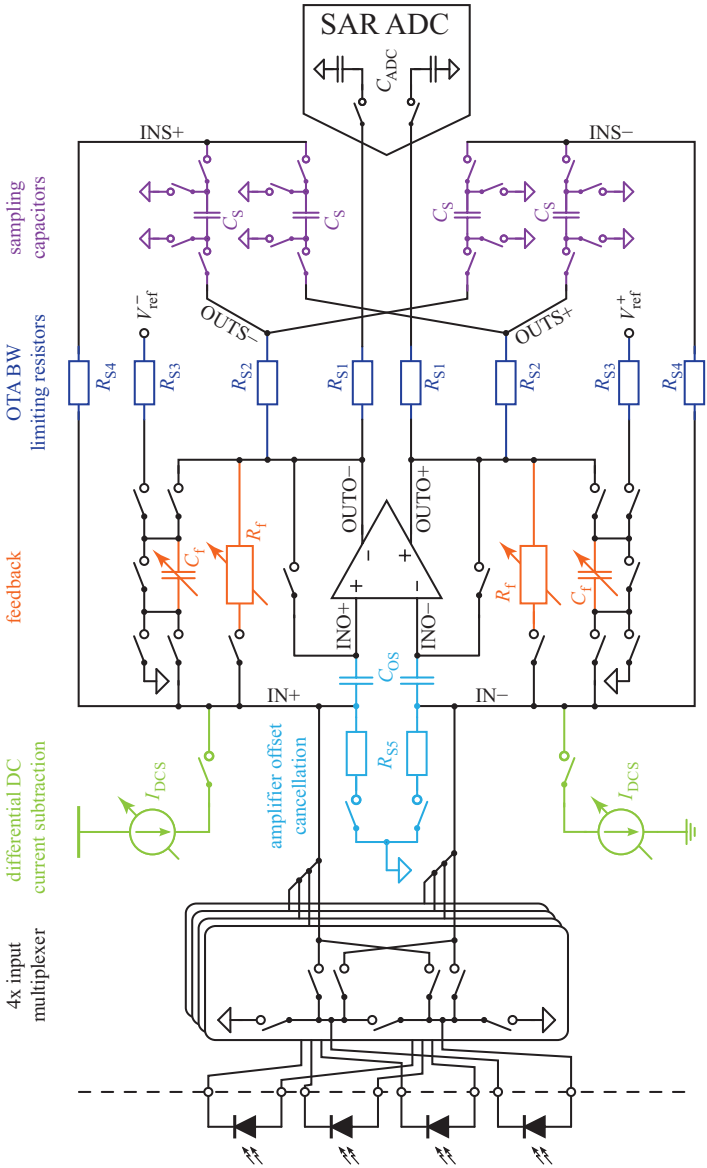

Figure 4.23: Schematic of *TMA-O's* receiver.

Table 4.3: Nominal Values of Receiver Circuit Elements

	Value (Range)		Granularity		
R_f	9.4 - 4800	kΩ	9.4/150	kΩ	9 bit
C_f	2.1 - 33.6	pF	2.1	pF	5 bit
I_DCS	0.02 - 10	μA	21/31/42/52	nA	8 bit
C_S	14.7	pF			
C_OS	25.2	pF			
C_ADC	14.9	pF			
R_S1	0 - 68	kΩ	17	kΩ	2 bit
R_S2	0 - 1.3	MΩ	167	kΩ	3 bit
R_S3	0 - 1.3	MΩ	167	kΩ	3 bit
R_S4	0 - 68	kΩ	17	kΩ	2 bit
R_S5	0 - 68	kΩ	17	kΩ	2 bit

signal and dark samples. Some circuit aspects are discussed in more detail later. Here follows a short walk-through to give the kind reader an overview on the function of sub-circuits and components:

Input Multiplexer. The input pins are shorted and tied to the common-mode voltage whenever they are not connected to the TIA. Mismatch of the photodiode operation points when connected to and disconnected from the TIA is thus minimised and a proper reset of the charge stored on the photodiode junction capacitance is ensured. The latter is mandatory in CTIA and incompletely settled RTIA operation. Finally, the multiplexer allows to connect any of the four input pin pairs to the TIA – connection direction can be chosen, which enables analogue ambient light cancellation in CTIA mode.

OTA Offset Cancellation. The OTA offset voltage is cancelled by means of CDS to minimise the input offset and thus operate the photodiode at zero bias. Furthermore, it reduces OTA flicker noise.

Differential Current Subtraction. To make better use of the available signal swing for the strictly positive input signal (the photogenerated current), a DC current corresponding to half the input swing is subtracted from the input current in RTIA mode (Fig. 4.26). By subtracting a larger current, the dynamic range can be enhanced as reasoned in Sec. 4.5.3. Being directly subtracted from the input current, requires it to be low noise.
In CTIA mode, the integrator feedback capacitances are precharged instead of a DC current being subtracted. However differential current subtraction (DCS) is still available for dynamic range enhancement.

Operational Transconductance Amplifier. A single-stage folded-cascode OTA with 80 dB DC-gain is used. The high gain guarantees good linearity and low requirements on driving strength allow the use of a single-stage topology.

Feedback Resistors and Capacitors. Both, C_f and R_f are configurable over a wide range and allow thus to select transimpedance and receiver bandwidth according to the needs of the application. The RTIA analogue ambient light cancellation scheme reuses some of C_f in the summation phase as feedback capacitor of the integrator.

Bandwidth Limiting Resistors. The bandwidth of the TIA transfer function (input current to output voltage) was found to be limited by R_f and C_f in RTIA mode and the integration time in CTIA configuration. Other noise sources however experience a different transfer function. The resistors R_S1-R_S5 limit the bandwidth of the OTA noise sources and thus curb their contribution to the overall noise power, as explored in more detail in Sec. 4.5.4.

Sampling Capacitors. For RTIA analogue ambient light cancellation, both, signal and dark samples, are first stored on the C_S capacitors. Then, the OTA is reused as integrator and the charges stored on C_S are transferred to the feedback capacitor resulting in summation of the charges.

Analogue-to-Digital Converter. A 13.5 ENOB SAR ADC with on-chip digital start-up calibration [106, 147] is finally used for digitisation. Different techniques are employed to battle thermal- and quantisation noise.

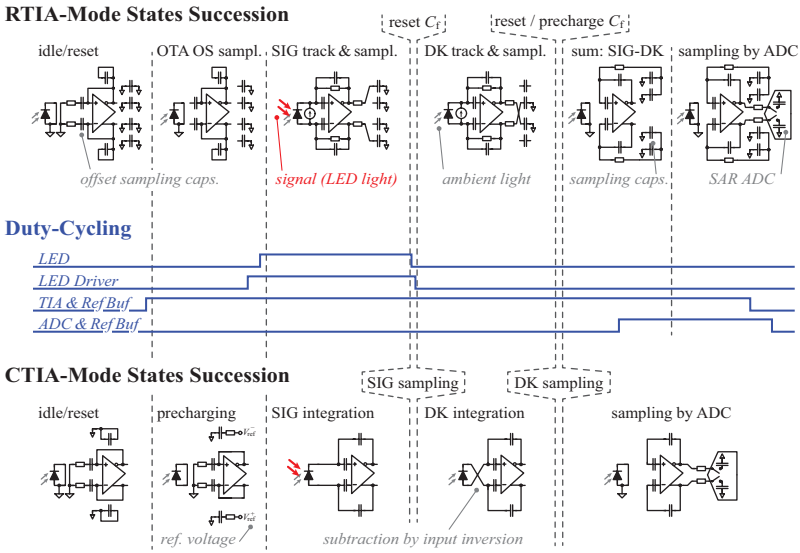

Figure 4.24: Simplified states succession in RTIA and CTIA modes with analogue ambient light cancellation active. Duty-cycling of sub-circuits and the LED is given conceptually.

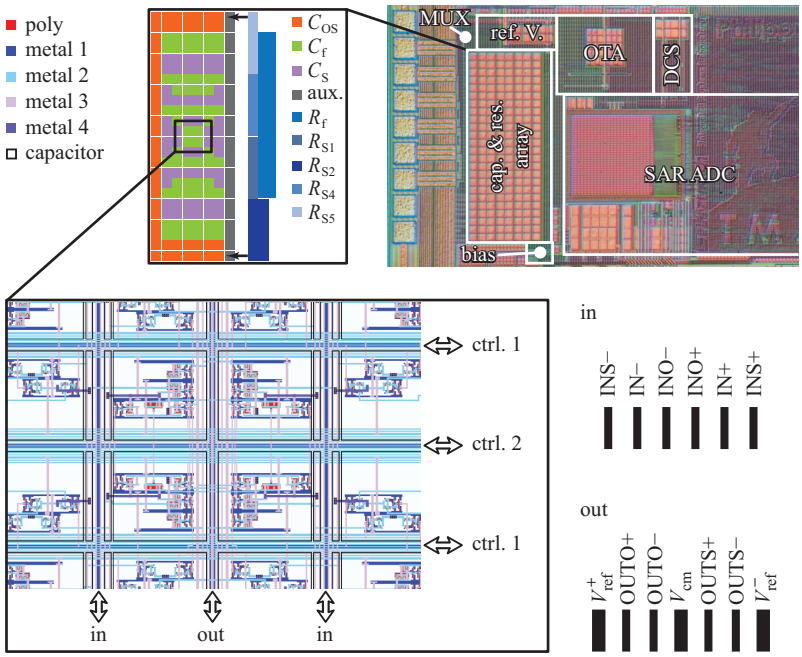

Figure 4.25: Micrograph of the receiver circuit and layout details of the capacitor- and resistor arrays. The routing arrangement of the analogue signals keeps nets which are sensitive to parasitic cross-coupling distant from each other and is illustrated in the lower right corner.

4.5.2 Capacitor Array

The C_{OS}, C_f, and C_S capacitors – as well as some 'auxiliary' capacitors introduced for the sake of stability and omitted in the schematic in Fig. 4.23 – are built by capacitor units of 1.05 pF. All of which are arranged in a 24×8 array. For accurate ambient light cancellation, the sampling C_S and feedback C_f capacitors should match both, among themselves and to each other, whereas no accurate matching is necessary for the offset sampling C_{OS} and auxiliary capacitors. Thus, as illustrated in Fig. 4.25, C_f and C_S are arranged with common centroid

in the inner of the array. The outer capacitors form C_{OS} and the auxiliaries and simultaneously guarantee good matching of the inner capacitors by forming a homogeneous surrounding. To avoid excessive metal routing as well as hardly comprehensible parasitic coupling between the nets, every unit capacitor comes with its own configuration and clocking switches underneath it. Only around a dozen analogue signal nets are routed below the capacitors, which allows for good control of parasitics. The lower half of Fig. 4.25 shows a snippet of the array layout, illustrating the bundles of analogue (vertical) and digital (horizontal) signals routed as a grid below the capacitors as well as the switches. The arrangement of the analogue signals in those lanes keeps pairs of nets, which are sensitive to capacitive cross-coupling, apart from each other and is depicted in the lower right corner of the figure.
Resistors R_{S1}, R_{S4}, R_{S5} and half of R_{S2} are located below the auxiliary capacitors while the R_{f} array is placed next to the capacitor array. Interleaved common-centroid layout ensures matching between the components of each half of the differential circuit whereas the matching of different resistors to each other is not required.

4.5.3 Differential Current Subtraction

The photo-generated current of a photodiode is strictly positive, the fully differential TIA however supports input currents ranging from $-\frac{I_{\mathrm{FS}}}{2}$ to $+\frac{I_{\mathrm{FS}}}{2}$ for a given configuration. To make use of the full input swing, a differential DC current $I_{\mathrm{DCS}} = \frac{I_{\mathrm{FS}}}{2}$ is subtracted from the input which shifts the input range of the overall receiver to $0 - I_{\mathrm{FS}}$, as illustrated in Fig. 4.26a. A schematic drawing of the differential current subtraction (DCS) circuit is given in Fig. 4.27. The circuit can generate currents ranging from 20 nA to 10 µA.
Current subtraction at the input node requires low noise, which is achieved by means of a large off-chip filter capacitor for bandwidth limitation, and source degeneration to curb flicker noise [148]. The large external capacitor leads to a slow settling of I_{DCS} after a configuration change of the 4 bit R-2R digital-to-analogue converter (DAC). However, it has no effect on the 2.6 bit current mirror stage, which can be reconfigured on a sample-to-sample basis.

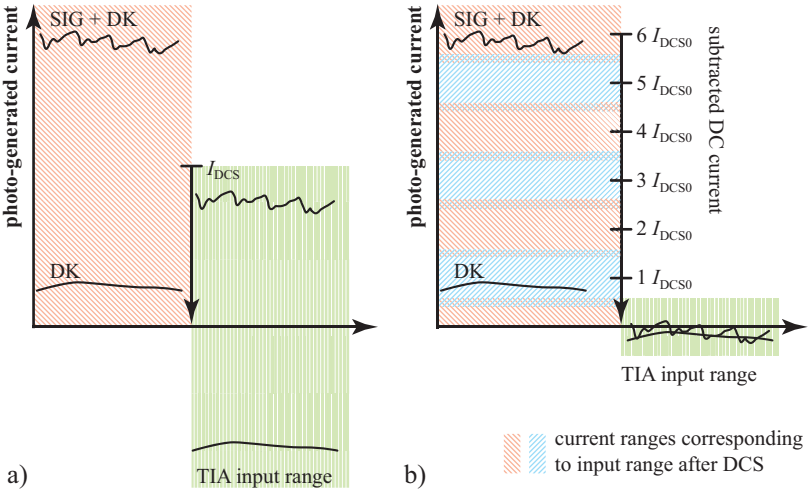

Figure 4.26: Subtraction of a constant current from the input signal to make use of the full input swing (a) and dynamic range enhancement by signal-dependent current subtraction and higher TIA gain (b).

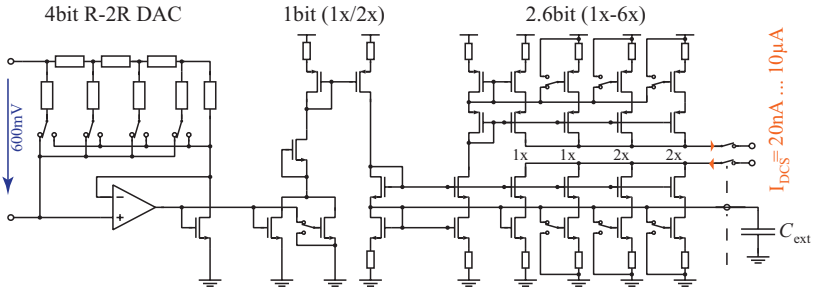

Figure 4.27: Schematic of the differential current subtraction circuit.

Dynamic Range Enhancement

The pulsatile component of PPG signals is usually well below 5% of its DC value, whereas motion artefacts can have larger amplitude, but usually below 20% of the DC value. Ambient light interference level is often quite constant and much lower than the signal. It is thus feasible to keep track of the DC level and subtract an appropriate constant current from the input, which allows for a higher TIA gain to be used and thus lowers the impact of circuit noise on the acquired signal – enhancing dynamic range. The FSM of *TMA-O* features a mode in which different DCS settings for dark (DK) and signal (SIG) samples can be set and where both are digitised and stored in separate output registers. This enables dynamic range enhancement (DRE) to be implemented in software in a MCU controlling the front-end ASIC. The concept of DRE is illustrated in Fig. 4.26b: The more significant bits of the DCS circuit are configured such that one current unit I_{DCS0} of the 2.6 bit current mirror stage is somewhat lower than the full scale input current I_{FS} for a given transimpedance setting. This results in an overlap of the input ranges covered by different DCS current mirror settings, easing signal tracking. The algorithm keeps the average signal at $6I_{\mathrm{DCS0}}$ by adjusting the LED current and tracks the dark trace, eventually adjusting the DCS setting for the latter. Then, the dark sample is subtracted from the signal sample and the DC level is digitally reconstructed. As discussed in Sec. 2.6.1 the DC value has not to be measured accurately for $S_{\mathrm{p}}O_2$ calculations. A deviation as high as 13% causes less than half a percent error in the oxygenation reading. Thus no sophisticated I_{DCS} calibration hardware is necessary – it is sufficient to measure the input DC level when no input is applied for $1I_{\mathrm{DCS0}}$ and $0I_{\mathrm{DCS0}}$ with half TIA gain.

4.5.4 TIA Noise Curbing

Generally, all noise contributions in an OTA can be summarised to an equivalent current noise source at the output node – as illustrated in Fig. 4.28a on the example of a simple single-stage OTA and the single transistors' thermal noise contributions. In a first order approximation, every single-stage OTA can be represented with the small signal equivalent circuit shown in Fig. 4.28b. The model of $\overline{i_{\mathrm{n,a}}^2}$ can

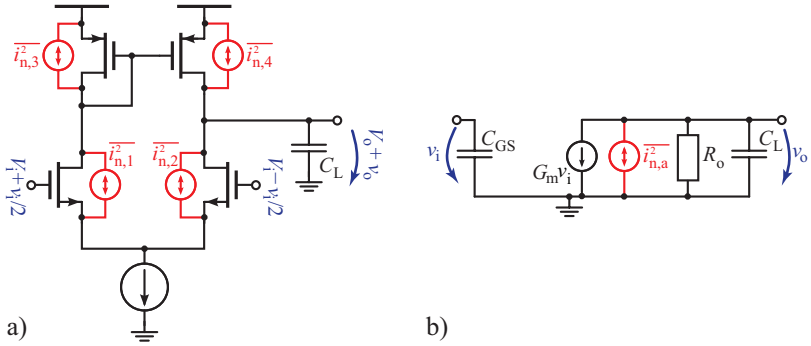

Figure 4.28: Simple single-stage OTA with thermal noise sources indicated (a) and its small signal equivalent circuit (b). The current noise variance of the equivalent total noise is $\overline{i^2_{n,a}} = \sum_{i=1}^{4} \overline{i^2_{n,i}}$.

be extended to include flicker noise. Amplifier noise is often modeled with an equivalent input noise voltage $\overline{v^2_{n,a}}$, which is related to the equivalent noise current with [149]

$$\overline{v^2_{n,a}} = \frac{1}{G^2_m} \overline{i^2_{n,a}}. \tag{4.45}$$

Here, we use the current noise model since describing noise as drain current fluctuations is more intuitive than imagining a modulation of the gate voltage.

The noise voltage variance of the parallel connection of a capacitor C and a resistor R is $k_B T/C$ [150]. Its independence of R is due to proportional scaling of the noise power density and inversely proportional scaling of the noise bandwidth with R. Generally, this sets a lower limit on the noise of a sampled analogue signal [149]. However, circuits with lower than $k_B T/C$ noise can be realised when the origins of noise and bandwidth limitation are separated [151]. More often the contrary is encountered: There are more noise sources than the one also limiting the noise bandwidth. For instance, when using the amplifier of Fig. 4.28 to load a capacitance, the bandwidth will be limited by its transconductance G_m which is equal to the

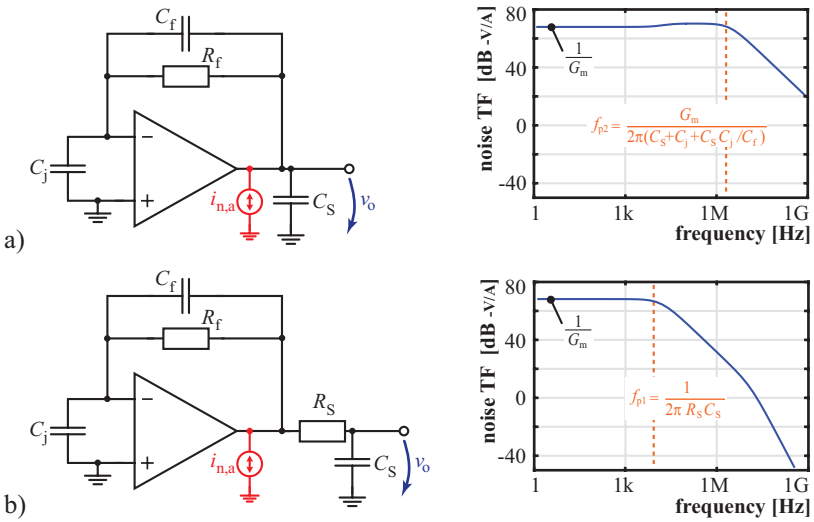

Figure 4.29: Transfer functions of the amplifier noise to the output voltage for a RTIA circuit with (b) and without (a) noise curbing resistor R_S in signal track & sample state.

transconductance $g_{m,n}$ of the NMOS transistors – all four transistors however contribute to the noise current $\overline{i^2_{n,a}}$. Thus the sampled noise will be considerably higher than $k_B T/C$.

This OTA excess noise can be curbed by increasing the series resistance of the capacitor until it gets dominant for both, noise and bandwidth, and thus overall noise approaches the $k_B T/C$ limit. For most circuits however, not only the OTA noise but also the signal bandwidth is reduced by doing so. In case of a PPG transimpedance receiver this is not of any concern since its signal bandwidth is only in the tens of kHz range while the dominant pole in the OTA noise transfer function is in the MHz range, as will be discussed in Sec. 4.5.4. Furthermore, in RTIA configuration with analogue ambient light cancellation, there is additional switched-capacitor (re)sampling which comes with further $k_B T/C$ (and excess) noise. Here, there is more than enough time between two PPG samples to run the circuit at low bandwidth.

The resistors $R_{S1} - R_{S5}$ in the receiver schematic (Fig. 4.23) serve as bandwidth limiters. The effect of each on the OTA noise bandwidth is discussed in more detail in the following.

RTIA Track & Sample State

Figure 4.29a depicts the TIA circuit in the *track* state. The input current source is omitted in the drawing since the focus here is on the impact of the amplifier noise $\overline{i_{n,a}^2}$ on the output voltage which will eventually be sampled and stored on the capacitor C_S.
As derived in App. A.5.1, for the original circuit (without noise-curbing resistor) the transfer function of the OTA noise to the output voltage is given by (A.30):

$$\frac{v_o}{i_{n,a}} = \frac{1}{G_m} \frac{1 + sR_f(C_j + C_f)}{(1 + sR_fC_f)\left(1 + s\frac{C_x}{G_m}\right)} \qquad C_x = C_j + C_S + \frac{C_jC_S}{C_f} \quad (4.46)$$

The zero and the first pole are very close, separated only by the frequency factor $(1 + C_j/C_f) \approx 1...2$, and thus effectively cancel each other. The noise bandwidth is determined by the second pole at

$$f_{p2} = \frac{G_m}{2\pi\left(C_S + C_j + \frac{C_j}{C_f}\right)}, \quad (4.47)$$

which for the small signal characteristics of the implemented circuit would be at roughly 3 MHz and thus more than two orders of magnitude higher than the signal bandwidth (4.19).
Addition of a series resistor R_S as shown in Fig. 4.29b creates a third pole. The transfer function (A.34) is now:

$$\frac{v_o}{i_{n,a}} = \frac{1}{G_m} \frac{1 + sR_f(C_f + C_j)}{(1 + sR_SC_S)(1 + sR_fC_f)\left(1 + s\frac{C_j}{G_m}\right)}. \quad (4.48)$$

The noise bandwidth is thus determined by this new pole

$$f_{p2} = \frac{1}{2\pi R_SC_S}. \quad (4.49)$$

It is best chosen only slightly higher than the feedback cut-off frequency which defines the signal bandwidth. If the pole is set lower, it becomes dominant also for the signal bandwidth.

OTA Offset Sampling and RTIA Summation States

OTA noise bandwidth is reduced analogously in other circuit states as illustrated in Fig. 4.30, derived in detail in App. A.5.2 to A.5.4 and summarised in the following:

Idle State: OTA offset and flicker noise are suppressed by means of CDS. The offset sampling capacitors C_{OS} are charged during the *idle* phase to the OTA offset. For $R_{\mathrm{S}} = 0$, the noise transfer function is given by (A.36)

$$\frac{v_{\mathrm{c}}}{i_{\mathrm{n,a}}} \approx \frac{1}{G_{\mathrm{m}}} \frac{1}{1 + s\frac{C_{\mathrm{OS}}}{G_{\mathrm{m}}}}. \tag{4.50}$$

By adding a series resistance R_{S}, the bandwidth is reduced and the transfer function is given by (A.39)

$$\frac{v_{\mathrm{c}}}{i_{\mathrm{n,a}}} \approx \frac{1}{G_{\mathrm{m}}} \frac{1}{1 + sR_{\mathrm{S}}C_{\mathrm{OS}}}. \tag{4.51}$$

Summation State: The charges stored previously on the sampling capacitors C_{S} for signal and dark samples are transferred to the feedback capacitor C_{f} and thus added together. The voltage v_{f} across the feedback capacitor is thus the difference between the sampled signal and dark voltages. For $R_{\mathrm{S}} = 0$, the transfer function of the noise to v_{f} is (A.42)

$$\frac{v_{\mathrm{f}}}{i_{\mathrm{n,a}}} \approx \frac{1}{G_{\mathrm{m}}} \frac{C_{\mathrm{S}}}{C_{\mathrm{f}}} \frac{1}{1 + s\frac{C_{\mathrm{S}}}{G_{\mathrm{m}}}}. \tag{4.52}$$

Amplifier noise bandwidth is reduced when adding a series resistance R_{S}, resulting in the transfer function (A.46)

$$\frac{v_{\mathrm{f}}}{i_{\mathrm{n,a}}} \approx \frac{1}{G_{\mathrm{m}}} \frac{C_{\mathrm{S}}}{C_{\mathrm{f}}} \frac{1}{1 + sR_{\mathrm{S}}C_{\mathrm{S}}}. \tag{4.53}$$

ADC Track State: The amplifier output voltage is finally sampled by the ADC. The amplifier noise transfer function for $R_{\mathrm{S1}} = R_{\mathrm{S2}} = 0$ is (A.49):

$$\frac{v_{\mathrm{o}}}{i_{\mathrm{n,a}}} \approx \frac{1}{G_{\mathrm{m}}} \frac{C_{\mathrm{S}} + C_{\mathrm{f}}}{C_{\mathrm{f}}} \frac{1}{1 + s\frac{C_{\mathrm{S}} + C_{\mathrm{ADC}} + C_{\mathrm{S}}C_{\mathrm{ADC}}/C_{\mathrm{f}}}{G_{\mathrm{m}}}}. \tag{4.54}$$

Amplifier noise curbing with resistors R_{S1} and R_{S2} results in the noise transfer function (A.54)

$$\frac{v_o}{i_{n,a}} \approx \frac{1}{G_m} \frac{C_S + C_f}{C_f} \frac{1 + sR_{S1}\frac{C_S C_f}{C_S + C_f}}{(1 + sR_{S1}C_S)(1 + sR_{S2}C_{ADC})}. \qquad (4.55)$$

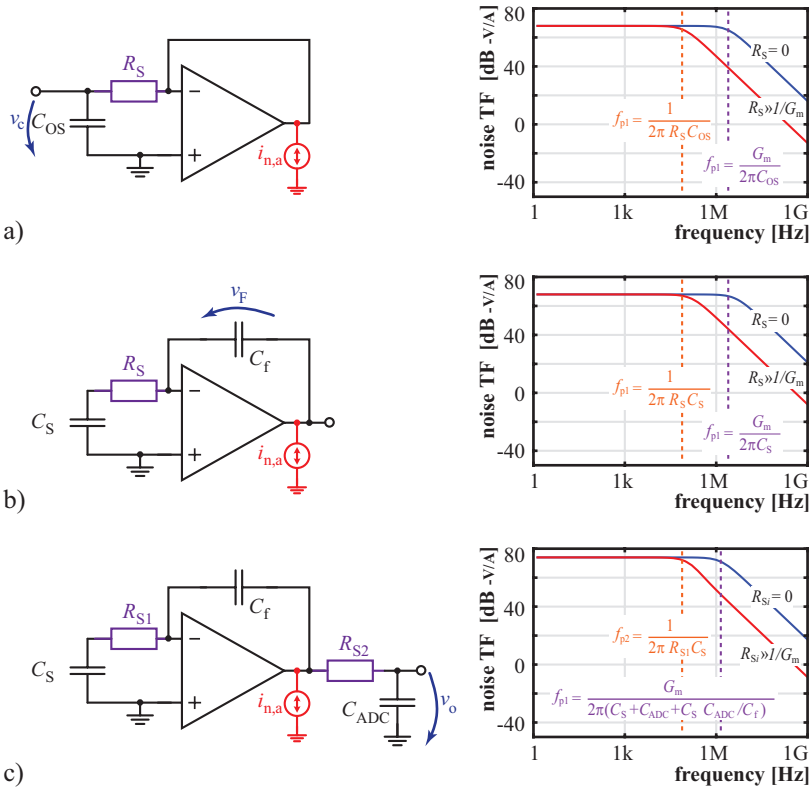

Figure 4.30: Noise transfer functions (with and without noise curbing) and simplified schematics of the TIA circuit in *idle* (a), *summation* (b), and *ADC track* states (c).

4.5.5 ADC Noise Curbing

The 14 bit SAR ADC [106] used for digitisation of the receiver output voltage features different noise reduction techniques itself.
A basic SAR ADC circuit is shown in Fig. 4.31a: It consists of a capacitor array on which the input voltage is initially sampled and then approximated to zero by charge redistribution induced by switching the bottom plates of the single capacitors to different reference voltages [152–154]. Four distinct sources contribute to the overall SAR ADC noise: sampling, comparator, reference buffers, and quantisation.
The fully-dynamic double-tail latch (DTL) comparator [155,156] used in our ADC is depicted in Fig. 4.31b. The first stage has limited gain of arround 10, reducing the effect of the second stage on both, noise and offset. In contrast to the scheme in [156] capacitors C_a and C_b have been added to reduce the bandwidth of the comparator and thus filter its noise [157]. The capacitor C_b is dimensioned large enough to render noise of the second stage insignificant and C_a is configurable in the range $22 - 800\,\mathrm{fF}$. Assuming ideal reference buffers, the total comparator-input referred noise can be approximated as [106]

$$\overline{v_{\mathrm{n,cir}}^2} \approx \frac{2k_\mathrm{B}\mathsf{T}}{C_\mathrm{ADC}} + 2 \cdot 4k_\mathrm{B}\mathsf{T}\frac{\gamma}{g_\mathrm{m}} f_\mathrm{BW} = 2k_\mathrm{B}\mathsf{T}\left(\frac{1}{C_\mathrm{ADC}} + \frac{\gamma}{C_\mathrm{a}}\right), \quad (4.56)$$

where g_m is the input transistors transconductance and C_ADC denotes the input capacitance of the ADC given by the capacitor array and $f_\mathrm{BW} = g_\mathrm{m}/4C_\mathrm{a}$ is the first stage's noise bandwidth [158]. Noise reduction comes with conversion speed reduction and an increase in power consumption. Since C_a – in contrast to C_ADC – is loaded and discharged in each conversion step, it contributes more to the power consumption. Furthermore, comparator noise is – due to redundancy in the capacitor array – only of concern for the least significant conversions. Thus instead of further increasing C_a, majority voting [159] is used to enhance performance where necessary. En passant, it does also reduce reference buffer noise and thus enables trading their power consumption for slightly increased conversion time.

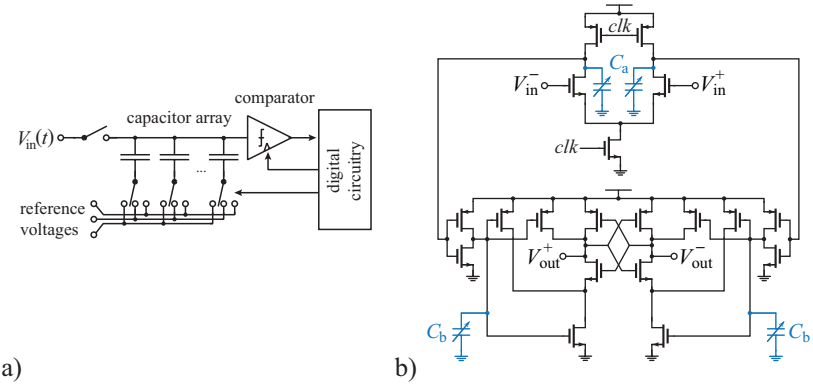

Figure 4.31: Essential SAR ADC circuit (a) and schematic of the implemented DTL comparator (b) with noise reduction capacitors C_a and C_b [106].

Quantisation noise can be battled by converting a single sample multiple times aplying non-subtractive and DC-free dither. To save conversion time and thus power, only the least few conversion steps are re-evaluated [106, 147].

4.5.6 Noise Analysis

The techniques discussed above minimise OTA and ADC excess noise, leaving $k_B T/C$ noise as the dominant source.
The noise sampled during the *idle* state on C_{OS} is later added to both, the signal and the dark samples. It is cancelled when the two samples are subtracted from each other to remove the signal share of ambient light. However, when analysing the charge redistribution from the C_S capacitors to the integration capacitor (parts of C_f) in the *summation* phase, it can be observed that the sampled noise on C_{OS} is equivalent to a small input offset v_n. As illustrated in Fig. 4.32, thus a charge Q_n remains on the C_S capacitors and is missing on the feedback capacitor which causes an error in the output voltage of

$$v_{o,err} = v_n + \frac{Q_n}{C_S} = v_n + \frac{2C_S v_n}{C_S} = 3v_n. \tag{4.57}$$

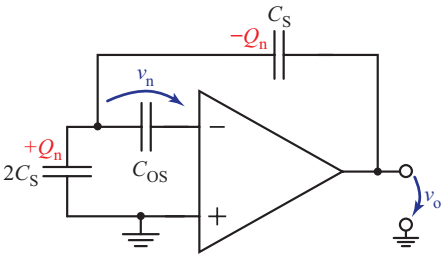

Figure 4.32: Multiplication effect on the sampled C_{OS} noise by charge redistribution.

The noise power initially sampled on C_{OS} is thus multiplied by a factor of nine. Overall $k_B T/C$ noise can be determined for the different RTIA operation modes to be:

Analogue Ambient Light Cancellation:

$$\begin{aligned}\overline{v_{n,tot}^2} &= 2k_B T \left[\underbrace{2\left(\frac{1}{C_f}+\frac{1}{C_S}\right)}_{\text{SIG-DK}} + \underbrace{\frac{1}{C_S}}_{\text{precharge}} + \frac{9}{C_{OS}} + \frac{1}{C_{ADC}} \right] \\ &= 2k_B T \left(\frac{9}{C_{OS}} + \frac{3}{C_S} + \frac{2}{C_f} + \frac{1}{C_{ADC}} \right)\end{aligned} \tag{4.58}$$

Digital Ambient Light Cancellation:

$$\overline{v_{n,tot}^2} = 4k_B T \left(\frac{1}{C_f} + \frac{1}{C_{ADC}} \right) \tag{4.59}$$

No Ambient Light Cancellation:

$$\overline{v_{n,tot}^2} = 2k_B T \left(\frac{1}{C_{OS}} + \frac{1}{C_f} + \frac{1}{C_{ADC}} \right) \tag{4.60}$$

Expected and measured dynamic ranges for the different RTIA modes are given in Tbl. 4.4, demonstrating that $k_B T/C$ noise indeed dominates. All values are without dynamic range enhancement. The

Table 4.4: Theoretical and Measured Dynamic Range (full BW)

	theoretical	meas. with dith.	meas. w/o dith.
no ALC	90 dB	89 dB	86 dB
digital ALC	88 dB	87 dB	84 dB
analogue ALC	84 dB	83 dB	82 dB

theoretical values are given for $k_B T/C$ noise only and a TIA output voltage swing of 1.2 V. Measurements are given for two different ADC configurations: with and without quantisation noise curbing by dithering. Note that a photodiode has at the chosen operating point itself a SNR_{DC} of 80 dB – considering ambient light cancellation, this reduces to ca. 79 dB.

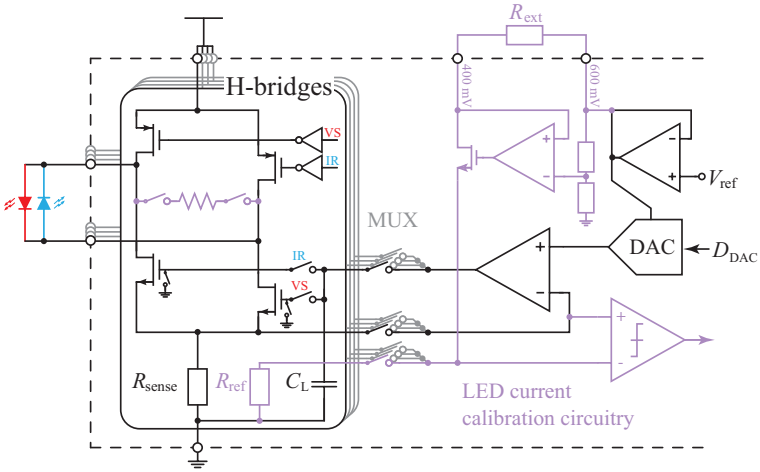

Figure 4.33: Schematic of *TMA-O's* LED driver.

4.6 LED Driver Implementation

An overview schematic drawing of the LED driver is given in Fig. 4.33 and its micrograph is depicted in Fig. 4.34. All clocking signals are generated by the same FSM that also controls the receiver. The LED driver analogue circuitry is connected to the digital circuit by 53 configuration- and control lines whereas the DAC comes with an extra of 130 lines.

Basically, the circuit consists of four current-controlled H-bridges sharing their control circuitry. The current is selected by the configuration of the DAC output voltage. The latter is implemented as an 8 bit resistor ladder, which ensures monotonicity – easing the realisation of (software) signal level control loops. Furthermore, there is a calibration circuit which allows for a start-up calibration of the current sense resistors R_{sense} against a precise external resistor R_{ext}. The H-bridge and the control loop OTA are implemented in 3.3 V voltage domain while the remaining circuitry is supplied by 1.2 V.

The driver is designed to have considerably higher bandwidth than the receiver; the latter thus clearly dominates the loop bandwidth, and therefore does also filter high-frequency noise originating from the transmitter's high bandwidth. A high LED driver bandwidth is desirable to ensure fast LED on/off switching and thus keeping LED on-time minimal.

As discussed in Sec. 4.3.3, LED shot noise can be neglected in a realistic PPG scenario – here photodiode noise clearly dominates. The SNR_{DC} of the driver, however, is required to outperform the photodiode SNR_{DC}.

4.6.1 H-Bridge

In order to support the classic pulse oximetry probes with two cross-connected LEDs, *TMA-O* features H-bridge drivers to allow for load polarity inversion. They are designed to preserve sufficient forward voltage for infra-red and red LEDs at high currents under a limited 3.3 V supply. Two parallel NMOS current control transistors are used to avoid an extra NMOS switch in series for flow direction selection. The series resistance is also kept minimal by a generous layout and

Table 4.5: Parasitic Resistance in the H-Bridge and Voltage Budget

	R	V @ 50 mA	V @ 100 mA
$3R_{\text{pad}}$	115 mΩ	5.75 mV	11.50 mV
$3R_{\text{bond}}$	300 mΩ	15 mV	30 mV
$R_{\text{on,p}}$	1 Ω	50 mV	100 mV
$R_{\text{par,p}}$	400 mΩ	20 mV	40 mV
$R_{\text{par,n}}$	35 mΩ	1.75 mV	3.50 mV
$V_{\text{DS,min}}$		41 mV	97 mV
R_{sense}	5 Ω	250 mV	500 mV
$R_{\text{par,R}}$	85 mΩ	4.25 mV	8.50 mV
$V_{\text{F,max}}$		2.91 V	2.50 V

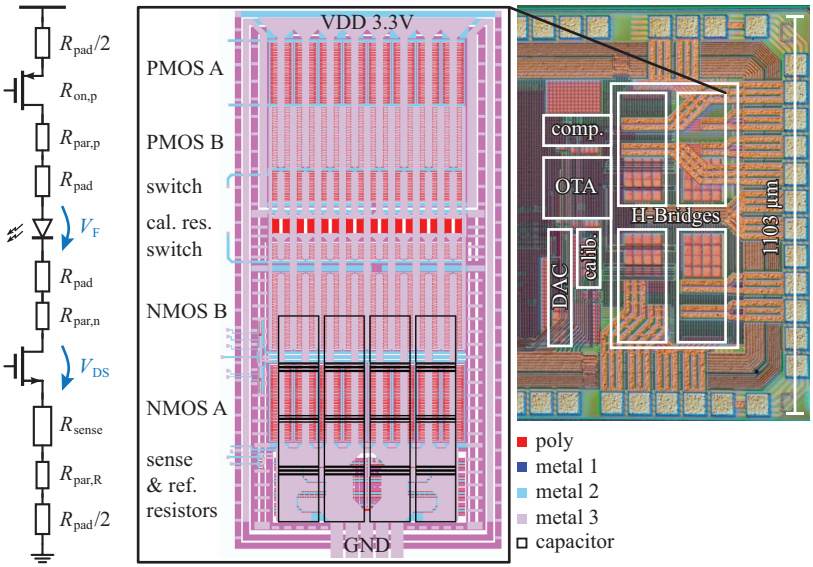

Figure 4.34: Micrograph of the LED driver circuit and layout detail of an H-bridge.

adapted low-resistance pad connections. Figure 4.34 shows the H-bridge layout and illustrates the resistances encountered in a H-bridge branch. The corresponding values obtained by circuit simulation and parasitic resistance extraction from the layout are given in Tbl. 4.5. To reduce series resistance, the circuit can operate in a current sink mode: Here the anodes of the LEDs are externally connected to the supply voltage and only their cathodes are controlled by the ASIC. Fixed anode connection however reduces the number of output channels to eight. In this operation mode, the LED supply may be chosen higher than the circuit's 3.3 V supply as long as the leakage current ensures enough forward voltage drop that the cathode voltage does not exceed 3.3 V. Cathode pin to ground leakage is measured to be equivalent to a 10 MΩ shunt resistance and thus ensures safe operation up to ca. 4.5 V for LEDs of dimensions which are reasonable for the currents encountered in PPG. This allows for instance to directly connect the LED anodes to a 3.7 V lithium-ion battery as is, e.g., required to drive the blue LEDs in the optogenetics head-stage presented in Sec. 6.3.

4.6.2 Operational Transconductance Amplifier

The voltage-to-current conversion circuit shown in Fig. 4.35a is used to set the LED current by the DAC output voltage. A feedback loop regulates the NMOS gate voltage such that the voltage drop on the current sense resistor R_{sense} equals the DAC output. A DC loop gain of ca. 70 dB ensures a high conversion accuracy – for forward voltages close to $V_{\mathrm{F,max}}$, the intrinsic gain of the NMOS transistor drops rapidly and with it the loop gain. Due to the large dimensions of the regulating transistor ($W = 4.5\,\mathrm{mm}$, $L = 350\,\mathrm{nm}$), its parasitic gate-drain and gate-source capacitances are considerably large: $C_{\mathrm{gd}} \approx 1.1\,\mathrm{pF}$, $C_{\mathrm{gs}} \approx 5.1\,\mathrm{pF}$. When considering a series inductance given by a lengthy external transmission line to the LED, this results in two poles followed by two complex-conjugate zeros and some higher-order poles as illustrated in the Bode plot of Fig. 4.35 (b). To ensure stability, the poles are further separated by an additional OTA load capacitance C_{L} of ca. 25 pF, which is placed in the layout above the H-bridge and thus does not cost any additional silicon area. The sub-kHz dominant pole of the loop gain does not coincide with the

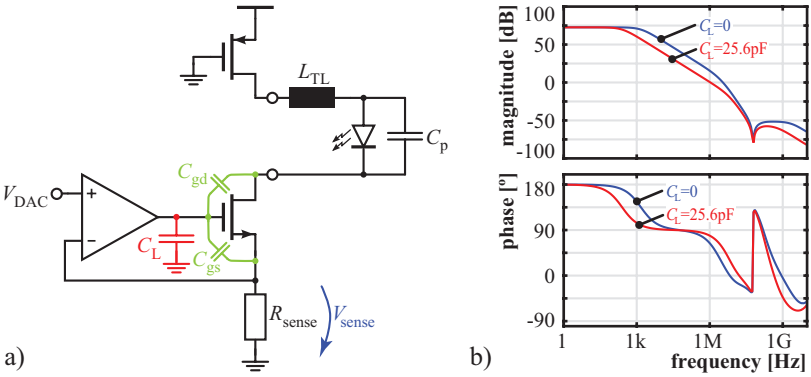

Figure 4.35: LED current regulation: schematic (a) including an off-chip transmission line and corresponding loop Bode plots (b).

-3 dB frequency of the transfer function V_{DAC}/V_{sense}, which lies at ca. 1 MHz and thus ensures high switching speed.
The OTA itself is depicted in Fig. 4.36 and realised in a folded-cascode topology. Source degeneration [148] is used to reduce flicker noise of the NMOS current source transistors. A set of additional transistors acting as switches are introduced to set the output voltage to zero and to disable the input pair while keeping the operating points stable – except for the output-branch which, however, recovers quickly. This allows to interrupt the feedback loop when changing the NMOS transistor to drive a different output. The loop is only closed during the short pulse the LED is on. The DAC is reconfigured while the loop is interrupted which relaxes design constraints on the settling time and eliminates the issue of output voltage glitches.

4.6.3 Calibration

Absolute values of passive components are usually not well controlled in integrated circuit processes – tolerances of $\pm 20 - 30\%$ are common [160]. Pulse oximetry is based on relative measurements (Sec. 2.4.1) and therefore does not require precise control of the LED current. Nonetheless it is desirable to have some control when considering

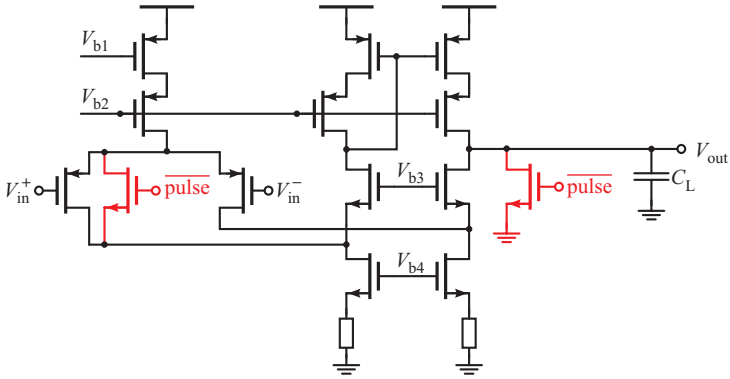

Figure 4.36: Folded cascode OTA with additional enable signal $\overline{\text{pulse}}$.

power and temperature management – the latter is of particular interest in implants (Chap. 6). The LED driver features circuitry to calibrate the internal 5 Ω sense resistor to an external 10 kΩ precision resistor R_{ext}, highlighted in purple in Fig. 4.33. The voltage drop on R_{ext} is regulated by a feedback loop and defined to be 200 mV. Thus $R_{\text{ext}} = 10\,\text{k}\Omega$ results in a reference current of 20 µA flowing through the internal reference resistor R_{ref}. The latter is well matched to R_{sense} by a common-centroid layout and nominally 10 kΩ as well. The high ratio of 2000 between the two matched resistors is achieved by series and parallel connection of unit elements: R_{sense} is composed of 100 parallel unit elements while R_{ref} is the series connection of 20 elements. Separation of power and sense terminals minimises calibration errors due to voltage drop on wiring resistance. The difference of the voltage drops on R_{sense} and R_{ref} is sensed by the comparator whose schematic is depicted in Fig. 4.37. It is a static latched comparator [161] with an additional low-resistance switch to suppress any memory on the previous decision while maintaining the preamplifier gain during the *track* phase, which is given by the input pair transconductance and the on-resistance of the latch-shorting transistor. Standard cell inverters are symmetrically connected to both latch branches for matched load capacitance on these nodes.

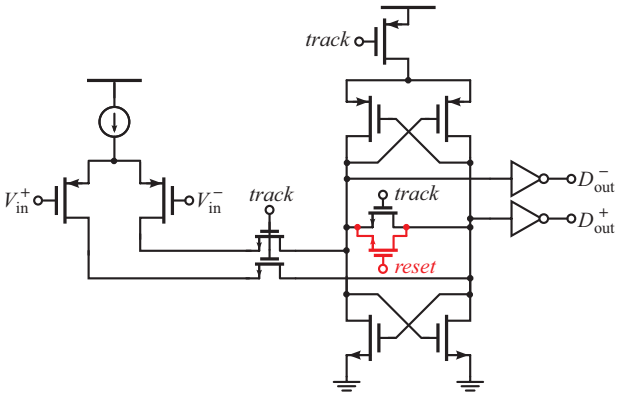

Figure 4.37: Comparator with low-resistance reset switch.

A small FSM is implemented in digital logic that runs a short calibration sequence: starting at zero, the DAC is incremented until a positive comparator output is detected. At this point the DAC setting is found for which the LED current is

$$I_{\text{LED}} = 2000\frac{\Delta V_{\text{ref}}}{R_{\text{ext}}} = 2000\frac{200\,\text{mV}}{10\,\text{k}\Omega} = 40\,\text{mA}. \tag{4.61}$$

Optionally, an internal $40\,\Omega$ resistor can be connected between the diode terminals to ensure correct operation when the ASIC is used in instrumentation with a detachable probe.

4.7 Digital Circuit

The analogue circuitry of *TMA-O* can embody different receiver topologies and allows to multiplex a multitude of input signals and LED driving channels. For maximal utilisation of those capabilities, a truly mixed-signal design approach is chosen: All configuration and clocking signals for the analogue circuitry of both, receiver and LED driver, are generated by a common synchronous digital circuit which has been created, simulated, and synthesised in a standard digital design flow. A total of 625 metal wires interconnect it with the analogue

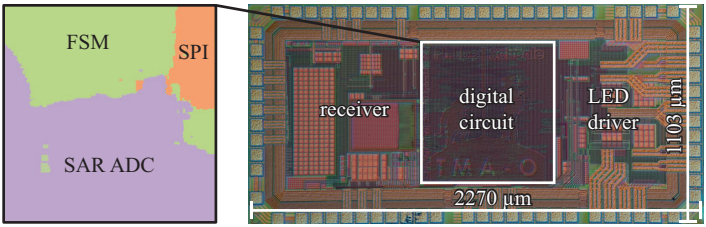

Figure 4.38: Area occupation of the digital circuits.

circuits. The main drawback of this architecture is limited control over the exact timing of clock signals. E.g., the clock signals controlling switched-capacitor circuits need to be non-overlapping [149] to avoid charge loss and often an early clock is desirable for bottom-plate sampling [77], to reduce the impact of charge injection by MOS switches. In a synchronous design, the minimum non-overlapping time of two generated clock signals is half a clock cycle. For a low-frequency design this is tolerable since the digital circuit can run at a comparatively high speed.
Figure 4.38 illustrates the silicon area distribution for the main parts of the digital circuit. The SAR ADC occupies the largest share and is discussed in detail in [147]. The PPG FSM controls the receiver, LED driver, and the FSM of the SAR ADC. Furthermore, it does duty-cycle all analogue circuitry including the reference voltage buffers of the ADC to curb power consumption.
The PPG FSM is designed to ease the use of the chip without sacrificing its flexibility. It can either run in RTIA or CTIA mode and supports up to ten consecutively executed program sequences. Each of which allows for individual configuration of:

- Transimpedance, bandwidth, subtracted I_{DCS}, and timing.
- Input and output channel selection – for both, concurrent operation is possible.
- Ambient light cancellation mode: analogue, digital, or none.
- Dynamic range enhancement.
- Oversampling.

The circuit is designed with integration in a SoC (Chap. 5) in mind. It is envisaged to be used in combination with a MCU and does not feature any hardware for LED emission intensity regulation, S_pO_2 calculation, or artefact suppression. Software implementations thereof give the application engineer more freedom to adapt it at the specific needs of a certain application.

4.8 Measurements

The reader may refer to Sec. 4.2 for the definitions of performance metrics used in this section.

4.8.1 Setup

The measurement setup and instrumentation used for the characterisation of the receiver is shown in Fig. 4.39. A *SRS DS360* ultra low distortion voltage function generator is connected with two series resistances of $R_S = 5 - 20\,\mathrm{M\Omega}$ to the input pads of the ASIC. To avoid distortion, the impedance of the circuit is matched to the signal generator output impedance by means of shunt resistors and the common mode voltage of the instrument is equalled to the chip's common mode voltage.
Assuming a noise-free generator, the current signal-to-noise ratio is limited by thermal noise generated by the series resistances:

$$SNR_{FS} = \frac{\frac{I_{pp}^2}{8}}{\overline{i_{n,}^2}} = \frac{\frac{V_{pp}I_{pp}}{16R_S}}{\frac{2k_B\mathsf{T}f_{BW}}{R_S}} = \frac{V_{pp}I_{pp}}{32k_B\mathsf{T}f_{BW}}. \tag{4.62}$$

For a given input peak-to-peak current I_{pp}, using a higher series resistance R_S allows for higher source voltage V_{pp} which results in an increased SNR. The *SRS DS360* can generate waveforms with differential output voltages of up to 40 V_{pp} which would allow for a 1 µA current with 94dB SNR_{FS} for a 100 kHz bandwidth. Including the instrument's voltage noise [162] over a 5 kHz bandwidth (defined by R_{im} and C_{filt}) this results in ca. 91dB SNR_{FS} – clearly above the expected performance of *TMA-O's* receiver.
The *TMA-O* test board includes LEDs and a photodiode for loop

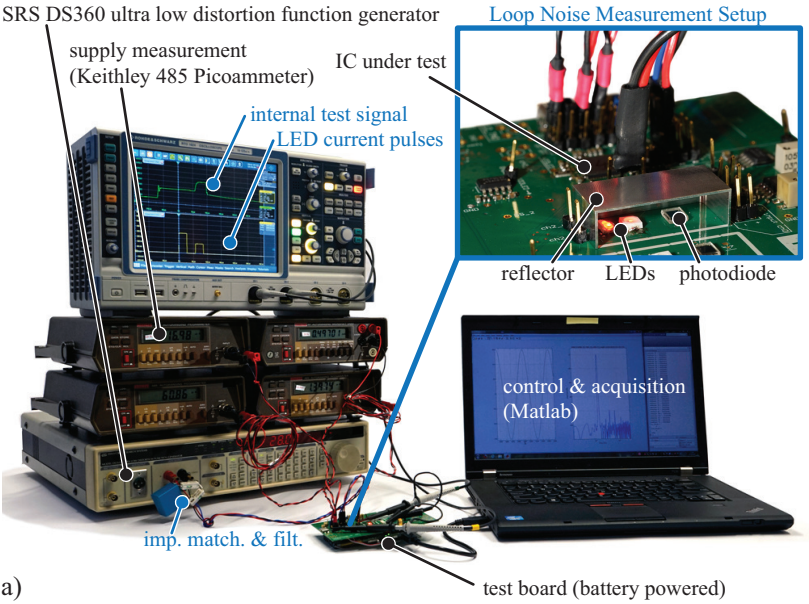

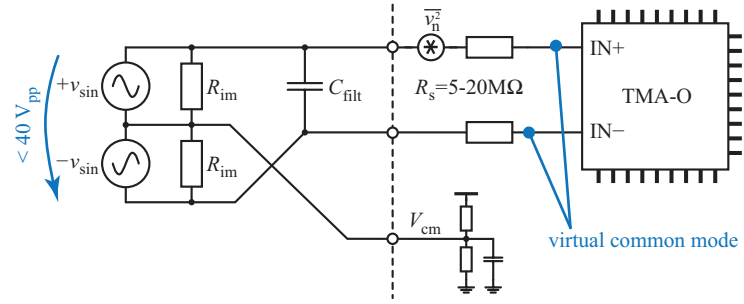

Figure 4.39: Measurement circuit schematic (b) and bench setup (a) for the receiver characterisation with inset depicting the optical setup used for the loop noise characterisation.

measurements as shown on the photograph in the inset of Fig. 4.39a. During measurements, the open side of the aluminium reflector is closed and the light incident to the photodiode is reduced by means of an optical filter which is trimmed for the desired transmission factor Θ.
The *TMA-O* ASIC has separate supply pins for the receiver, the ADC, the LED driver, and the digital circuit. All supply currents are measured with *Keithley 485* picoammeters or *FLUKE 8846A* precision multimeters. Accurate mean DC current measurement for duty-cycled load has been verified by a comparative oscilloscope based measurement.

4.8.2 Measurement Results

Key performance measurands are summarised for *TMA-O* in the characterisation measurements shown on page 114 and discussed in the following. A comparison to the state-of-the-art is given in the next section.

Dynamic Range

The dynamic range measurements for the receiver in RTIA (a) and CTIA (b) modes demonstrate constant receiver performance, independent of the transimpedance configuration. This confirms the effectiveness of the noise curbing techniques discussed in Sec. 4.5.4 - 4.5.5: the remaining receiver noise is dominated by $k_\mathrm{B}\mathsf{T}/C$ noise, which is independent of the transimpedance. The values in the graphs (a,b) are given for a balanced sinusoidal test input signal and with both, ambient light cancellation (ALC) and DC current subtraction, disabled. Here, dynamic range is calculated from the measured SNR_FS resulting in slightly worse results compared to a SNR_DC measurement. Noise is integrated over the full bandwidth, which is due to aliasing independent of the PRF (sampling frequency). A constant SFDR of ca. 80 dB was measured over the given range in RTIA mode while it degraded in CTIA mode from 80 dB to 75 dB for high transimpedance values.
Loop DR can be traded against PRF and spans for a 20 Hz signal

band from 85 dB (for 40 Hz PRF) to 109 dB (for 10 kHz PRF[1]) as illustrated in Fig. 4.11.

Differential Current Source

For an imbalanced input signal – e.g., photo-generated current of a photodiode – the receiver dynamic range gets degraded by the differential current subtraction (DCS) at the TIA input. The current DAC noise is reduced by means of an external filter capacitor, as discussed in Sec. 4.5.3 and illustrated in the graph (c) by an increase in dynamic range with external filter capacitance. For a 10 µF capacitor, the noise added by the DCS reduces dynamic range only by 1.3 dB. The DCS circuit can further be used for dynamic range enhancement of the receiver by up to 14 dB.

Ambient Light Cancellation

Measured high-pass characteristics for the implemented CDS ambient light cancellation are depicted in (d) for both modes, CTIA and RTIA. For the latter the characteristics for both, analogue and digital cancellation, are given for $R_\mathrm{f} = 450\,\mathrm{k\Omega}, C_\mathrm{f} = 16.8\,\mathrm{pF}$ and 28 µs LED on-time. Due to ADC conversion time, the time difference T_ALC between the two samples is higher for digital ALC which results in a lower rejection for non-DC interferers.
The observed flattening of the filter characteristics at low frequencies is likely caused by timing inaccuracies, i.e., a difference in settling (integration) time for the *signal* and the *dark* sample. Here, the limited control over exact clocking given by the chosen mixed-signal design approach reveals its drawback.

Power Consumption

The graphs (e) and (f) break down the power consumption of the main building blocks and power domains. With exception of the DCS, all analogue circuits are duty-cycled to reduce power consumption. Power thus scales linearly with the PRF – the low offset of the ADC and LED driver traces indicates marginal overhead due to start-up. The

[1] maximum PRF for two-LEDs operation

TIA curve includes a constant power consumption given by the DCS which should not be duty-cycled when its noise is filtered by means of an external capacitor. The digital circuit consumes ca. 200 µW of power independent of PRF when clocked at 2 MHz. Although a 1 MHz clock gives sufficient timing precision for the PPG FSM, the ADC performance degrades in certain dither and oversampling modes for clock frequencies lower than 2 MHz. The cause for this has been identified to be charge loss from the SAR ADC [106, 147] capacitor array due to limited off-resistance of the switches connecting the TIA output or the calibration DAC to the capacitor top plates.

Power Supply Rejection Ratio

The fully-differential implementation of the receiver results in a high power supply rejection ratio (PSRR). The graphs depicted in (g) are ADC input-referred, i.e., the following definition is used:

$$PSRR_{\text{rec}} = 20 \cdot \log_{10} \left(\frac{V_{\text{supply ripple, RMS}}}{V_{\text{ADC in, RMS}}} \right). \tag{4.63}$$

Interferers of different frequencies are induced by a signal generator on the supply – the corresponding ADC input RMS interference voltage is calculated from the power of the interferer observed in the acquired data. The mean measured value is ca. 77 dB.
The LED driver (LD) is a single-ended design. Its far lower PSRR, shown in (h), will thus dominate in a real application. Different definitions are used for the three independent power domains. Interference on the 1.2 V supply modulates the DAC output voltage and thus results in a LED current ripple which scales proportionally with the current. A relative measure is used to meet this effect:

$$PSSR_{\text{LD1V2}} = 20 \cdot \log_{10} \left(\frac{\frac{V_{\text{supply,ripple}}}{V_{\text{supply,DC}}}}{\frac{V_{\text{load,ripple}}}{V_{\text{load,DC}}}} \right). \tag{4.64}$$

For the measurements, a resistive load is used in place of the LED. A current ripple which is independent of the configured LED current is observed for interferers on the 3.3 V supplies: the effect of a current

regulation loop (Fig. 4.35) perturbation is fairly independent of DAC output voltage. An absolute measure is thus used:

$$PSSR_{\mathrm{LD3V3/LED3V3}} = 20 \cdot \log_{10}\left(\frac{V_{\mathrm{supply,ripple}}}{V_{\mathrm{load,ripple}}}\right), \tag{4.65}$$

again for a resistive load replacing the LED.

4.8.3 Comparison to the State-of-the-Art

Comparison to other work is aggravated by a non-uniform set of performance metrics reported in different publications and datasheets. Some ASICs are characterised including the optoelectronic elements, some excluding them and others without defining whether they are included or not. A further difficulty is the reluctance to indicate the input signal level for which a certain receiver (or loop) performance is measured.
Against all odds, a comparison to [145, 163–169] is dared in Tbl. 4.6 and 4.7 while the data situation for, e.g., [21,24,170] inhibits a comparison of performance metrics to those chips. For direct comparability, some of the printed metrics are derivatives of originally reported ones: e.g., receiver characterisation is given for all ASICs for the same noise bandwidth. All calculations and necessary assumptions are given in detail in App. B.
As discussed in Sec. 4.3.4, dynamic range can be traded for power by adapting PRF, and LED current. The dynamic range required for a $S_{\mathrm{p}}O_2$ or other PPG measurement varies widely with physiological parameters and the measurement setup, e.g., probe placement. Circuit characterisation with specific applications in mind leads thus to reported performances for different PRF, LED currents, and input signal levels. Direct comparison can thus be missleading. The FoM (4.4) introduced in Sec. 4.2.1 is a loop dynamic range measure normalised for overall power consumption, signal bandwidth, and LED-to-photodiode current transmission:

$$FoM = DR_{\mathrm{f_{BW}}} + 10\log_{10}\left(\frac{f_{\mathrm{BW}}}{1\mathrm{Hz}} \cdot \frac{1\,\mathrm{mW}}{P_{\mathrm{tot}}} \cdot \frac{10\mathrm{ppm}}{\Theta}\right) \qquad [\mathrm{dB}].$$

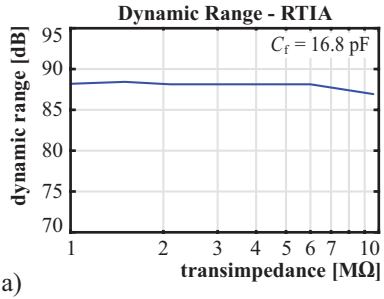
Dynamic Range - RTIA
dynamic range [dB]
95
90
85
80
75
70
C_f = 16.8 pF
1
2
3
4
5
6
7
10
transimpedance [MΩ]

a)

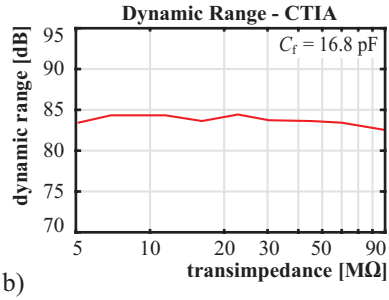
Dynamic Range - CTIA
dynamic range [dB]
95
90
85
80
75
70
C_f = 16.8 pF
5
10
20
30
50
90
transimpedance [MΩ]

b)

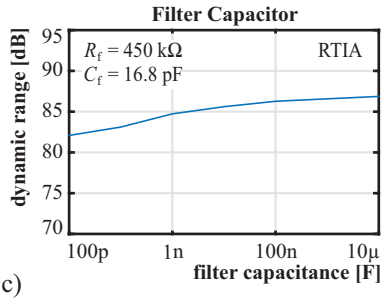
Filter Capacitor
dynamic range [dB]
95
90
85
80
75
70
R_f = 450 kΩ
C_f = 16.8 pF
RTIA
100p
1n
100n
10µ
filter capacitance [F]

c)

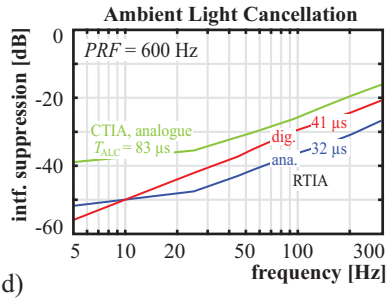
Ambient Light Cancellation
intf. suppression [dB]
0
-20
-40
-60
PRF = 600 Hz
CTIA, analogue
T_{ALC} = 83 µs
dig.
41 µs
ana.
32 µs
RTIA
5
10
20
50
100
300
frequency [Hz]

d)

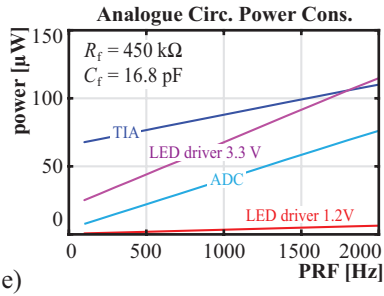
Analogue Circ. Power Cons.
power [µW]
150
100
50
0
R_f = 450 kΩ
C_f = 16.8 pF
TIA
LED driver 3.3 V
ADC
LED driver 1.2V
0
500
1000
1500
2000
PRF [Hz]

e)

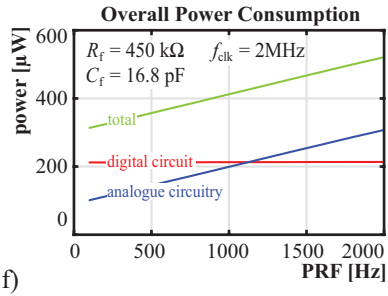
Overall Power Consumption
power [µW]
600
400
200
0
R_f = 450 kΩ
C_f = 16.8 pF
f_{clk} = 2MHz
total
digital circuit
analogue circuitry
0
500
1000
1500
2000
PRF [Hz]

f)

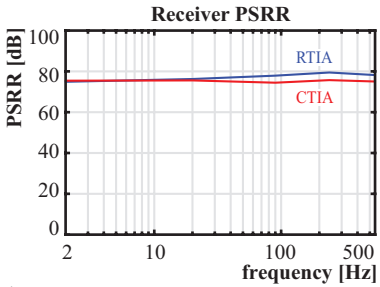
Receiver PSRR
PSRR [dB]
100
80
60
40
20
0
RTIA
CTIA
2
10
100
500
frequency [Hz]

g)

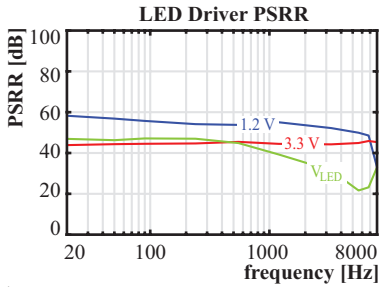
LED Driver PSRR
PSRR [dB]
100
80
60
40
20
0
1.2 V
3.3 V
V_{LED}
20
100
1000
8000
frequency [Hz]

h)

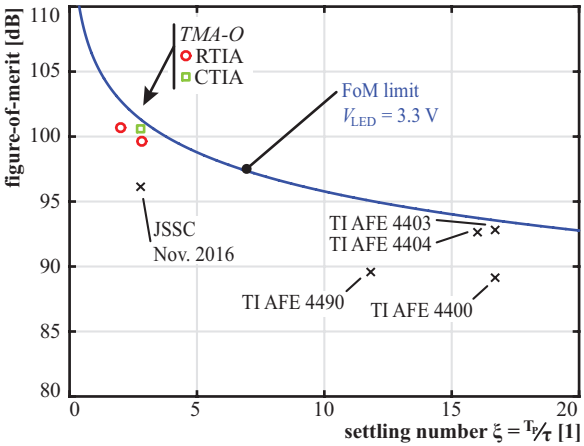

Figure 4.40: Comparison of the FoMs of *TMA-O* and different competing ICs [165–169].

The loop dynamic range includes noise originating from the optoelectronic components, while the transmission Θ covers differences in the measurement setup including varying sizes and efficiencies of the optoelectronic components. The FoM is thus a measure for the power efficiency of a PPG ASIC. In Sec. 4.4.1 it is shown that this FoM is ultimately limited by the LED driver supply voltage and the settling number $\xi = T_\mathrm{p}/\tau$ which relates the LED on-time T_p to the receiver bandwidth represented with the corresponding time constant τ.
In Fig. 4.40 the FoM of *TMA-O* is compared to the current state-of-the-art PPG chips from industry and academia. It is observed that both, *AFE4403* and *AFE4404* are close to the limit for their respective ξ, indicating low power consumption overhead, and that the loop dynamic range is limited not by receiver noise but by shot noise originating from the photodiode. These chips require a minimum ξ of ten, which limits their theoretical maximum FoM to 96 dB. The capability to support incomplete settling without suffering performance degradation in RTIA mode enables *TMA-O* to be operated at low settling numbers. The performance maximum is shown in Sec. 4.4.1 to be achieved for a $\xi \approx 2$ – here *TMA-O* has a 5 dB higher FoM than the current state-of-the-art ASIC which corresponds to a

power reduction by 68% for same signal quality. Figure 4.40 shows the efficiency of *TMA-O* for three different operation modes: for the two RTIA modes also reported in the comparison tables (once for maximum loop DR and once for maximum FoM) and for CTIA mode. TIA input range and LED current are chosen as close as possible to the values considered for the characterisation of the *TI* chips for maximal comparability: all three measurements have been performed for a 650 nA photodiode input current and 50 mA LED current.

Table 4.6: Performance Summary and Comparison to the State-of-the-Art – Part I

	TBioCAS 2013 [145]	JSSC Jul. 2016 [164]	JSSC Nov. 2016 [169]	AFE4403 2014 [167]	**TMA-O 2016**	
die size [mm^2]	1.15[a]	2	5.04[a]	9.00	**2.50**	
tech. node	350 nm	250 nm	180 nm	-	**130 nm**	
supplies [V]	3.3	-	3.3	3.0 / 3.3[b]	**1.2 / 3.3**	
# PD / LED ch.	1 / 2	1 (integ.) / 2	2 / 64	1 / 2 (3)	**4 / 32**	
Receiver						
DR 0.1-20 Hz [dB]	-	-	94	106	**98**	
DR, enhanced [dB]	-	-	-	-	**112**	
transimpedance [Ω]	-	-	16k-2.2M	10k-1M	**19k-90M**	
Loop: Tx-LED-PD-Rx						
settl. number ξ	-	-	2.8	16.7	**2.9**	**2.0**
DR 0.1-20 Hz	72[c]	85[d]	93	92	**96**	**93**
LED duty-cycle [%]	4[c]	4[d]	6.1[e]	5	**1.7**	**0.8**
LED power [mW]	1.4[c]	13.2[d]	20.3[e]	16.5	**5.5**	**2.6**
IC power [mW]	0.5	3.02	0.3[e]	2.03	**0.5**	**0.3**
FoM [dB]	74	86	96	93	**100**	**101**

$R_{\mathrm{TI}} = 450/500\,\mathrm{k\Omega}$ $f_{\mathrm{PR}} = 600$ Hz $I_{\mathrm{LED}} = 50\,\mathrm{mA}$ 2 LEDs with ADC avg./dith.

[a] active area [b] min. LED supply for 2.5 V forward voltage

[c] $f_{\mathrm{PR}} = 100$ Hz [d] $f_{\mathrm{PR}} = 64$ Hz [e] $f_{\mathrm{PR}} = 4$ kHz

Table 4.7: Performance Summary and Comparison to the State-of-the-Art – Part II

	AFE4400 2012 [165]	AFE4490 2012 [166]	AFE4404 2015 [168]	MAX30100 2014 [163]	**TMA-O 2016**	
die size [mm^2]	-	-	3.75	0.75	**2.50**	
tech. node	-	-	-	-	**130 nm**	
supplies [V]	3.0 / 3.5^b	3.0 / 3.5^b	3.0	1.8 / 3.3	**1.2 / 3.3**	
# PD / LED ch.	1 / 2	1 / 2	1 / 3	1 / 2	**4 / 32**	
Receiver						
DR 0.1-20 Hz [dB]	92	98	100	-	**98**	
DR, enhanced [dB]	-	-	-	-	**112**	
transimpedance [Ω]	10k-1M	10k-1M	10k-1M	-	**19k-90M**	
Loop: Tx-LED-PD-Rx						
settl. number ξ	16.7	11.8	16	-	**2.9**	**2.0**
DR 0.1-20 Hz	89	96^c	89^d	94^e	**96**	**93**
LED duty-cycle [%]	5	25^c	2^d	16^e	**1.7**	**0.8**
LED power [mW]	17.5	87.5^c	6^d	52.8^e	**5.5**	**2.6**
IC power [mW]	2.79	2.79	1.94	0.94	**0.5**	**0.3**
FoM [dB]	89	90	93	90	**100**	**101**

$R_{\mathrm{TI}} = 450/500\,\mathrm{k\Omega}$ $f_{\mathrm{PR}} = 600$ Hz $I_{\mathrm{LED}} = 50\,\mathrm{mA}$ 2 LEDs with ADC avg./dith.

^{a} active area ^{b} min. LED supply for 2.5 V forward voltage

$^c f_{\mathrm{PR}} = 1.2$ kHz $^d f_{\mathrm{PR}} = 100$ Hz $^e f_{\mathrm{PR}} = 400$ kHz

Chapter 5

Towards a Biomedical System-on-Chip

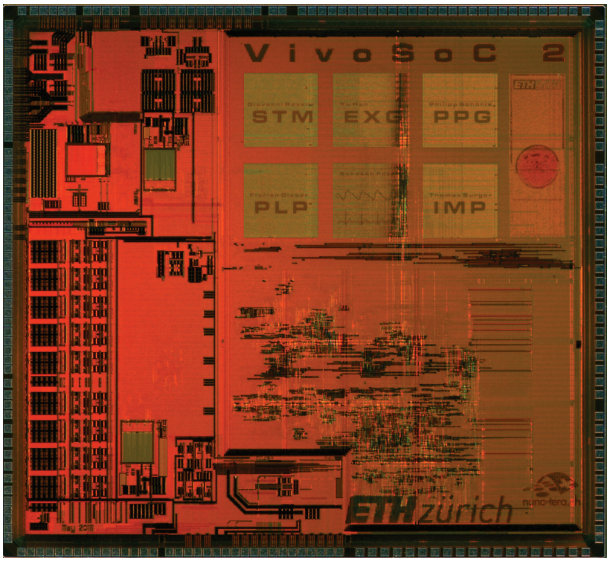

Figure 5.1: Chip micrograph of the *VivoSoC 2* biomedical SoC.

The technological advances in microelectronics of the past decades gave rise to today's small-sized portable computers including 'smart' phones. The enormous marked value of this business did also drive R&D in related fields, such as PCB manufacturing, displays, batteries, MEMS, and power electronics – enabling miniaturisation and cost reductions for other electronic devices as well.
The technological possibilities and increasing health cost in industrialised and emerging nations, led to the vision of – and demand for – low-cost miniaturised medical instrumentation for non-obtrusive long-term monitoring of vital signs. The step from a hospital's bench instrumentation to wearable medical devices involves more than just reducing size and power consumption of the electronics: with non-obtrusiveness comes mobility. Motion however interferes with the recording of physiological signals such as ECG, PPG, or blood pressure. Furthermore, raw data acquisition alone is not tremendously useful: the recorded signals need to be analysed. Both, motion resilience and signal analysis, involve plenty of computation.
In-instrument computation allows for live feedback to the user and cuts the amount of data which has to be stored on an embedded memory or is transmitted by a radio frequency (RF) link to, e.g., a mobile phone. Both, radio transmission and storage, are power-hungry – in-instrument computation can thus be essential for energy efficient solutions.
The goal of ongoing research and engineering effort at our lab is to create a hard- and software platform for wearable and implantable medical instrumentation based on a SoC which comprises analogue front-ends for the acquisition of various vital signs and a powerful multi-core processor unit.
In the remainder of this chapter, the *VivoSoC 2* system-on-chip and previous work which contributed to its hardware is presented. A demonstration prototype of a wearable biomedical sensor platform based on the *VivoSoC 2* chip is introduced in Sec. 5.2 while Chap. 6 discusses an envisioned implantable platform and first prototypes towards it.

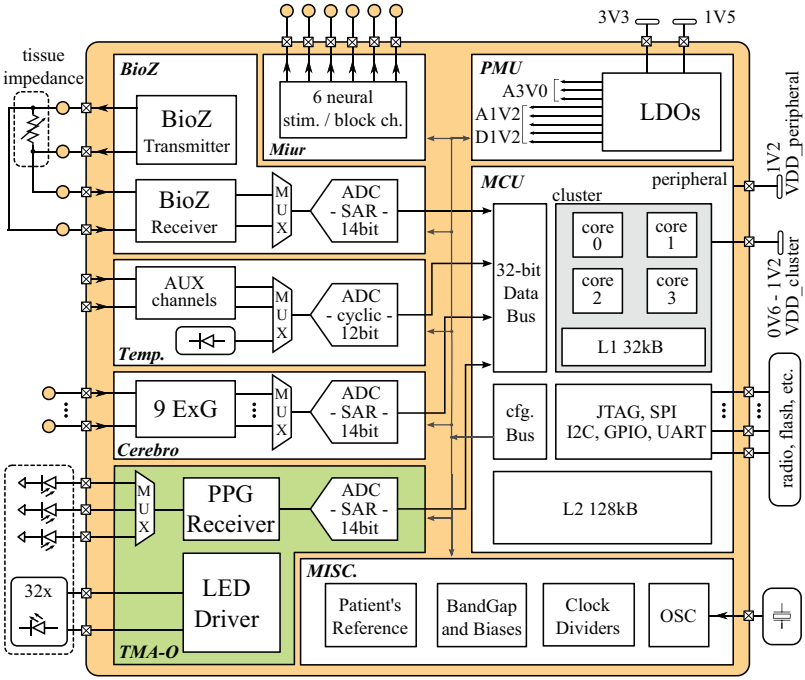

Figure 5.2: Block diagram of the *VivoSoC 2* biomedical SoC comprising *TMA-O's* PPG circuitry (highlighted). *By courtesy of G. Rovere.*

5.1 VivoSoC 2

VivoSoC 2 is a biomedical system-on-chip implemented in a 130 nm CMOS technology. The block diagram in Fig. 5.2 gives an overview on the SoC. Along with *TMA-O's* PPG circuit it comprises analogue front-ends for electrodes-based data acquisition (ExG), bio-impedance measurement, temperature sensing, neural stimulation and two single-ended auxiliary ADC inputs. The PPG circuit is discussed in detail in Chap. 4 while the ExG AFE and the temperature sensor are based on previous work [171] and will be introduced in Sec. 5.3 together with the six-channel neural stimulation hardware. The SoC further

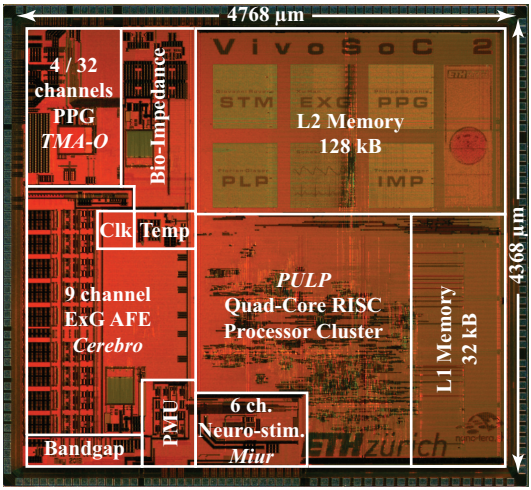

Figure 5.3: *VivoSoC 2* micrograph with area distribution marked for the main sub-circuits.

comprises multiple output-capacitor-free low drop-out (LDO) regulators – described in detail in [172] – for the independent supply of the analogue circuits. The AFEs are supplied independently not only to prevent leakage in circuitry which is shut-off for a certain application, but more importantly to avoid power supply noise induced by one circuit to affect the performance of others. This enables duty-cycling of analogue circuitry as is done, e.g., in TMA-O (Sec. 4.24). Further auxiliary analogue circuitry includes a bandgap reference circuit and an oscillator with configurable clock propagation and division for the single sub-circuits.

The analogue circuits are connected by a shared configuration bus and separate data buses to the MCU which, as illustrated in Fig. 5.3, occupies more than half of the silicon area. The processor unit is a parallel ultra-low power (PULP) cluster design with four *openRISC* [173] cores sharing a 32 kB L1 cache and separate clock and power domains for the cores, peripherals, and the L2 memory. Direct memory access (DMA) engines manage data transfer between peripherals (including the AFEs) or the L1 cache and the 128 kB L2 memory. The design is

based on the recent *Fulmine* implementation [174, 175] of the *PULP* platform [176–178].
Core voltage scaling allows for further power reduction at low clock frequencies while the division of the general purpose input/output (GPIO) and interface pins into five I/O voltage domains eases system-level interconnection with different periphery, such as MEMS sensors, memory, and wireless communication ICs.

5.2 Wearable Instrumentation Platform

A first demonstration prototype of a wearable medical instrumentation platform based on the *VivoSoC 2* chip is shown in Fig. 5.4. The PCB measures $35 \times 55\,\mathrm{mm}^2$ and has, including the battery, a height of ca. 5 mm. This corresponds roughly to the measures of a matchbox, as illustrated in Fig. 1.1. The numerous sensing capabilities of the SoC are extended with external environmental MEMS sensors connected by an inter-IC (I^2C) bus: a *Bosch BMX055* 9-axes absolute orientation sensor and a *Bosch BMP280* barometric pressure sensor. The program code for the SoC is stored on an external flash memory chip and copied into the L2 memory on start-up by the SoC's boot-loader. While data acquisition and processing is done on the *VivoSoC 2* multi-core cluster, data storage on the on-board secure digital (SD) memory card and communication to the tablet computer user interface software is handled by a commercial *ATMEL AVR32*[1] MCU. This structure is inherited from the modular development platform reported in [179]. Although convenient to implement USB mass-storage functionality for simple access to the data stored on the SD card, it is inefficient in terms of PCB area, cost, and power consumption and thus planned to be omitted in the future evolution of the platform.
For the communication with tablet computers and 'smart'-phones serves the dual-mode *Bluetooth* RF front-end *CC2564MODN* in combination with a *MSP430F5438A* MCU, both commercial *Texas Instruments* products. The dual-mode capability allows to switch between *Bluetooth* low energy (BLE) and classic enhanced data rate (EDR). The former is designed for applications with low data throughput and

[1] AT32UC3A3256S

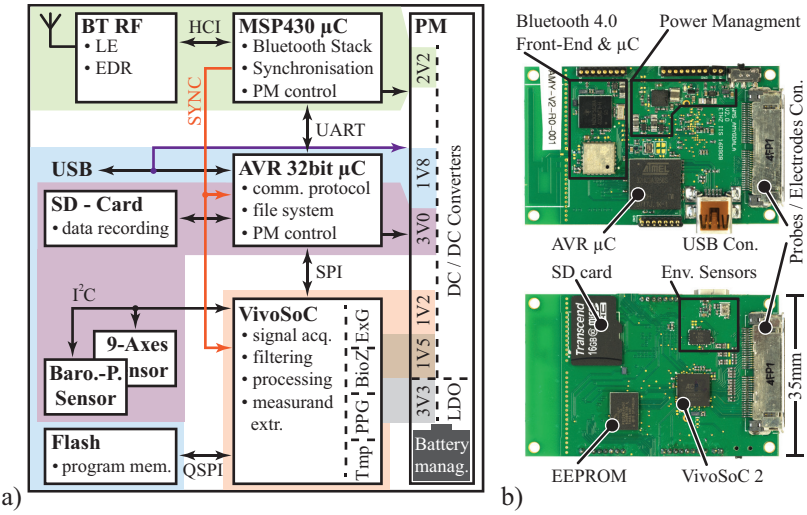

Figure 5.4: Block diagram (a) and PCB photographs (b) of the matchbox sized wearable platform demonstrator based on *VivoSoC 2*.

no standing connection, e.g., sensor nodes which occasionally transmit single measurement values. In contrast, continuous connection is foreseen for the classic *Bluetooth* modes, well-suited for data streaming. Our prototype is usually in low-energy mode in which it periodically advertises and when connected to by a tablet computer exchanges device information and receives commands. When however high data rate is required to provide a live preview of recorded physiological signals, the device switches to EDR.

Besides the *Bluetooth* stack, the *MSP430* MCU further hosts code for power management and the synchronisation of multiple recording platforms – a key prerequisite for body sensor networks – by broadcasting time-stamps in BLE advertising mode from a master device to one or multiple slaves. Experimental verification showed that synchronisation errors below 2 ms can be achieved, corresponding to less than a sample period when considering that sampling rates for typical ECG or pulse oximetry recordings are in the low hundreds of Hertz.

5.3 Miur: A Neural Interface ASIC

Miur is a ASIC designed for implants addressing the study of visceral and peripheral neural pathways [180], i.e., for further development of the implantable system presented later in Sec. 6.2. Such implantable medical instrumentation provides clinical researchers tools for improving the understanding of living objects, e.g., in long-term experiments with freely moving animals. The need for miniaturisation is obvious for implantable telemetry systems (Chap. 6) when considering that most experiments are conducted with rodents.

The *Miur* chip[2] features eight ExG channels intended for neural activity recording, a six-channel neural stimulation hardware and an on-chip temperature sensor as illustrated in the block diagram in Fig. 5.5. The latter offers two auxiliary inputs for the use of more accurate external sensing components. Both, the ExG AFE and the temperature sensor are inherited from the original *Cerebro* design reported in [171].

The ExG AFEs consist of a chopper-stabilised instrumentation amplifier (IA) [181] followed by a low-pass filter with configurable bandwidth between 3.2 kHz and 12.8 kHz. The eight front-ends share a common 14 bit SAR ADC [106] which supports sampling rates of up to 25.6 kHz per channel. Neural signals usually consist of trains of (compound) action potentials. These are sharp pulses with durations well below 1 ms [182–184]. Acquisition bandwidths of 10 kHz [54] and above are thus required – exceeding the bandwidth of ExG signals by far.

The contact between electrode and tissue is a metal-to-electrolyte interface which results in the superposition of a DC half-cell potential to the biomedical signal [54]. This offset can exceed the signal of interest for up to four orders of magnitude and is time-varying due to changes in the electrode-to-tissue interface. Usually this manifests in a slow drift, however abrupt changes due to pressure or motion can cause relatively fast offset-changes. Traditionally, AC-coupling is used to prevent saturation of the AFE, requiring large (off-chip) capacitors which prevent miniaturisation. Alternatively, the DC-offset

[2]The hardware description includes eventual improvements that have been implemented later while transferring the circuitry to *VivoSoC 2*.

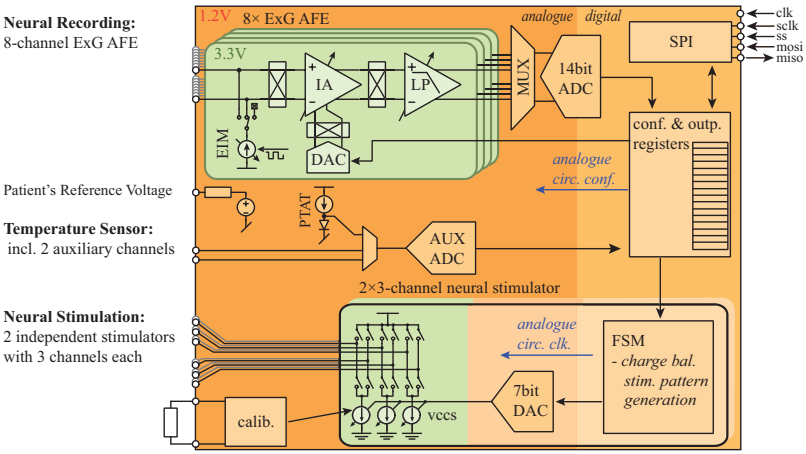

Figure 5.5: Block diagram of the *Miur* neural stimulation and recording ASIC.

is subtracted by means of a DAC from the input signal prior to amplification [185, 186]. The offset tracking and DAC regulation is performed on a MCU – in case of *VivoSoC 2* on the on-chip PULP cluster.

The AFE of each channel further includes an electrode impedance measurement (EIM) circuit for poor electrode contact detection by the injection of a weak current (100 pA – 110 nA) which is square-wave modulated at a near-Nyquist frequency to ease the removal of the superimposed waveform from the biological signal.

5.3.1 Neural Stimulation

Extracellular Neural Stimulation

The resting transmembrane potential of a neuron is ca. −70 mV [187]. A depolarisation of this potential above a certain threshold potential (ca. −55 mV) initiates an *action potential* – a short local voltage impulse. The currents induced by the latter can cause depolarisation of neighbouring membrane and thus trigger action potentials there. Repetition of this process results in the propagation of the impulse

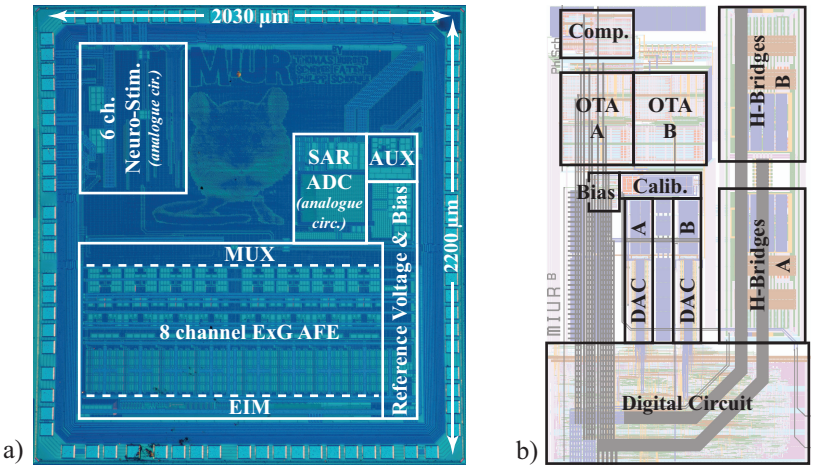

Figure 5.6: *Miur* micrograph (a) with area distribution marked for the main analogue sub-circuits and layout (b) of the stimulation circuit as implemented on *VivoSoC 2*.

along the axon.

As illustrated in Fig. 5.7a, a current applied through an extracellular electrode causes local depolarisation at the cathode and hyperpolarisation at the anode (with adjacent weakly depolarised regions) [188] which can trigger action potentials. Depending on the electrode design, electrical stimulation can cause bidirectional or unidirectional propagation of the action potential [189, 190]. Charge transfer from the electrode to the tissue occurs by the capacitative electrode-tissue interface and through electron transfer across the surface [191] by reduction-oxidation (redox) reactions. These can be irreversible or reversible [192]. The former cause corosion of the electrodes and potentially damage both, the electrodes and surrounding tissue. The right choice of electrode material and low charge density limit corosion. Reversible reactions do neither damage tissue nor electrodes if charge injection into the electrodes is balanced [191, 193]. Charge balancing is achieved by current-controlled biphasic stimulation waveforms with zero net charge transfer. Additional passive or active charge balancing circuitry [194,195] can improve the precision of the charge balance and

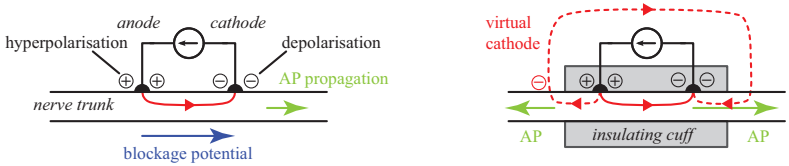

a) b)

Figure 5.7: In an ideal scenario (a) all stimulation current flows through the nerve trunk. The longitudinal differential electrodes voltage blocks action potential (AP) propagation in one direction. In a realistic scenario (b) with an insulating cuff, a fraction of the stimulation current flows as leakage exterior to the cuff causing a virtual cathode exciting an AP propagating in the opposite direction. *According to [189].*

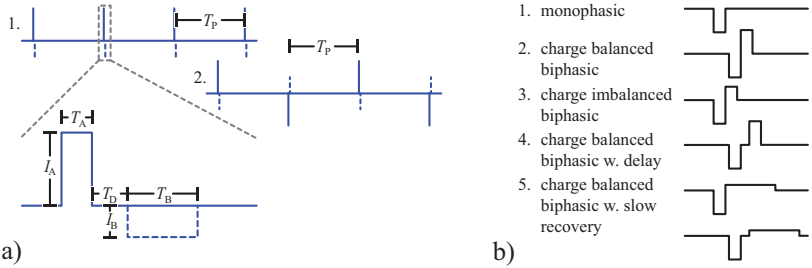

a) b)

Figure 5.8: Stimulation current pulse waveform configurability (a) and classification of possible pulse-types (b) according to [192].

increase long-term stability of an electrode-nerve interface.
Neural activity can be blocked by electrical stimulation at frequencies in the range of $5-20\,\mathrm{kHz}$ by two distinct mechanisms [196]: endplate depletion block due to an over-excitation of a motor neuron, and local action potential transmission blockage due to inhibited recovery of the sodium channels in the axon membrane.

Multi-Channel Neural Stimulator

The six-channel neural stimulator in *Miur* and *VivoSoC 2* is based on the analogue circuitry of *TMA-O's* LED driver (Fig. 4.33). Lower current densities allow for higher on-resistances in the H-bridges: three sub-channels share the circuit area previously occupied by a single LED H-bridge. The sense resistors are configurable between 30 Ω and 300 Ω which translates to full-scale currents ranging from 1 mA to 20 mA. The technology conditioned voltage limitation to 3.3 V would however require very low electrode impedance to exploit this range.
For simultaneous low-frequency stimulation and high-frequency blockage, the stimulator comprises two independent instances of the current regulation loop and the digital FSM circuitry – marked in Fig. 5.6b as channels *A* and *B*. Current calibration circuitry is shared and allows independent calibration for each of the six sub-channels.
As illustrated in Fig. 5.8a, the generated waveform of the *Miur* stimulator generally consists of a first stimulation pulse, a dead time, and an optional second pulse for charge balancing. All parameters can be configured with low granularity: amplitudes are defined by a 7 bit DAC, time period granulation is ca.[3] 1 µs. The circuit is able to generate all the commonly used waveforms shown in Fig. 5.8b. Given varying merits in efficacy, safety, and electrode corrosion for the different waveforms [192], optimum pattern selection is an application-specific trade-off. Stimulation frequency and duration are configured by the time period T_P inbetween two pulses and the pulse count, respectively. Multiple sub-channels can be used simultaneously if stimulation frequency is equal or a low integer multiple.
In general, pulse polarity matters since strong depolarisation and thus action potential triggering occurs only at the cathode, while the longitudinal voltage from anode to cathode blocks the propagation of an action potential in the direction from cathode to anode [189]. This can be used to ensure unidirectional propagation of the impulse. In a simple differential cuff electrode design as used in [197], leakage current flowing from anode to cathode around the cuff results in a virtual cathode at the cuff's edge [189], which triggers a second action potential that can propagate in the opposite direction (Fig. 5.7b). Excitation and propagation is thus independent of the waveform polarity.

[3] depending on the clock frequency & prescaling configuration.

For such applications, the stimulator supports a charge balancing mode in which the polarity of the configured waveform toggles as illustrated in Fig. 5.8a2 to enhance symmetry and thus reduce long-time charge imbalance.

Chapter 6

Implantable Medical Instrumentation

Considerable progress has been made in the past decades in implantable bioelectronics [198–200], driven by the need of neuroscience and medical research for precise and non-obtrusive instrumentation in preclinical research in animal models. The specific demands of individual experiments led to the development of a multitude of single-purpose systems for vital signs monitoring, electrical stimulation, and blocking of nerves as well as the recording of their activity. Each of which furthered knowledge in its respective field. More recently, the rise of optogenetics created a demand for optical neural interface devices.
Besides brain research which recently gets a lot of attention in both, the scientific community and popular science, there is also continuing high interest in interfacing visceral and peripheral nerves [201, 202] as well as the spinal cord [203, 204]. The aim is a better understanding of the neurophysiological mechanisms but also towards restoring impaired functions by establishing uni- or bidirectional interfaces between nerves and electronics. Motor and sensory neuroprosthetics include such different applications like bladder control [205], cochlea implants [206], restoration of swallowing [207], and hypertension treatment [208, 209].
Behavioural studies with freely moving animals demand for partially-

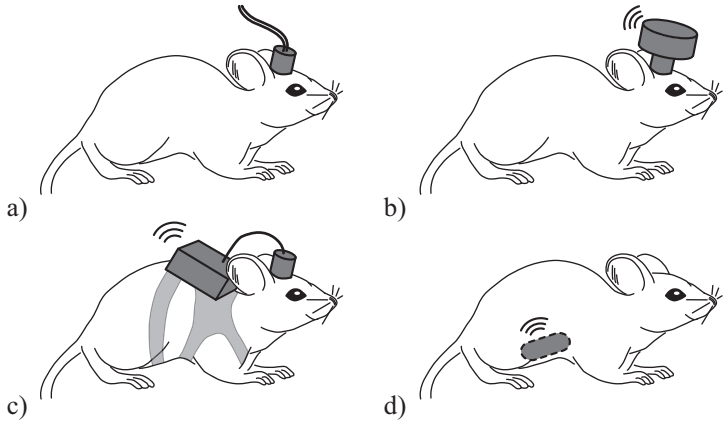

Figure 6.1: Common approaches of (partially) implanted systems for tethered (a) and wireless animal experiments in awake condition coming with different degrees of obtrusion: (b) head-stage, (c) backpack, and (d) fully implanted.

or fully implanted wireless systems. Figure 6.1 gives an overview on the most common approaches for such systems coming with different degrees of obtrusion for the animal. When aiming on an implant for mice and rats, which are the most widely used animals in such studies, small size of the implantable device is a key prerequisite.

In the remainder of this chapter we give first (Sec. 6.1) an outlook on the envisioned platform for nerve stimulation and the acquisition of vital signs and neural signals. Then the results from first steps towards this miniaturised implantable device are reported. The chapter is two-part, discussing preliminary hardware prototypes of fully and partially implantable systems for electrical (Sec. 6.2) and optical (Sec. 6.3) neural signal stimulation and acquisition on the one hand, and implantable PPG-based methods for blood oxygenation and pressure measurements on the other hand (Sec. 6.4). Together these parts describe the vision of a versatile tool for pre-clinical research in form of a highly integrated and miniaturised system that can be fully implanted in laboratory animals for long-term (behavioural) experiments.

6.1 Envisioned Platform for Implants

The comprehensive features of *VivoSoC 2* (Sec. 5.1) allow to build a fairly sophisticated system with only a few additional components and thus enable massive miniaturisation. The block diagram depicted in Fig. 6.2 shows an envisioned minimal platform for implants in rodents. Besides our SoC, it comprises a large flash memory chip, a power- and battery management IC and a BLE SoC. The latter hosts the *Bluetooth* stack and handles the communication to the base station. Using BLE for the wireless link instead of a proprietary protocol allows for the use of an off-the-shelf *Android* tablet computer running a proprietary software as base station. Using such a prevalent and cheap portable commercial device makes handling in the field more convenient and the distribution of the system simpler.

The incorporation of ExG, PPG, electrical stimulation, and temperature measurement AFEs in the SoC allows to cover a variety of functions with the same hardware. As illustrated in Fig. 6.2 those include subcutaneous ECG [210] and neural activity recording by the ExG front-end, electrical neural stimulation (Sec. 5.3.1), optical neural stimulation (Sec. 6.3) using the LED driver of the PPG front-end, and various PPG-based measurements including blood oxygenation and -pressure as further discussed in Sec. 6.4.

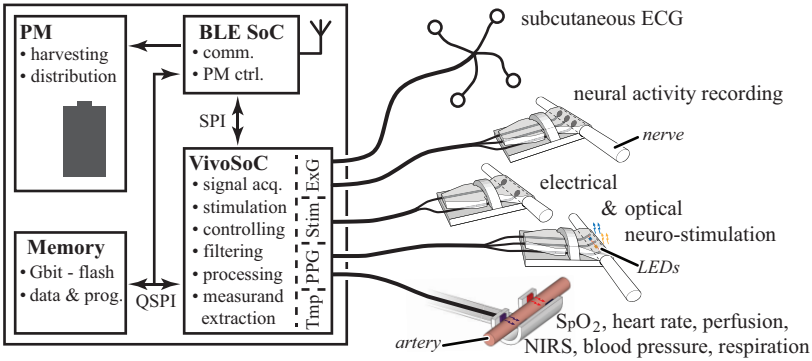

Figure 6.2: Block diagram of the planned miniaturised platform for implants in rodents and the functions covered by it.

Different embodiments of the hardware, i.e., realisations incorporating a different subset of the provided functionality, require some adaptations of the PCB layout for the interconnection of electrodes and probes, its core design however remains.

The platform conception is pursued not only for the design of the hardware, but equally important also in firm- and software design. Due to positive experiences made with the device definition file (DDF) concept in our modular development and evaluation platform – reported in [179] – we incorporate some of the ideas also in the miniaturised platform. It is built on the principle to reuse software code wherever possible. The main advantage of which is reduced maintenance work when different platform embodiments are supported simultaneously. The same *Android* user interface software (UIS) is used for all embodiments, independent of the functionality provided for a specific use-case. The actual device configuration is read by the UIS upon connection and its graphical user interface (GUI) adapts to it. The *VivoSoC* firmware is two-part as illustrated in Fig. 6.3: A common software base provides low-level drivers to interface AFEs and digital peripherals, mid-level AFE specific driver functions, e.g., for LED current regulation in PPG or offset tracking in ExG, file-system support, and high-level routines for initialisation, interfacing the RF SoC and other shared tasks. A limited and predefined set of functions and constants build the interface between the DDF and the common main software routine. The configuration of the AFEs, peripherals and the GUI are set in the DDF and all signal processing and application-specific control functions are called from within a mandatory DDF function. The algorithm functions themselves are also separated from the device definition and form application libraries, which may be shared by different platform embodiments having some of the supported functionality in common.

The firmware of the BLE SoC is independent of the application-specific embodiment of the platform. Information required on it by the BLE SoC, e.g., for the GUI setup on the tablet computer, is stored together with the *VivoSoC* program code in a shared memory. The shared memory access further enables the wireless connectivity SoC to read data previously stored by *VivoSoC* for transmission, without requiring to power on the latter.

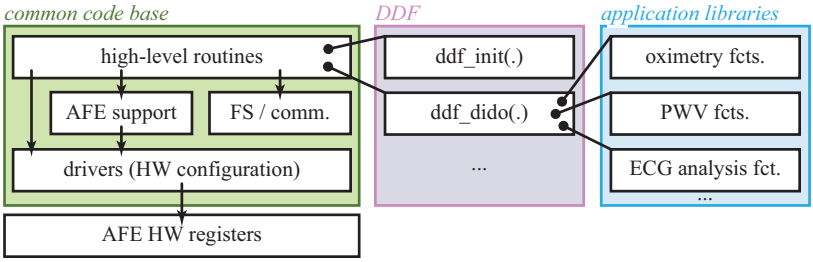

Figure 6.3: Firmware architecture of the envisioned platform with a large common code base and predefined interface functions for application specific definition (DDF).

6.2 Prototype of a Wireless System for Neural Recording and Stimulation

The preliminary prototypeshown in Fig. 6.4 and described in this section is a first step towards this envisioned platform. The implant features three neural recording and two stimulation channels. Including a 3.7 V lithium polymer (LiPo) battery, which lasts for 94 days of standby operation or 18 hours of continuous recording and stimulation, it measures only $13.5 \times 10.5 \times 9.75\,\mathrm{mm}^3$ and weighs 1.7 g. It comes with a wireless link for device configuration and control as well as data transmission.

In difference to other published systems for similar purpose [199, 211–214] our work aims at a fully implantable system which avoids any through skin connectors or cables as in typical head-stage or backpack designs (Fig. 6.1). We expect enhanced acceptance by and mobility of the animal when used in behavioural studies over prolonged time and reduced infection risk by avoidance of any skin openings.

This section is based on P. Schönle et al., "A Wireless System with Stimulation and Recording Capabilities for Interfacing Peripheral Nerves in Rodents," *Annual Int. Conf. of the IEEE Engineering in Medicine and Biology Society (EMBC)*, pp. 4439–4442, Aug. 2016.

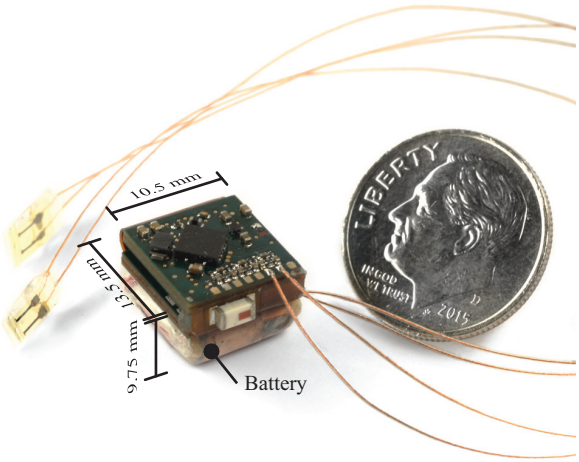

Figure 6.4: Preliminary prototype of a miniaturised system for neural stimulation and nerve activity recording. For size comparison depicted with an US dime, similar in size to a Swiss 50 cent coin.

6.2.1 Miniaturised Electronics

This first prototype preceded the design of the *VivoSoC* (Sec. 5.1) and *Miur* (Sec. 5.3) ASICs. As illustrated by the block diagram in Fig. 6.6, it is based on the commercial BLE SoC *nRF51822* [215] and features the *Cerebro* [106, 171] ExG IC for neural signal acquisition. Three of its channels are connected via discrete band-pass filters to pads on which electrode cables are soldered. The recording bandwidth is limited to 1 kHz by the SoC's performance in reading data from the serial peripheral interface (SPI) and writing it to the memory over the I^2C interface. The use of a discrete band-pass filter instead of *Cerebro's* DC-tracking functionality means less processing and SPI traffic but requires a significant amount of PCB area, as can be seen in Fig. 6.5.
Device size restrictions and the lack of dedicated on-chip hardware for electrical neural stimulation (at that time) means that stimulation hardware is kept minimal: The SoC controls a pair of tri-state level shifters to generate a differential voltage stimulation pattern. Amplitude can be configured in four steps by different combinations of series resistances – there is no current control and charge balance is achieved by inverting the polarity of every other pulse as illustrated in the pulse train in Fig. 5.8a2. Supported are the monophasic (b1) and simple charge-balanced biphasic (b2) waveforms.
Precise temperature sensing is provided with an off-chip negative temperature coefficient (NTC) thermistor and the auxiliary ADC of *Cerebro*, which is also part of *VivoSoC*.

6.2.2 Power Budget Considerations

Power efficiency is crucial for the miniaturisation of electronic hardware. As for our first prototype, about half of the device volume is bound on the battery (Fig. 6.4). In difference to wearable applications (Sec. 5.2) the base station can remain connected to the mains for the given usage scenario of laboratory experiments. The communication between the implant and the tablet computer takes this power budget asymmetry into account: The device is normally in deep-sleep where most of the electronics (including the radio) is shut off, while the tablet is permanently scanning for connectible devices. Experiment

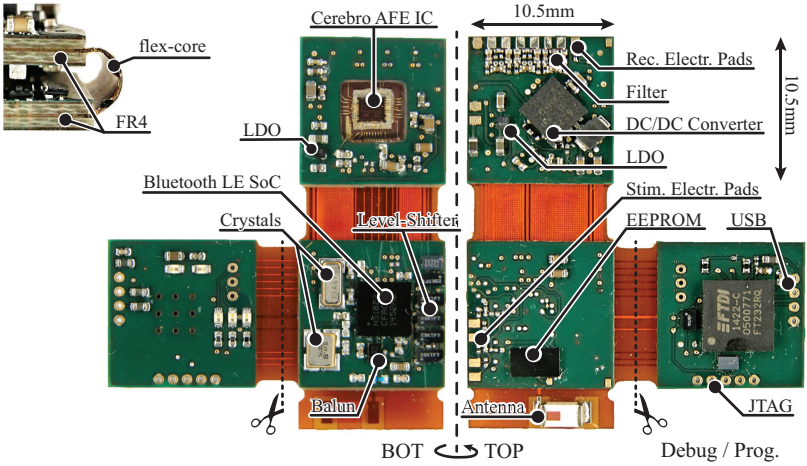

Figure 6.5: Structure of the flex-rigid PCB (top-left) and both sides of the miniaturised electronics prior to folding. The ExG IC *Cerebro* is bonded as bare die in a cavity (later moulded) to reduce the device thickness. The program and debug interface is cut off after programming.

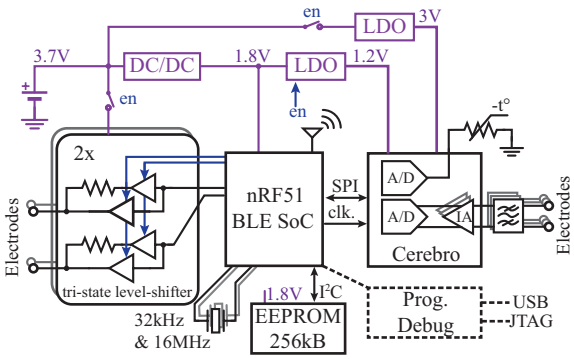

Figure 6.6: Block diagram of the preliminary prototype.

sequences, i.e., time periods during which the device is supposed to record and/or stimulate, are configured in advance with the tablet software. Periodically, the implant establishes a connection to check if a new experiment has been planned. If so, the information is transferred to the device and executed. Such a check takes 5-15 seconds and consumes 1.3 mW of power. An hourly check is considered in the previously stated 94 days of stand-by time.
A sequence consists of an initial sleep period by which the exact experiment start time is set and the configurations for the recording/stimulation period, i.e., its duration, channel selection, recording sample rate, stimulation frequency, etc. During the experiment all recorded data is written to the on-board memory rather than streamed to the base station. This reduces SoC workload and eases guaranteeing data integrity. After the sequence has been executed, the device connects to the tablet again, sends the acquired data and reads (if available) the settings of the next sequence, and goes back in deep sleep mode. This sleep periods can be long, e.g., the next experiment may be planned in two days. Although the experiment sequence configuration is already read by the device, it can still be changed if necessary due to the aforementioned periodic checks.

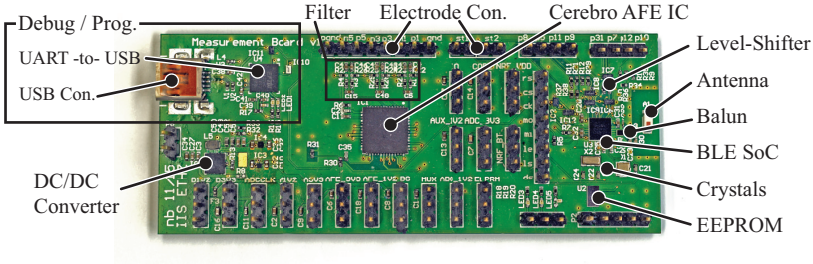

Figure 6.7: A larger-scale version of the circuit in the implant prototype: the same components are used, except for test pins which allow detailed characterisation and ease putting the circuit into operation.

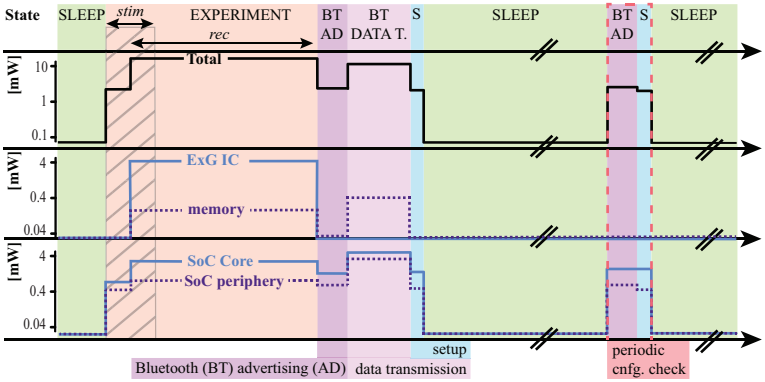

Figure 6.8: Generic experiment program sequence with power consumption indicated for the total and main sub-circuits. The diagram includes a short active phase to check for new configuration. Such phases are executed periodically in long sleep periods to grant accessibility.

6.2.3 Characterisation

Characterisation of the electronics for the implantable device has been done on a larger-scale version thereof with identical components and schematic, except for additional measurement and test points. This version, depicted in Fig. 6.7, allows for the measurement of the power consumed by sub-circuits such as memory, ExG IC, SoC core, and -periphery. Figure 6.8 illustrates total and sub-circuit power consumption in the different operation states and Tbl. 6.1 characterises key features of the system and summarises total power consumption for the most important operation states.

Results & Conclusions

The construction of the here reported preliminary prototype demonstrates the feasibility of a wireless implant small enough to be implanted in laboratory rats. Many of its shortcomings are addressed by the *VivoSoC 2* design:

Table 6.1: Performance Summary

Neural Recording		**Neuron Stimulation**	
# channels:	3	# channels:	2
max. sampling freq.:	1 kHz	min. pulse-width:	100 µs
IR noise (1-100 Hz) [106]:	0.89 μV_{RMS}	max. frequency:	200 Hz
Temperature Recording			
resolution:	0.02 K		
accuracy:	0.9 K		
Power Consumption ($V_{bat} = 3.7$ V)			
sleep:	76 µW	radio, advertising:	3.2 mW
recording:	11 mW	radio, connected:	2.9 mW
stimulating:	3.8 mW	radio, transmission:	9.5 mW

- *Stimulation* of the ADN has been successfully demonstrated in acute experiments, reported in [197], with the minimalistic hardware and simple pulse pattern described. This however does not imply that it is safe to use in long-term experiments since missing current control may result in some charge imbalance and thus tissue damage.
  The electrical stimulation circuit in *VivoSoC 2* allows for precise 7-bit current control and offers various charge-balanced waveforms to choose from.

- *Recording bandwidth* is limited to 1 kS/s by the BLE SoC performance in transferring data from the ExG IC to the memory. The multi-core MCU in *VivoSoC 2* in combination with a fast quad-SPI external memory can easily handle the data stream generated by the revised ExG AFE at its full 25.6 kHz sampling rate.

- *Memory* capacity limits the recording length for the first prototype to ca. two minutes. The use of recently released Gbit low-voltage (1.8 V) flash ICs with quad-SPI will allow up to nearly 3 hours of recording at the highest sampling rate. First such devices [216,217] are available with 1-4 Gbit in a $8{\times}6\,mm^2$ package. Furthermore, considerable on-chip processing bandwidth enables on-the-fly signal analysis and feature extraction which does not only reduce necessary memory capacity but more

importantly also reduces radio transmission time and thus power consumption: For the PPG-based blood pressure estimation discussed in Sec. 6.4 40 kByte/s of raw data are acquired to compute a single 3-digit value per second. RF transmission payload can here be reduced by on-chip processing by a factor of 20,000.

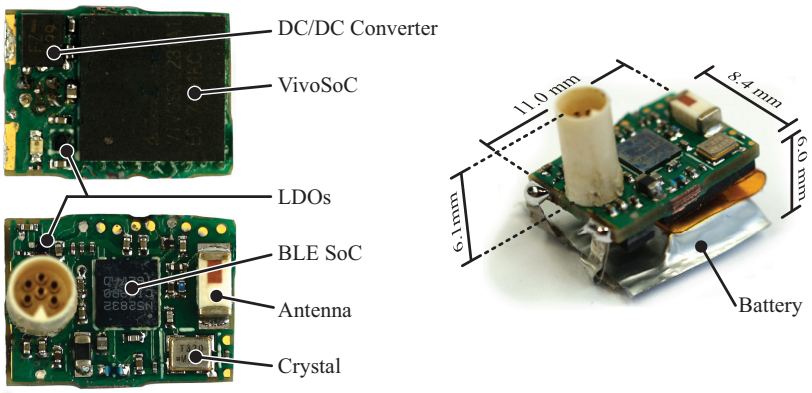

Figure 6.9: Head-stage PCB with components (left) and dimensions (right) indicated.

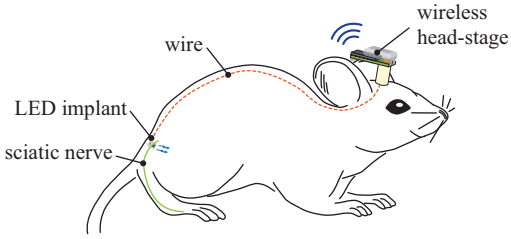

Figure 6.10: Planned experimental setup.

6.3 Optogenetic Stimulation Head-Stage

A first application specific embodiment of the envisioned *VivoSoC 2* based platform described in Sec. 6.1 is the wireless optogenetic stimulation head-stage depicted in Fig. 6.9. It is designed for an experiment which aims at the optogenetic stimulation of the sciatic nerve in freely moving mice.
In optogenetics [218], a transgene is delivered by means of a genetically modified virus to the targeted nerve. Here, opsins – light-sensitive proteins – are expressed and populate the neuron membranes. The most commonly used opsins are channelrhodopsin-2 (ChR2) and Natronomonas pharaonis (NpHR). The former is a cation channel which when activated with blue light causes depolarisation and thus evokes an action potential. The latter is a chloride pump which, when activated by yellow light, leads to hyperpolarisation and thus blocks the propagation of action potentials.
In the given experiment, blue LEDs are implanted directly at the sciatic nerve and electrically connected to a head-plug in which our miniaturised head-stage is plugged during experiments as illustrated in Fig. 6.10. In previous work [219, 220] optical waveguides and an external LED or laser light source were used, but more recently the direct implantation of the light source gets more popular [221–223].
The system comprises the commercial *nRF52832* [224] BLE SoC, the *VivoSoC 2* IC, a 12 mAh LiPo battery as well as a DC/DC converter and some LDOs for supply distribution. Since no recording is required in this application, the flash memory chip is omitted. *VivoSoC 2* is programmed by the *nRF52* BLE SoC at start-up.
Of all the functionality offered by *VivoSoC 2* only the LED driver of the *TMA-O* PPG circuit is used in this application. Two driving channels are connected to the plug and can generate current controlled pulses of 3-20 ms LED on-time, either as single pulses or as pulse trains with 1-20 Hz pulse repetition frequency (PRF) – remotely configured and controlled by an *Android* tablet computer. The head-stage can be plugged on a dedicated charging PCB by which it is activated before an experiment and shut-off thereafter. Extension of the device with electrical and optical data acquisition capability for combined stimulation and recording experiments [221, 225, 226] would require the addition of a memory chip adding ca. 1 mm to the device height.

Prior to silicone encapsulation, the device weighs 0.84 g including the battery and measures only $8.4 \times 11.0 \times 6.0\,\mathrm{mm}^3$ which is smaller and lighter than previously published work [220, 223] for similar purpose.

6.4 Implantable Oxygenation and Blood Pressure Measurement

Although PPG and NIRS are widely used as non-invasive means to measure oxygenation, tissue perfusion, or pulse transit time (PTT), there is only little previous work on implantable PPG and NIRS devices. An elastic silicone cuff PPG probe to be wrapped around a blood vessel is reported in [227, 228] (without the corresponding electronics) and proposed for long-term monitoring in high-risk cardiovascular patients. Other work envisions a PPG and NIRS based implantable system for real-time monitoring of organ perfusion following transplantation [229,230]. This work includes acute animal experiments with a preliminary prototype of a telemetric system, which however lacks sufficient miniaturisation for long-term implantation. Finally, a combined electrocorticography (ECoG) and NIRS probe for the recording of cortical activity is reported in [231] for subdural implantation in laboratory animals. Reported acute experiments in this work were done with bench instrumentation.
For pre-clinical cardiovascular research, the monitoring of blood pressure and arterial blood oxygenation in long-term animal experiments is desirable. The combination of neural stimulation, nerve activity recording, and PPG-based measurements of oxygenation and blood pressure with a single miniaturised device would be a priceless tool especially in ongoing hypertension research on blood pressure control by stimulation of baroreflex nerves [209, 232].

6.4.1 Acute Animal Experiments

The propagation speed of the arterial pressure wave, i.e., the pulse wave velocity (PWV), is a function of the arterial wall compliance and the arterial blood pressure, as discussed in detail in Chap. 3. The main difficulty in computing blood pressure from measured PWV or

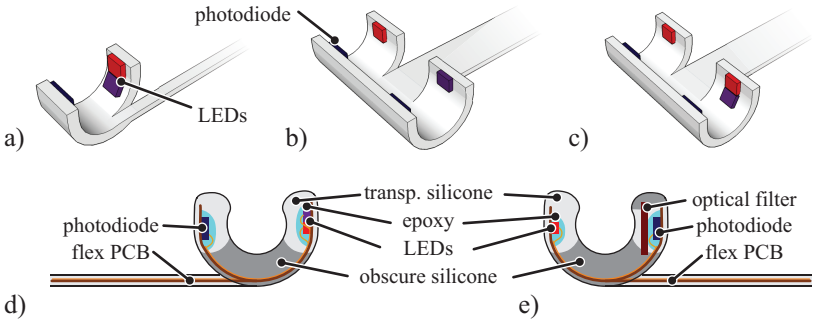

Figure 6.11: Probes to measure (a) S_pO_2, (b) PWV and (c) the combination of both on the exposed artery in acute animal experiments. (d,e) Cross sections thereof.

PTT is vasomotion (Sec. 3.2.3), i.e., the modulation of the overall compliance by muscular arteries. By measuring the PWV on the elastic trunk of the arterial tree, this problem can be overcome.

Probes and Measurement Setup

In Fig. 6.11 the designs of different PPG probes for acute experiments on an exposed artery are illustrated. The probes are based on a flex-PCB substrate on which bare-die LEDs [233,234] and photodiodes [124] are mounted. A rigid and transparent epoxy encapsulation protects the bond-wire from shear forces whereas an outer layer of silicone ensures a soft contact with the artery and tissue. Obscure silicone is used to block direct light paths between LED and photodiode. The open half-pipe shape allows for some adaptation on the vessel size and eases handling in acute experiments – given the lack of any means for fixation it is however not suited for long-term implantation. A design similar to the one reported in [227] might be envisaged for such purpose.
For PWV measurement, we use a probe with two LED-photodiode pairs (Fig. 6.11b) separated by 5-8 mm. The PWV is found as the inverse of the observed delay between the PPG signals measured at the two points. For typical PWV values in the order of 10 $\frac{\mathrm{m}}{\mathrm{s}}$ [72] the

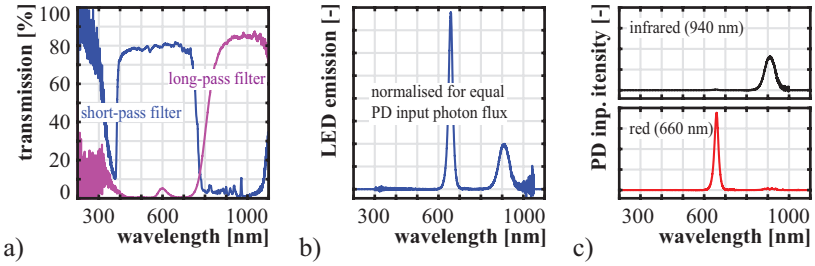

Figure 6.12: Transmission measurements (a) of the optical filters used in the PWV probe and resulting separation (c) assuming an incident equal-flux two-wavelength LED emission (b). The interfering components are suppressed by 40 dB/27 dB (long/short-pass).

recorded waveforms are temporally separated by as little as 0.5 ms which thus requires high sampling rates to be resolved accurately. For an optimum data situation in preliminary acute experiments, the sampling rate was thus maximised by using two synchronously running *TMA-O* chips with 20 kS/s each. To avoid optical cross-talk between the two channels, LEDs of two different wavelengths (660 nm/ 940 nm) are used in combination with optical filters mounted in front of the photodiodes as illustrated in Fig. 6.11e. A 150 µm thin *3M CCF500* short-pass filter foil is used to block infrared light in the 660 nm light barrier. As long-pass filter in the 940 nm barrier serves an overexposed and developed 35 mm photographic negative colour film (*Kodak GOLD ISO200*). Transmission spectra for both filters have been measured with an *Ocean Optics HR4000* high-resolution spectrometer and are shown in Fig. 6.12a. The suppression of the interfering LED emission is 40 dB (long-pass) and 27 dB (short-pass) and illustrated in Fig. 6.12c for an input illumination with equal photon flux at both wavelengths.

Although the PWV probe includes both wavelengths used in pulse oximetry, acute experiments have shown that it cannot be used for accurate blood oxygenation estimation. As discussed in Sec. 2.4, the ratio-of-ratios $\Re$ calculation is insensitive to DC transmission components only if they have the same provenance, i.e., the light travels on the same path from LED to photodiode. For S_pO_2 measurement, the

two LEDs should be placed as close together as possible, as illustrated in Fig. 6.11a.
Simultaneous PPG acquisition gets the maximum data rate but comes with the price of a more complex probe design and the need for two *TMA-O* chips or at least two of it's TIA receivers. However, an evaluation based on the data acquired with two chips revealed that virtually no performance degradation is to be expected for an interleaved 2×10 kS/s sampling scheme if the (a priori known) delay between the sampling points is accounted for and interpolation is applied to reduce granularity for the extracted waveform shift. The kind reader perceives that high sampling rate is employed not due to high signal bandwidth but to resolve the temporal shift of the two recorded waveforms.
For interleaved – i.e., time multiplexed – sampling, optical cross-talk cannot occur and thus optical filters are omitted. A combined PWV and S_pO_2 probe can thus be constructed as illustrated in Fig. 6.11c: two red LEDs form the light barriers for PWV measurement while a third, infrared, LED adds S_pO_2 functionality.
An alternative approach for the estimation of PWV is the measurement of the PTT, i.e., the time difference between the R-peak of an ECG recording and the systolic edge of the PPG waveform. This method allows for a smaller probe and comes with the advantage of a longer distance (heart-to-probe) and thus lower granulation at equal sampling rate. However, the exact distance is difficult to assess and may vary due to probe displacement.

Acute Experiments

A series of acute experiments on anaesthetised Wistar rats were performed to assess the feasibility of both, PWV based blood pressure (BP) estimation and implanted S_pO_2 measured directly on an artery. Figure 6.13 illustrates the experimental setup. A catheter is placed on the right carotid artery and connected to a calibrated pressure transducer to record a blood pressure reference signal. The PPG probe is placed on the exposed left carotid artery and a bipolar *CorTec* micro cuff sling electrode interfaces the aortic depressor nerve (ADN). The electrodes are connected to a stimulation device based on the *Miur* chip (Sec. 5.3). Blood pressure drops when stimulating the ADN

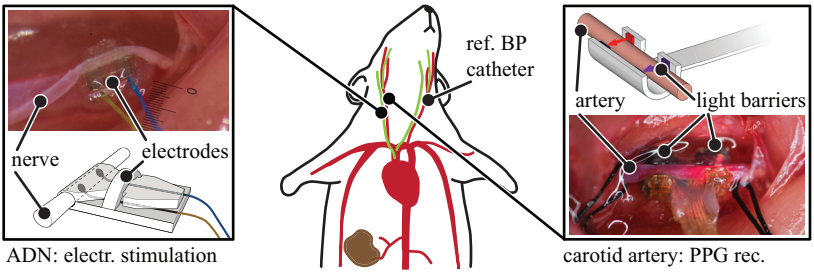

Figure 6.13: Experimental setup for PWV based BP measurement assessment. Electrical stimulation of the ADN allows to induce a controlled drop in blood pressure and thus PWV which is observed in the recorded PPG signals. Reference BP is recorded with a catheter.

and slowly recovers to its natural value afterwards. Figure 6.14a shows raw and analysed data of such an experiment. The pressure drop reduces light absorption and is thus already visible in the raw data – absorption itself is however highly dependent on the probe placement and non-linear – thus not suited for blood pressure measurement on its own. The extracted foot-to-foot (measured at 3% of normalised amplitude) temporal shift ΔT of the recorded PPG signals (averaged over 10 heart beats) increases from 0.5 ms to 1.0 ms as the blood pressure drops from 120 mmHg to 85 mmHg. The light-barriers – of the probe used in this specific experiment – are separated for 5 mm; the measured ΔT thus correspond to pressure wave velocities ranging between 10 $\frac{\mathrm{m}}{\mathrm{s}}$ and 5 $\frac{\mathrm{m}}{\mathrm{s}}$.

The lowest graph in Fig. 6.14a shows the reference mean BP and the BP estimation based on the PWV measurement. The estimation is based on a linear correlation of computed PWV to measured reference blood pressure. As described in Sec. 3.2.2, PWV was found to depend on both, blood pressure and heart rate. Usually, this aggravates discrimination of the two effects. For the shown measurement however, heart rate was constantly 360 BPM during the whole blood pressure recovery period. When the independent effects of heart rate and blood pressure on the PWV are known, the BP estimation can be

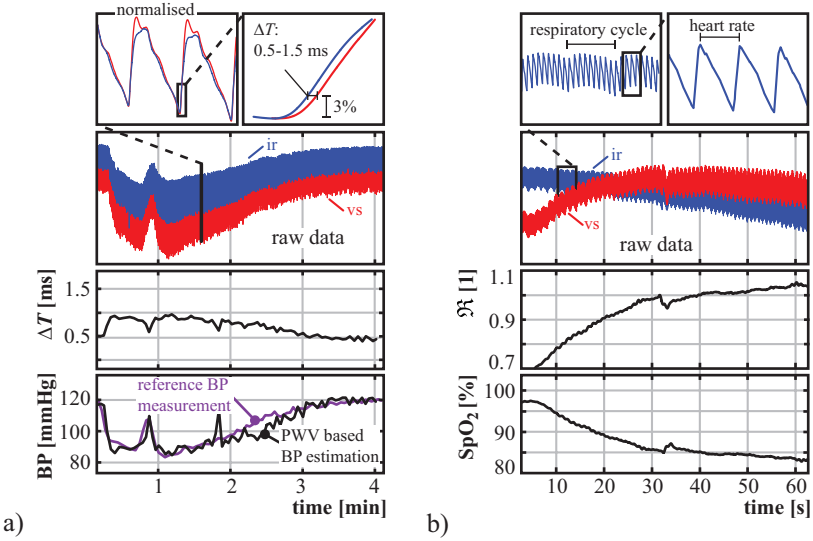

Figure 6.14: Raw (absorption) data and thereof computed blood pressure (a) and S_pO_2 (b) values. The insets illustrate the determination of the wave travel time ΔT (a), respiratory cycle and heart rate (b).

corrected for heart rate since the latter is available from the same PPG recording.

It shall be noted here that follow-up experiments did show worse correlation between blood pressure and PWV than was observed in the one shown in Fig. 6.14a; possibly due to a strong physiological reaction of the arterial system to the artificially induced blood pressure drop. The acute experiments demonstrated the importance of proper probe placement and a thin probe design to avoid bending of the artery at the edges which can cause wave reflections and thus distort the PPG signal. Recent advances in the design of LED implants for optogenetics [235] and in flexible organic optoelectronics [236] however demonstrate solutions therefore.

The setup for the acute experiments on anaesthetised rats (Fig. 6.15) includes a gas mixture control apparatus with which the oxygen concentration of the supplied ventilation gas mixture can be adjusted

precisely between 10% and 21%. This allows to induce controlled hypoxia resulting in stable arterial oxygenation levels, which enables calibration against blood samples taken from the catheterised right carotid artery and analysed with an *i-STAT 1* blood-gas analyser with *CG4* cartridges. For quick recovery of the animal one inlet of the gas mixture apparatus can be switched to pure oxygen, extending the range of configurable oxygen concentrations to 10...100% at the cost of lower precision.
Recorded PPG signals, computed ratio-of-ratios $\Re$, and $S_\mathrm{p}O_2$ values for an experiment, at the beginning of which the oxygen concentration of the ventilation gas is reduced, is depicted in Fig. 6.14b. In comparison to tissue PPG, the signals recorded directly on the artery have a considerably higher modulation ratio AC/DC of ca. 20%. As discussed in Sec. 3.3.2, blood pressure is modulated with respiration – the resulting modulation in light absorption can be observed in the PPG signals.

Conclusions

Implantable PPG is a promising method for the acquisition of heart rate, respiratory cycle, $S_\mathrm{p}O_2$, and blood pressure with a single probe in long-term animal studies. The current state-of-the-art for continuous blood pressure monitoring in conscious and freely moving rodents requires the insertion of a fluid-filled catheter into an artery which connects to a pressure transducer. The latter can be external (tethered head-stage connection) [237] or fully-implantable [238]. The implantation of the catheter is a rather invasive operation and potentially causes blood clotting. Less invasive implantable but extravascular blood pressure measurement approaches have been reported: In [228] a strain-gauge is wrapped around an artery while the attachment of two accelerometers on the arterial wall was proposed in [239] for a PWV based BP estimation. Both systems aim at arteries of larger animals (pig/rabbit) and especially for the second approach adaptation for rodents seems difficult. An impressive but mechanically complex implantable system for laboratory mice based on a capacitive MEMS pressure sensor is reported in [240]: A silicone cuff including the MEMS and readout chips is clamped on the artery, silicone oil couples arterial pressure and sensor.

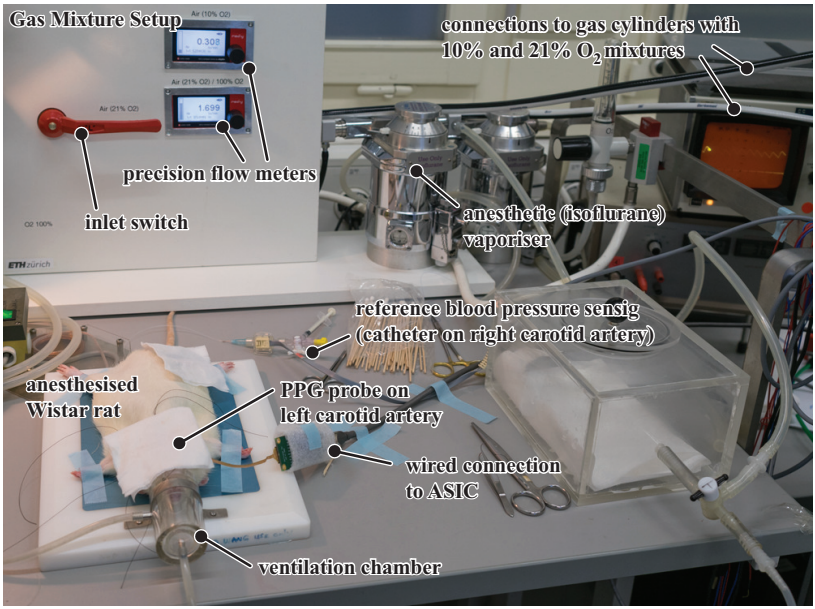

Figure 6.15: Setup for acute S_pO_2 experiments.

Implantable PPG based blood pressure estimation has the advantage of a much simpler mechanical probe design than [240], consisting solely of two LEDs and photodiodes. Given the determination of the PWV based on the foot-to-foot temporal shift of the waveforms, it is a measure for diastolic blood pressure only (although often correlated to the mean blood pressure, as in Fig. 6.14a), while pressure transducer based systems can trace the whole pressure waveform and thus also systolic pressure is measured.

Chapter 7

Conclusions & Outlook

Emerging applications in mobile health as well as in clinical and preclinical research require miniaturised and low-cost instrumentation in a variety of applications ranging from portable apparatuses to wearable- and implantable telemetry systems. Many of the envisioned scenarios require – or profit from – the simultaneous acquisition of different physiological signals and measurands, demanding a multi-biosensor SoC.

The evolution of numerous spectrophotometry and PPG based monitoring and imaging techniques makes the PPG front-end a key component of such a SoC, which enables it to cover a wide variety of applications ranging from cerebral activity imaging and organ tissue perfusion assessment to common pulse oximetry and heart-rate monitoring. The convenience and non-invasive nature of the optical tissue interface greatly helped the acceptance and spread of these methods – both, in monitoring particularly vulnerable patients such as neonates and in consumer applications such as sport watches and activity trackers, where wearing comfort is crucial. However, this comes at the cost of considerable current demand for tissue illumination which can outweigh SoC core power and be on a par with RF front-end consumption. A PPG analogue front-end with emphasis on low (overall) power consumption is thus of uttermost importance.

The multitude of targeted applications and differences in physiology and health condition of individual users demand a high degree of

adaptability in order to optimally trade noise, bandwidth, and ambient interference suppression against power, and to support different measurement setups with spectral- or spatial diversity.
The present thesis reports design considerations for – and the implementation of – a power efficient multi-purpose PPG AFE which was taped out both, as single-chip and integrated in a multi-biosensor system-on-chip. Further emphasis is given on the development of demonstration prototypes for both, wearable and implantable, telemetry systems and the presentation of a novel PPG-based method for long-term blood pressure monitoring in small laboratory animals. In the following, key findings are highlighted, conclusions drawn, and an outlook is given on possible future improvements and pending work.

7.1 PPG Front-End

The thorough study of PPG on system- and circuit level allows for the conclusion that:

- Photodiode shot noise limits in a real-world application the dynamic range for state-of-the-art PPG receiver circuits.
- Power can be traded against noise-bandwidth and pulse repetition frequency which enables agile adaptability on signal quality requirements: The loop dynamic range[1] of our front-end can be selected between 88 dB and 109 dB for PRFs ranging from 100 Hz to 10 kHz. Power efficiency is limited by the product of LED pulse duration and receiver bandwidth. A figure-of-merit is introduced with which the power-efficiency of PPG ASICs can be compared regardless of different assumptions for operating conditions, signal bandwidth, and PRF.
- The relatively low receiver bandwidth allows to effectively curb amplifier excess noise as well as thermal- and quantisation noise in the ADC – enabling an area-efficient low-noise receiver implementation.
- Incomplete settling of the receiver TIA is possible without sacrificing linearity. In combination with low receiver noise, this

[1] 20 Hz bandwidth.

allows for 68% lower power consumption for equal loop DR and PRF in comparison to the state-of-the-art.

- Shorter settling time also enhances ambient light resilience. In-band interference rejection of 50 dB was measured for the presented chip, while a highly adjustable PRF enables the avoidance of out-of-band interferer.

7.2 Prototype Systems

Work on first prototype systems based on our ASICs have demonstrated that:

- Sub-cm^3 devices for fully- or partially implanted telemetry systems for animal experiments with rodents are feasible. Such a system can offer the acquisition of a comprehensive set of physiological signals and vital signs as well as multiple electrical and optical stimulation channels. On-chip processing is a key prerequisite for signal analysis and measurand extraction and can allow to massively reduced the data volume that needs to be transmitted over the wireless link.

- The bill-of-materials and power consumption for wearable medical instrumentation can be greatly reduced which in turn allows for a small form factor.

- Firmware and software maintenance is reduced by a common code base for all embodiments of the hardware platform and a modular, general-purpose implementation of the user interface software.

- Synchronisation of multiple devices with *Bluetooth* low-energy is possible with reasonable accuracy. This is a key prerequisite for body sensor networks.

7.3 Implantable S_pO_2 and BP Monitoring

The results of a series of acute experiments on anaesthetised Wistar rats let us conclude that:

- Implantable PPG is a promising method for the acquisition of heart rate, respiratory cycle, S_pO_2, and blood pressure for long-term studies with animal models.
- The proposed optical probe on the carotid artery is mechanically simple and less invasive than the current state-of-the-art for blood pressure monitoring which is based on fluid-filled catheters for pressure coupling to a transducer.

7.4 Outlook and Future Work

The PPG front-end reported in this thesis outperforms concurring ASICs in terms of energy efficiency. As the established FoM-limit demonstrates, further advances would require to overcome the linkage of signal-referred receiver bandwidth and receiver amplifier settling time for pulsed inputs.
A fair bit of work still impends on the system level regarding the development of wearable and implantable platforms based on the *VivoSoC* chip. Power management and distribution in our first prototypes still involves numerous components and significant PCB wiring. Centralised power management offering multiple DC/DC converters and LDO's as well as energy harvesting and battery charging capabilities in a single separate chip, or even included in the SoC, could be a sensible extension of the hardware platform.
Although the proposed PWV-based blood pressure estimation showed promising results in first acute experiments, more experiments are necessary to obtain conclusive data on inter-animal variability, age dependency, the influence of heart-rate on measured pulse wave velocity, and the compliance stability of elastic arteries. PTT-based estimation could replace the double-light-barrier setup with a single light-barrier and subcutaneous ECG electrodes. This would allow for smaller arterial probes, easing implantation and allow the use in smaller laboratory animals like mice. Also, probes for long-term implantation need to be designed.

Appendix A

Mathematical Derivations

A.1 TIA Input Current in NIRS

In order to reach deeper lying tissue, the emitter and detector optoelectronic components are further separated in NIRS probes (30-40 mm) than in reflective pulse oximetry probes (5-8 mm). The absorption probability of a photon increases exponentially with its pathlength and thus transmittance rapidly decreases.
At a given wavelength, incident intensity on the photodiode is for a setup i according to [241] given by

$$\mathcal{I}_i = \mathcal{I}_0 \; e^{-\Sigma_{\text{eff}} d_i DPF_i + G_i}, \tag{A.1}$$

with d_i denoting the emitter-detector separation, DPF_i the *differential pathlength factor*, and G_i a constant that takes into account the probe geometry. The effective absorption coefficient Σ_{eff} is according to [242] ca. 0.02 1/mm, while [241] reports that the DPF ranges from five to seven.
From (A.1) follows that the relation between the transmission for two different pathlengths is given by

$$\frac{\mathcal{I}_2}{\mathcal{I}_0} = \frac{\mathcal{I}_1}{\mathcal{I}_0} \; e^{-\Sigma_{\text{eff}} DPF (d_2 - d_1)} \tag{A.2}$$

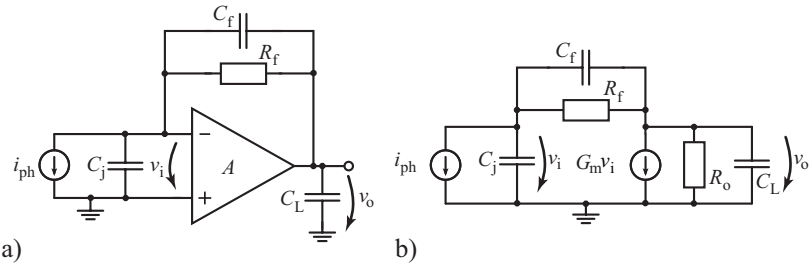

Figure A.1: RTIA circuit (a) and small-signal equivalent assuming an ideal OTA as amplifier (b). The photodiode is modelled as ideal current source connected in parallel to the junction capacitance C_j.

when assuming same geometry and DPF in both setups. For the above stated ranges of emitter-detector separation, we find that the light intensity incident to the detector is for equal transmitter strength 15 to 65 times lower for NIRS probes compared to reflective pulse oximetry.

A.2 RTIA Input Offset

A.2.1 Single-Stage OTA

In this section, a short analysis of the effect a constant input current has in a RTIA circuit on the amplifier input voltage is given first assuming an OTA and later for when a two-stage amplifier is used instead.
The small-signal equivalent circuit is given in Fig. A.1 (b). Kirchhoff's current law (KCL) states that:

$$0 = i_{ph} + v_i \cdot sC_j + (v_i - v_o)\left(\frac{1}{R_f} + sC_f\right) \tag{A.3}$$
$$0 = G_m v_i + v_o\left(\frac{1}{R_o} + sC_L\right) + (v_o - v_i)\left(\frac{1}{R_f} + sC_f\right).$$

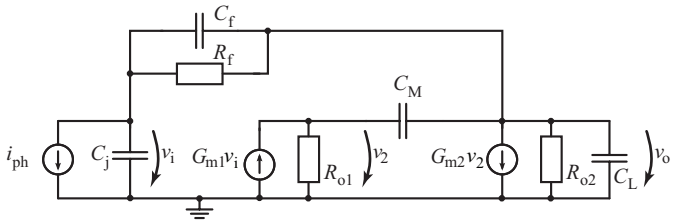

Figure A.2: Small-signal equivalent of the RTIA circuit assuming a Miller OpAmp as amplifier.

At DC, this simplifies to

$$\begin{aligned} v_\mathrm{o} &= v_\mathrm{i} + i_\mathrm{ph} R_\mathrm{f} \\ 0 &= v_\mathrm{i}\left(G_\mathrm{m} - \frac{1}{R_\mathrm{f}}\right) + v_\mathrm{o}\left(\frac{1}{R_\mathrm{o}} + \frac{1}{R_\mathrm{f}}\right). \end{aligned} \tag{A.4}$$

Finally we find

$$v_\mathrm{i} = -i_\mathrm{ph}\frac{R_\mathrm{f} + R_\mathrm{o}}{1 + G_\mathrm{m} R_\mathrm{o}} \approx -\frac{i_\mathrm{ph}}{G_\mathrm{m}} \qquad R_\mathrm{o} \gg R_\mathrm{f}. \tag{A.5}$$

A.2.2 Two-Stage Miller OpAmp

The small-signal equivalent circuit for the RTIA configuration employing an operational amplifier instead of an OTA is given in Fig. A.2. Again, we are interested in the effect of a constant input current i_ph on the circuit's input offset voltage v_i. At DC, the KCL states for $R_\mathrm{o2} \gg R_\mathrm{f}$:

$$\begin{aligned} 0 &= v_\mathrm{o} - v_\mathrm{i} - i_\mathrm{ph} R_\mathrm{f} \\ 0 &= G_\mathrm{m1} v_\mathrm{i} - \frac{v_2}{R_\mathrm{o1}} \\ 0 &= G_\mathrm{m2} v_2 + \frac{v_\mathrm{o}}{R_\mathrm{o2}} + \frac{v_\mathrm{o}}{R_\mathrm{f}} \approx G_\mathrm{m2} v_2 + \frac{v_\mathrm{o}}{R_\mathrm{f}}. \end{aligned} \tag{A.6}$$

We find that

$$v_2 = G_\mathrm{m1} R_\mathrm{o1} v_\mathrm{i}, \tag{A.7}$$

$$v_\mathrm{o} \approx -G_\mathrm{m1} R_\mathrm{o1} G_\mathrm{m2} R_\mathrm{f} v_\mathrm{i}, \tag{A.8}$$

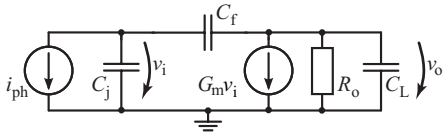

Figure A.3: Small-signal equivalent circuit of a CTIA with an ideal OTA as amplifier.

and finally

$$v_i = -i_{ph} \cdot \frac{R_f}{1 + G_{m1} R_{o1} G_{m2} R_f} \approx -i_{ph} \cdot \frac{1}{G_{m1} R_{o1} G_{m2}} \tag{A.9}$$

The TIA input offset results from limited loop gain which is severely reduced for low R_f in a design employing an OTA. The use of a two-stage amplifier is here beneficial since the gain of the first stage is preserved also for low R_f.

A.3 CTIA Input Offset

A.3.1 Single-Stage OTA

As in RTIA configuration, an input voltage offset is also observed for the CTIA topology if a constant input current i_{ph} is applied. As will be shown in the following analysis, it is caused by the limited transconductance G_m of the OTA rather than loop gain. We assume a CTIA implementation with small-signal equivalent circuit as depicted in Fig. A.3. To discriminate the current induced offset due to limited transconductance G_m from the effect of limited voltage gain, $R_o \to \infty$ is assumed. According to KCL, we get

$$\begin{aligned} 0 &= i_{ph} + v_i \cdot sC_j + (v_i - v_o) \cdot sC_f \\ 0 &= G_m v_i + (v_o - v_i) \cdot sC_f + v_o \cdot sC_L. \end{aligned} \tag{A.10}$$

This can be solved to

$$0 = v_i \left[G_m + s \left((C_j + C_f) \frac{C_L - C_f}{C_f} - C_f \right) \right] + i_{ph} \frac{C_f + C_L}{C_f}, \tag{A.11}$$

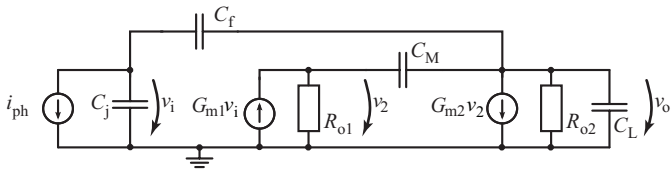

Figure A.4: Small-signal equivalent of the CTIA circuit assuming a Miller OpAmp as amplifier.

which at DC is

$$v_\mathrm{i} = -i_\mathrm{ph}\frac{C_\mathrm{f}+C_\mathrm{L}}{G_\mathrm{m}C_\mathrm{f}}. \tag{A.12}$$

A.3.2 Two-Stage Miller OpAmp

The corresponding small-signal equivalent circuit for a CTIA configuration with a two-stage Miller amplifier in place of the single-stage OTA is shown in Fig. A.4. Again, we study the effect of a constant input current i_ph on the input offset v_i due to finite transconductance while neglecting the effect of limited voltage gain, i.e., we assume $R_\mathrm{o1} \to \infty$ and $R_\mathrm{o2} \to \infty$. According to KCL, we get:

$$\begin{aligned} 0 &= i_\mathrm{ph} + sC_\mathrm{j}v_\mathrm{i} + sC_\mathrm{f}(v_\mathrm{i}-v_\mathrm{o}) \\ 0 &= G_\mathrm{m1}v_\mathrm{i} + sC_\mathrm{M}(v_\mathrm{o}-v_2) \\ 0 &= G_\mathrm{m2}v_2 + sC_\mathrm{M}(v_\mathrm{o}-v_2) + sC_\mathrm{f}(v_\mathrm{o}-v_\mathrm{i}) + sC_\mathrm{L}v_\mathrm{o}. \end{aligned} \tag{A.13}$$

Solving for v_2 and then v_o, we get:

$$\begin{aligned} v_2 &= v_\mathrm{o} + v_\mathrm{i}\frac{G_\mathrm{m1}}{sC_\mathrm{M}}, \\ v_\mathrm{o} &= v_\mathrm{i}\cdot\frac{-G_\mathrm{m1}G_\mathrm{m2} + sC_\mathrm{M}G_\mathrm{m1} + s^2C_\mathrm{f}C_\mathrm{M}}{sC_\mathrm{M}\left[G_\mathrm{m2}+s(C_\mathrm{f}+C_\mathrm{L})\right]}. \end{aligned} \tag{A.14}$$

Thus when solving the equation system (A.13) for v_i, we get:

$$0 = i_\mathrm{ph} + v_\mathrm{i}\left[sC_\mathrm{j} + sC_\mathrm{f} + \frac{sC_\mathrm{f}}{sC_\mathrm{M}}\cdot\frac{G_\mathrm{m1}G_\mathrm{m2} - sC_\mathrm{M}G_\mathrm{m1} - s^2C_\mathrm{f}C_\mathrm{M}}{G_\mathrm{m2}+s(C_\mathrm{f}+C_\mathrm{L})}\right],$$

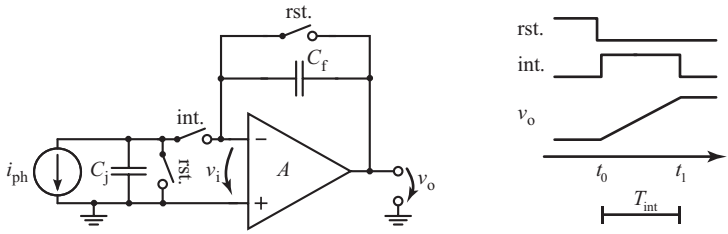

Figure A.5: Simplified CTIA circuit and timing diagram. The photodiode is represented by an ideal current source i_{ph} and its junction capacitance C_{j}.

which at DC results in

$$v_{\mathrm{i}} = -i_{\mathrm{ph}} \frac{C_{\mathrm{M}}}{G_{\mathrm{m1}} C_{\mathrm{f}}}. \tag{A.15}$$

In a realistic implementation, C_{M} is of equal order of magnitude as C_{L} and C_{f}. Thus the CTIA configuration does not profit from a two-stage amplifier design.

A.4 CTIA Transfer Function

In this section we derive the frequency characteristic of the simplified CTIA depicted in Fig. A.5 based on [243].
In time domain, the CTIA is characterised during the integration phase $t_0 < t < t_1$ by

$$i_{\mathrm{ph}}(t) + \frac{dv_{\mathrm{i}}(t)}{dt} C_{\mathrm{j}} = \frac{d\left[v_{\mathrm{o}}(t) - v_{\mathrm{i}}(t)\right]}{dt} C_{\mathrm{f}}. \tag{A.16}$$

If the circuit is properly reset at t_0, i.e., $v_{\mathrm{i}}(t_0) = v_{\mathrm{o}}(t_0) = 0$, the situation at the sampling time t_1 is thus described by

$$\int_{t_0}^{t_1} i_{\mathrm{ph}}(t)dt + v_{\mathrm{i}}(t_1) C_{\mathrm{j}} = \left[v_{\mathrm{o}}(t_1) - v_{\mathrm{i}}(t_1)\right] C_{\mathrm{f}}. \tag{A.17}$$

The integral of the photodiode current can be rearranged as

$$\begin{aligned}\int_{t_0}^{t_1} i_{\mathrm{ph}}(t)dt &= \int_{-\infty}^{\infty} i_{\mathrm{ph}}(t)\left[u(t-t_0)-u(t-t_1)\right]dt \\ &= (i_{\mathrm{ph}} * u)(t_1) - (i_{\mathrm{ph}} * u)(t_1 - T_{\mathrm{int}}),\end{aligned} \tag{A.18}$$

with $u(t)$ denoting the step function and T_{int} representing the integration period:

$$u(t) = \begin{cases} 1, & t \geq 0 \\ 0, & t < 0 \end{cases} \tag{A.19}$$

The Laplace transform of (A.17) is thus:

$$\begin{aligned} I_{\mathrm{ph}}(s) \cdot \frac{1}{s}\left[1 - e^{-sT_{\mathrm{int}}}\right] &= C_{\mathrm{f}}\left[V_{\mathrm{o}}(s) - V_{\mathrm{i}}(s)\right] - V_{\mathrm{i}}(s)C_{\mathrm{j}} \\ I_{\mathrm{ph}}(s) \cdot e^{-s\frac{T_{\mathrm{int}}}{2}} \cdot \frac{e^{s\frac{T_{\mathrm{int}}}{2}} - e^{-s\frac{T_{\mathrm{int}}}{2}}}{s} &= V_{\mathrm{o}}(s)\frac{\left[A(s)+1\right]C_{\mathrm{f}} + C_{\mathrm{j}}}{A(s)}, \end{aligned} \tag{A.20}$$

with $A(s)$ denoting the amplifier characteristics. The frequency characteristic is found by plugging in $s = j2\pi f$:

$$I_{\mathrm{ph}}(f)e^{-j\pi f T_{\mathrm{int}}}\frac{\sin\left(\pi f\, T_{\mathrm{int}}\right)}{\pi f} = V_{\mathrm{o}}(f)\frac{[A(f)+1]C_{\mathrm{f}} + C_{\mathrm{j}}}{A(f)} \tag{A.21}$$

$$\frac{V_{\mathrm{o}}(f)}{I_{\mathrm{ph}}(f)} = e^{-j\pi f\ T_{\mathrm{int}}} \cdot \mathrm{sinc}(fT_{\mathrm{int}})\frac{A(f)\cdot T_{\mathrm{int}}}{[A(f)+1]C_{\mathrm{f}} + C_{\mathrm{j}}}. \tag{A.22}$$

A.4.1 First Order Approximation

When assuming an ideal amplifier characteristic $A(f)$, i.e., infinite amplification over all frequencies, magnitude frequency characteristic is thus given by

$$\left|\frac{V_{\mathrm{o}}(f)}{I_{\mathrm{ph}}(f)}\right| \approx \left|\frac{T_{\mathrm{int}}}{C_{\mathrm{f}}} \cdot \mathrm{sinc}(f\ T_{\mathrm{int}})\right|. \tag{A.23}$$

A.4.2 Second Order Approximation

We assume now that the amplifier has first-order low-pass characteristics, i.e.:

$$A(f) = \frac{A_{\mathrm{DC}}}{1 + j\frac{f}{f_{\mathrm{p}}}}. \tag{A.24}$$

The right-most part of (A.22) is thus given by:

$$\frac{A(f) \cdot T_{\mathrm{int}}}{[A(f)+1]C_{\mathrm{f}} + C_{\mathrm{j}}} = \frac{A_{\mathrm{DC}}}{1 + j\frac{f}{f_{\mathrm{p}}}} \cdot \frac{T_{\mathrm{int}}}{\left(1 + \frac{A_{\mathrm{DC}}}{1+jf/f_{\mathrm{p}}}\right) C_{\mathrm{f}} + C_{\mathrm{j}}} \tag{A.25}$$

$$\approx \frac{T_{\mathrm{int}}}{C_{\mathrm{f}}} \cdot \frac{1}{1 + j\frac{f}{A_{\mathrm{DC}} f_{\mathrm{p}}} \cdot \frac{C_{\mathrm{f}}+C_{\mathrm{j}}}{C_{\mathrm{f}}}}, \tag{A.26}$$

for $A_{\mathrm{DC}} \gg 1$.
The magnitude frequency characteristic is thus

$$\left|\frac{V_{\mathrm{o}}(f)}{I_{\mathrm{ph}}(f)}\right| \approx \left|\frac{T_{\mathrm{int}}}{C_{\mathrm{f}}} \cdot \mathrm{sinc}(f\ T_{\mathrm{int}}) \cdot \frac{1}{1 + jf\frac{C_{\mathrm{f}}+C_{\mathrm{j}}}{GBP \cdot C_{\mathrm{f}}}}\right|, \tag{A.27}$$

with the gain-bandwidth product $GBP = A_{\mathrm{DC}} f_{\mathrm{p}}$.

A.5 OTA Noise Transfer Functions

A.5.1 RTIA Track & Sample State

Without Noise Curbing

Figure A.6 depicts the small signal equivalent circuit and the corresponding signal flow graph [244] for the RTIA in the track & sample state. $G_{\mathrm{m}} \ll \frac{1}{R_{\mathrm{f}}}$ is assumed and the node impedances are given by:

$$Z_1 = \frac{R_{\mathrm{f}}}{1 + sR_{\mathrm{f}}(C_{\mathrm{f}} + C_{\mathrm{j}})}, \tag{A.28}$$

$$Z_2 = \frac{R_{\mathrm{f}}}{1 + sR_{\mathrm{f}}(C_{\mathrm{f}} + C_{\mathrm{S}})}. \tag{A.29}$$

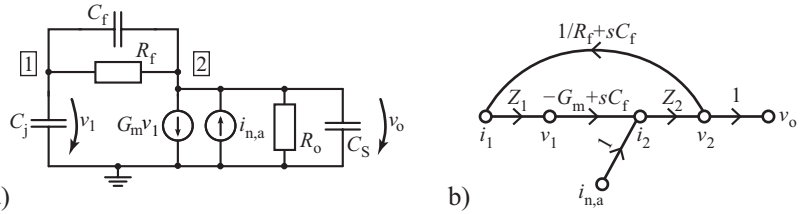

Figure A.6: Small signal equivalent circuit (a) and corresponding signal flow graph (b) of a RTIA circuit in track & sample state.

The transfer function from the noise source $i_{n,a}$ to the output voltage v_o is thus given by:

$$\begin{aligned}
\frac{v_o}{i_{n,a}} &= \frac{Z_2}{1+(G_m - sC_f)\left(\frac{1}{R_f}+sC_f\right)Z_1 Z_2} \qquad \text{(A.30)}\\
&= \frac{R_f[1+sR_f(C_j+C_f)]}{[1+sR_f(C_j+C_S)][1+sR_f(C_f+C_S)]+(G_m R_f - sR_f C_f)(1+sR_f C_f)}\\
&= \frac{1}{G_m}\frac{1+sR_f(C_j+C_f)}{1+s\left(R_f C_f+\frac{C_f+C_j+C_S}{G_m}\right)+s^2\frac{[(C_j+C_f)(C_f+C_S)-C_f^2]R_f}{G_m}}\\
&\approx \frac{1}{G_m}\frac{1+sR_f(C_j+C_f)}{1+sR_f C_f+s^2\frac{R_f C_f C_x}{G_m}}\\
&= \frac{1}{G_m}\frac{1+sR_f(C_j+C_f)}{(1+sR_f C_f)\left(1+s\frac{C_x}{G_m}\right)}.
\end{aligned}$$

with $C_x = C_j + C_S + C_j C_S/C_f$.

With Noise Curbing

The small signal equivalent circuit and its corresponding signal flow graph [244] are given in Fig. A.7 for the RTIA in track & sample state including the noise curbing resistor R_S. $G_m \ll \frac{1}{R_f}$ is assumed and the node impedances are given by:

$$Z_1 = \frac{R_f}{1+sR_f(C_f+C_j)} = \frac{R_f}{1+sR_f C_x}, \qquad \text{(A.31)}$$

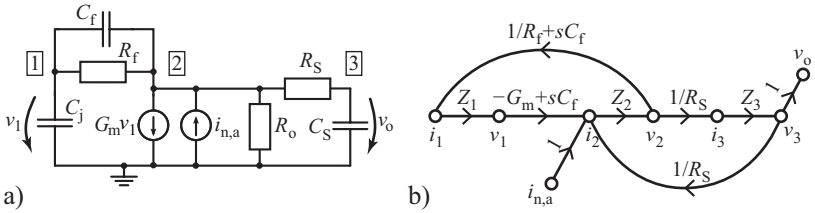

Figure A.7: Small signal equivalent circuit (a) and corresponding signal flow graph (b) of a RTIA circuit in track & sample state with noise curbing resistor R_S.

$$Z_2 = \frac{R_f||R_S}{1+s(R_f||R_S)C_f} = \frac{R_x}{1+sR_xC_f}, \tag{A.32}$$

$$Z_3 = \frac{R_S}{1+R_SC_S}. \tag{A.33}$$

The transfer function from the noise source $i_{n,a}$ to the output voltage v_o is thus given by:

$$\begin{aligned}
\frac{v_o}{i_{n,a}} &= \frac{\frac{1}{R_S}Z_2Z_3}{1+(G_m-sC_f)\left(\frac{1}{R_f}+sC_f\right)Z_1Z_2-\frac{1}{R_S^2}Z_2Z_3} \qquad (A.34)\\
&= R_x(1+sR_fC_x)\Big(-\frac{R_x}{R_S}(1+sR_fC_x)\\
&\quad +(1+sR_SC_S)\left[(1+sR_xC_f)(1+sR_fC_x)+(G_mR_x-sR_xC_f)(1+sR_fC_f)\right]\Big)^{-1}\\
&\approx \frac{1}{G_m}\frac{1+sR_fC_x}{(1+sR_SC_S)\left[1+sR_fC_f+s^2\left(R_f\frac{C_fC_x}{G_m}-R_f\frac{C_f^2}{G_m}\right)\right]-s\frac{R_f}{R_S}\frac{C_x}{G_m}}\\
&\approx \frac{1}{G_m}\frac{1+sR_f(C_f+C_j)}{(1+sR_SC_S)(1+sR_fC_f)\left(1+s\frac{C_j}{G_m}\right)}.
\end{aligned}$$

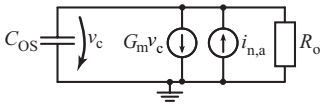

Figure A.8: Small signal equivalent circuit of the TIA in idle/reset state, sampling the TIA offset on the C_{OS} capacitor.

A.5.2 OTA Offset Sampling

Without Noise Curbing

The small signal equivalent circuit is given in Fig. A.8 for the TIA circuit in the idle state during which the OTA offset is sampled on the C_{OS} capacitors. With KCL we get:

$$0 = -i_{n,a} + G_m v_o + v_o \left(\frac{1}{R_o} + sC_{OS} \right). \tag{A.35}$$

The transfer function of the OTA noise to the capacitor voltage vc is thus found to be:

$$\frac{v_c}{i_{n,a}} = \frac{1}{G_m + \frac{1}{R_o} + sC_{OS}} \approx \frac{1}{G_m} \frac{1}{1 + s\frac{C_{OS}}{G_m}}, \tag{A.36}$$

assuming $G_m R_o \ll 1$.

With Noise Curbing

In Fig. A.9 both, the small signal equivalent circuit and the signal flow graph [244] are given for the TIA circuit with noise curbing resistor R_S when in idle state. Assuming $R_o \ll R_S$, the node impedances are given by:

$$Z_1 = \frac{R_S}{1 + sR_S C_{OS}} \tag{A.37}$$

$$Z_2 = R_S. \tag{A.38}$$

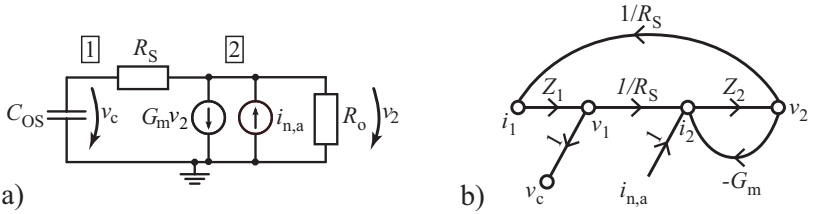

Figure A.9: Small signal equivalent circuit (a) and corresponding signal flow graph (b) of the TIA in idle/reset state with noise curbing resistor R_S, sampling the TIA offset on the C_{OS} capacitor.

The transfer function from the noise source $i_{n,a}$ to the capacitor voltage v_c is thus (assuming $G_m \ll 1/R_S$):

$$\begin{aligned}\frac{v_c}{i_{n,a}} &= \frac{Z_1 Z_2 \frac{1}{R_S}}{1 - Z_1 Z_2 \frac{1}{R_S^2} + G_m Z_2} \\ &= \frac{1}{G_m + \left(G_m + \frac{1}{R_S}\right) s R_S C_{OS}} \approx \frac{1}{G_m} \frac{1}{1 + s R_S C_{OS}}.\end{aligned} \tag{A.39}$$

A.5.3 Subtraction SIG-DK

Without Noise Curbing

Small signal equivalent circuit and corresponding signal flow graph for the TIA circuit in *summation* state are given in Fig. A.10. The node impedances are:

$$Z_1 = \frac{1}{s(C_f + C_S)} \tag{A.40}$$

$$Z_2 = \frac{R_o}{1 + s R_o C_f}. \tag{A.41}$$

The transfer function from the noise source $i_{n,a}$ to the (differential) feedback capacitor voltage v_f is thus:

$$\frac{v_f}{i_{n,a}} = \frac{Z_2 - s C_f Z_1 Z_2}{1 + s C_f (G_m - s C_f) Z_1 Z_2} \tag{A.42}$$

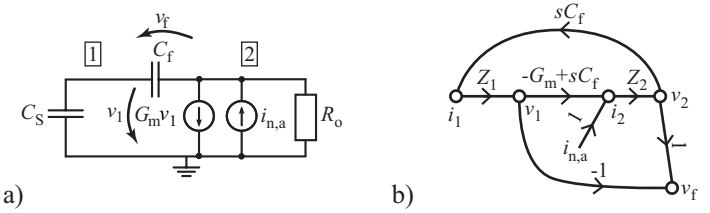

Figure A.10: Small signal equivalent circuit (a) and corresponding signal flow graph (b) of the TIA in the subtraction state. The noise transfer to the feedback capacitor C_f is studied.

$$= \frac{sR_o(C_f + C_S) - sR_oC_f}{s(C_S + C_f)(1 + sR_oC_f) + sC_fR_oG_m\left(1 - s\frac{C_f}{G_m}\right)}$$
$$\approx \frac{1}{G_m}\frac{C_S}{C_f}\frac{1}{1 + s\frac{C_S}{G_m}}.$$

With Noise Curbing

The small signal equivalent circuit and corresponding signal flow graph for the TIA circuit with noise curbing resistor R_S in *summation* state are depicted in Fig. A.11. The node impedances are given as:

$$Z_1 = \frac{R_S}{1 + sR_SC_S} \tag{A.43}$$
$$Z_2 = \frac{R_S}{1 + sR_SC_f} \tag{A.44}$$
$$Z_3 = \frac{R_o}{1 + sR_oC_f}. \tag{A.45}$$

The transfer function from the noise source $i_{n,a}$ to the (differential) feedback capacitor voltage v_f is:

$$\frac{v_f}{i_{n,a}} = \frac{Z_3\left(1 - \frac{1}{R_S^2}Z_1Z_2\right) - sC_fZ_2Z_3}{1 + sC_f(G_m - sC_f)Z_2Z_3 - \frac{1}{R_S^2}Z_1Z_2} \tag{A.46}$$

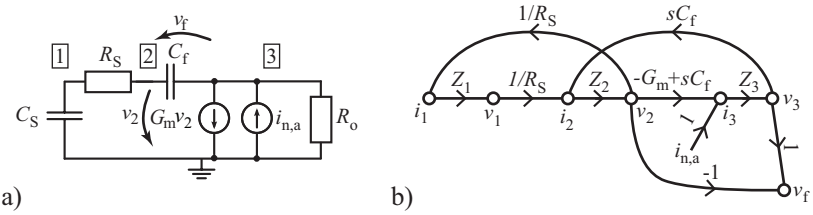

Figure A.11: Small signal equivalent circuit (a) and corresponding signal flow graph (b) of the TIA in the subtraction state with noise curbing resistor R_S.

$$
\begin{aligned}
&= \left[R_o(1+sR_SC_S)(1+sR_SC_f) - R_o - sC_fR_oR_S(1+sR_SC_S)\right] \\
&\quad \cdot \left[(1+sR_oC_f)(1+sR_SC_S)(1+sR_SC_f) - (1+sR_oC_f)\right. \\
&\quad \left. + sC_fR_SG_mR_o\left(1-\frac{sC_f}{G_m}\right)(1+sR_SC_S)\right]^{-1} \\
&\approx \frac{1}{G_m}\frac{sR_SC_s}{sR_SC_f(1+sR_SC_S)} \\
&= \frac{1}{G_m}\frac{C_S}{C_f}\frac{1}{1+sR_SC_S}.
\end{aligned}
$$

A.5.4 ADC Track & Sample

Without Noise Curbing

Figure A.12 depicts the small signal equivalent circuit and its corresponding signal flow graph for the TIA circuit in *ADC track* state. The node impedances are:

$$Z_1 = \frac{1}{s(C_f + C_S)} \tag{A.47}$$

$$Z_2 = \frac{R_o}{1+sR_o(C_f + C_{ADC})}. \tag{A.48}$$

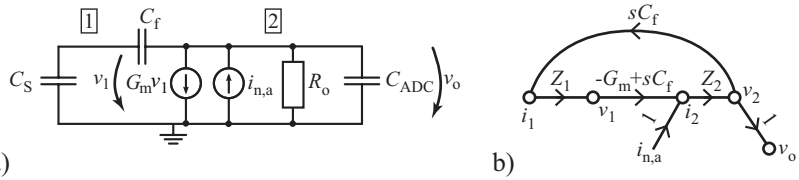

Figure A.12: Small signal equivalent circuit (a) and corresponding signal flow graph (b) of the TIA in ADC track state.

The transfer function from the noise source $i_{n,a}$ to the sampling capacitor of the ADC is:

$$\begin{aligned}\frac{v_o}{i_{n,a}} &= \frac{Z_2}{1+(G_m - sC_f)sC_f Z_1 Z_2} \\ &= \frac{sR_o(C_S+C_f)}{s(C_S+C_f)[1+sR_o(C_f+C_{ADC})] + R_o G_m\left(1 - s\frac{C_f}{G_m}\right)sC_f} \\ &\approx \frac{1}{G_m}\frac{s(C_S+C_f)}{sC_f + s^2\frac{C_S C_f + C_{ADC}C_f + C_S C_{ADC}}{G_m}} \\ &= \frac{1}{G_m}\frac{C_S+C_f}{C_f}\frac{1}{1+s\frac{C_S+C_{ADC}+C_S C_{ADC}/C_f}{G_m}},\end{aligned} \tag{A.49}$$

assuming $G_m R_o \ll 1$.

With Noise Curbing

The small signal equivalent circuit and signal flow graph of the TIA circuit with noise curbing resistors in *ADC track* state are given in Fig. A.13. The node impedances are:

$$Z_1 = \frac{R_{S1}}{1+sR_{S1}C_S} \tag{A.50}$$

$$Z_2 = \frac{R_{S1}}{1+sR_{S1}C_f} \tag{A.51}$$

$$Z_3 = \frac{R_{S2}}{1+sR_{S2}C_f} \tag{A.52}$$

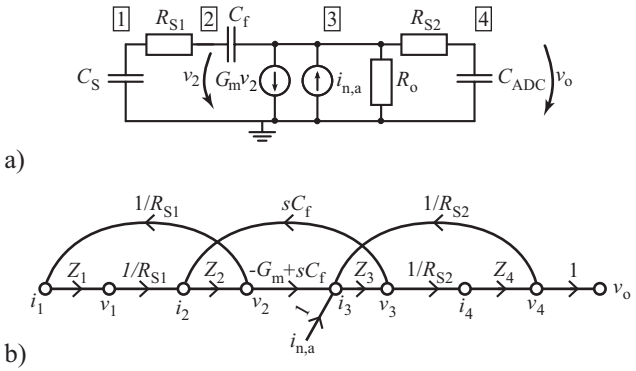

Figure A.13: Small signal equivalent circuit (a) and corresponding signal flow graph (b) of the TIA with noise curbing resistors R_{S1} and R_{S2} in ADC track state.

$$Z_4 = \frac{R_{S2}}{1 + sR_{S2}C_{ADC}}. \tag{A.53}$$

The transfer function from the noise source $i_{n,a}$ to the sampling capacitor of the ADC is:

$$\begin{aligned}
\frac{v_o}{i_{n,a}} &= \frac{\frac{1}{R_{S2}} Z_3 Z_4 \left(1 - \frac{1}{R_{S1}^2} Z_1 Z_2\right)}{1 - \frac{1}{R_{S1}^2} Z_1 Z_2 + (G_m + sC_f) sC_f Z_2 Z_3 - \frac{1}{R_{S2}^2} Z_3 Z_4 + \frac{1}{R_{S1}^2 R_{S2}^2} Z_1 Z_2 Z_3 Z_4} \\
&\approx \frac{1}{G_m} \frac{sR_{S1}(C_S + C_f) + s^2 R_{S1}^2 C_S C_f}{sR_{S1}C_f(1 + sR_{S1}C_S)(1 + sR_{S2}C_{ADC})} \\
&= \frac{1}{G_m} \frac{C_S + C_f}{C_f} \frac{1 + sR_{S1}\frac{C_S C_f}{C_S + C_f}}{(1 + sR_{S1}C_S)(1 + sR_{S2}C_{ADC})}.
\end{aligned} \tag{A.54}$$

Appendix B

FoM Calculations

The figure-of-merit (FoM) introduced in Sec. 4.2.1 for PPG circuits is (4.4):

$$FoM = DR_{\mathrm{f_{BW}}} + 10\log_{10}\left(\frac{f_{\mathrm{BW}}}{1\mathrm{Hz}} \cdot \frac{1\,\mathrm{mW}}{P_{\mathrm{tot}}} \cdot \frac{10\mathrm{ppm}}{\Theta}\right) \qquad [\mathrm{dB}],$$

with f_{BW} denoting the bandwidth for which the loop dynamic range $DR_{f_{\mathrm{BW}}}$ has been measured, P_{tot} the total power consumption of the circuit including two LEDs and $\Theta = \frac{I_{\mathrm{ph}}}{I_{\mathrm{LED}}}$ the transmission factor.
The measurands provided in academic publications and datasheets of commercial ASICs vary widely and are often incomplete. For the sake of clearity and transparency, this appendix chapter reproduces the derivation of the FoM for each ASIC to which TMA-O is compared to in this work.

B.1 MAX30100

The *Maxim Integrated MAX30100* [163] is a sensor module integrating a PPG ASIC together with red and infrared LEDs and a photodiode in a single $5.6 \times 2.8 \times 1.2\,\mathrm{mm}^3$ package. Thus, we assume that the receiver characteristics include photodiode noise – although not clearly specified in the datasheet. There is no specification given for the photodiode input current under which the stated resolutions have been

measured – experience with similar setups suggests that $\Theta = 10\text{ppm}$ is a reasonable assumption for the transmission and that best loop dynamic range and FoM are measured with highest LED current. The comparison is thus done assuming $I_{\text{LED}} = 50\,\text{mA}$. The module can be operated at a PRF of 600 Hz which is thus chosen here for better direct comparison with the *Texas Instruments* chips and our work. According to [163, Tbl. 8] this PRF is only available for the shortest LED on-time of 200 µs in which the ADC resolution is given as 13 bit. Higher ADC resolutions up to 16 bit are stated for longer on-times – then again the *sensor characteristics* on page 2 state a typical resolution of 14 bit.
We interpret this contradictory statements such that the sensor has a maximum dynamic range corresponding to 14 bit wherease the ADC could resolve finer. The best FoM for *MAX30100* would then be expected for a $PRF = 400$ Hz and $T_{\text{LED}} = 400\,\mu\text{s}$ configuration [163, Tbl. 8]. The FoMs for both usage scenarios are given in the following.

B.1.1 PRF = 600 Hz

Dynamic Range: 13 bit - this corresponds to $SNR_{\text{DC}} = 78.3\,\text{dB}$.

Duty Cycle: LED on-time is 200 µs, thus duty-cycle is 12%.

LED Power Consumption: For a typical LED supply of 3.3 V [163, p.2] and two LEDs with 50 mA we get thus $P_{\text{LED}} = 39.6\,\text{mW}$.

Bandwidth: The resolution versus sampling rate tables [163, p.19] suggest that the resolution is given for Nyquist bandwidth. Thus $f_{\text{BW}} = 300\,\text{Hz}$.

IC Power Consumption: 865 µW according to [163, Tbl.10].

The FoM is thus:

$$\begin{aligned} FoM_{\text{PRF600}} &= 78.3\,\text{dB} + 10 \cdot \log_{10}\left(\frac{300\text{ Hz}}{1\text{ Hz}}\frac{1\,\text{mW}}{40.5\,\text{mW}}\frac{10\text{ppm}}{10\text{ppm}}\right) \\ &= 87.0\,\text{dB}. \end{aligned} \tag{B.1}$$

B.1.2 PRF = 400 Hz

Dynamic Range: 14 bit - this corresponds to $SNR_{\mathrm{DC}} = 84.3\,\mathrm{dB}$.

Duty Cycle: LED on-time is 400 µs, thus duty-cycle is 16%.

LED Power Consumption: For a typical LED supply of 3.3 V [163, p.2] and two LEDs with 50 mA we get thus $P_{\mathrm{LED}} = 52.8\,\mathrm{mW}$.

Bandwidth: $f_{\mathrm{BW}} = 200\,\mathrm{Hz}$.

IC Power Consumption: 944 µW according to [163, Tbl.10].

The FoM is thus:

$$\begin{aligned} FoM_{\mathrm{PRF400}} &= 84.3\,\mathrm{dB} + 10 \cdot \log_{10}\left(\frac{200\ \mathrm{Hz}}{1\ \mathrm{Hz}}\frac{1\,\mathrm{mW}}{53.7\,\mathrm{mW}}\frac{10\mathrm{ppm}}{10\mathrm{ppm}}\right) \\ &= 90.0\,\mathrm{dB}. \end{aligned} \tag{B.2}$$

B.2 TI AFE44xx

The *Texas Instruments* series of analogue front-end ASICs for PPG and pulse oximeters comprises currently the *AFE4400* [165], *AFE4490* [166], *AFE4403* [167], *AFE4404* [168] and *AFE4405* chips. The last one has been released shortly prior to the writing of this thesis. Its full datasheet is not released to public by now[1] – thus it can't be included in this comparison.
All ASICs are characterised for a typical receiver input full-scale of 1 µA for which the datasheets give input-referred noise current values which include transmitter and receiver contributions – however, since they characterise the ASIC itself, noise contributed by the optoelectronic external components are not included in this measurements. For the loop dynamic range used in the FoM we add the expected photodiode shot-noise for $I_{\mathrm{PD}} = I_{\mathrm{FS}}/2$ to the specified input-referred overall circuit noise. The information provided in the datasheets allows to reconstruct the minimum receiver bandwidth for the configuration under which these characterisation measurements have been

[1] 17th January 2017.

done – this allows to calculate both, the integrated photodiode shot-noise and the settling number ξ. The *TI AFE44xx* series features a switched-RC filter [245, 246] which reduces the bandwidth in the analogue domain. Since it is a sampled filter, noise aliasing is not avoided and thus there is no advantage in terms of noise-power over an equivalent digital filter applied on filter-less sampled data. Transmission $\Theta = I_{\mathrm{PD}}/I_{\mathrm{LED}}$ is assumed to be 10ppm, resulting in a LED current of 50 mA.
In the following, the detailed FoM calculations for the single ASICs are provided.

B.2.1 AFE 4400

Integrated input-referred noise current including transmitter loop back is given as $i_{\mathrm{n,tr,5Hz}} = 13\,\mathrm{pA_{RMS}}$ over a 5 Hz bandwidth for $R_{\mathrm{f}} = 500\,\mathrm{k\Omega}$, $f_{\mathrm{PR}} = 600\,\mathrm{Hz}$ and a duty cycle of 5% [165, p.9]. The input swing for for $R_{\mathrm{f}} = 500\,\mathrm{k\Omega}$ is specified as $I_{\mathrm{FS}} = 1\,\mu\mathrm{A}$. According to [165, p.22], the receiver bandwidth has to be configured in order to have a settling number larger than 10. With the given choice [165, p.64] for C_{f} the minimum bandwidth with $\xi > 10$ is

$$f_{\mathrm{BW}} = \frac{\pi}{2}\frac{1}{2\pi \cdot 500\,\mathrm{k\Omega} \cdot 10\,\mathrm{pF}} = 50\,\mathrm{kHz}, \tag{B.3}$$

which corresponds to $\xi = 16.7$. Photodiode shot noise is thus

$$i_{\mathrm{n,PD,5Hz}} = \sqrt{2q\frac{I_{\mathrm{FS}}}{2}f_{\mathrm{BW}}}\sqrt{\frac{5\,\mathrm{Hz}}{300\,\mathrm{Hz}}} = 11.5\,\mathrm{pA_{RMS}}. \tag{B.4}$$

Overall input-referred noise will thus be

$$i_{\mathrm{n,t,5Hz}} = \sqrt{i^2_{\mathrm{n,tr,5Hz}} + i^2_{\mathrm{n,PD,5Hz}}} = 17.36\,\mathrm{pA_{RMS}}, \tag{B.5}$$

which is equivalent to a dynamic range of 95.2 dB for the 5 Hz signal bandwidth.
For 3.5 V LED driver supply the LED power consumption is

$$P_{\mathrm{LEDs}} = 2 \cdot 5\% \cdot 50\,\mathrm{mA} \cdot 3.5\,\mathrm{V} = 17.5\,\mathrm{mW}, \tag{B.6}$$

total ASIC power consumption sums up to another 2.79 mW.
The FoM is thus:

$$FoM = 95.2\,\mathrm{dB} + 10 \cdot \log_{10}\left(\frac{5\,\mathrm{Hz}}{1\,\mathrm{Hz}}\frac{1\,\mathrm{mW}}{20.3\,\mathrm{mW}}\frac{10\mathrm{ppm}}{10\mathrm{ppm}}\right) = 89.11\,\mathrm{dB}. \tag{B.7}$$

B.2.2 AFE 4490

Integrated input-referred noise current including transmitter loop back is given as $i_{\mathrm{n,tr,20Hz}} = 13\,\mathrm{pA_{RMS}}$ over a 20 Hz bandwidth for $R_\mathrm{f} = 500\,\mathrm{k\Omega}$, $f_\mathrm{PR} = 1200\,\mathrm{Hz}$ and a duty cycle of 25% [166, p.10]. The input swing for for $R_\mathrm{f} = 500\,\mathrm{k\Omega}$ is specified as $I_\mathrm{FS} = 1\,\mu\mathrm{A}$. According to [166, p.28] the receiver bandwidth has to be configured in order to have a settling number larger than 10. With the given choice [166, p.74] for C_f the minimum bandwidth with $\xi > 10$ is

$$f_\mathrm{BW} = \frac{\pi}{2}\frac{1}{2\pi \cdot 500\,\mathrm{k\Omega} \cdot 35\,\mathrm{pF}} = 14.3\,\mathrm{kHz}, \tag{B.8}$$

which corresponds to $\xi = 11.8$. Photodiode shot noise is thus

$$i_{\mathrm{n,PD,20Hz}} = \sqrt{2q\frac{I_\mathrm{FS}}{2}f_\mathrm{BW}}\sqrt{\frac{20\,\mathrm{Hz}}{600\,\mathrm{Hz}}} = 8.74\,\mathrm{pA_{RMS}}. \tag{B.9}$$

Overall input-referred noise will thus be

$$i_{\mathrm{n,t,20Hz}} = \sqrt{i^2_{\mathrm{n,tr,20Hz}} + i^2_{\mathrm{n,PD,20Hz}}} = 15.66\,\mathrm{pA_{RMS}}, \tag{B.10}$$

which is equivalent to a dynamic range of 96.1 dB for the 20 Hz signal bandwidth.
For 3.5 V LED driver supply the LED power consumption is

$$P_\mathrm{LEDs} = 2 \cdot 25\% \cdot 50\,\mathrm{mA} \cdot 3.5\,\mathrm{V} = 87.5\,\mathrm{mW}, \tag{B.11}$$

total ASIC power consumption sums up to another 2.79 mW.
The FoM is thus:

$$FoM = 96.1\,\mathrm{dB} + 10 \cdot \log_{10}\left(\frac{20\,\mathrm{Hz}}{1\,\mathrm{Hz}}\frac{1\,\mathrm{mW}}{90.29\,\mathrm{mW}}\frac{10\mathrm{ppm}}{10\mathrm{ppm}}\right) = 89.6\,\mathrm{dB}. \tag{B.12}$$

B.2.3 AFE 4403

Integrated input-referred noise current including transmitter loop back is given as $i_{\mathrm{n,tr,20Hz}} = 6\,\mathrm{pA_{RMS}}$ over a 20 Hz bandwidth for $R_\mathrm{f} = 500\,\mathrm{k\Omega}$, $f_\mathrm{PR} = 600\,\mathrm{Hz}$ and a duty cycle of 5% [167, p.7]. The input swing for for $R_\mathrm{f} = 500\,\mathrm{k\Omega}$ is specified as $I_\mathrm{FS} = 1\,\mu\mathrm{A}$. According to [167, p.21] the receiver bandwidth has to be configured in order to have a settling number larger than 10. With the given choice [167, p.72] for C_f the minimum bandwidth with $\xi > 10$ is

$$f_\mathrm{BW} = \frac{\pi}{2}\frac{1}{2\pi \cdot 500\,\mathrm{k\Omega} \cdot 10\,\mathrm{pF}} = 50\,\mathrm{kHz}, \tag{B.13}$$

which corresponds to $\xi = 16.7$. Photodiode shot noise is thus

$$i_\mathrm{n,PD,20Hz} = \sqrt{2q\frac{I_\mathrm{FS}}{2}f_\mathrm{BW}}\sqrt{\frac{20\,\mathrm{Hz}}{300\,\mathrm{Hz}}} = 23.11\,\mathrm{pA_{RMS}}. \tag{B.14}$$

Overall input-referred noise will thus be

$$i_\mathrm{n,t,20Hz} = \sqrt{i^2_\mathrm{n,tr,20Hz} + i^2_\mathrm{n,PD,20Hz}} = 23.88\,\mathrm{pA_{RMS}}, \tag{B.15}$$

which is equivalent to a dynamic range of 92.4 dB for the 20 Hz signal bandwidth.
For 3.3 V LED driver supply the LED power consumption is

$$P_\mathrm{LEDs} = 2 \cdot 5\% \cdot 50\,\mathrm{mA} \cdot 3.3\,\mathrm{V} = 16.5\,\mathrm{mW}, \tag{B.16}$$

total ASIC power consumption sums up to another 2.03 mW.
The FoM is thus:

$$\begin{aligned} FoM &= 92.4\,\mathrm{dB} + 10 \cdot \log_{10}\left(\frac{20\,\mathrm{Hz}}{1\,\mathrm{Hz}}\frac{1\,\mathrm{mW}}{18.53\,\mathrm{mW}}\frac{10\mathrm{ppm}}{10\mathrm{ppm}}\right) \\ &= 92.8\,\mathrm{dB}. \end{aligned} \tag{B.17}$$

B.2.4 AFE 4404

Receiver SNR_DC over a 20 Hz bandwidth for $R_\mathrm{f} = 500\,\mathrm{k\Omega}$, $f_\mathrm{PR} = 100$ Hz and a duty cycle of 2% [168, p.6] is given as 100 dB. The input swing for for $R_\mathrm{f} = 500\,\mathrm{k\Omega}$ is specified as $I_\mathrm{FS} = 1\,\mu\mathrm{A}$, thus the

input referred noise current equals $10\,\mathrm{pA_{RMS}}$. According to [168, p.15] the receiver bandwidth has to be configured in order to have a settling number larger than 5. With the given choice [168, p.51] for C_f the minimum bandwidth for $R_\mathrm{f} = 500\,\mathrm{k\Omega}$ is

$$f_\mathrm{BW} = \frac{\pi}{2}\frac{1}{2\pi \cdot 500\,\mathrm{k\Omega} \cdot 25\,\mathrm{pF}} = 20\,\mathrm{kHz}, \tag{B.18}$$

which corresponds to $\xi = 16$. Photodiode shot noise is thus

$$i_\mathrm{n,PD,20Hz} = \sqrt{2q\frac{I_\mathrm{FS}}{2}f_\mathrm{BW}}\sqrt{\frac{20\,\mathrm{Hz}}{50\,\mathrm{Hz}}} = 36.80\,\mathrm{pA_{RMS}}. \tag{B.19}$$

Overall input-referred noise will thus be

$$i_\mathrm{n,t,20Hz} = \sqrt{i^2_\mathrm{n,tr,20Hz} + i^2_\mathrm{n,PD,20Hz}} = 37.17\,\mathrm{pA_{RMS}}, \tag{B.20}$$

which is equivalent to a dynamic range of 88.6 dB for the 20 Hz signal bandwidth.
For 3.0 V LED driver supply the LED power consumption is

$$P_\mathrm{LEDs} = 2 \cdot 2\% \cdot 50\,\mathrm{mA} \cdot 3.0\,\mathrm{V} = 6.0\,\mathrm{mW}, \tag{B.21}$$

total ASIC power consumption sums up to another 1.94 mW.
The FoM is thus:

$$\begin{aligned} FoM &= 88.6\,\mathrm{dB} + 10 \cdot \log_{10}\left(\frac{20\,\mathrm{Hz}}{1\,\mathrm{Hz}}\frac{1\,\mathrm{mW}}{7.94\,\mathrm{mW}}\frac{10\mathrm{ppm}}{10\mathrm{ppm}}\right) \\ &= 92.6\,\mathrm{dB}. \end{aligned} \tag{B.22}$$

B.3 K. N. Glaros et al., 2013

The pulse oximetry front-end [145] published by K.N.Glaros et al. does not include an ADC. For the comparison thus just front-end noise is considered.
The measurement results given in the paper include the optoelectronic components. An output referred overall noise of $445\,\mu\mathrm{V_{RMS}}$ for a 2.5 V swing is given for a 10 Hz bandwidth sampled with 100 Hz PRF. This corresponds to a dynamic range of 75.0 dB.

This measurements were done for 7.1 mA LED current and a transmission of

$$\Theta = \frac{1}{16084} = 62.2\text{ppm}. \tag{B.23}$$

Power consumption of the ASIC itself is reported as 0.53 mW (without ADC) and the total power consumption including two LEDs is 1.89 mW.
The FoM is thus:

$$\begin{aligned} FoM &= 75.0\,\text{dB} + 10 \cdot \log_{10}\left(\frac{10\,\text{Hz}}{1\,\text{Hz}}\frac{1\,\text{mW}}{1.89\,\text{mW}}\frac{10\text{ppm}}{62.2\text{ppm}}\right) \\ &= 74.3\,\text{dB}. \end{aligned} \tag{B.24}$$

The design is described in more detail in [247]. A sampled integrator is used to reduce aliasing of the RTIA stage amplifier noise – which is achieved in TMA-O with bandwidth limiting resistors. As discussed in Sec. 4.4.2, a sampled integrator has a relatively low settling number of $\xi = 2.78$. The conceptual timing diagrams in [145, 247] however suggest that considerable LED on-time overhead results from settling of the driver and the receivers first (RTIA) stage. The effective settling number will thus be higher.

B.4 L. Sant et al., 2016

An optical proximity, heart rate and oximetry sensor ASIC with integrated photodiode is presented in [20, 164]. The lack of detailed information makes a comparison to other work difficult.
The LED duty-cycle is reported in [164, Tbl. I] as 8%. Although not clearly stated, we assume it to comprise the active time of both LEDs due to the stated duty-cylce of the *TI AFE4403* [167] to which it is compared. There is no indication on the LED supply voltage, thus 3.3 V is assumed for driving 50 mA, resulting in a LED power consumption of 13.2 mW. The ASIC power is given as 3.02 mW. When further assuming that the reported dynamic range of 85 dB for a 20 Hz

bandwidth includes photodiode noise and was done under comparable illumination conditions, the FoM is:

$$\begin{aligned} FoM &= 85\,\mathrm{dB} + 10 \cdot \log_{10}\left(\frac{20\,\mathrm{Hz}}{1\,\mathrm{Hz}}\frac{1\,\mathrm{mW}}{16.22\,\mathrm{mW}}\frac{10\mathrm{ppm}}{10\mathrm{ppm}}\right) \\ &= 86\,\mathrm{dB}. \end{aligned} \tag{B.25}$$

B.5 M. Konijnenburg et al., 2016

Although the provided data in [19,169] is relatively sparse, it provides enough insight to calculate receiver bandwidth and FoM.
The reported sample rate is 128 Hz – after decimation by 32 [19, 169]. We thus conclude that the PRF is

$$f_{\mathrm{PR}} = 32 \cdot 128\,\mathrm{Hz} = 4.096\,\mathrm{kHz}. \tag{B.26}$$

A range of possible LED-on times are reported but it is not indicated with which the reported results have been obtained. Receiver noise values are given only for the two extremes of the configurable transimpedance range, while the LED driver is not characterised (we thus have to neglect it). The FoM was found to be significantly higher for the maximum transimpedance (2.16 MΩ) – this operating condition is thus assumed. Given that the bandwidth is limited by the second stage and that receiver noise is dominated (> 80% [169]) by the TIA and the integration stage, it is to be assumed that the reported performance values have been measured for maximum integration time in order to provide best possible numbers. We thus assume $T_{\mathrm{int}} = 15\,\mu\mathrm{s}$, for which the second stage bandwidth is according to (4.31)

$$f_{\mathrm{BW}}[Rx] \approx \frac{0.696}{T_{\mathrm{int}} = 46.4\,\mathrm{kHz}}, \tag{B.27}$$

which clearly dominates over the 250 kHz bandwidth of the RTIA stage.
From reported dynamic range and input-referred noise level, the full-scale input current in this configuration is found to be:

$$I_{\mathrm{FS}} = 15.4\,\mathrm{pA} \cdot 10^{89/20} = 434\,\mathrm{nA}, \tag{B.28}$$

and raw photodiode shot noise is thus

$$i_{\mathrm{n,PD,4kHz}} = \sqrt{2q\frac{I_{\mathrm{FS}}}{2}f_{\mathrm{BW}}[Rx]} = 56.8\,\mathrm{pA_{RMS}}. \tag{B.29}$$

Decimation by 32 does reduce amplifier-, quantisation-, and photodiode noise. For the 64 Hz signal band, the latter is

$$i_{\mathrm{n,PD,64Hz}} = i_{\mathrm{n,PD,4kHz}} \cdot \sqrt{\frac{1}{32}} = 10.6\,\mathrm{pA_{RMS}}. \tag{B.30}$$

Therefore, overall noise is

$$i_{\mathrm{n,t,64Hz}} = \sqrt{i^2_{\mathrm{n,PD,64Hz}} + i^2_{\mathrm{n,rx,64Hz}}} = 18.4\,\mathrm{pA_{RMS}}. \tag{B.31}$$

This corresponds to a dynamic range of 87.5 dB for the 64 Hz bandwidth. With a LED on-time T_{p} of 15 µs, the duty cycle is

$$\delta = f_{\mathrm{PR}} \cdot T_{\mathrm{p}} = 6.14\%. \tag{B.32}$$

With two LEDs operated at 50 mA from 3.3 V supply, this results in a power consumption of

$$P_{\mathrm{LED}} = 2\delta \cdot 50\,\mathrm{mA} \cdot 3.3\ \mathrm{V} = 20.3\,\mathrm{mW}. \tag{B.33}$$

IC power consumption is reported to be 135 µW for the receiver and 316 µW for the LED driver, resulting in an overall power consumption of 20.6 mW. The transmission corresponding to assumed LED driving strength and photo-generated current is

$$\Theta = \frac{I_{\mathrm{FS}}}{2 \cdot I_{\mathrm{LED}}} = \frac{217\,\mathrm{nA}}{50\,\mathrm{mA}} = 4.3\mathrm{ppm}. \tag{B.34}$$

Finally, the FoM is:

$$\begin{aligned} FoM &= 87.5\,\mathrm{dB} + 10 \cdot \log_{10}\left(\frac{64\,\mathrm{Hz}}{1\,\mathrm{Hz}}\frac{1\,\mathrm{mW}}{20.6\,\mathrm{mW}}\frac{10\mathrm{ppm}}{4.3\mathrm{ppm}}\right) \\ &= 96.1\,\mathrm{dB}. \end{aligned} \tag{B.35}$$

Notation and Acronyms

Symbols

δ	[1]	duty cycle
ε	[F/m]	electric permittivity
ε	$[\mathrm{m}^2/\mathrm{kg}]$	mass extinction coefficient
ϵ	[1]	strain
η_e	[1]	extraction efficiency
η_ex	[1]	external efficiency
η_iqe	[1]	internal quantum efficiency
η_q	[1]	quantum efficiency
Θ	[1]	transmission factor (current ratio)
κ	[1]	folding number
λ	[m]	wavelength
ξ	[1]	settling coefficient
ρ	$[\mathrm{kg}/\mathrm{m}^3]$	mass density
Σ_a	[1/m]	absorption coefficient
Σ_s	[1/m]	scattering coefficient
σ	[Pa]	stress
ϕ	[1/s]	photon flux
Ψ	[1]	optical transmission
Ω	[sr]	solid angle

$\mathcal{A}$	[1]	absorbance
A	$[\mathrm{m}^2]$	area
A	[1]	amplification
AC		pulsatile part of a PPG signal
$\mathsf{C_A}$	$[\mathrm{m}^2/\mathrm{Pa}]$	area compliance
$\mathsf{C_D}$	[m/Pa]	diameter compliance
$\mathsf{C_V}$	$[\mathrm{m}^3/\mathrm{Pa}]$	volume compliance
C	[F]	capacitance
c	[m/s]	speed of light
c	[m/s]	wave velocity
D	[m]	diameter
DC		constant part of a PPG signal
DR	[dB]	dynamic range
d	[m]	light path length
$\mathsf{E_V}$	$[\mathrm{Pa}/\mathrm{m}^3]$	volume elastance
E	[Pa]	Young's modulus of elasticity
E_g	[eV]	bandgap energy
F	[N]	force
FS		full scale
f_c	[Hz]	corner frequency
f_PR	[Hz]	pulse repetition frequency
f_s	[Hz]	sampling frequency
h	$[\mathrm{m}^2\mathrm{kg}/\mathrm{s}]$	Planck's constant
h	[m]	thickness
$\mathcal{I}$		light intensity
I, i	[A]	electric current (large signal, small signal)

J	$\left[\mathrm{A/m^2}\right]$	current density
$\mathsf{K_A}$	[Pa]	area distensibility
$\mathsf{K_D}$	[Pa]	diameter distensibility
$\mathsf{K_V}$	[Pa]	volume distensibility
k	$\left[\mathrm{kg/m^3}\right]$	concentration (of a substance in a solution)
k_B	$\left[\frac{\mathrm{m^2 kg}}{\mathrm{s^2 K}}\right]$	Boltzmann constant
l	[m]	length
P	[Pa]	pressure
P	[W]	power
PI	[1]	perfusion index
Q	$\left[\mathrm{m^3/s}\right]$	volumetric flow rate
Q	[As]	charge
q	[As]	elementary charge
$\mathcal{R}_\mathrm{LED}$	[W/A]	responsivity of a LED
$\mathcal{R}_\mathrm{PD}$	[A/W]	responsivity of a photodiode
R	$\left[\mathrm{Pa \cdot s/m^3}\right]$	vascular resistance
$\mathfrak{R}$	[1]	ratio-of-ratios
R	[Ω]	resistance
r	[m]	radius
$\mathcal{T}$	[1]	transmittance
T	[K]	temperature
T	[s]	time period
V	$\left[\mathrm{m^3}\right]$	volume
V, v	[V]	electric voltage (large signal, small signal)
Z	[Ω]	impedance

Units

1 BPM	$= \frac{1}{60}$ Hz	beats per minute	frequency
1 F	$= 1\ \frac{\mathrm{A \cdot s}}{\mathrm{V}}$	Farad	capacitance
1 Hz	$= 1\ \frac{1}{\mathrm{s}}$	Hertz	frequency
1 J	= 1 Ws	Joule	energy
1 l	$= 10^{-3}\ \mathrm{m}^3$	liter	volume
1 M	$= 1\ \frac{\mathrm{mol}}{\mathrm{l}}$	molar	concentration
1 N	$= 1\ \frac{\mathrm{kg \cdot m}}{\mathrm{s}^2}$	Newton	force
1 Ω	$= 1\ \frac{\mathrm{V}}{\mathrm{A}}$	Ohm	resistance
1 Pa	$= 1\ \frac{\mathrm{kg}}{\mathrm{m \cdot s}^2}$	Pascal	pressure
1 W	= 1 VA	Watt	power
1 mmHg	= 133 Pa	millimetre-mercury	pressure
sr	dimensionless	steradian	solid angle

Operators

$\lvert . \rvert$	absolute value
$\lfloor . \rceil$	nearest integer function
$\log_{10}(.)$	base-10 logarithm
$\sigma(.)$	standard deviation

Acronyms

ADC	analogue-to-digital converter
ADN	aortic depressor nerve
AFE	analogue front-end
ALC	ambient light cancellation
ASIC	application-specific integrated circuit
AWGN	additive white Gaussian noise
BLE	*Bluetooth* low energy

BP	blood pressure
CCO	cytochrome-c-oxidase
CDS	correlated double sampling
ChR2	channelrhodopsin-2
CMOS	complementary metal-oxide semiconductor
CRT	capillary refill time
CSN	carotid sinus nerve
CTIA	capacitive feedback TIA
CW	continuous wave
DAC	digital-to-analogue converter
DCS	differential current subtraction
DDF	device definition file
DMA	direct memory access
DR	dynamic range
DRE	dynamic range enhancement
DRPR	dynamic range to power ratio
DTL	double-tail latch
ECG	electrocardiography
ECoG	electrocorticography
EDR	enhanced data rate
EEG	electroencephalography
EMG	electromyography
EOG	electrooculography
ExG	collective term for various electrodes based measurements, such as ECG, EMG, EEG and EOG
FL	fluorescence lamp
FoM	figure-of-merit
FSM	finite state machine

GBP	gain-bandwidth product
GPIO	general purpose input/output
GUI	graphical user interface
Hb	deoxyhaemoglobin
HbCO	carboxyhaemoglobin
HbO_2	oxyhaemoglobin
Hi	methehaemoglobin
I^2C	inter-IC
IA	instrumentation amplifier
IC	integrated circuit
ICG	impedance cardiography
INL	integral non-linearity
KCL	Kirchhoff's current law
LDO	low drop-out
LED	light emitting diode
LiPo	lithium polymer
MCU	microcontroller unit
MEMS	microelectromechanical systems
mHealth	mobile health
MRI	magnetic resonance imaging
NIRI	near-infrared imaging
NIRS	near-infrared spectroscopy
NpHR	Natronomonas pharaonis
NTC	negative temperature coefficient
OTA	operational transconductance amplifier
PCB	printed circuit board

PCG	phonocardiography
PD	photodiode
PPG	photoplethysmography
PRF	pulse repetition frequency
PSRR	power supply rejection ratio
PTT	pulse transit time
PULP	parallel ultra-low power
PWV	pulse wave velocity
redox	reduction-oxidation
R&D	research and development
RF	radio frequency
RMS	root mean square
RTIA	resistive feedback TIA
Rx	receiver
$S_\mathrm{a}O_2$	arterial oxygen saturation
SAR	successive approximation register
SD	secure digital
SDR	signal-to-distortion ratio
SFDR	spurious free dynamic range
SNR	signal-to-noise ratio
SoC	system-on-chip
SPI	serial peripheral interface
$S_\mathrm{p}O_2$	arterial oxygen saturation estimated by a oximeter
TIA	transimpedance amplifier
TMA-O	transimpedance medical amplifier for oximetry
Tx	transmitter
UIS	user interface software

Bibliography

[1] A. Pellicer and M. del Carmen Bravo, "Near-infrared spectroscopy: A methodology-focused review," *Seminars in Fetal & Neonatal Medicine*, vol. 16, no. 1, pp. 42–49, Feb. 2011.

[2] F. Scholkmann, S. Kleiser, A. J. Metz, R. Zimmermann, J. M. Pavia, U. Wolf, and M. Wolf, "A review on continuous wave functional near-infrared spectroscopy and imaging instrumentation and methodology," *NeuroImage*, vol. 85, no. 1, pp. 6–27, Jan. 2014.

[3] T. W. L. Scheeren, P. Schober, and L. A. Schwarte, "Monitoring tissue oxygenation by near infrared spectroscopy (NIRS): background and current applications," *Journal of Clinical Monitoring and Computing*, vol. 26, no. 4, pp. 279–287, Aug. 2012.

[4] G. Naulaers, B. Meyns, M. Miserez, V. Leunens, S. Van Huffel, P. Casaer, and H. Devlieger, "Measurement of the liver tissue oxygenation by near-infrared spectroscopy," *Intensive Care Medicine*, vol. 31, no. 1, Jan. 2005.

[5] M. Weiss, G. Schulz, I. Teller, A. Dullenkopf, A. Kolarova, H. Sailer, C. M. Dillier, H. U. Bucher, A. C. Gerber, and O. Baenzinger, "Tissue oxygenation monitoring during major pediatric surgery using transcutaneous liver near infrared spectroscopy," *Pediatric Anesthesia*, vol. 14, no. 12, Dec. 2004.

[6] G. E. Owens, K. King, J. G. Gurney, and J. R. Charpie, "Low renal oximetry correlates with acute kidney injury after infant cardiac surgery," *Pediatric Cardiology*, vol. 32, no. 2, Feb. 2011.

[7] G. M. Hoffman, N. S. Ghanayem, and J. S. Tweddell, "Non-invasive monitoring of oxygen delivery," in *Pediatric and Congenital Cardiology, Cardiac Surgery and Intensive Care*, E. M. Da Cruz, D. Ivy, and J. Jagger, Eds. Springer, 2014, vol. 1.

[8] J.-K. Choi, J.-M. Kim, G. Hwang, J. Yang, M.-G. Choi, and H.-M. Bae, "Time-divided spread-spectrum code-based 400 fw-detectable multichannel fNIRS IC for portable functional brain imaging," *IEEE Journal of Solid-State Circuits*, vol. 51, no. 2, pp. 484–495, Feb. 2016.

[9] K. Yoshino, N. Oka, K. Yamamoto, H. Takahashi, and T. Kato, "Functional brain imaging using near-infrared spectroscopy during actual driving on an expressway," *Frontiers in Human Neuroscience*, Dec. 2013.

[10] H. Karim, S. I. Fuhrman, P. Sparto, J. Furman, and T. Huppert, "Functional brain imaging of multi-sensory vestibular processing during computerized dynamic posturography using near-infrared spectroscopy," *NeuroImage*, vol. 74, Feb. 2013.

[11] G. Bale, S. Mitra, J. Meek, N. Robertson, and I. Tachtsidis, "A new broadband near-infrared spectroscopy system for in-vivo measurements of cerebral cytochrome-c-oxidase changes in neonatal brain injury," *Biomedical Optics Express*, vol. 5, no. 10, pp. 3450–3466, Sept. 2014.

[12] A. A. Alian and K. H. Shelley, "Photoplethysmography: Analysis of the pulse oximeter waveform," in *Monitoring Technologies in Acute Care Environments*, J. M. Ehrenfeld and M. Cannesson, Eds. Springer, 2013.

[13] C. C. Y. Poon and Y. T. Zhang, "Cuff-less and noninvasive measurements of arterial blood pressure by pluse transit time," *Annual Int. Conf. of the IEEE Engineering in Medicine and Biology Society (EMBC)*, pp. 5877–5880, Sept. 2005.

[14] D. B. McCombie, P. A. Shaltis, A. T. Reisner, and H. Harry Asada, "Adaptive hydrostatic blood pressure calibration: Development of a wearable, autonomous pulse wave velocity blood

pressure monitor," *Annual Int. Conf. of the IEEE Engineering in Medicine and Biology Society (EMBC)*, pp. 370–373, Aug. 2007.

[15] E. Aguilar-Peláez and E. Rodríguez-Villegas, "Low-power differential photoplethysmographic pulse transit time detector for ambulatory cardiovascular monitoring," *Proc. of IEEE Int. Symp. on Circuits and Systems (ISCAS)*, pp. 1104–1107, May 2008.

[16] J. Solà, "Continuous non-invasive blood pressure estimation," Ph.D. dissertation, ETH Zürich, Zurich, Switzerland, 2011.

[17] N. Kumar, A. Agrawal, and S. Deb, "Cuffless BP measurement using a correlation study of pulse transient time and heart rate," *Proc. of IEEE Int. Conf. on Advances in Comp., Comm. and Inf. (ICACCI)*, pp. 1538–1541, Sept. 2014.

[18] P. V. Rajesh, J. M. Valero-Sarmiento, L. Yan, A. Bozkurt, C. Van Hoof, N. Van Helleputte, R. F. Yazicioglu, and M. Verhelst, "A 172µW compressive sampling photoplethysmographic readout with embedded direct heart-rate and variability extraction from compressively sampled data," *IEEE Int. Solid-State Circuits Conf. (ISSCC) Dig. Tech. Papers*, pp. 386–387, Feb. 2016.

[19] M. Konijnenburg, S. Stanzione, L. Yan, D.-W. Jee, J. Pettine, R. van Wegberg, H. Kim, C. van Liempd, R. Fish, J. Schluessler *et al.*, "A battery-powered efficient multi-sensor acquisition system with simultaneous ECG, BIO-Z, GSR, and PPG," *IEEE Int. Solid-State Circuits Conf. (ISSCC) Dig. Tech. Papers*, pp. 480–481, Feb. 2016.

[20] L. Sant, A. Fant, S. Stojanović, S. Fabbro, and J. L. Cevallos, "A 13.2 optical proximity sensor system with 130klx ambient light rejection capable of heart rate and blood oximetry monitoring," *Proc. of IEEE European Solid-State Circuits Conf. (ESSCIRC)*, pp. 372–375, Sept. 2016.

[21] Silicon Labs, *Proximity/Ambient light sensor IC with I^2C interface*, Si1141/42/43 datasheet, May 2015, rev. 1.41.

[22] M. J. Hayes and P. R. Smith, "A new method for pulse oximetry possessing inherent insensitivity to artifact," *IEEE Trans. on Biomedical Engineering*, vol. 48, no. 4, pp. 452–461, April 2001.

[23] J. Lee, K. Matsumura, K. Yamakoshi, P. Rolfe, S. Tanaka, and T. Yamakoshi, "Comparison between red, green and blue light reflection photoplethysmography for heart rate monitoring during motion," *Annual Int. Conf. of the IEEE Engineering in Medicine and Biology Society (EMBC)*, pp. 1724–1727, July 2013.

[24] E. S. Winokur, T. O'Dwyer, and C. G. Sodini, "A low-power, dual-wavelength photoplethysmogram (PPG) SoC with static and time-varying interferer removal," *IEEE Trans. on Biomedical Circuits and Systems*, vol. 9, no. 4, pp. 581–589, Aug. 2015.

[25] M. Shokouhian, R. Morling, and I. Kale, "Interference resilient sigma delta-based pulse oximeter," *IEEE Trans. on Biomedical Circuits and Systems*, vol. 10, no. 3, pp. 623–631, June 2016.

[26] J. W. Severinghaus and P. B. Astrup, "History of blood gas analysis. VI. Oximetry," *Journal of Clinical Monitoring*, vol. 2, no. 4, pp. 270–288, Oct. 1986.

[27] F. Jöbsis, "Noninvasive, infrared monitoring of cerebral and myocardial oxygen sufficiency and circulatory parameters," *Science*, vol. 198, no. 4323, pp. 1264–1267, Dec. 1977.

[28] J. Saliba, H. Bortfeld, D. J. Levitin, and J. S. Oghalai, "Functional near-infrared spectroscopy for neuroimaging in cochlear implant recipients," *Hearing Research*, vol. 338, pp. 64–75, Aug. 2016.

[29] Q. Huang, F. Piazza, P. Orsatti, and T. Ohguro, "The impact of scaling down to deep submicron on CMOS RF circuits," *IEEE Journal of Solid-State Circuits*, vol. 33, no. 7, pp. 1023–1036, July 1998.

[30] A. A. Abidi, "RF CMOS comes of age," *IEEE Journal of Solid-State Circuits*, vol. 39, no. 4, pp. 549–561, April 2004.

[31] R. G. Haahr, S. B. Duun, M. H. Toft, B. Belhage, J. Larsen, K. Birkelund, and E. V. Thomsen, "An electronic patch for wearable health monitoring by reflectance pulse oximetry," *IEEE Trans. on Biomedical Circuits and Systems*, vol. 6, no. 1, pp. 45–53, Feb. 2012.

[32] M. A. Hernandez-Silveira, S. S. Ang, and A. Burdett, "Challenges and trade-offs involved in designing embedded algorithms for a low-power wearable wireless monitor," *International Conference on Biomedical Engineering (ICBME)*, vol. 43, pp. 416–419, Dec. 2013.

[33] PricewaterhouseCoopers, *My health, connected*, http://www.pwcmegatrends.co.uk/mylifeconnected/health.html [accessed 10-December-2016].

[34] T. Bannister, M. Liber, A. Dordai, P. Hanin, J. Hankin, N. Kinsey, and T. Salamone, *StartUp Health Insights: Digital Health Funding Rankings (Q3 2016)*, http://www.startuphealth.com [accessed: 10-December-2016], Oct. 2016.

[35] AliveCor, *Kardia Mobile*, https://www.alivecor.com [accessed: 10-December-2016].

[36] DoctorKePaas, *On Demand Healthcare at your Doorstep*, https://www.doctorkepaas.com/remotecare [accessed: 10-December-2016].

[37] P. Lamkin, *Wearable Tech Market To Be Worth $34 Billion By 2020*, http://www.forbes.com/sites/paullamkin/2016/02/17/wearable-tech-market-to-be-worth-34-billion-by-2020 [accessed: 10-December-2016], Feb. 2016.

[38] S. Shemkus, *Fitness trackers are popular among insurers and employers – but is your data safe?*, https://www.theguardian.com/lifeandstyle/2015/apr/17/fitness-trackers-wearables-insurance-employees-jobs-health-data [accessed: 11-December-2016], April 2015.

[39] R. D. Simoni, R. L. Hill, M. Vaughan, and H. Tabor, "A classic instrument: The Beckman DU spectrophotometer and its

inventor, Arnold O. Beckman," *Journal of Biological Chemistry*, vol. 278, no. 49, p. e1, Dec. 2003.

[40] J. G. Webster, *Design of Pulse Oximeters*. Taylor & Francis Group, 1997.

[41] D. F. Swinehart, "The Beer-Lambert law," *Journal of Chemical Education*, vol. 39, no. 7, pp. 333–335, July 1962.

[42] C. Blatter, *Lineare Algebra: für Ingenieure, Chemiker und Naturwissenschafter*, 2nd ed. vdf Hochschulverlag an der ETH, 1999.

[43] W. G. Zijstra, A. Buursma, and W. P. M. van der Roest, "Absorption spectra of human fetal and adult oxyhemoglobin, de-oxyhemoglobin, carboxyhemoglobin, and methemoglobin," *Clinical Chemistry*, vol. 37, no. 9, pp. 1633–1638, 1991.

[44] C. Kolyva, I. Tachtsidis, A. Ghosh, T. Moroz, C. E. Cooper, M. Smith, and C. E. Elwell, "Systematic investigation of changes in oxidized cerebral cytochrome c oxidase concentration during frontal lobe activation in healthy adults," *Biomedical Optics Express*, vol. 3, no. 10, pp. 2550–2566, 2012.

[45] W. G. Zijlstra, A. Buursma, H. E. Falke, and J. F. Catsburg, "Spectrophotometry of hemoglobin: absorption spectra of rat oxyhemoglobin, deoxyhemoglobin, carboxyhemoglobin, and methemoglobin," *Comparative Biochemistry and Physiology Part B: Comparative Biochemistry*, vol. 107B, no. 1, pp. 161–166, 1994.

[46] J. G. Kim, M. Xia, and H. Liu, "Extinction coefficients of hemoglobin for near-infrared spectroscopy of tissue," *IEEE Engineering in Medicine and Biology Magazine*, pp. 118–121, March/April 2005.

[47] D. B. Dill and D. L. Costill, "Calculation of percentage changes in volumes of blood, plasma, and red cells in dehydration," *Journal of Applied Physiology*, vol. 37, no. 2, pp. 247–248, Aug. 1974.

[48] M. W. Wukitsch, M. T. Petterson, D. R. Tobler, and J. A. Pologe, "Pulse oximetry: Analysis of theory, technology, and practice," *Journal of Clinical Monitoring*, vol. 4, no. 4, pp. 290–301, Oct. 1988.

[49] M. Touger, E. J. Gallagher, and J. Tyrell, "Relationship between venous and arterial carboxyhemoglobin levels in patients with suspected carbon monoxide poisoning," vol. 25, no. 4, pp. 481–483, April 1995.

[50] E. A. G. Goldie, "A device for the continuous indication of oxygen saturation of circulating blood in man," *Journal of Scientific Instruments*, vol. 19, no. 2, pp. 23–25, 1942.

[51] J. T. B. Moyle, *Pulse Oximetry*, 2nd ed. BMJ Books, 2002.

[52] E. H. Rubinstein and D. I. Sessler, "Skin-surface temperature gradients correlate with fingertip blood flow in humans," *Anesthesiology*, vol. 73, pp. 541–545, Sept. 1990.

[53] A. Lima and J. Bakker, "Noninvasive monitoring of peripheral perfusion," *Intensive Care Medicine*, vol. 31, no. 10, pp. 1316–1326, Oct. 2005.

[54] J. G. Webster, *Medical Instrumentation*, 4th ed. Wiley, 2010.

[55] J. P. de Kock and L. Tarassenko, "Pulse oximetry: theoretical and experimental models," *Medical and Biological Engineering and Computing*, vol. 31, no. 3, pp. 291–300, May 1993.

[56] I. Yoshiya, Y. Shimada, and K. Tanaka, "Spectrophotometric monitoring of arterial oxygen saturation in the fingertip," *Medical and Biological Engineering and Computing*, vol. 18, no. 1, pp. 27–32, Jan. 1980.

[57] B. Anderson, A.-M. Kelly, D. Kerr, M. Clooney, and D. Jolley, "Impact of patient and environmental factors on capillary refill time in adults," *The American Journal of Emergency Medicine*, vol. 26, no. 1, pp. 62–65, 2008.

[58] J. K.-J. Li, *Dynamics of the vascular system: Series on bioengineering & Biomedical Engineering.* World Scientific Publishing Company, 2004.

[59] B. E. A. Saleh and M. C. Teich, *Fundamentals of Photonics*, 2nd ed. Wiley, 2007.

[60] H. D. Hummler, A. Engelmann, F. Pohlandt, J. Högel, and A. R. Franz, "Decreased accuracy of pulse oximetry measurements during low perfusion caused by sepsis: is the perfusion index of any value?" *Intensive Care Medicine*, vol. 32, pp. 1428–1431, June 2006.

[61] M. R. Clark, "Mean corpuscular hemoglobin concentration and cell deformability," *Annals of the New York Academy of Sciences*, vol. 565, pp. 284–294, July 1989.

[62] J. Wallach, *Interpretation of Diagnostic Tests*, 8th ed. Lippincott Williams & Wilkins, 2007.

[63] V. C. Roberts, "Photoplethysmography – fundamental aspects of the optical properties of blood in motion," *Transactions of the Institute of Measurement and Control*, vol. 4, no. 2, pp. 101–106, 1982.

[64] R. Graaft, "Tissue optics applied to reflectance pulse oximetry," Ph.D. dissertation, Rijksuniversiteit Groningen, Groningen, Netherlands, 1993.

[65] R. R. Anderson and J. A. Parrish, "The optics of human skin," *Journal of Investigative Dermatology*, vol. 77, no. 1, pp. 13–19, 1981.

[66] J. Spigulis, L. Gailite, A. Lihachev, and R. Erts, "Simultaneous recording of skin blood pulsations at different vascular depths by multiwavelength photoplethysmography," *Applied Optics*, vol. 46, no. 10, pp. 1754–1759, April 2007.

[67] J. Giltvedt, A. Sira, and P. Helme, "Pulsed multifrequency photoplethysmograph," *Medical and Biological Engineering and Computing*, vol. 22, no. 3, pp. 212–215, May 1984.

[68] P. D. Mannheimer, M. E. Fein, and J. R. Casciani, "Physiooptical considerations in the design of fetal pulse oximetry sensors," *European Journal of Obstetrics & Gynecology and Reproductive Biology*, vol. 72, no. 1, pp. 9–19, March 1997.

[69] J. M. Schmitt, "Simple photon diffusion analysis of the effects of multiple scattering on pulse oximetry," *IEEE Trans. on Biomedical Engineering*, vol. 38, no. 12, pp. 1194–1203, Dec. 1991.

[70] P. D. Mannheimer, M. P. O'Neil, and E. Konecny, "The influence of larger subcutaneous blood vessels on pulse oximetry," *Journal of Clinical Monitoring and Computing*, vol. 18, pp. 179–188, 2004.

[71] P. D. Mannheimer, "The light-tissue interaction of pulse oximetry," *Anesthesia & Analgesia*, no. 6, pp. 10–17, Dec. 2007.

[72] N. Westerhof, N. Stergiopulos, and M. Noble, *Snapshots of Hemodynamics*, 2nd ed. Springer, 2010.

[73] V. K. Sud and G. S. Sekhon, "Blood flow subject to a single cycle of body acceleration," *Bulletin of Mathematical Biology*, vol. 46, no. 5/6, pp. 937–949, 1984.

[74] V. K. Sud and G. S. Sekhon, "Arterial flow under periodic body acceleration," *Bulletin of Mathematical Biology*, vol. 47, no. 1, pp. 35–52, 1985.

[75] P. Chaturani and A. S. A. Waasf Isaac, "Blood flow with body acceleration forces," *International Journal of Engineering Science*, vol. 33, no. 12, pp. 1807–1820, Oct. 1995.

[76] Y. Maeda, M. Sekine, and T. Tamura, "Relationship between measurement site and motion artifacts in wearable reflected photoplethysmography," *Journal of Medical Systems*, vol. 35, no. 5, pp. 969–976, Oct. 2011.

[77] M. J. M. Pelgrom, *Analog-to-Digital Conversion*, 2nd ed. Springer, 2012.

[78] B. Razavi, *Design of Analog CMOS Integrated Circuits*, int. ed. McGrawn-Hill, 2001.

[79] A. Kamal, J. Harness, G. Irving, and A. Mearns, "Skin photoplethysmography – a review," *Computer Methods and Programs in Biomedicine*, vol. 28, no. 4, pp. 257–269, April 1989.

[80] G. A. Holzapfel and T. C. Gasser, "A new constitutive framework for arterial wall mechanics and a comparative study of material models," *Journal of Elasticity and the Physical Science of Solids*, vol. 61, no. 1, pp. 1–48, July 2000.

[81] R. F. Rushmer, *Structure and Function of the Cardiovascular System.* Saunders, 1972.

[82] R. E. Shadwick, "Mechanical design in arteries," *Journal of Experimental Biology*, vol. 202, no. 23, pp. 3305–3313, 1999.

[83] W. W. Nichols, M. F. O'Rourke, and C. Vlachopoulos, *McDonald's Blood Flow in Arteries: Theoretical, experimental and clinical principles*, 6$^{\text{th}}$ ed. Hodder Arnold, 2011.

[84] P. B. Dobrin and A. A. Rovick, "Influence of vascular smooth muscle on contractile mechanics and elasticity of arteries," *American Journal of Physiology*, vol. 217, no. 6, pp. 1644–1651, Dec. 1969.

[85] P. Lacolley, S. N. Thornton, and Y. Bezie, "Animal models for studies of arterial stiffness," in *Blood Pressure and Arterial Wall Mechanics in Cardiovascular Diseases*, M. E. Safar, M. F. O'Rourke, and E. D. Frohlich, Eds. Springer, 2014.

[86] P. Fridez, M. Zulliger, F. Bobard, G. Montorzi, H. Miyazaki, K. Hayashi, and N. Stergiopulos, "Geometrical, functional, and histomorphometric adaptation of rat carotid artery in induced hypertension," *Journal of Biomechanics*, vol. 36, no. 5, pp. 671–680, May 2003.

[87] F. Hansen, P. Mangell, B. Sonesson, and T. Länne, "Diameter and compliance in the human common carotid artery – variations with age and sex," *Ultrasound in Medicine & Biology*, vol. 21, no. 1, pp. 1–9, 1995.

[88] S. Laurent, B. Caviezel, L. Beck, X. Girerd, E. Billaud, P. Boutouyrie, A. Hoeks, and M. Safar, "Carotid artery distensibility and distending pressure in hypertensive humans," *Hypertension*, vol. 23, pp. 878–883, 1994.

[89] R. F. Rushmer, "Structure and function of the cardiovascular system," in *Handbook of Research Methods in Cardiovascular Behavioral Medicine*, N. Schneiderman, S. M. Weiss, and P. G. Kaufmann, Eds. Springer, 1982, pp. 5–22.

[90] B. B. Lieber, "Arterial macrocirculatory hemodynamics," in *Biomechanics: Principles and Applications*, D. J. Schneck and J. D. Bronzino, Eds. CRC Press, 2002, pp. 205–214.

[91] J. Crighton Bramwell and A. V. Hill, "The velocity of the pulse wave in man," *Proc. of the Royal Society of London*, vol. 93, no. 652, pp. 298–306, April 1922.

[92] M. Zamir, *Hemo-Dynamics*. Springer, 2016.

[93] A. A. Mangoni, L. Mircoli, C. Giannattasio, A. U. Ferrari, and G. Mancia, "Heart rate-dependence of arterial distensibility in vivo," *Journal of Hypertension*, vol. 14, no. 7, pp. 897–901, July 1996.

[94] P. Lantelme, C. Mestre, M. Lievre, A. Gressard, and H. Milon, "Heart rate: An important confounder of pulse wave velocity assessment," *Hypertension*, vol. 39, pp. 1083–1087, 2002.

[95] C. S. Hayward, A. P. Avolio, and M. F. O'Rourke, "Arterial pulse wave velocity and heart rate," *Hypertension*, vol. 40, pp. e8–e9, 2002.

[96] I. Tan, M. Butlin, Y. Y. Liu, K. Ng, and A. P. Avolio, "Heart rate dependence of aortic pulse wave velocity at different arterial pressures in rats," *Hypertension*, vol. 60, pp. 528–533, 2012.

[97] A. Redheuil, W.-C. Yu, C. O. Wu, E. Mousseaux, A. de Cesare, R. Yan, N. Kachenoura, D. Bluemke, and J. A. C. Lima, "Reduced ascending aortic strain and distensibility: Earliest manifestations of vascular aging in humans," *Hypertension*, vol. 55, pp. 319–326, 2010.

[98] J. Calabia, P. Torguet, M. Garcia, I. Garcia, N. Martin, B. Guasch, D. Faur, and M. Vallés, "Doppler ultrasound in the measurement of pulse wave velocity: agreement with the Complior method," *Cardiovascular Ultrasound*, vol. 9, no. 1, p. 1, 2011.

[99] L. Joly, C. Perret-Guillaume, A. Kearney-Schwartz, P. Salvi, D. Mandry, P.-Y. Marie, G. Karcher, P. Rossignol, F. Zannad, and A. Benetos, "Pulse wave velocity assessment by external nonivasive devices and phase-contrast magnetic resonance imaging in the obese," *Hypertension*, vol. 54, pp. 421–426, 2009.

[100] J. Solà, O. Chételat, C. Sartori, Y. Allemann, and S. F. Rimoldi, "Chest pulse-wave velocity: a novel approach to assess arterial stiffness," *IEEE Trans. on Biomedical Engineering*, vol. 58, no. 1, pp. 215–223, 2011.

[101] A. P. Avolio, S.-G. Chen, R.-P. Wang, C.-L. Zhang, M.-F. Li, and M. O'Rourke, "Effects of aging on changing arterial compliance and left ventricular load in a northern Chinese urban community," *Circulation*, vol. 68, pp. 50–58, 1983.

[102] A. Benetos, C. Adamopoulos, J.-M. Bureau, M. Temmar, C. Labat, K. Bean, F. Thomas, B. Pannier, R. Asmar, M. Zureik *et al.*, "Determinants of accelerated progression of arterial stiffness in normotensive subjects and in treated hypertensive subjects over a 6-year period," *Circulation*, vol. 105, pp. 1202–1207, 2002.

[103] R. Brandes and R. Busse, "Kreislauf," in *Physiologie des Menschen: mit Patophysiologie*, 31st ed., R. F. Schmidt, F. Lang, and M. Heckmann, Eds. Springer, 2011.

[104] G. Parati, J. L. Izzo, and B. Gavish, "Respiration and blood pressure," in *Hypertension Primer: The Essentials of High*

Blood Pressure, J. L. Izzo and H. R. Black, Eds. Lippincott Williams & Wilkins, 2003, pp. 117–120.

[105] M. V. Pitzalis, F. Mastropasqua, F. Massari, A. Passantino, R. Colombo, A. Mannarini, C. Forleo, and P. Rizzon, "Effect of respiratory rate on the relationships between RR interval ans systolic blood pressure flucutations: a frequency-dependent phenomenon," *Cardiovascular Research*, vol. 38, pp. 332–339, 1998.

[106] S. Fateh, P. Schönle, L. Bettini, G. Rovere, L. Benini, and Q. Huang, "A reconfigurable 5-to-14 bit SAR ADC for battery-powered medical instrumentation," *IEEE Trans. on Circuits and Systems – I: Regular Papers*, vol. 62, no. 11, pp. 2685–2694, Nov. 2015.

[107] E. D. Chan, M. M. Chan, and M. M. Chan, "Pulse oximetry: Understanding its basic principles facilitates appreciation of its limitations," *Respiratory Medicine*, vol. 107, pp. 789–799, March 2013.

[108] J. R. Feiner, J. W. Severinghaus, and P. E. Bickler, "Dark skin decreases the accuracy of pulse oximeters at low oxygen saturation: The effects of oximeter probe type and gender," *Anesthesia & Analgesia*, vol. 105, no. 6, pp. S18–S23, Dec. 2007.

[109] K. H. Shelley, "Photoplethysmography: Beyond the calculation of arterial oxygen saturation and heart rate," *Anesthesia & Analgesia*, vol. 105, no. 6, pp. S31–S36, Dec. 2007.

[110] J. Hinkelbein, H. V. Genzwuerker, R. Sogl, and F. Fiedler, "Effect of nail polish on oxygen saturation determination by pulse oximetry in critically ill patients," *Resuscitation*, vol. 72, no. 1, pp. 82–91, June 2007.

[111] S. J. Barker, J. Curry, D. Redford, and S. Morgan, "Measurement of carboxyhemoglobin and methemoglobin by pulse oximetry," *Anesthesiology*, vol. 105, no. 5, pp. 892–897, Nov. 2006.

[112] M. Verhovsek, M. P. A. Henderson, G. Cox, H. Luo, M. H. Steinberg, and D. H. K. Chui, "Unexpectedly low pulse oximetry measurements associated with variant hemoglobins: A systematic review," *American Journal of Hematology*, vol. 85, no. 11, pp. 882–885, Nov. 2010.

[113] A. Piñero, J. Illana, C. García-Palenciano, F. Cañizares, M. Canteras, V. Cañadillas, E. Durán, and P. Parrilla, "Effect on oximetry of dyes used for sentinel lymph node biopsy: Are there differences?" *Archives of Surgery*, vol. 139, no. 11, pp. 1204–1207, Nov. 2004.

[114] M. S. Scheller, R. J. Unger, and M. J. Kelner, "Effects of intravenously administered dyes on pulse oximetry," *Anesthesiology*, vol. 65, no. 5, pp. 550–552, Nov. 1986.

[115] Y. Mendelson, D. K. Dao, and K. H. Chon, "Multi-channel pulse oximetry for wearable physiological monitoring," *IEEE Int. Conf. on Body Sensor Networks (BSN)*, May 2013.

[116] K. H. Shelly, D. Tamai, D. Jablonka, M. Gesquiere, R. G. Stout, and D. G. Silverman, "The effect of venous pulsation on the forehead pulse oximeter wave form as a possible source of error in $S_{\mathrm{p}}O_2$ calculation," *Anesthesia & Analgesia*, no. 3, pp. 743–747, March 2005.

[117] M. R. Macknet, M. Allard, R. L. Applegate, and J. Rook, "The accuracy of noninvasive and continuous total hemoglobin measurement by pulse co-oximetry in human subjects undergoing hemodilution," *Anesthesia & Analgesia*, vol. 111, no. 6, pp. 1424–1426, Dec. 2010.

[118] S. J. Matcher, C. E. Elwell, C. E. Cooper, M. Cope, and D. T. Delpy, "Performance comparison of several published tissue near-infrared spectroscopy algorithms," *Analytical Biochemistry*, vol. 227, no. 1, pp. 54–68, May 1995.

[119] G. Sjøgaard, L. Rosendal, J. Kristiansen, A. K. Blangsted, J. Skotte, B. Larsson, B. Gerdle, B. Saltin, and K. Søgaard, "Muscle oxygenation and glycolysis in females with trapezius

myalgia during stress and repetitive work using microdialysis and NIRS," *European Journal of Applied Physiology*, vol. 108, no. 4, pp. 657–669, Nov. 2010.

[120] D. M. Hueber, S. Fantini, A. E. Cerussi, and B. Barbieri, "New optical designs for absolute (self-calibrating) NIR tissue hemoglobin measurements," *Proc. SPIE Conference on Optical Tomography and Spectroscopy of Tissue*, vol. 3597, pp. 618–631, Dec. 1999.

[121] Advanced Photonix Inc., *Photodiode in Plastic Surface Mount Package*, PDB-C171SM datasheet, Feb. 2007, rev. 2/13/07.

[122] Advanced Photonix Inc., *Photodiode in Plastic Surface Mount Package*, PDB-C152SM datasheet, Feb. 2012, rev. 2/1/12.

[123] Everlight Electronics Co., *Silicon PIN Photodiode*, PD15-22C/TR8 datasheet, Sept. 2007, rev. 1.

[124] Light Avenue, *Premium Edition PIN diode 26 mil*, LA PD26HP1 datasheet, March 2016, rev. 1.2.

[125] A. Yadav, *Solid State Devices and Circuits*. University Science Press - Laxmi Publications, 2008.

[126] D. A. Neamen, *Semiconductor Physics and Devices*, 3rd ed. McGrawn-Hill, 2003.

[127] Bivar, *Surface mount LED ultraviolet, 0603 package*, SM0603UV-395 datasheet, June 2014, rev. A.

[128] Lite-On, LTST-C193TBKT-5A datasheet, June 2012.

[129] Lite-On, *SMD LED: Product Data Sheet*, LTST-C193KGKT-5A datasheet, March 2007.

[130] Lite-On, *SMD LED: Product Data Sheet*, LTST-C193KSKT-5A datasheet, April 2007.

[131] Lite-On, *SMD LED: Product Data Sheet*, LTST-C193KFKT-5A datasheet, Oct. 2010.

[132] Lite-On, LTST-C193KRKT-2A datasheet, Oct. 2012.

[133] Lite-On, LTST-C170CKT datasheet, March 2003.

[134] Everlight Electronics Co., *0.8mm height flat top infrared LED*, HIR19-21C/L11/TR8 datasheet, June 2013, rev. 4.

[135] Everlight Electronics Co., *0.8mm height flat top infrared LED*, SIR19-21C/TR8 datasheet, June 2013, rev. 3.

[136] Everlight Electronics Co., *0.8mm height flat top infrared LED*, IR19-21C/TR8 datasheet, June 2013, rev. 3.

[137] Seoul Semiconductor, *Mid power LED - 2525 series*, STB0FS12A, March 2014, rev. 00.

[138] F. Reifegerste and J. Lienig, "Modelling of the temperature and current dependence of LED spectra," *Journal of Light & Visual Environment*, vol. 32, no. 3, pp. 18–24, 2008.

[139] Y. Gu, N. Narendran, T. Dong, and H. Wu, "Spectral and luminous efficacy change of high-power LEDs under different dimming methods," *Proc. SPIE: Sixth Internaltional Conference on Solid State Lighting*, vol. 63370, pp. 1–7, Aug. 2006.

[140] Luna Optoelectronics, *GaAlAs high power dual IR LED emitters*, APW-MW2-1210-010, April 2016, rev. 01-04-16.

[141] K. J. Reynolds, J. P. D. Kock, L. Tarassenko, and J. T. B. Moyle, "Temperature dependence of LED and its theoretical effect on pulse oximetry," *British Journal of Anaesthesia*, vol. 67, no. 5, pp. 638–643, 1991.

[142] A. Van der Ziel, "Noise in solid-state devices and lasers," *Proc. of the IEEE*, vol. 58, no. 8, pp. 1178–1206, Aug. 1970.

[143] V. Palenskis, J. Matukas, and S. Pralgauskaitė, "Light-emitting diode quality investigation via low-frequency noise characteristics," *Solid-State Electronics*, vol. 54, no. 8, pp. 781–786, Aug. 2010.

[144] V. Palenskis, J. Matukas, S. Pralgauskaitė, and B. Šaulys, "A detail analysis of electrical and optical fluctuations of green light-emitting diodes by correlation method," *Fluctuation and Noise Letters*, vol. 9, no. 2, pp. 179–192, June 2010.

[145] K. N. Glaros and E. M. Drakakis, "A sub-mW fully-integrated pulse oximeter front-end," *IEEE Trans. on Biomedical Circuits and Systems*, vol. 7, no. 3, pp. 363–375, June 2013.

[146] A. Boucouvalas, "Indoor ambient light noise and its effect on wireless optical links," *IEE Proc. - Optoelectronics*, vol. 143, no. 6, pp. 334–338, Dec. 1996.

[147] S. Fateh, "Calibration techniques for digitally assisted Nyquist-rate ADCs," Ph.D. dissertation, ETH Zürich, Zurich, Switzerland, 2016.

[148] W. M. Sansen, *Analog Design Essentials*. Springer, 2006.

[149] D. A. Johns and K. Martin, *Analog Integrated Circuit Design*. Wiley, 1997.

[150] J. R. Pierce, "Physical sources of noise," *Proc. of the IRE*, vol. 44, no. 5, pp. 601–608, May 1956.

[151] R. Kaputsa, H. Zhu, and C. Lyden, "Sampling circuits that break the kT/C thermal noise limit," *IEEE Journal of Solid-State Circuits*, vol. 49, no. 8, pp. 1694–1701, Aug. 2014.

[152] J. L. McCreary, "Successive approximation analog-to-digital conversion in MOS integrated circuits," Ph.D. dissertation, University of California, Berkeley, CA, USA, 1975.

[153] J. L. McCreary and P. R. Gray, "All-MOS charge redistribution analog-to-digital conversion techniques – Part I," *IEEE Journal of Solid-State Circuits*, vol. 10, no. 6, pp. 371–379, Dec. 1975.

[154] V. Hariprasath, J. Guerber, S.-H. Lee, and U.-K. Moon, "Merged capacitor switching based SAR ADC with highest switching energy-efficiency," *Electronics Letters*, vol. 46, no. 9, pp. 620–621, 2010.

[155] D. Schinkel, E. Mensink, E. Klumperink, E. van Tuijl, and B. Nauta, "A double-tail latch-type voltage sense amplifier with 18ps setup+hold time," *IEEE Int. Solid-State Circuits Conf. (ISSCC) Dig. Tech. Papers*, pp. 314–315, Feb. 2007.

[156] H. Jeon and Y.-B. Kim, "A CMOS low-power low-offset and high-speed fully dynamic latched comparator," *Proc. of IEEE Int. SOC Conf.*, pp. 285–288, Sept. 2010.

[157] Y.-H. Chung, M.-H. Wu, and H.-S. Li, "A 12-bit 8.47fJ/conversion-step capacitor-swapping SAR ADC in 110-nm CMOS," *IEEE Trans. on Circuits and Systems – I: Regular Papers*, vol. 62, no. 1, pp. 10–18, Jan. 2015.

[158] T. Sepke, "Comparator design and analysis for comparator-based switched-capacitor circuits," Ph.D. dissertation, Massachusetts Institute of Technology (MIT), Cambridge, MA, USA, 2006.

[159] M. Ahmadi and W. Namgoong, "Comparator power reduction in low-frequency SAR ADC using optimized vote allocation," *IEEE Trans. on Very Large Scale Integration (VLSI) Systems*, vol. 23, no. 11, pp. 2384–2394, 2015.

[160] A. Hastings, *The Art of Analog Layout*, 2nd ed. Pearson Prentice Hall, 2006.

[161] B. Razavi, *Principles of Data Conversion System Design.* IEEE Press, 1995.

[162] Stanford Research Systems, *Model DS360 Ultra Low Distortion Function Generator: Operating Manual and Programming Reference*, May 2016, rev. 2.6.

[163] Maxim Integrated, *Pulse Oximeter and Heart-Rate Sensor IC for Wearable Health*, MAX30100 datasheet, Sept. 2014, rev. 0.

[164] L. Sant, A. Fant, S. Stojanović, S. Fabbro, and J. L. Cevallos, "A 13.2 b optical proximity sensor system with 130 klx ambient light rejection capable of heart rate and blood oximetry monitoring," *IEEE Journal of Solid-State Circuits*, vol. 51, no. 7, pp. 1674–1683, July 2016.

[165] Texas Instruments, *AFE4400 Integrated analog front-end for heart rate monitors and low-cost pulse oximeters*, SBAS601H, Dec. 2012, rev. July 14.

[166] Texas Instruments, *AFE4490 Integrated analog front-end for pulse oximeters*, SBAS602H, Dec. 2012, rev. Oct. 14.

[167] Texas Instruments, *AFE4403 Ultra-small, integrated analog front-end for heart rate monitors and low-cost pulse oximeters*, SBAS650B, May 2014, rev. July 14.

[168] Texas Instruments, *AFE4404 Ultra-small, integrated AFE for wearable, optical, heart-rate monitoring and bio-sensing*, SBAS689C, June 2015, rev. May 16.

[169] M. Konijnenburg, S. Stanzione, L. Yan, D.-W. Jee, J. Pettine, R. van Wegberg, H. Kim, C. van Liempd, R. Fish, J. Schluessler *et al.*, "A multi(bio)sensor acquisition system with integrated processor, power management, 8 × 8 LED drivers, and simultaneously synchronized ECG, BIO-Z, GSR, and two PPG readouts," *IEEE Journal of Solid-State Circuits*, vol. 51, no. 11, pp. 2584–2595, Nov. 2016.

[170] Maxim Integrated, *High-Sensitivity Pulse Oximeter and Heart-Rate Sensor for Wearable Health*, MAX30102 datasheet, Sept. 2015, rev. 0.

[171] P. Schönle, F. Schulthess, S. Fateh, R. Ulrich, F. Huang, T. Burger, and Q. Huang, "A DC-connectable multi-channel biomedical data acquisition ASIC with mains frequency cancellation," *Proc. of IEEE European Solid-State Circuits Conf. (ESSCIRC)*, pp. 149–152, Sept. 2013.

[172] X. Han, T. Burger, and Q. Huang, "An output-capacitor-free adaptively biased LDO regulator with robust frequency compensation in 0.13 µm CMOS for SoC application," *Proc. of IEEE Int. Symp. on Circuits and Systems (ISCAS)*, pp. 2699–2702, May 2016.

[173] OpenRISC Community, *OpenRISC project overview*, http://openrisc.io [accessed 06-November-2016].

[174] M. Gautschi et al., "Tailoring instruction-set extensions for an ultra-low power tightly-coupled cluster of OpenRISC cores," *IFIP/IEEE Int. Conf. Very Large Scale Integration (VLSI-SoC)*, pp. 25–30, Oct. 2015.

[175] F. K. Gürkaynak, R. Schilling, M. Muehlberghuber, F. Conti, S. Mangard, and L. Benini, "Multi-core data analytics SoC with a flexible 1.76 Gbit/s AES-XTS cryptographic accelerator in 65 nm CMOS," *Proc. Workshop on Cryptography and Security in Computing Systems*, pp. 19–24, Jan. 2017.

[176] ETH Zürich and University of Bologna, *PULP: parallel ultra low power*, http://www.pulp-platform.org [accessed 06-November-2016].

[177] F. Conti, D. Rossi, A. Pullini, I. Loi, and L. Benini, "Energy-efficient vision on the PULP platform for ultra-low power parallel computing," *IEEE Workshop on Signal Processing Systems (SiPS)*, pp. 1–6, 2014.

[178] M. Gautschi, D. Rossi, and L. Benini, "Customizing an open source processor to fit in an ultra-low power cluster with a shared L1 memory," *Proc. of ACM Great Lakes Symposium on VLSI (GLSVLSI)*, pp. 87–88, 2014.

[179] P. Schönle, P. Bunjaku, S. Fateh, and Q. Huang, "Modular multi-sensor platform for portable and wireless medical instrumentation," *Proc. of IEEE Biomedical Circuits and Systems Conference (BioCAS)*, pp. 165–168, Oct. 2014.

[180] GlaxoSmithKline, *Bioelectronics R&D*, http://www.gsk.com/en-gb/partnerships/bioelectronics-research-network/#bioelectronics-innovation-challenge [accessed 06-November-2016].

[181] Q. Huang and C. Menolfi, "A 200 nV offset 6.5 nV/$\sqrt{\text{Hz}}$ noise PSD 5.6 kHz chopper instrumentation amplifier in 1 µm digital cmos," *IEEE Int. Solid-State Circuits Conf. (ISSCC) Dig. Tech. Papers*, pp. 362–363, Feb. 2001.

[182] R. B. Stein, T. R. Nichols, J. Jhamandas, L. Davis, and D. Charles, "Stable long-term recordings from cat perihperal nerves," *Brain Research*, vol. 128, no. 1, pp. 21–38, Sept. 1976.

[183] J. A. Hoffer, G. E. Loeb, and C. A. Pratt, "Single unit conduction velocities form averaged nerve cuff electrode records in freely moving cats," *Journal of Neuroscience Methods*, vol. 4, no. 3, pp. 211–225, Oct. 1981.

[184] X. Kang, J.-Q. Liu, H. Tian, B. Yang, Y. Nuli, and C. Yang, "Self-closed parylene cuff electrode for peripheral nerve recording," *Journal of Microelectromechanical Systems*, vol. 24, no. 2, pp. 319–332, April 2015.

[185] R. Yazicioglu, P. Merken, R. Puers, and C. Van Hoof, "A 200 µW eight-channel EEG acquisition ASIC for ambulatory EEG systems," *IEEE Journal of Solid-State Circuits*, vol. 43, no. 12, pp. 3025–3038, Dec. 2008.

[186] R. Muller, S. Gambini, and J. Rabaey, "A 0.013 mm^2, 5 µW, DC-coupled neural signal acquisition IC with 0.5 V supply," *IEEE Journal of Solid-State Circuits*, vol. 47, no. 1, pp. 232–243, Jan. 2012.

[187] C. R. Noback, N. L. Strominger, R. J. Demarest, and D. A. Ruggiero, *The Human Nervous System*, 6^{th} ed. Humana Press, 2005.

[188] P. J. Basser and B. J. Roth, "New currents in electrical stimulation of excitable tissues," *Annual Review of Biomedical Engineering*, vol. 2, pp. 377–397, Aug. 2000.

[189] C. van den Honert, "A technique for collision block of peripheral nerve: Single stimulus analysis," *IEEE Trans. on Biomedical Engineering*, vol. 28, no. 5, pp. 373–378, May 1981.

[190] J. D. Sweeney and T. Mortimer, "An asymmetric two electrode cuff for generation of unidirectionally propagated action potentials," *IEEE Trans. on Biomedical Engineering*, vol. 33, no. 6, pp. 541–549, June 1986.

[191] N. Pour Aryan, H. Kaim, and A. Rothermel, *Stimulation and recording electrodes for neural prostheses*, ser. SpringerBriefs in Electrical and Computer Engineering. Springer, 2015.

[192] D. R. Merrill, "Electrical stimulation of excitable tissue: design of efficacious and safe protocols," *Journal of Neuroscience Methods*, vol. 141, no. 2, pp. 171–198, Feb. 2005.

[193] S. F. Cogan, "Neural stimulation and recording electrodes," *Annual Review of Biomedical Engineering*, vol. 10, pp. 275–309, Aug. 2008.

[194] J.-J. Sit and R. Sarpeshkar, "A low-power blocking-capacitor-free charge-balanced electrode-stimulator chip with less than 6 nA DC error for 1-mA full-scale stimulation," *IEEE Trans. on Biomedical Circuits and Systems*, vol. 1, no. 3, pp. 172–183, Sept. 2007.

[195] C.-L. Lee and C.-C. Hsieh, "A 0.8V 64x64 CMOS imager with integrated sense-and-stimulus pixel for artificial retina applications," *IEEE Asian Solid-State Circuits Conference (A-SSCC)*, pp. 192–196, Nov. 2011.

[196] R. P. Williamson and B. J. Andrews, "Localized electrical nerve blocking," *IEEE Trans. on Biomedical Circuits and Systems*, vol. 52, no. 3, pp. 362–370, March 2005.

[197] P. Schönle, F. Michoud, N. Brun, A. Guex, S. P. Lacour, Q. Wang, and Q. Huang, "A wireless system with stimulation and recording capabilities for interfacing peripheral nerves in rodents," *Annual Int. Conf. of the IEEE Engineering in Medicine and Biology Society (EMBC)*, pp. 4439–4442, Aug. 2016.

[198] H. Sherk and E. J. Wilkinson, "A novel system for recording from single neurons in unrestrained animals," *Journal of Neuroscience Methods*, vol. 173, no. 2, pp. 201–207, Aug. 2008.

[199] T. A. Szuts, V. Fadeyev, S. Kachiguine, A. Sher, M. V. Grivich, M. Agrochão, P. Hottowy, W. Dabrowski, E. V. Lubenov, A. G. Siapas *et al.*, "A wireless multi-channel neural amplifier for

freely moving animals," *Nature Neuroscience*, vol. 14, no. 2, pp. 263–270, Feb. 2011.

[200] K. A. Ng, E. Greenwald, Y. P. Xu, and N. V. Thakor, "Implantable neurotechnologies: a review of integrated circuit neural amplifiers," *Medical and Biological Engineering and Computing*, vol. 54, no. 1, pp. 45–62, Jan. 2016.

[201] S. Raspopovic, M. Capogrosso, F. M. Petrini, M. Bonizzato, J. Rigosa, G. Di Pino, J. Carpaneto, M. Controzzi, T. Boretius, E. Fernandez *et al.*, "Restoring natural sensory feedback in real-time bidirectional hand prostheses," *Science Translational Medicine*, vol. 6, no. 222, Feb. 2014.

[202] S. P. Lacour, S. Benmerah, E. Tarte, J. FitzGerald, J. Serra, S. McMahon, J. Fawcett, O. Graudejus, Z. Yu, and B. Morrison, "Flexible and stretchable micro-electrodes for in vitro and in vivo neural interfaces," *Medical and Biological Engineering and Computing*, vol. 48, no. 10, pp. 945–954, Oct. 2010.

[203] P. Gad, J. Choe, M. S. Nandra, H. Zhong, R. R. Roy, Y.-C. Tai, and V. R. Edgerton, "Development of a multi-electrode array for spinal cord epidural stimulation to facilitate stepping and standing after a complete spinal cord injury in adult rats," *Journal of NeuroEngineering and Rehabilitation*, vol. 10, no. 2, Jan. 2013.

[204] K. Kumar, R. S. Taylor, L. Jacques, S. Eldabe, M. Meglio, J. Molet, S. Thomson, J. O'Callaghan, E. Eisenberg, G. Milbouw *et al.*, "Spinal cord stimulation versus conventional medical management for neuropathic pain: A multicentre randomised controlled trial in patients with failed back surgery syndrome," *Pain*, vol. 132, no. 1–2, pp. 179–188, Nov. 2007.

[205] S. Jezernik, M. Craggs, W. M. Grill, G. Creasey, and N. J. M. Rijkhoff, "Electrical stimulation for the treatment of bladder dysfunction: Current status and future possibilities," *Neurological Research*, vol. 24, no. 5, pp. 413–430, 2002.

[206] F.-G. Zeng, S. Rebscher, X. Sun, and H. Feng, "Cochlear implants: System design, integration, and evaluation," *IEEE Reviews in Biomedical Engineering*, vol. 1, pp. 115–142, 2008.

[207] C. M. Steele, A. T. Thrasher, and M. R. Popovic, "Electric stimulation approaches to the restoration and rehabilitation of swallowing: a review," *Neurological Research*, vol. 29, no. 1, pp. 9–15, 2007.

[208] I. J. M. Scheffers, A. A. Kroon, and P. W. de Leeuw, "Carotid baroreflex activation: Past, present, and future," *Current Hypertension Reports*, vol. 12, no. 2, pp. 61–66, April 2010.

[209] T. Alnima, P. W. de Leeuw, and A. A. Kroon, "Baropacing as a new option for treatment of resistant hypertension," *European Journal of Pharmacology*, vol. 763, pp. 23–27, Sept. 2015.

[210] D. Ho, X. Zhao, S. Gao, C. Hong, D. E. Vatner, and S. F. Vatner, "Heart rate and electrocardiography monitoring in mice," *Current Protocols in Mouse Biology*, vol. 1, pp. 123–139, March 2011.

[211] R. C. Pinnell, J. Dempster, and J. Pratt, "Miniature wireless recording and stimulation system for rodent behavioural testing," *Journal of Neural Engineering*, vol. 12, no. 6, Aug. 2015.

[212] P. Ruther, T. Holzhammer, S. Herwik, P. D. Rich, J. W. Dalley, O. Paul, and T. Holtzman, "Compact wireless neural recording system for small animals using silicon-based probe arrays," *Annual Int. Conf. of the IEEE Engineering in Medicine and Biology Society (EMBC)*, pp. 2284–2287, Sept. 2011.

[213] D. Fan, D. Rich, T. Holtzman, P. Ruther, J. W. Dalley, A. Lopez, M. A. Rossi, J. W. Barter, D. Salas-Meza, S. Herwik *et al.*, "A wireless multi-channel recording system for freely behaving mice and rats," *PLoS one*, vol. 6, no. 7, July 2011.

[214] G. N. Angotzi, F. Boi, S. Zordan, A. Bonfanti, and A. Vato, "A programmable closed-loop recording and stimulating wireless system for behaving small laboratory animals," *Scientific Reports*, vol. 4, Aug. 2014.

[215] Nordic Semiconductor, *Multiprotocol Bluetooth low energy/2.4GHz RF system on chip*, nRF51822 product specification, 2014, rev. 3.1.

[216] Micron Technology, *Micron Serial NOR Flash Memory*, N25Q00AA datasheet, Oct. 2011, rev. M.

[217] Giga Device, *SPI (x1/x2/x4) NAND Flash*, GD5F4GQ4xC datasheet, March 2015, rev. 1.4.

[218] M. R. Warden, J. A. Cardin, and K. Deisseroth, "Optical neural interfaces," *Annual Review of Biomedical Engineering*, vol. 16, pp. 103–129, July 2014.

[219] C. Towne, K. L. Montgomery, S. M. Iyer, K. Deisseroth, and S. L. Delp, "Optogenetic control of targeted peripheral axons in freely moving animals," *PLoS one*, vol. 8, no. 8, Aug. 2013.

[220] C. T. Wentz, J. G. Bernstein, P. Monahan, A. Guerra, A. Rodriguez, and E. S. Boyden, "A wirelessly powered and controlled device for optical neural control of freely-behaving animals," *Journal of Neural Engineering*, June 2011.

[221] T. Kim, J. G. McCall, Y. H. Jung, X. Huang, E. R. Siuda, Y. Li, Y. M. Song, H. A. Pao, R.-H. Kim, C. Lu *et al.*, "Injectable, cellular-scale optoelectronics with applications for wireless optogenetics," *Science*, vol. 340, no. 6129, pp. 211–216, April 2013.

[222] K. L. Montgomery, A. J. Yeh, J. S. Ho, V. Tsao, S. M. Iyer, L. Grosenick, E. A. Ferenczi, Y. Tanabe, K. Deisseroth, S. L. Delp *et al.*, "Wirelessly powered, fully internal optogenetics for brain, spinal and peripheral circuits in mice," *Nature Methods*, vol. 12, no. 10, pp. 969–974, Oct. 2015.

[223] M. A. Rossi, V. Go, T. Murphy, Q. Fu, J. Morizio, and H. H. Yin, "A wirelessly controlled implantable LED system for deep brain optogenetic stimulation," *Frontiers in Integrative Neuroscience*, vol. 9, Feb. 2015.

[224] Nordic Semiconductor, *Multiprotocol Bluetooth low energy, ANT/ANT+ and 2.4GHz proprietary System-on-Chip*, nRF52832 product brief, 2016, rev. 1.4.

[225] S. Ayub, F. Barz, O. Paul, and P. Ruther, "Heterogeneous 3D optrode with variable spatial resolution for optogenetic stimulation and electrophysiological recording," *Annual Int. Conf. of the IEEE Engineering in Medicine and Biology Society (EMBC)*, pp. 1762–1765, Aug. 2016.

[226] G. Gagnon-Turcotte, A. A. Kisomi, R. Ameli, C.-O. D. Camaro, Y. LeChasseur, J.-L. Néron, P. B. Bareil, P. Fortier, C. Bories, Y. de Koninck *et al.*, "A wireless optogenetic headstage with multichannel electrophysiological recording capability," *Sensors*, vol. 15, pp. 22 776–22 797, Sept. 2015.

[227] S. Reichelt, J. Fiala, A. Werber, K. Förster, C. Heilmann, R. Klemm, and H. Zappe, "Development of an implantable pulse oximeter," *IEEE Trans. on Biomedical Engineering*, vol. 55, no. 2, pp. 581–588, Feb. 2008.

[228] P. Bingger, J. Fiala, A. Seifert, N. Weber, A. Moser, F. Goldschmidtboeing, K. Foerster, C. Heilmann, F. Beyersdorf, P. Woias *et al.*, "Implantable multi sensor system for in vivo monitoring of cardiovascular parameters," *Int. Solid-State Sensors, Actuators and Microsystems Conf. (TRANSDUCERS)*, pp. 1469–1472, June 2009.

[229] M. N. Ericson, M. A. Wilson, G. L. Coté, C. L. Britton, W. Xu, J. S. Baba, M. Bobrek, M. S. Hileman, M. R. Moore, and S. S. Frank, "Development of an implantable oximetry-based organ perfusion sensor," *Annual Int. Conf. of the IEEE Engineering in Medicine and Biology Society (EMBC)*, pp. 2235–2238, Sept. 2004.

[230] T. J. Akl, M. A. Wilson, M. N. Ericson, E. Farquhar, and G. L. Coté, "Wireless monitoring of liver hemodynamics in vivo," *PLoS one*, vol. 9, no. 7, July 2014.

[231] T. Yamakawa, T. Inoue, Y. He, M. Fujii, M. Suzuki, and M. Niwayama, "Development of an implantable flexible probe

for simultaneous near-infrared spectroscopy and electrocorticography," *IEEE Trans. on Biomedical Engineering*, vol. 61, no. 2, pp. 388–395, Feb. 2014.

[232] D. T. T. Plachta, M. Gierthmuehlen, O. Cota, N. Espinosa, F. Boeser, T. C. Herrera, T. Stieglitz, and J. Zentner, "Blood pressure control with selective vagal nerve stimulation and minimal side effects," *Journal of Neural Engineering*, vol. 11, no. 3, May 2014.

[233] Light Avenue, *Premium Edition Hyper Red 12 mil*, LA HR12WP5 datasheet, May 2015, rev. 1.1.

[234] Light Avenue, *Premium Edition Mid Infrared 12 mil*, LA MI12WP4 datasheet, May 2015, rev. 1.1.

[235] S. I. Park, D. S. Brenner, G. Shin, C. D. Morgan, B. A. Copits, H. U. Chung, M. Y. Pullen, K. N. Noh, S. Davidson, S. J. Oh *et al.*, "Soft, strechable, fully implantable miniaturized optoelectronic systems for wireless optogenetics," *Nature Biotechnology*, vol. 33, no. 12, pp. 1281–1286, Dec. 2015.

[236] T. Yokota, P. Zalar, M. Kaltenbrunner, H. Jinno, N. Matsuhisa, H. Kitanosako, Y. Tachibana, W. Yukita, M. Koizumi, and T. Someya, "Ultraflexible organic photonic skin," *Science Advances*, vol. 2, no. 4, p. e1501856, April 2016.

[237] Q. Wang, H. R. Brunner, and M. Burnier, "Determination of cardiac contractility in awake unsedated mice with a fluid-filled catheter," *American Journal of Physiology*, vol. 286, no. 2, pp. H806–H814, Feb. 2004.

[238] Data Sciences International (DSI), *PhysioTel HD: Enabling New Research Possibilities*, product brochure, 2015.

[239] M. Theodor, J. Fiala, D. Ruh, K. Förster, C. Heilmann, F. Beyersdorf, Y. Manoli, H. Zappe, and A. Seifert, "Implantable accelerometer system for the determination of blood pressure using reflected wave transit time," *Sensors and Actuators A: Physical*, vol. 206, pp. 151–158, Feb. 2014.

[240] P. Cong, N. Chaimanonart, W. H. Ko, and D. J. Young, "A wireless and batteryless 10-bit implantable blood pressure sensing microsystem with adaptive RF powering for real-time laboratory mice monitoring," *IEEE Journal of Solid-State Circuits*, vol. 44, no. 12, pp. 3631–3644, Dec. 2008.

[241] F. Scholkmann and M. Wolf, "General equation for the differential pathlength factor of the frontal human head depending on wavelength and age," *Journal of Biomedical Optics*, vol. 18, no. 10, Oct. 2013.

[242] S. J. Matcher, M. Cope, and D. T. Delpy, "In vivo measurements of the wavelength dependence of tissue-scattering coefficients between 760 and 900 nm measured with time-resolved spectroscopy," *Applied Optics*, vol. 36, no. 1, pp. 387–396, Jan. 1997.

[243] G. Xu and J. Yan, "Performance analysis of general charge sampling," *IEEE Trans. on Circuits and Systems – II: Express Briefs*, vol. 52, no. 2, pp. 107–111, Feb. 2005.

[244] S. J. Mason, "Feedback theory – some properties of signal flow graphs," *Proc. of the IRE*, vol. 41, pp. 1144–1156, Sept. 1953.

[245] J. A. Kaehler, "Periodic-switched filter networks – a means of amplifying and varying transfer functions," *IEEE Journal of Solid-State Circuits*, vol. 4, no. 4, pp. 225–230, Aug. 1969.

[246] R. L. Shuler, "Switched RC multi-pole filter," *NASA Symposium on VLSI Design*, Oct. 1999.

[247] K. N. Glaros, "Low-power pulse oximetry and transimpedance amplifiers," Ph.D. dissertation, Imperial College London, 2011.

Curriculum Vitae

Philipp Christoph Schönle
14th December 1986

Work Experience

since 2017	**Advanced Circuit Pursuit AG**, Zürich *Senior Design Engineer*
2011-2016	**Integrated Systems Laboratory**, ETH Zürich *Research & Teaching Assistant*
2008-2011	**Arcotronic AG**, Zürich *Part-time, R&D in Lighting Engineering*

Education

2011-2016	**Integrated Systems Laboratory**, ETH Zürich *Ph.D. Candidate in Electrical Engineering*
2006-2011	**ETH Zürich** *M.Sc. in Electrical Engineering*
1999-2005	**Gymnasium Klosterschule Disentis** *Grammar School: Focus Physics&Maths, interm. Latin*

Selected Publications

Conference Papers

[a] P. Schönle et al., "A power-efficient multi-channel PPG ASIC with 112dB receiver DR for pulse oximetry and NIRS," *IEEE Custom Integrated Circuits Conference (CICC)*, May 2017.

[b] D. Bellasi, P. Schönle et al., "A wide tuning-range ADFLL for mW-SoCs with dithering-enhanced accuracy in 65 nm CMOS," *Proc. IEEE Int. Symp. Circuits and Syst. (ISCAS)*, May 2017.

[c] P. Schönle et al., "A wireless system with stimulation and recording capabilities for interfacing peripheral nerves in rodents," *Annual Int. Conf. of the IEEE Engineering in Medicine and Biology Society (EMBC)*, pp. 4439-4442, Aug. 2016.

[d] D. Mack, P. Schönle et al., "An EOG-based, head-mounted eye tracker with 1 KHz sampling rate", *Proc. IEEE Biomedical Circuits and Systems Conference (BioCAS)*, Oct. 2015.

[e] P. Schönle et al., "Modular multi-sensor platform for portable and wireless medical instrumentation," *Proc. IEEE Biomedical Circuits and Systems Conference (BioCAS)*, pp. 165-168, Oct. 2014.

[f] P. Schönle et al., "A DC-connectable multi-channel biomedical data acquisition ASIC with mains frequency cancellation," *Proc. IEEE European Solid-State Circuits Conf. (ESSCIRC)*, pp. 149-152, Sept. 2013.

Journal Papers

[g] S. Fateh, P. Schönle et al., "A reconfigurable 5-to-14 bit SAR ADC for battery-powered medical instrumentation," *IEEE Trans. on Circuits Syst. I*, vol. 62, no. 11, pp. 2685-2694, Nov. 2015.

[h] P. Leidenberger, P. Schönle, C. Hafner, "Simulations of a dielectric slot tip for scanning near-field microwave microscope," *J. Comput. Theor. Nanos.*, vol. 8, no. 8, pp. 1556-1563, Aug. 2011.